Monte Carlo simulations and benchmarks for the radiological characterization of the LHC experiments

Zur Erlangung des akademischen Grades eines
Doktors der Naturwissenschaften (Dr. rer. nat.)
von der KIT-Fakultät für Physik des
Karlsruher Instituts für Technologie (KIT)

angenommene

DISSERTATION

von

Davide Bozzato, M. Sc.

aus Magenta (Italien)

Tag der mündlichen Prüfung: 26.05.2023

Referent:	PD Frank Hartmann	Institut für Experimentelle Teilchenphysik
Korreferent:	Prof. Dr. Thomas Müller	Institut für Experimentelle Teilchenphysik

Davide Bozzato:
Monte Carlo simulations and benchmarks for the radiological characterization of the LHC experiments
January 2023

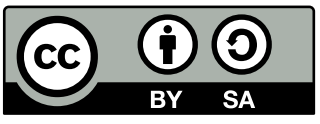

Ai miei genitori e a mia sorella
per il loro supporto incondizionato

Abstract

At high-energy accelerator facilities like the ones that are part of the accelerator complex at the European Organization for Nuclear Research (CERN), the typical radiation environment is characterized by the presence of various particle species whose energies can span from thermal energies up to hundreds or even thousands of GeV. One of the consequences of the operation of accelerators and collider experiments in these conditions is certainly induced activation in detector and infrastructure components.

Since it may impose access restrictions, safety requirements, installation of additional shielding, and more generally affect the technical operation of facilities, the calculation of induced radioactivity is an essential part in various steps of the life cycle of any component to be installed in accelerators or high-energy physics detectors. It is required during the design phase for the selection of appropriate materials, and it is of paramount importance for the estimation of residual dose rates for planned exposure situations during shutdown periods to establish the appropriate protection measures needed to keep doses to levels as low as reasonably achievable (ALARA principle). At the same time, the knowledge of the radionuclide inventory is fundamental for the decommissioning of the accelerators and detectors themselves to determine the appropriate pathways for the disposal of each component and the related costs.

The Large Hadron Collider (LHC) is expected to collect more integrated luminosity during Run 3 than in Run 1 and Run 2 combined and, to guarantee the full exploitation of its potential, the High Luminosity LHC (HL-LHC) project will aim to deliver an instantaneous luminosity which would be beyond the original design value by a factor of five to seven, allowing to almost tenfold the integrated luminosity by the early 2040s. With these expected harsher radiation conditions, the computation of induced radioactivity will soon become a more relevant and pressing need to fully ensure a smooth and safe operation of the LHC and its large experiments over a very extended period of time.

As soon as one deviates from simple textbook cases, the study of the generation and the time evolution of the induced radioactivity quickly becomes very challenging. As a consequence, Monte Carlo radiation transport codes have to be employed to face the non-trivial task of performing the radiological characterization of activated components at the LHC and LHC experiments. Radionuclide activities can be computed with several approaches, each with its advantages and disadvantages: these calculations seldom require very high accuracy, but on the other hand they must be efficiently performed in very complex problems for a large number of components and scenarios.

This thesis work was performed within the Radiation Protection group at CERN: one of the main objectives was the further development of a computational method to be applied in radiological characterization studies, in particular at the LHC experiments.

After a general introduction in Chapter 1, the basics of radiation-matter interaction mechanisms are recalled in Chapter 2: at the end of the chapter, the extended activation formalism is discussed together with relevant radiation protection aspects. Following a brief presentation in Chapter 3 of the two Monte Carlo codes used for the radiation simulations of this thesis work, Chapter 4 is entirely dedicated to the explanation of the novel fluence conversion coefficients method applied to radiological studies. Radiation protection assessments typically consist in estimating quantities defined within European or national regulations (hazard factors) to be compared with legally defined thresholds. The main idea behind this approach is to pre-compute energy- and particle-dependent coefficients for a given irradiation condition, material to be characterized, and hazard factor to be estimated: these coefficients can then be applied to fluence estimators during transport calculations allowing direct estimation of the desired hazard factors with the advantages of fast convergence, automatic normalization, and most importantly good visualization capabilities.

A second objective of this work was to extensively test the method and the radionuclide production database specifically produced for the task: Chapter 5 is fully dedicated to activation benchmarks tailored to practical applications of the method discussed in this thesis. Since the present work is mostly focused on the LHC experiments, CMS in particular, the benchmarks would have been ideally performed directly in the experiments radiation environments: owing to the shift in the Run 3 restart due to the Covid-19 pandemic, this was not a feasible solution. For many practical applications, similar irradiation conditions can be found at CERN irradiation facilities which, in virtue of their design, mimic the LHC radiation environment and permit to reach higher intensities allowing for shorter irradiations. Chapter 5 presents three different sets of experiments conducted at the CERN High energy AcceleRator Mixed field (CHARM) facility and a full-scale comparison with LHCb Run 2 activation samples data that had never been analysed before: all these benchmark data proved to be a very valuable input for a critical evaluation of the results of Chapter 6.

To fully illustrate the capabilities and advantages of the method even in very complex cases, Chapter 6 collects a selection of simulation studies for the LHC experiments that had important practical consequences. The first study is dedicated to the evaluation of the effectiveness of various solutions for the reinforcement of the present CMS forward shield, while the second focuses instead on the assessment of the activation of the steel of the absorber plates of the future CMS HGCal and on the consequences for its procurement. The third case presents a preliminary radiological zoning at ALICE for clearance and decommissioning operations in the Long Shutdown 3 and 4, and finally the last one presents radiation protection studies for ATLAS and CMS which significantly contributed to the preparation of the 2021 LHC pilot beam conducted as part of the commissioning of the LHC experiments and machine before the restart of the LHC with Run 3 in 2022.

Contents

Chapter 1

Introduction

The first chapter of this thesis work aims to give a general but effective introduction, setting the basis for what will be outlined in the following chapters. First, the Large Hadron Collider (LHC) will be presented and two of the most relevant parameters that characterise its performance and operation, namely the collision energy and the instantaneous luminosity, will be discussed. Then, the operational principles common to high-energy physics detectors will be introduced and, finally, a brief description of the four LHC experiments in their current status will be provided: whenever pertinent and useful for the subsequent discussions, the main features of the future upgrades of the detectors will be summarised.

1.1 The Large Hadron Collider

The Large Hadron Collider (LHC) [1] at the European Organization for Nuclear Research (CERN), is currently the largest two-ring, superconducting, hadron accelerator and collider. Built in the previously existing 26.7 km long tunnel hosting the LEP (Large Electron-Positron Collider), it is designed to accelerate proton beams up the energy of 7 TeV and fully stripped lead ions up to 2.76 TeV/nucleon. The 1232 main superconducting dipoles generate an 8.3 T field responsible for keeping the beams in their main orbit, quadrupoles impart the necessary focusing (either vertically or horizontally), while higher order multipoles (sextupoles, octupoles and decapoles) provide the necessary corrections.

The LHC is the last stage of the CERN accelerator complex. H^- ions are accelerated up to 160 MeV by the LINAC 4 and are then stripped of their two electrons before being injected into the Proton Synchrotron Booster (PSB). After reaching an energy of 2 GeV, protons are injected into the Proton Synchrotron (PS) where they are further accelerated to 25 GeV and are effectively packed in bunches having a 25 ns spacing: at this stage, the beams can be injected into the Super Proton Synchrotron (SPS) where they reach 450 GeV before being injected into the LHC. The LHC itself consists of eight arcs and eight straight sections, the latter serving as utility or experimental insertions. The four particle physics experiments, ATLAS, ALICE, CMS, and LHCb, are located respectively at Point 1, Point 2, Point 5, and Point 8, while the remaining

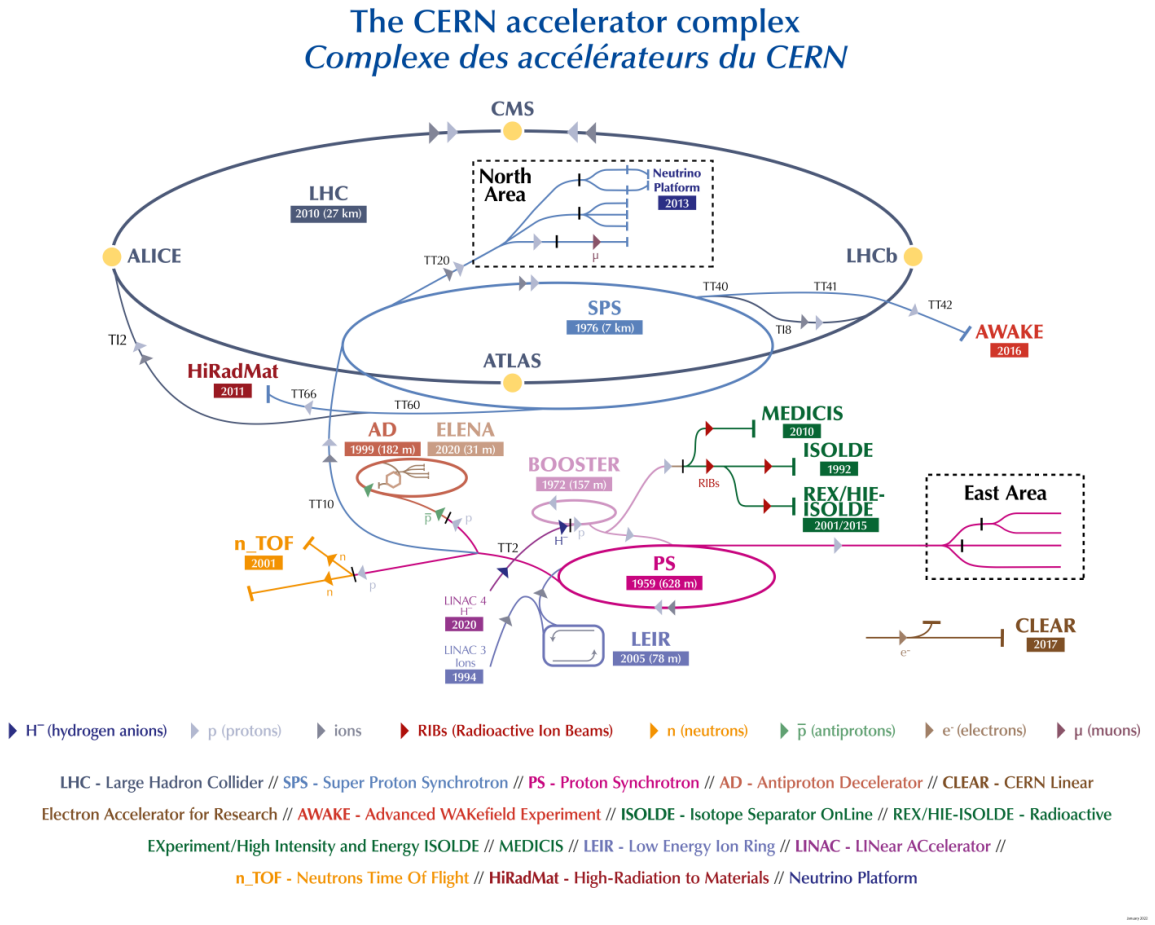

Figure 1.1: Layout of the CERN accelerator complex as of 2022 [2].

sections, not having beam crossings, contain collimators (Point 3 and 7), two radio-frequency systems (one for each beam, Point 4), and the beam dump systems (Point 6). A schematic overview of the accelerator complex and the location of the four LHC experiments is offered in figure 1.1, while a brief description of the experiments is given in Section 1.3.

The aim of the LHC is to collect major physics discoveries at the high-energy frontier. Even though the full potential of the machine was not being exploited, the recorded data in the period 2010-2012 allowed for the discovery of a particle consistent with the Standard Model Higgs boson [3, 4].

During the operational years 2010-2012, commonly referred to as Run 1, the LHC operated at beam energies of 3.5 TeV and 4 TeV in the first and second half respectively. After a first Long Shutdown (LS1, 2013-2015), operation resumed at the beam energy of 6.5 TeV for the full period 2015-2018, commonly referred to as Run 2: during this period, a record peak luminosity of $2.0 \times 10^{34}\,\mathrm{cm}^{-2}\,\mathrm{s}^{-1}$ was reached, twice the nominal design value. Both Run 1 and Run 2 also saw a mix of lead-lead and proton-lead setups provided during the last weeks of the operational year: the only exception was in 2017 when collisions between fully stripped xenon ions were provided instead.

During the years 2018-2022, the LHC complex was in LS 2 and the LHC machine

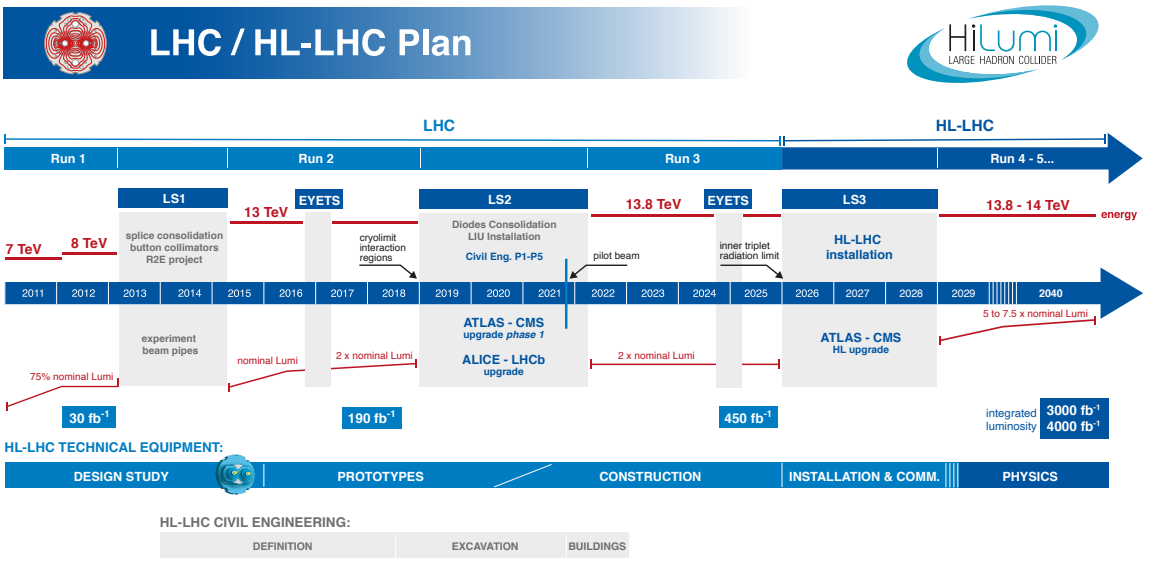

Figure 1.2: Current LHC baseline plan for the next decade and beyond, showing the collision energy (upper line) and luminosity (lower line) [5].

and experiments underwent several upgrades. For the former, these include the replacement of 22 superconducting magnets and improvement of electrical insulation of the magnet diodes, the consolidation of the support system of the beam dumps, the installation of new collimators, the installation of new internal and neutral beam absorbers, and finally the installation of high-performance cold boxes at Point 4 to increase the overall cryogenic power.

As a consequence of the Covid-19 pandemic, LS 2 was prolonged almost by one year with respect to what foreseen and, after a successful pilot beam run in October 2021, the LHC is now at the beginning of Run 3 and beams have been accelerated to the record energy of 6.8 TeV. During Run 3, presently scheduled to last till the end of 2025, it would be possible to collect more data than in the first two runs combined, allowing for precision measurements of the properties of the Higgs boson and search for physics beyond the Standard Model.

1.1.1 The High-Luminosity LHC

Figure 1.2 illustrates the currently foreseen plan for the LHC for the next decade and beyond. The third and three-year-long shutdown, LS 3, will be concluded by 2028 and it will be followed by the High-Luminosity LHC [6] (HL-LHC): for the LHC experiments this period is also commonly referred to as Phase II. Confirmed as the top priority of the European Strategy for Particle Physics [7], the HL-LHC upgrade project will ensure the full exploitation of the LHC potential, aiming to deliver an integrated luminosity of $250\,\mathrm{fb}^{-1}$ per year in ATLAS and CMS and to reach $5 \times 10^{34}\,\mathrm{cm}^{-2}\,\mathrm{s}^{-1}$ in peak instantaneous luminosity with levelling operation. Exploiting the design margins,

it is also expected that it will be possible to push the machine peak levelled luminosity to $7.5 \times 10^{34}\,\mathrm{cm}^{-2}\,\mathrm{s}^{-1}$ enabling the collection of 300 to $400\,\mathrm{fb}^{-1}$ per year: in terms of total integrated luminosity, the ultimate performance could then yield about $4000\,\mathrm{fb}^{-1}$. A brief comparison of the LHC and HL-LHC machine parameters is offered in table 1.1 in Section 1.2.2.

1.2 Performance of particle colliders

Two of the most important parameters that allow quantifying the performances of a particle collider are the collision energy and the instantaneous luminosity.

1.2.1 Colliding beams

The collision energy is the total energy available to two colliding particles and is then clearly setting an upper limit to the mass of new particles that can be produced in the process. For two particles having rest mass m and four-momenta p^μ and q^μ respectively, the energy available in the centre of mass system is given by the following relation:

$$E_{cm} = \sqrt{s} = \sqrt{(p_\mu + q_\mu) \cdot (p^\mu + q^\mu)} \tag{1.1}$$

In the specific case of two colliding particles for which $p^\mu = (E/c, \vec{p})$ and $q^\mu = (E/c, -\vec{p})$, the center of mass energy is $E_{cm} = \sqrt{s} = 2E$. In a fixed target experiment, for which for example $p^\mu = (E/c, \vec{p})$ and $q^\mu = (mc, 0)$, the center of mass energy would instead be $E_{cm} = \sqrt{s} = \sqrt{2m^2c^4 + 2mc^2E}$. Considering 7 TeV protons for a simple and yet valuable example, one would obtain $E_{cm} = 14\,\mathrm{TeV}$ in the first case and $E_{cm} = 114.6\,\mathrm{GeV}$ in the second one (approximately $\sqrt{2mc^2E}$).

1.2.2 The concept of luminosity

Particle colliders are built to investigate very rare physics events, that is phenomena characterized by a very low cross section. The rate of a certain process, dN_{ev}/dt, is related to its cross section through the instantaneous luminosity $\mathcal{L}_{inst}$:

$$\frac{dN_{ev}}{dt} = \mathcal{L}_{inst} \cdot \sigma \tag{1.2}$$

The instantaneous luminosity has the dimensions of $[\mathrm{length}^{-2} \cdot \mathrm{time}^{-1}]$ and it is often expressed in units of Hz/µb or $\mathrm{cm}^{-2}\,\mathrm{s}^{-1}$.

The instantaneous luminosity is a quantity that depends only on the machine/beam parameters and, under the hypothesis of Gaussian beams, for a particle collider it can be expressed as [1, 6]

$$\mathcal{L}_{inst} = \gamma \frac{k_b N_1 N_2 f}{4\pi\beta^* \varepsilon_n} F \tag{1.3}$$

Parameter		LHC (design)	HL-LHC (design)
Beam energy	E	7.0 TeV	7.0 TeV
Bunch population	N	1.15×10^{11}p.p.b.†	2.2×10^{11}p.p.b.†
Colliding bunch pairs	k_b	2808	2748
Revolution frequency	f	11 245 Hz	11 245 Hz
β function at IP 1 and IP 5	β^*	0.55 m	0.15 m
Normalized transverse emittance	ε_n	3.75 µm	2.5 µm
Half-crossing angle at IP 1 and IP 5	$\theta_{h.c.}$	142.5 µrad	250 µrad
Longitudinal bunch length (r.m.s.)	σ_z	7.55 cm	9.0 cm

† p.p.b. stands for protons per bunch.

Table 1.1: LHC and HL-LHC main machine design parameters for operation with a 25 ns bunch spacing [1, 6].

where γ is the relativistic gamma factor, k_b is the number of colliding bunch pairs at the interaction point (IP), N_1 and N_2 are the bunch populations of the first and second beam respectively, f is the revolution frequency in the machine, β^* is the value of the beta function at the IP, and ε_n is the normalized transverse emittance here assumed to be the same for the two beams. The factor F is a luminosity reduction factor which, in the more general case, takes into account the beams separation, the hourglass effect[1] and the presence of a crossing angle between the beams. Neglecting for simplicity the corrections that would be needed for the first two aforementioned effects, the luminosity reduction factor can be written as [1]:

$$F = \left(1 + \left(\frac{\theta_{h.c.}\sigma_z}{\sigma_t}\right)^2\right)^{-1/2} \tag{1.4}$$

where $\theta_{h.c}$ is the half-crossing angle between the beams and σ_z and σ_t are the r.m.s. longitudinal and transverse bunch sizes respectively.

Table 1.1 summarises the main nominal machine design parameters for the LHC and the foreseen HL-LHC operation: using these numbers and substituting them in equation 1.3, one obtains in this simplified approach an instantaneous luminosity of approximately $1.0 \times 10^{34}\,\mathrm{cm}^{-2}\,\mathrm{s}^{-1}$ and $7.0 \times 10^{34}\,\mathrm{cm}^{-2}\,\mathrm{s}^{-1}$ for the LHC and HL-LHC nominal operation. It is also interesting to estimate the average number of interactions per bunch crossing, or pile-up, which can be expressed as:

$$\mu = \sigma_{inel}\frac{\mathcal{L}_{inst}}{k_b f} \tag{1.5}$$

Assuming that σ_{inel} is 79.5 mb and 81 mb for collisions at 13 TeV and 14 TeV c.o.m. respectively [8], one obtains a pile-up of approximately 25 and 200 for the two cases. The increase in luminosity required for precision measurements of the Higgs boson and

[1]The hourglass effect accounts for the increase of the beta function upstream and downstream of the IP along the bunch longitudinal distribution.

the search of physics beyond the Standard Model comes with the price that the number of interactions per bunch crossing increases.

The luminosity is not constant with time during a physics run. This is mostly due to the fact that the two beams get depleted by the collisions (luminosity burn-off), but other effects can contribute: these include particle losses, interaction with residual gas in the vacuum chambers, and beam-beam interactions responsible for an emittance increase. An effective way of realistically describing the time evolution of the luminosity during a run is through a decaying exponential whose decay constant is simply the sum of the decay constants associated with all the different processes contributing to the luminosity decrease: as an order of magnitude, the luminosity lifetime in LHC nominal operation is of the order of 15 hours.

Since new physics discoveries depend ultimately on the total number of events collected (N_{ev}), an equally important figure of merit is the integrated luminosity $\mathcal{L}$, which is simply defined as the integral over a time period of $\mathcal{L}_{inst}$. The integrated luminosity is then connected to the total number of events by the relation that trivially follows from equation 1.2: $N_{ev} = \mathcal{L} \cdot \sigma$. $\mathcal{L}$ has the dimensions of [length^{-2}] and is often expressed in units of fb^{-1}. The luminosity integrated over an operational year depends clearly on the instantaneous luminosity, but also on other factors that contribute to the definition of the global machine availability, an efficiency parameter which can be seen as a measure of the effective time spent in stable beam operation. This particular aspect will be further developed in Section 4.8 in relation to the assumptions that it is necessary to make when performing predictive studies of the radiation levels in the LHC experiments.

A last but still pertinent remark on luminosity, is that the *delivered* luminosity to an experiment is what is relevant for any radiation study, and not the *recorded* one: indeed, the latter refers only to the luminosity measured in the time window in which the experiment was taking data and usually differs from what was delivered by the machine.

1.3 The LHC Experiments

The purpose of this section is to introduce the four LHC experiments, namely ATLAS, ALICE, CMS, and LHCb, as they are in their present status: a summary of their relevant upgrades beyond Run 3 will also be given whenever pertinent for the studies performed for this thesis work and that will be discussed in Chapter 6. Before briefly describing their main components and characteristics, it can be fruitful to summarise the operation principles that are common to high-energy physics detectors in general.

High-energy physics detectors operate by identifying the decay products of the fast-decaying particles produced in the collisions: their full characterization, including the determination of their momentum, energy, charge, mass, spin, and lifetime, is of paramount importance for the event reconstruction.

To achieve this challenging task, the high-energy physics detectors comprise several

sub-systems specifically designed and tuned to be sensitive to one or more types of particles (i.e., hadrons, muons, photons, electrons, and positrons). These essential components are a tracking system, a magnet system, calorimeters, muon detectors and, optionally, particle identification (PID) devices: by combining the various pieces of information provided by the sub-detectors, the full reconstruction and characterization of an event becomes possible [9].

The charge, the momentum, and the energy of charged particles can be determined by the inner tracking systems and outer muon detectors in combination with a suitable magnetic field which is providing the needed bending force. By stopping particles and absorbing their energy, calorimeters (electromagnetic and hadronic) measure the intrinsic particle energy. The mass of the particles may be estimated by combining the momentum information with a velocity measurement obtained in turn by means of an energy deposition measurement (dE/dx, see Section 2.1.1) or by another PID detector, such as a Time of Flight (ToF) system or a Ring Imaging Cherenkov (RICH) detector. A full angular momentum analysis would allow for a determination of the particle spin. Finally, the lifetime of very short-lived particles of interest can be inferred by measuring their path length from production to decay [9].

It is also helpful to describe at this stage the coordinate system that is commonly adopted by the LHC experiments and that will be referenced in the following sections and chapters. All the LHC experiments adopt a right-handed local coordinate system whose origin is set in correspondence of their nominal IP: the $x-$axis points from the IP towards the centre of the LHC ring, the $y-$axis points from the IP upwards, and the $z-$axis, whose orientation is determined in relation to the other two, lies on the beam-pipe axis. Since most of the experiments' sub-systems have an azimuthal symmetry around the $z-$axis, cylindrical coordinates are often employed, being r and φ the distance from the $z-$axis and the azimuthal angle around it. Given the polar angle θ with respect to the beam axis, the pseudorapidity η is given by the relation:

$$\eta = -\ln\left[\tan\left(\frac{\theta}{2}\right)\right] \tag{1.6}$$

1.3.1 ATLAS

Being approximately 46 m long and 25 m wide, the ATLAS (A Toroidal LHC Apparatus) detector [10, 11] is the largest detector in operation at the LHC and was designed to investigate a wide physics program, from the Higgs boson search and precision measurements of the Standard Model to the search of new physics. The sub-detectors are placed in an onion-shell arrangement with the barrel systems being complemented by forward equivalents to guarantee almost a 4π coverage. A schematic overview of the ATLAS detector is offered in figure 1.3.

As of Run 3, the inner detector system is composed, in sequence, of a Pixel Detector (four-layer barrel, three-disk endcaps), a Semiconductor Tracker (four-layer barrel, nine-disk endcaps) and a Transition Radiation Tracker which allows for electron/pion discrimination.

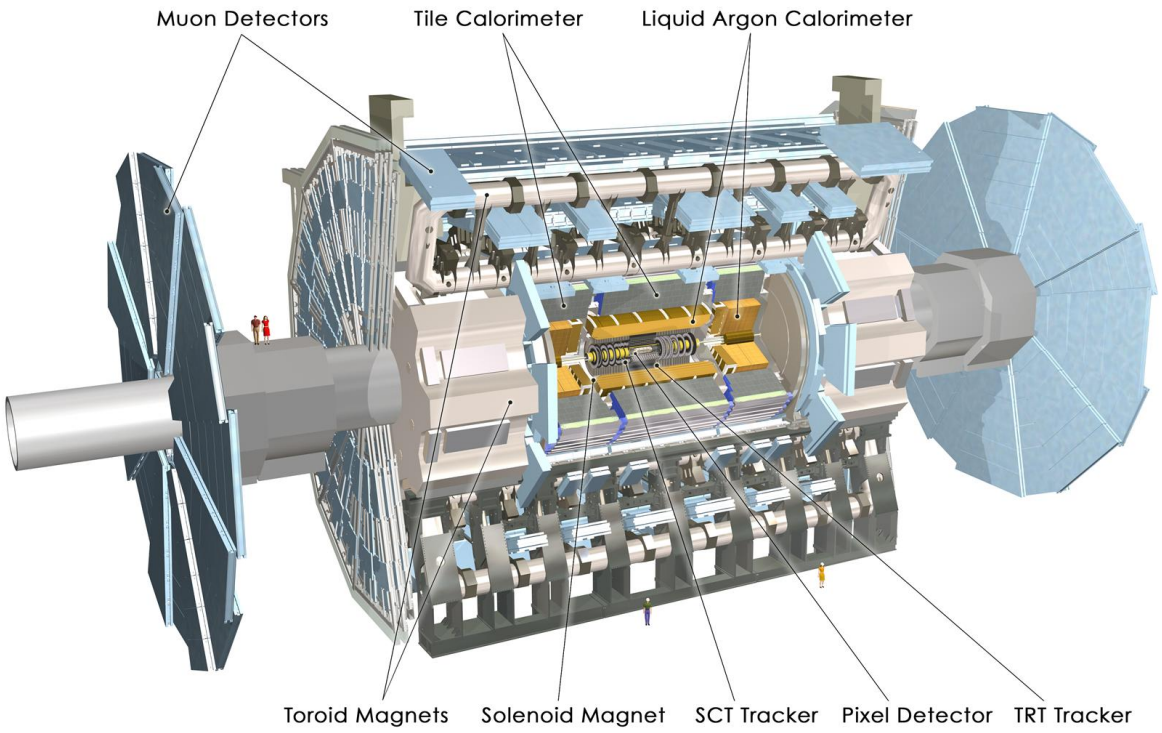

Figure 1.3: Schematic drawing of the ATLAS detector and its main components [10].

The Liquid Argon (LAr) Calorimeter surrounds the inner detector: particle showers are initiated on layers of metals (tungsten, copper, or lead) while the liquid argon serves as active medium. The LAr Calorimeter is used for both electromagnetic and hadronic calorimetry and, including the endcap calorimeter, provides coverage around the IP up to $|\eta| < 4.9$. The Tile Calorimeter (steel and scintillator sampling calorimeter) was designed around the LAr Calorimeter in order to measure the energy of hadrons that are not fully stopped by the previous system.

The bending force to charged particles is provided by a superconducting magnet system which is constituted by a central 2 T solenoid surrounding the inner detectors, one eight-coil barrel toroid (25.3 m long, 20.1 m in diameter) and two endcap eight-coil toroids (5.0 m long, 10.7 m in diameter) respectively providing a field integral up to 5.5 Tm and 7.5 Tm [11].

Last but surely not least, the muon spectrometer complements the function of the other sub-detectors by identifying muons and measuring their momentum. Different technologies are employed depending on the location: monitored drift tubes for track measurements are installed in the barrel and the endcap big wheels, thin gap chambers for triggering and coordinate measurement in the non-bending direction are also mounted on the endcap big wheels, while resistive plate chambers for triggering and coordinate measurement are present in the barrel layers only. As part of the upgrades performed during LS 2 and which will serve not only for Run 3 but also for the HL-LHC, new endcap small wheels were installed replacing the old small wheels (cathode strip chambers) [12]: these new additions deploy micromegas and small-strip thin-gap

chambers for improved resolution and better trigger capabilities. Also during LS 2, 8 small diameter monitored drift tube modules and 16 next-generation resistive plate chambers were installed in the inner barrel layer of the muon system and, being able to withstand higher rates, are now being used as test modules for future HL-LHC installations.

ATLAS upgrades beyond Run 3

To cope with the challenging conditions that the HL-LHC will pose, ATLAS will undergo extensive upgrades during the next LS 3. Among the most relevant ones, the present Inner Detectors will be completely replaced by a silicon strip and silicon pixel tracker (Inner Tracker, ITk) [13, 14] which will extend the acceptance up to $|\eta| = 4.0$. To improve timing capabilities and mitigate the consequences of the pile-up increase in the forward region, a silicon High Granularity Timing Detector (HGTD) will also be installed to cover the range $2.4 < |\eta| < 4.0$ [15].

1.3.2 ALICE

ALICE (A Large Ion Collider Experiment) [16, 17] is a 10 000 tons detector built to study the quark-gluon plasma which forms under the extreme energy density and temperature conditions that can be obtained in nucleus-nucleus collisions. The ALICE detector is approximately 26 m long and 16 m in diameter and it hosts within its volume several different sub-systems, each designed to achieve the established physics goals. As it is shown in the schematic drawing in figure 1.4, the ALICE detector can be considered as the union of a central barrel part, which is embedded in the large solenoid from the L3 experiment of LEP, and of a forward muon spectrometer.

The two innermost systems are the Inner Tracking System (ITS) and the Time Projection Chamber (TPC). Until the end of 2018, the ITS consisted of two layers of Silicon Pixel Detectors (SPD), two layers of Silicon Drift Detectors (SDD), and two outer layers of Silicon Strip Detectors (SDD). During LS 2 this system has been replaced by a new ITS consisting of 7 layers of silicon pixel sensors for a total of $10\,\mathrm{m}^2$ active surface. The ALICE TPC has a cylindrical drift volume of approximately $90\,\mathrm{m}^3$ and the readout is now performed by means of Gas Electron Multiplier (GEM) detectors which have replaced the old Multi-Wire Proportional Chambers and will allow reconstructing tracks from lead-lead collisions up to rates of 50 kHz. The information from the ITS and the TPC is used for tracking and particle identification by means of dE/dx measurement. Still within the innermost volume, between the ITS and the absorber around the beam pipe, the Muon Forward Tracker (MFT) has been recently installed: it consists of silicon pixel sensors of the same kind as the ones employed in the ITS for a total of $0.5\,\mathrm{m}^2$ of active surface and it will provide high-resolution tracking towards the forward rapidity region.

The ALICE experiment has excellent particle identification capabilities since it is equipped with three additional PID systems installed around the inner systems: in sequence, one finds the Transition Radiation Detector (TRD), the Time Of Flight

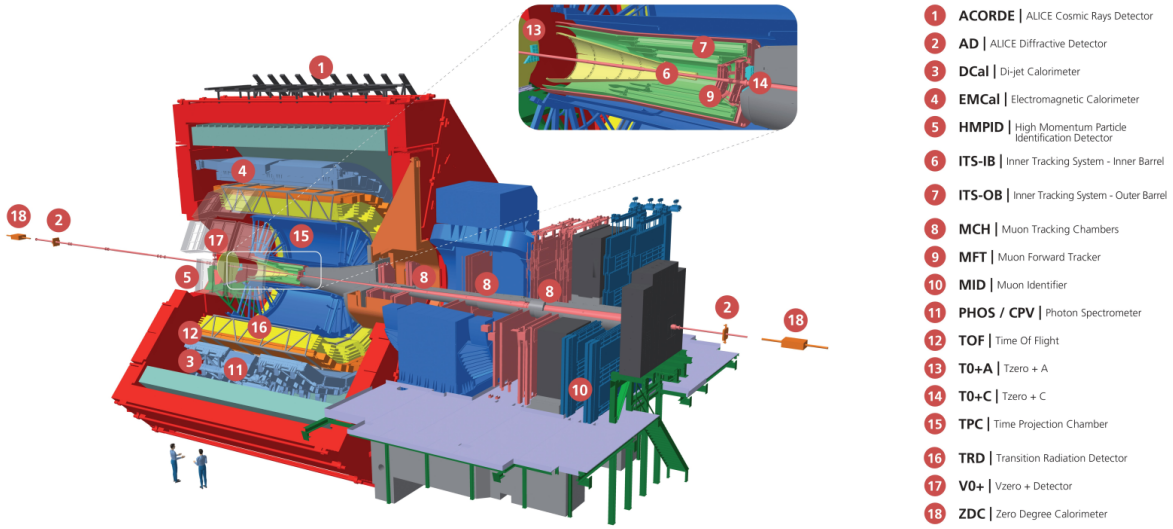

Figure 1.4: Schematic drawing of the ALICE detector and its main components [18].

detector (TOF), and the High Momentum Particle Identification Detector (HMPID) based on a ring imaging Cherenkov detector.

Measurement of the energy of photons is performed by the Photon Spectrometer (PHOS), which is based on lead-tungstate ($PbWO_4$) scintillator crystals and has a limited acceptance range to the central pseudorapidity, and the Electromagnetic Calorimeter (EMCal), a lead-scintillator sampling calorimeter with an acceptance of $|\eta| < 0.7$: EMCal does not cover the full azimuth and opposite to it one finds the lead-scintillator Di-jet Calorimeter (DCal), optimized for the measurements of back-to-back jets.

The ALICE forward arm covers the small angular range between 2° and 9°: it consists of ten planes of cathode strip chambers arranged before and after a dipole magnet with a 3 T m field integral, and four resistive plate chambers used for muon identification and triggering. Heavy composite absorbers and iron absorbers are used to highly suppress hadrons while a dense conical tube of approximately 60 cm outer diameter is used to suppress the particles created by the collision secondaries in the beam pipe.

In addition to the main larger systems briefly described so far, ALICE employs a set of small ancillary detectors, mostly located at very forward angles, which provide global event characterization and trigger. The upgraded T0 and V0 detectors (T0+ and V0+), the Zero Degree Calorimeter (ZDC) and the ALICE Diffractive detector (AD) are now part of the new Fast Interaction Trigger (FIT). Finally, the ALICE Comic Ray Detector (ACORDE) located on top of the L3 magnet provides trigger against cosmic rays.

ALICE upgrades beyond Run 3

Albeit at the time of writing the long-term schedule of the LHC does not officially foresee an extension of the heavy-ion program after Run 4, there are two relevant upgrades foreseen during LS 3 that are worth mentioning. The first proposed is the

replacement of the three layers of the ITS [19]: the new system will consist of three cylindrical layers of silicon sensors featuring an extremely low material budget (about 0.05% x/X_0 per layer) and with the first layer installed at a radial distance of 18 mm from the IP. The second upgrade scheduled for LS 3 is the addition of a Forward Calorimeter (FoCal) [20] located approximately at 7 m from the IP and which will cover the pseudorapidity range $3.4 < \eta < 5.8$: it will consist of an electromagnetic calorimeter ($20X_0$) with 18 layers of tungsten absorbers and silicon sensors, and a sampling hadronic calorimeter ($6\lambda_I$).

1.3.3 CMS

The Compact Muon Solenoid (CMS) [23, 24] is a large general-purpose detector at the LHC built to both perform precision measurements of the Standard Model and investigate the physics beyond it: located near Cessy (France), its overall dimensions are approximately 25 m in length, 15 m in diameter and 14 000 tons in weight. As it can be seen from the schematic layout offered in figure 1.5, CMS is composed of several sub-detectors that are placed, as is often the case, in an onion-shell arrangement: all the systems in the barrel region have a forward equivalent (endcap) on either side of the IP to guarantee as much as possible the hermeticity of the detector. As explained in the previous sections, each sub-system of a high-energy physics detector has to be designed and optimised to perform a specific measurement with the ultimate aim of reconstructing collision events. Figure 1.6 qualitatively illustrates for one slice of CMS how different particles can interact with the various detectors producing useful signal: particles that leave the system without interacting (e.g. neutrinos) are reconstructed from the deficit of transverse energy.

One of the many unique features of CMS is its large superconducting solenoid which, having a diameter of approximately 7 m and a length of 13 m, is the largest ever built. The niobium-titanium (NbTi) coils operating at 4 K generate a magnetic field up to 3.8 T: this is an element of paramount importance since by bending the trajectory of charged particles allows for the measurement of their momenta with good resolution.

To reconstruct the tracks of charged particles and perform particle identification by means of dE/dx measurements, CMS deploys a silicon tracking system that is currently the largest in the world. In its innermost part, the system is constituted by a four-layer barrel, three-disk endcaps silicon Pixel detector which covers up to $|\eta| = 3.0$. The Pixel detector is then followed by a silicon strip Tracker which is organized in a four-layer inner barrel (TIB) complemented by a three-disk inner endcap on each side (TID), and a six-layer outer barrel (TOB) with two nine-disk endcaps (TEC). The overall system covers approximately the range $|\eta| < 2.5$.

The Tracker is followed by the Electromagnetic Calorimeter (ECAL) which is a homogeneous calorimeter employing lead-tungstate ($PbWO_4$) crystals. In total there are nearly 61 000 crystals in the barrel calorimeter and 7300 in each of the two endcaps: the crystals have a cross section area of 2.2 cm × 2.2 cm and are 23 cm long (approximately 25 X_0). Including the lead and silicon pre-shower detector installed in the

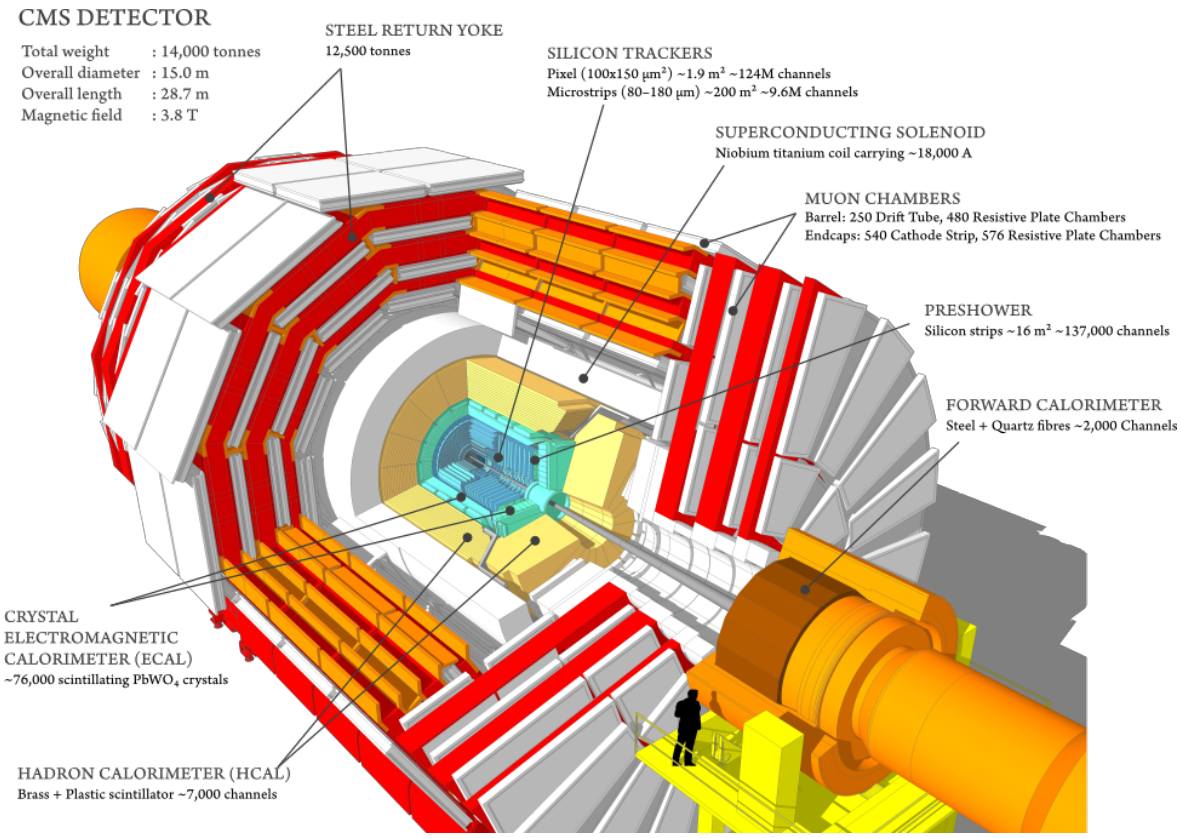

Figure 1.5: Schematic drawing of the CMS detector and its main components [21].

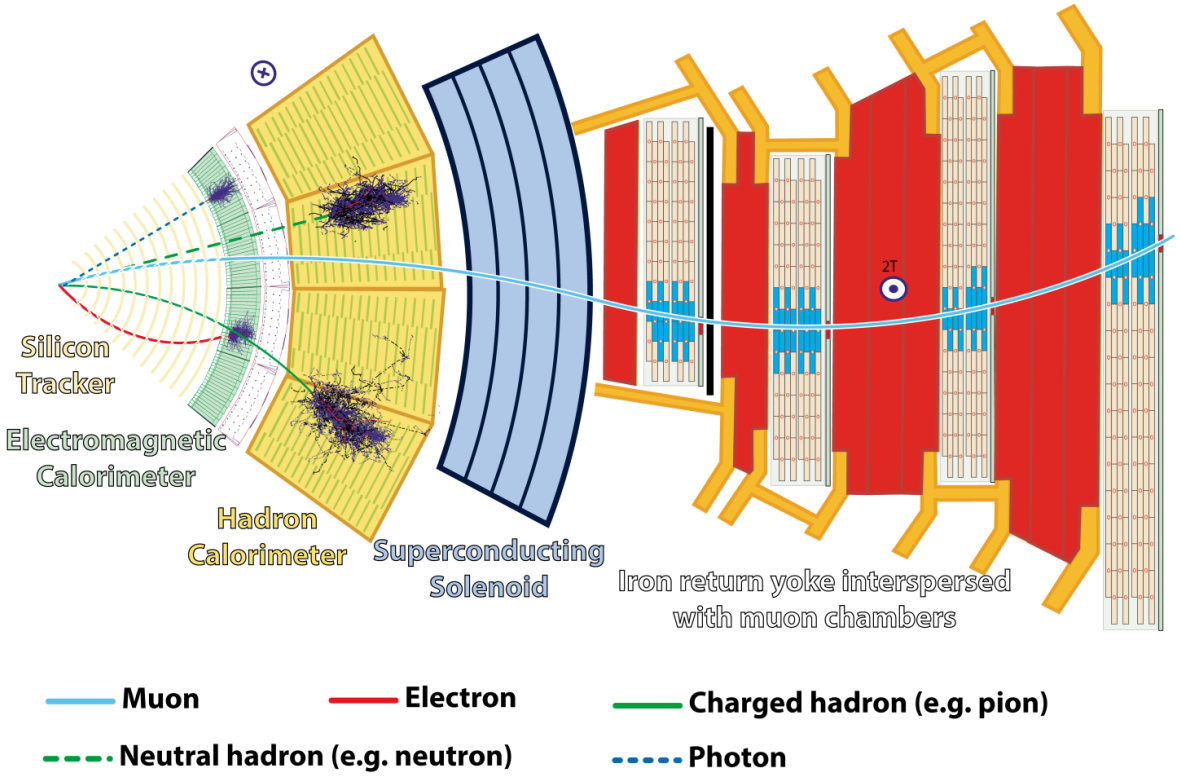

Figure 1.6: Drawing of one slice of CMS showing how different particles can interact with the different sub-detectors generating useful signal [22].

endcaps, the pseudorapidity acceptance of ECAL is $|\eta| < 3$. Surrounding ECAL, one finds the hadronic calorimeter (HCAL), a sampling calorimeter (brass and scintillator tiles) covering up to $|\eta| = 3$: coverage up to $|\eta| = 5$ is provided by iron/quartz-fibre forward calorimeters (HF) located approximately at 11.5 m from the IP.

While the tracking and the calorimetric systems (with the only exception of HF) are hosted within the magnet volume, the CMS muon system is outside it and its various detector stations are interleaved with the massive iron return yokes. Muon tracking and identification is one of the most important tasks of CMS and several detector solutions are being employed. Four layers of Drift Tubes (DT) chambers and Resistive Plate Chambers (RPC) form the barrel part of the muon system, while Cathode Strip Chambers (CSC), RPCs and Gas Electron Multiplier (GEM) chambers are arranged in between the endcap disks. Indeed, during the last LS 2, 144 GEM detectors have been installed in the two endcaps (36 modules per endcap, two detectors per module): these cover a cone of approximately 10° with respect to the beam axis and, although additional chambers will be installed before HL-LHC, these stations effectively constitute the first Phase II system to be already installed in CMS and already contributing to physics data taking.

As for all the LHC experiments, the trigger system is an invisible and yet critical one. The amount of data recorded by the different detectors amounts approximately to 1 MB per collision event: with a bunch crossing rate of 40 MHz it becomes impossible with existing technologies to read-out or store this large amount of data. The so-called Level-1 Trigger [25], a hardware system based on commercial Field Programmable Gate Arrays (FPGAs) and custom-made Application Specific Integrated Circuits (ASICs), decides within approximately 3.4 µs whether to trigger the other systems or not based on the information from the calorimeters and the muon detectors: this first stage reduces the event rate to about 100 kHz. The second stage, the so-called High Level Trigger, is software-based and allows to further reduce the event rate down to a couple of kHz.

CMS upgrades beyond Run 3

The Phase II upgrades of CMS will be necessary to maintain the outstanding performances of the detector while coping with the challenging radiation conditions imposed by the HL-LHC operation. The Phase II Inner and Outer Tracker [26] will have to be more radiation tolerant and with a higher granularity to keep the channel occupancy below few percent even at a pile-up of 200. The Inner Tracker will comprise a four-layer barrel complemented by two twelve-disk endcaps both instrumented with silicon pixel sensors: with this new layout, the pseudorapidity coverage will be extended up to $|\eta| = 4.0$. The Outer Tracker will be instead composed of a six-layer barrel having on each side a five double-disk endcap: the first three layers and the inner rings of the endcaps will consist of modules with a macro pixel and a strip sensor (the so-called PS modules), while for the outer layers the modules will have strip sensors (the so-called 2S modules). A schematic drawing of one quarter of the Phase II CMS Tracker is offered in figure 1.7. One of the major novelties introduced with the new Outer Tracker

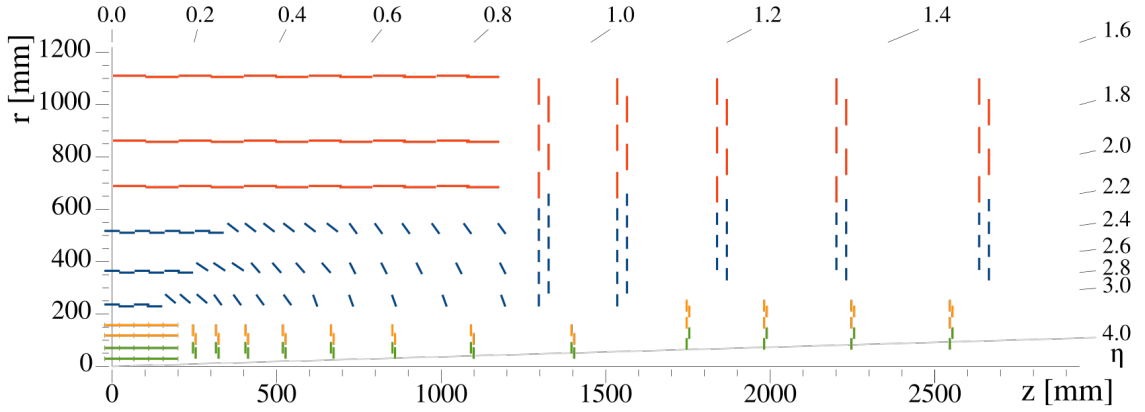

Figure 1.7: Schematic drawing of one quarter of the Phase II CMS Tracker. Each coloured line corresponds to a sensor layer: green and yellow lines correspond to Inner Tracker modules with respectively two and four readout chips, double blue and double red lines represent PS and 2S Outer Tracker modules [26].

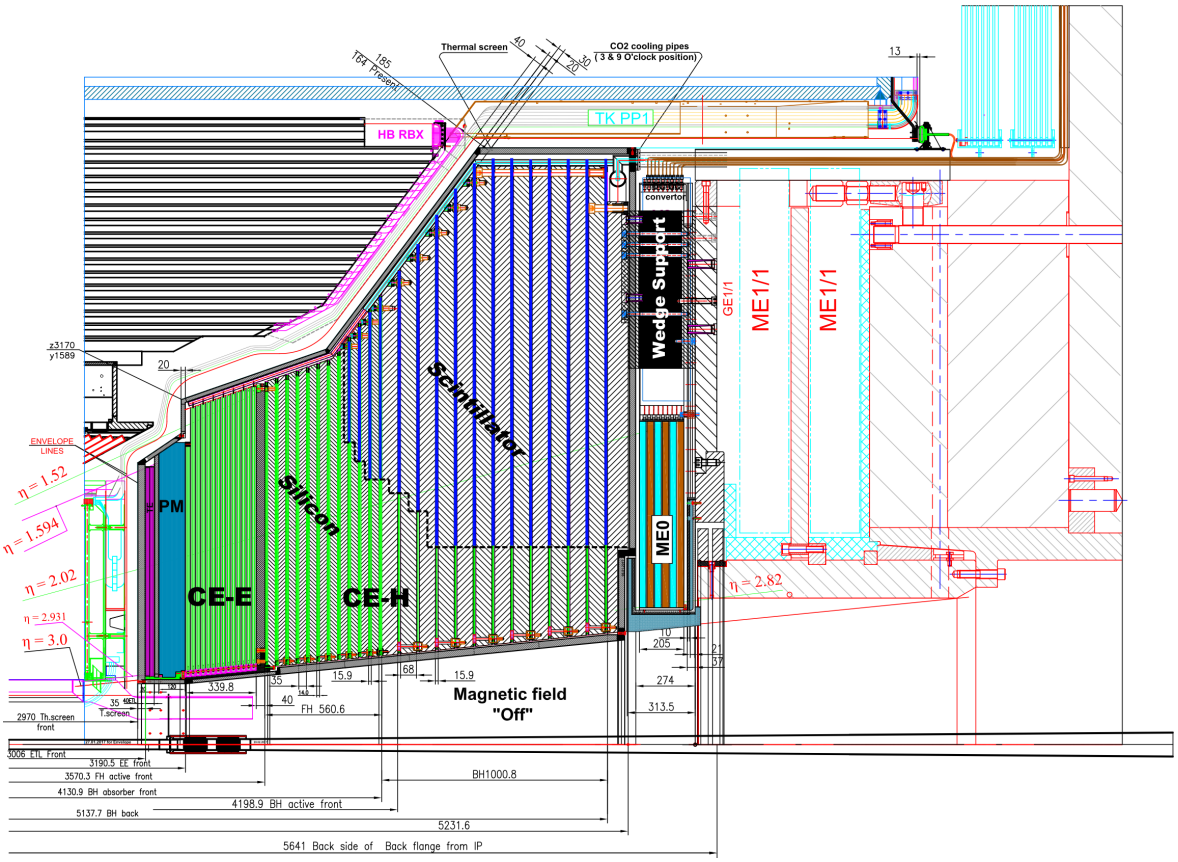

Figure 1.8: Longitudinal cross section of the upper half of the CMS High Granularity Calorimeter [27].

will be the possibility to contribute to the Level 1 Trigger: its modules (2S and PS, also referred to as p_T modules) will allow selecting particles with transverse momentum above a certain threshold and a hardware-based logic will perform real-time tracking of the selected particles supporting the decision of the Level 1 Trigger.

The MIP Timing Detector (MTD) [28] will be a new addition to CMS: this detector will allow resolving collisions that occur close together in space during bunch crossing but are distributed in time with an r.m.s. of 180 ps due to the longitudinal extension of the bunches themselves. The MTD will provide timing both in the barrel and in the endcap with a resolution of 30 ps at the start of operation and a 60 ps end-of-life (EOL) resolution: the barrel layer (BTL) located at 114.8 cm from the beam axis and covering up to $|\eta| < 1.48$ will be employing LYSO crystals with a readout based on silicon photomultipliers, while the endcap layers (ETL) located approximately at ± 3 m from the IP and with an acceptance of $1.6 < |\eta| < 3.0$ will employ Low Gain Avalanche Detectors (LGADs) due to the harsher radiation conditions.

The present endcap calorimeters were designed for an integrated luminosity of approximately 500 fb^{-1} above which the degradation of their performance would lead to an unacceptable loss in physics performance. The CMS Collaboration will replace the existing systems with a High Granularity Calorimeter (HGCal) [27] which will have to be more radiation tolerant, highly dense to preserve the shower compactness, and with a high transverse and longitudinal granularity for improved energy resolution, pattern recognition and discrimination against high pile-up. Figure 1.8 shows a schematic view of the longitudinal cross section of the upper of HGCal: HGCal consists of a total of 47 sampling layers[2] subdivided between an electromagnetic and hadronic compartment, labelled respectively as CE-E and CE-H in figure 1.8, embedded in a thermally shielded volume maintained at $-30\,^{\circ}\text{C}$. The electromagnetic part will comprise 26 sampling layers whose modules are constituted by silicon sensors sandwiched between a copper-tungstate baseplate and a printed circuit board: the modules are tiled on either side of a copper cooling plate which forms an absorber layer together with the copper-tungstate baseplates, while the alternate absorber is made out of lead cladded in stainless steel. The absorber of the hadronic compartment is instead entirely made out of austenitic stainless steel and it consists of 21 plates whose thickness can be of 3.5 cm or 6.8 cm depending on the distance from the IP: in the gaps between the absorber layers, silicon modules and scintillator tiles are mounted on copper cooling plates. As it is shown in figure 1.8, the radius at which the active element changes from silicon to scintillator is different for each layer and was determined by considerations on the tolerable light loss in scintillators due to the radiation levels.

Finally, also the muon detectors will undergo relevant upgrades. The measurements of muons in the very forward region will be enhanced by adding new forward detectors extending the acceptance to $|\eta| = 2.4$: the first and second muon stations will be equipped with GEM detectors, while improved RPC detectors will be added to the third and fourth muon stations.

[2]With respect to the initial design of HGCal shown in figure 1.8, the number of layers has been reduced from 28 to 26 in the electromagnetic compartment, and from 24 to 21 in the hadronic one.

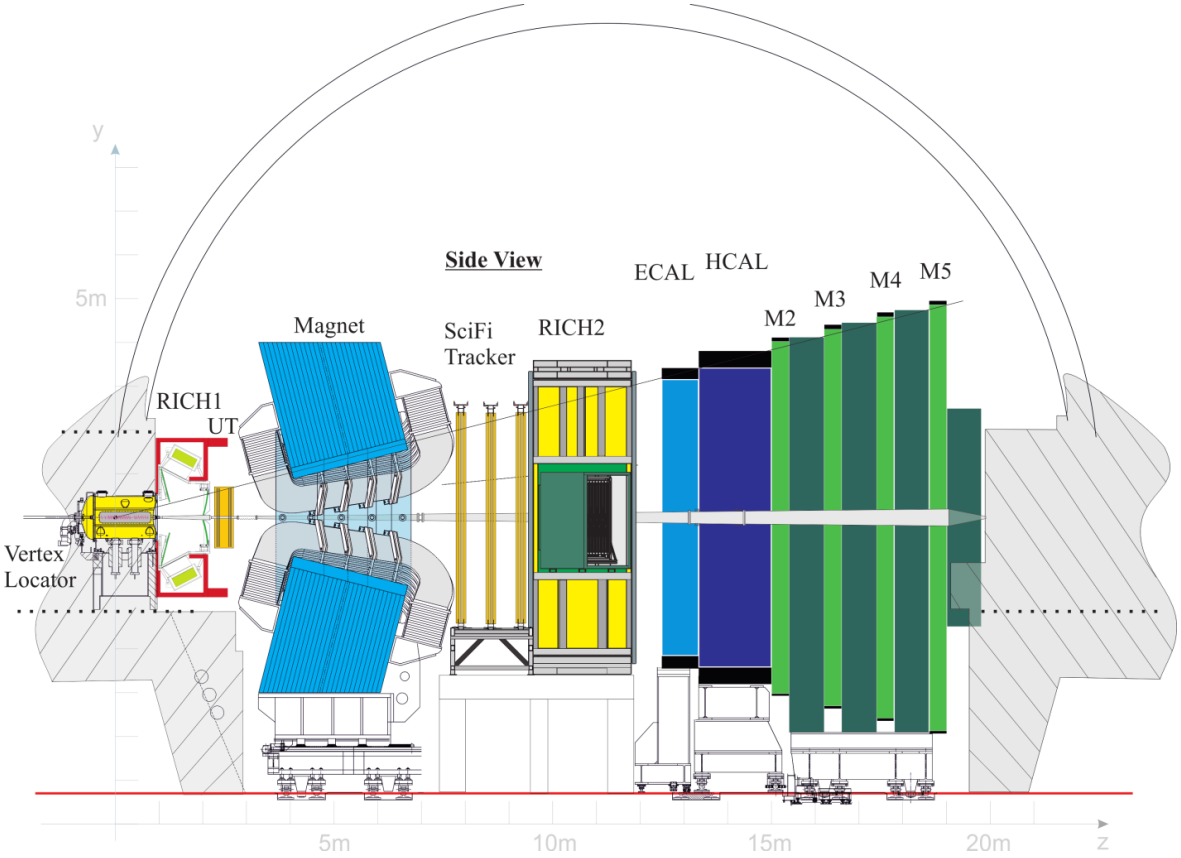

Figure 1.9: Schematic drawing of the LHCb detector and its main components [29].

1.3.4 LHCb

The LHCb (LHC-*beauty*) experiment [30, 31] was built to primarily perform precision measurements of the decay of B mesons and the investigation of CP violation. Its design is driven by the fact that the b and $\bar{b}$ pairs from high-energy proton-proton collisions are produced in the same direction and at small polar angles with respect to the beam axis. For this reason, LHCb is a 21 m long, 10 m high and 13 m wide single-arm forward spectrometer with an angular acceptance of 10 mrad–250 mrad and 10 mrad–300 mrad in the vertical and horizontal planes respectively (approximately $2 < \eta < 5$): a schematic side view of the experiment is shown in figure 1.9.

One of the largest components of LHCb is the dipole magnet located approximately 5 m away from the IP: with its saddle-shaped aluminium coils embedded in a carbon steel yoke, it generates a magnetic field having a 4 Tm field integral providing the bending power necessary to measure the momenta of charged particles with good resolution. During the data taking period, the magnet polarity is periodically switched aiming to reduce systematic measurement uncertainties due to possible left-right asymmetries.

Performing precision measurements of the B meson system requires excellent reconstruction of secondary vertices, tracking and particle identification capabilities. The VErtex LOcator (VELO) system is a silicon detector surrounding the interaction region and has been recently upgraded to cope with instantaneous luminosities up to five times what was achieved during Run 2 and to operate with a 40 MHz readout. Until

the end of 2018, it consisted of two retractable halves each with 21 silicon strip modules whose innermost channels could get as close as 8 mm to the beams in stable conditions. At present, the VELO is constituted of approximately 41 million pixels arranged in 52 modules (26 for each half) that can even be as close as 5.1 mm to the beams. Since the two halves of the VELO are retractable, the whole system is operated in a secondary vacuum.

For reasons similar to those for the VELO upgrade, the LHCb tracking system has also been improved during the past LS 2. The once Tracker Turicensis (TT) was placed upstream of the dipole and right after the VELO and was used for the track reconstruction of particles decaying outside the sensitive volume of the latter: it will now be replaced by a four-layer silicon strip detector called Upstream Tracker (UT). The three tracking stations (T1, T2 and T3) downstream of the magnet employed two different technologies: silicon strips were used at high pseudorapidity (Inner Tracker, IT), while straw drift tubes (Outer Tracker, OT) were used at lower pseudorapidity. The T-stations have been completely substituted by the Scintillating Fibre Tracker (SciFi) which is composed of twelve layers of 2.5 m long scintillating fibres arranged in vertical direction and read-out by silicon photomultipliers.

Two ring imaging Cherenkov detectors, one placed upstream of the dipole (RICH1) and one downstream of the tracker (RICH2), provide identification capabilities for particles in the momentum ranges of 2 GeV/c–60 GeV/c and 15 GeV/c–150 GeV/c respectively.

To measure the energy of electrons, photons and charged hadrons, LHCb is equipped with a calorimetric system which comprises a pre-shower detector (PS/SPD), an electromagnetic (ECAL) and a hadronic (HCAL) calorimeter. They are both sampling calorimeters but ECAL is made of lead and scintillator tiles while HCAL employs iron and scintillator tiles running parallel to the beam axis.

Finally, five stations are used for muon tracking and identification: the first one (M1) consists of a combination of GEM detectors at low η and Multi-Wire Proportional Chambers at high η and is placed in front of the calorimeters for triggering. The other four Multi-Wire Proportional Chambers, M2 to M5, are placed downstream of HCAL and are interleaved with iron filters.

LHCb upgrades beyond Run 3

The major improvements of the LHCb Upgrade I were successfully concluded during the past LS 2 and the second part of the proposed upgrades (Upgrade II) would be scheduled during LS 4: the goal of this upgrade would be to operate the detector at the maximum instantaneous luminosity of $1.5\times10^{34}\,\mathrm{cm}^{-2}\mathrm{s}^{-1}$ and a pile-up of approximately 40, and ultimately integrate up to $300\,\mathrm{fb}^{-1}$ over the whole HL-LHC [32]. To cope with the harsher conditions, the existing spectrometer component will have to be replaced to increase granularity, reduce the material budget in the spectrometer acceptance and, most importantly, include precision timing of the order of a few tens of ps: due to the higher pile-up, the latter will be essential across a number of sub-systems to allow the association of secondary particles with the correct interaction vertex.

The current arrangement of the sub-detectors will be largely maintained. The tracking system will consist of a Vertex Locator (VELO), tracking stations covering the magnet side walls (Magnet Stations, MS), and stations placed upstream (Upstream Tracker, UT) and downstream of the magnet (Mighty Tracker, MT): the latter will consist of a Silicon Tracker covering the inner region, and a Scintillating Fibre Tracker (SciFi) covering the outer region. A time-of-flight detector with a time resolution of a few tens of ps (TORCH) will also be added in front of RICH2. Finally, extra shielding will be required in front of the muon detector and this can be achieved by replacing HCAL with up to 1.7 m of iron.

Chapter 2

Interaction of radiation with matter

The knowledge of the principles of particle-matter interactions is clearly needed to understand how particle detectors work. In addition, it is of paramount importance to explain and predict the macroscopic consequences that these interactions can lead to, primarily radiation damage and induced activation. The performance of electronic devices exposed to harsh radiation conditions can indeed be degraded or, over extended periods of time, even compromised. At the same time, induced activation may impose access restrictions, installation of additional shielding to reduce residual radiation levels in planned interventions, and the proper assessment of the disposal pathways of activated components at the end of their useful lifetime.

This subject poses itself to be quite extensive since many particles are of interest (hadrons, leptons, and photons) and the energy range spanned by them can easily be quite vast as well. Therefore, this chapter aims to provide the necessary pieces of information required to explain the basic working principles of high-energy detectors and, most importantly, to introduce with the needed formalism all the radiation-related quantities that will be referred in the calculations and benchmarks detailed in the second half of this work.

2.1 Main radiation-matter interaction mechanisms

By considering the valuable example of high-energy protons impacting on a target material, it is possible to have an effective overview of the most relevant interaction mechanisms, from the high-energy to the very low-energy ones. After losing a small fraction of their energy due to ionisation in the material, the protons will be most likely subject to a nuclear inelastic interaction generating secondary hadrons (Section 2.1.4): some of these secondaries may have in turn enough energy to sustain a hadronic cascade (Section 2.1.5). Some hadrons, π^0 for example, will almost instantly decay and the high-energy decay products can initiate an electromagnetic shower (Section 2.1.3). The energy of the particles populating the two showers will progressively decrease from one generation to another until the hadron energies fall below the pion production threshold (Section 2.1.5), and the electron and positron energies fall below the critical energy (Sections 2.1.1 and 2.1.2). The nuclear interactions can also give rise to neutrons with

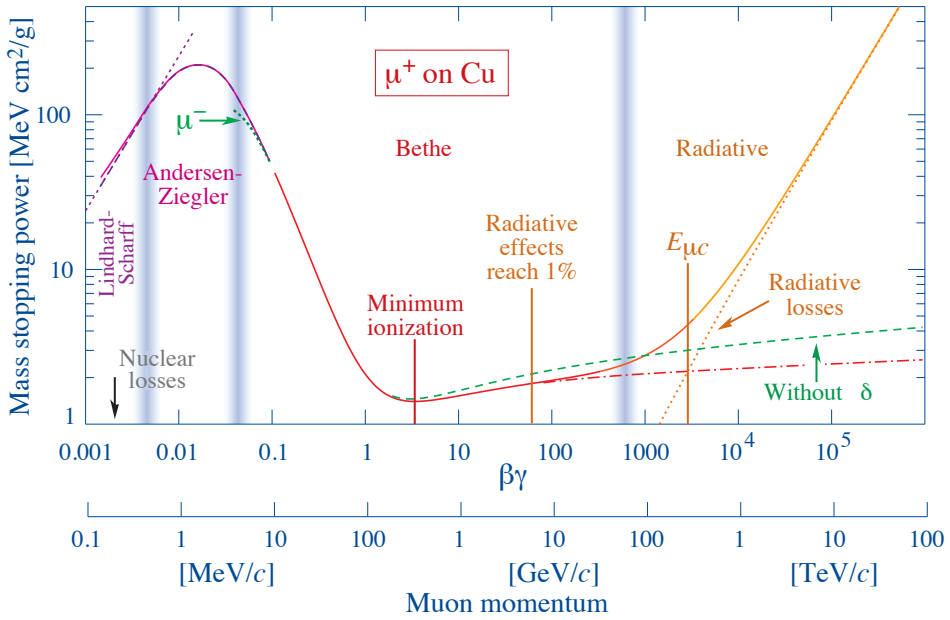

Figure 2.1: Mass stopping power for positive muons in copper as a function of $\beta\gamma$. The total mass stopping power is represented by the solid line [33].

relatively low energy which can undergo several elastic nuclear collisions until they are thermalized and captured. Finally, residual radiation will be emitted by the decaying unstable nuclei left as a result of these processes.

2.1.1 Charged particles interactions

Ionising energy loss

Charged particles travelling inside a material are subject to Coulomb interactions with atomic electrons leading to the excitation or the ionisation of atoms with the consequent emission of electrons. For charged particles heavier than electrons, that is moderately relativistic hadrons and muons, the average energy loss per unit path length due to ionisations, also called electronic stopping power or collision energy loss, is described by the Bethe formula [33, 34]:

$$\left\langle -\frac{dE}{dx} \right\rangle_{coll} = \frac{e^4 z^2}{4\pi\varepsilon_0^2 m_e c^2 \beta^2} \frac{\rho N_{AV} Z}{A} \left[\frac{1}{2} \ln \left(\frac{2m_e c^2 \beta^2 \gamma^2 T_{max}}{I^2} \right) - \beta^2 - \frac{\delta(\beta\gamma)}{2} \right] \quad (2.1)$$

where e is the electron charge, z the projectile charge as multiples of e, $v = \beta c$ the projectile velocity, N_{AV} the Avogadro's number, and ρ, Z, and A indicate respectively the density, the atomic number and mass number of the target material. T_{max} is the maximum energy that can be transferred to an atomic electron in a single collision, while I is the mean ionisation and excitation energy of the material. The term δ is a correction term discussed in the next paragraphs.

Figure 2.1 shows the mass stopping power, that is the stopping power divided by the material density ($\rho^{-1} \langle -dE/dx \rangle$), for positive muons in copper as a function of

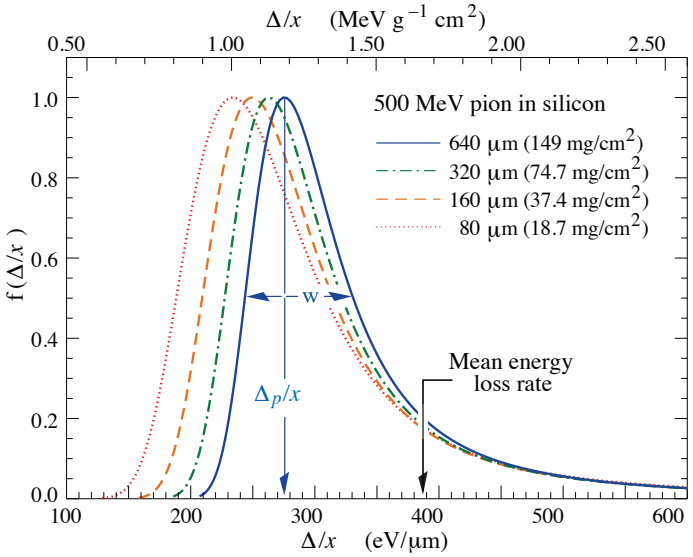

Figure 2.2: Straggling function of 500 MeV pions for various silicon thicknesses: the distributions have been normalized to unity at the most probable value [33].

$\beta\gamma$. In the so-called Bethe region, the dependency on the material is rather weak since there is a direct proportionality to the ratio Z/A and a logarithmic dependence from the mean ionisation and excitation energy of the material I. In the Bethe regime, the trend is instead inversely proportional to β and a broad minimum is reached around $\beta\gamma \approx 3.0 - 3.5$: particles in this minimum are called minimum ionising particles.

For a decreasing momentum, the stopping power increases rapidly due to the dependence from $1/\beta^2$: when a particle is slowing down it loses more and more energy and the energy transferred to the material will increase to a maximum before dropping significantly. The curve of the specific ionisation as a function of depth in the material will therefore show a maximum referred to as Bragg peak [35]. For increasing momenta from the minimum ionising region, the stopping power instead increases as $\ln(\beta\gamma)$: this increase is reduced by the density effect which accounts for the polarization of the medium (δ term in equation 2.1) [33].

When the projectile speed is comparable to that of the atomic electrons, the Bethe equation breaks down [36]: to accurately describe ionising energy losses one has to account for corrections for the atomic shells [33], for the differences between particle and antiparticle (Barkas effect [37]) and for the perturbation of the atomic wave functions (Bloch correction) [38].

Processes of energy loss and transfer are stochastic and discrete by nature and the Bethe equation gives only the average energy loss owing to collisions with atomic electrons. For moderately thin detectors (up to few mm in the case of silicon) the energy loss probability distribution is well represented by the Landau-Vavilov-Bichsel distribution [33]. The distribution is asymmetric and the most probable value (MVP) can be significantly smaller than the average energy loss predicted by the Bethe equation: additionally, while the average energy loss predicted does not depend on the thickness, the MVP approximately scales with the logarithm of the thickness. The Landau dis-

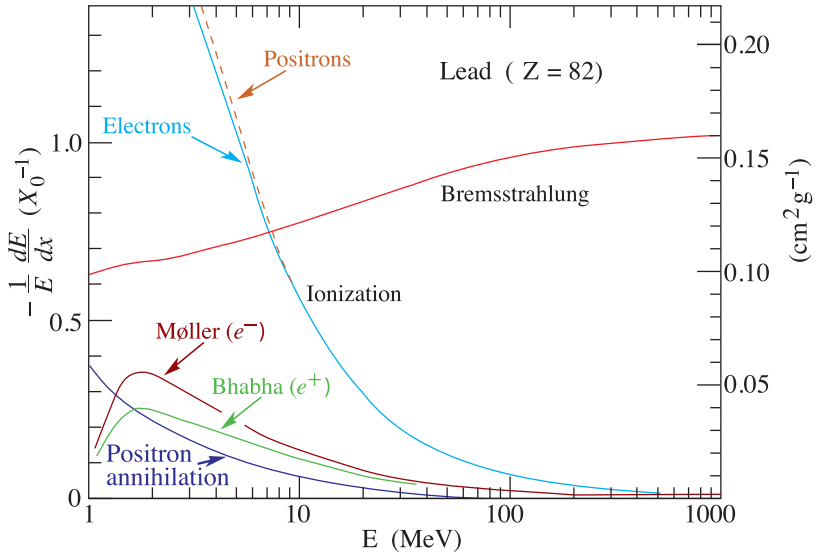

Figure 2.3: Contribution of various processes to the energy loss in lead as a function of electron or positron energy: the energy loss is shown as fractional energy loss per radiation length [33].

tribution fails to correctly describe the energy loss in thin absorbers since the actual distributions are significantly wider than the Landau width. As an example, figure 2.2 shows the straggling functions for 500 MeV pions for different thicknesses of silicon: the large fluctuations due to rare and high-energy transfer collisions make the distribution larger and for thick absorbers the distribution is less asymmetric, approaching a Gaussian.

Electrons and positrons also lose energy by ionisation, but, because of the kinematics (mass, charge, identity of the incident electron with the electrons it ionises), the stopping power differs from that of heavy charged particles: additionally, the stopping power for electrons is also somewhat different from that of positrons. Albeit the different expression, the previously discussed main dependencies of the average energy loss due to ionisations are the same [33].

Radiative energy losses

The mechanism of energy loss by ionisation is the most important one up to when radiative losses (Bremsstrahlung), and nuclear inelastic interactions in the case of hadrons, become dominant. For electrons and positrons, radiative losses start to dominate already at few MeV in high Z materials: figure 2.3 shows for example the contributions of various processes to the energy loss of electrons and positrons in lead. Radiative losses start becoming non-negligible around few GeV for muons and at even higher energies for charged hadrons.

The energy threshold at which Bremsstrahlung losses are comparable to ionising losses is called critical energy E_c: according to the definition given by Berger and Seltzer [39], E_c is the energy at which the electronic stopping power is exactly equal to the radiative stopping power. A useful parametrization for the electron's critical

energy is offered by the following relations [33]:

$$E_c = \frac{610\,\text{MeV}}{Z + 1.24} \quad \text{for solids} \qquad E_c = \frac{710\,\text{MeV}}{Z + 0.92} \quad \text{for gases} \tag{2.2}$$

As it can also be inferred from figure 2.1, the rate at which particles lose energy by Bremsstrahlung is essentially proportional to their energy. A convenient way of expressing the radiative energy loss is then given by the relation [40, 33]:

$$\left(-\frac{dE}{dx}\right)_{radiative} = \frac{E}{X_0} \tag{2.3}$$

where X_0 is the so-called radiation length and represents the average distance over which a high-energy electron/positron reduces its energy by a factor $1/e$ by radiative emissions. As it will be discussed in Section 2.1.3, the radiation length is a quantity that is naturally suited to describe the longitudinal evolution of electromagnetic showers. For a material with density ρ, atomic number Z and mass number A, the radiation length can be expressed as

$$\rho X_0 = \frac{A}{4\alpha N_{AV} Z^2 r_e^2 \ln 183 Z^{-1/3}} \tag{2.4}$$

where α and r_e are respectively the fine structure constant and the classical electron radius. More sophisticated definitions and parametrisations of X_0 are, for example, given by the relations provided by Tsai [41].

2.1.2 Photon interactions

There are several different processes by which the intensity of a photon beam can be attenuated and the most relevant ones are recalled here.

Photoelectric effect The photon is absorbed by an atomic electron which is emitted with a kinetic energy given by the difference between the photon initial energy and the electron binding energy. This process is important at low energies and for high Z materials since its cross section approximately scales with Z^5.

Compton scattering The photon interacting with a loosely bound electron is scattered at a different angle and with different energy and the electron is emitted from the atom. This process is important in the MeV range and the cross section depends linearly on the atomic number Z.

Pair production In the Coulomb field of a nucleus of mass m_N, a photon of energy E_γ can create an electron-positron pair if its energy satisfies the threshold condition:

$$E_\gamma \geq 2m_e c^2 \left(1 + \frac{m_e}{m_N}\right) \approx 2m_e c^2 = 1.022\,\text{MeV} \tag{2.5}$$

This process is dominant at higher energies and its cross section approximately depends on Z^2.

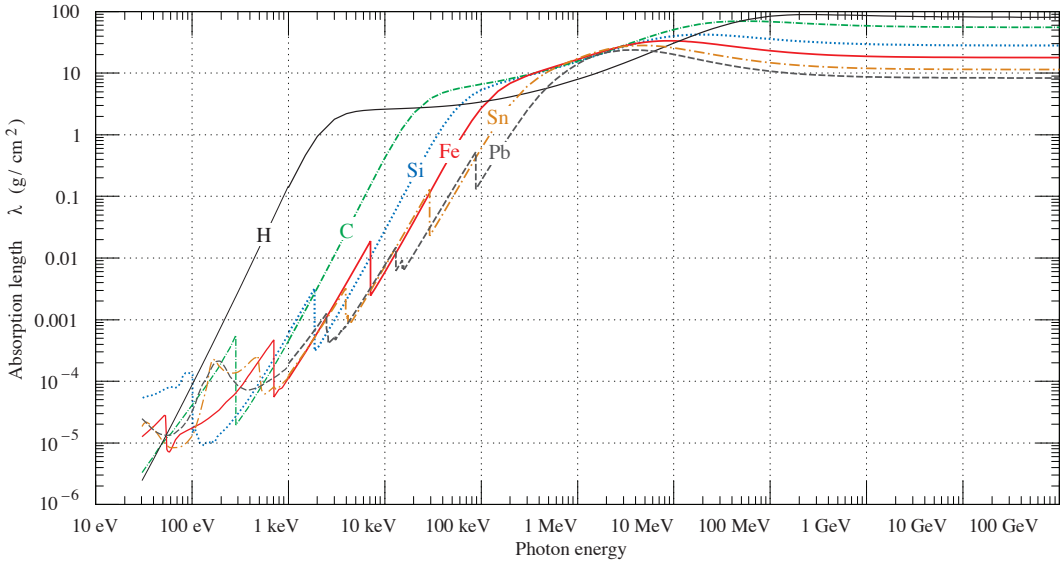

Figure 2.4: Photon mass attenuation length for various elements as a function of the photon energy [33].

The total microscopic cross section for the interaction of photons will be the sum of the microscopic cross sections of the individual processes that can contribute to the attenuation of the intensity of a photon beam. Figure 2.4 shows the mass attenuation length $\rho\lambda = A/(N_{AV}\sigma)$ [g cm^{-2}] for photons in various elements as a function of the photon energy: the intensity I_γ of a photon beam traversing a material of thickness x will be attenuated according to the Lambert-Beer law $I_\gamma = I_\gamma^0 \exp(-x/\lambda)$. It can be noticed that when thresholds for the ionisation of specific atomic levels are reached (absorption edges), the photoelectric cross section is enhanced, and the attenuation length drops. At energies above few MeV where the pair production mechanism is dominant, the attenuation length stabilizes to a value that is material dependent, in particular inversely proportional to the radiation length: in this regime, the pair production cross section can indeed be approximated by [33]

$$\sigma_{pair} \approx \frac{7}{9}\frac{A}{\rho N_{AV} X_0} \tag{2.6}$$

Other than those described before, there are other processes which can contribute to photon attenuation. For instance, these include elastic scattering (Rayleigh scattering with atoms, Thompson scattering with electrons) and photonuclear interactions: for the latter, the most important ones are often giant dipole resonance reactions which consist in a collective excitation of the nucleus and occur after thresholds of 20 MeV for light nuclei and of 7 MeV–8 MeV for heavy nuclei [42].

2.1.3 Electromagnetic cascade

As it was previously described, electrons and positrons above few MeV mainly lose energy by Bremsstrahlung while the photon interactions are dominated by the pair production mechanisms. Above the critical energy E_c, a particle multiplication process

known as electromagnetic cascade (or electromagnetic shower) is possible. From one particle generation to another, the average energy will decrease and the shower will not further develop once the particle's energy falls below the critical energy.

Some simplified models, such as the Heitler model [43], have been developed to qualitatively describe the longitudinal and lateral development of the electromagnetic cascades. These models allow predicting that the shower maximum, occurring where the number of particles is maximum, depends on the logarithm of the initial energy, while the number of particles at the shower maximum approximately scales with the initial energy. These simplified approaches are useful for a qualitative description but fail, for example, to predict the absolute number of each particle species in the shower and often do not take into account the differences in the showers depending on the initiating particle [40]: for a more accurate analysis of electromagnetic showers, Monte Carlo transport codes are often used [40].

Due to its connections with the radiative losses of electrons and positrons and the pair production cross section of high-energy photons, the radiation length X_0 is the natural quantity that can be used to describe the spatial profiles of particle showers. The 95% of the shower is longitudinally contained within approximately $10X_0$, while the 95% of the lateral spread, which is ruled by Coulomb scattering of electrons/positrons and roughly independent of the initial energy, is kept within twice the Molière radius R_M [33, 42] defined as:

$$R_M = \frac{\sqrt{4\pi\alpha} m_e c^2}{E_c} X_0 \tag{2.7}$$

2.1.4 Nuclear interactions

For hadrons travelling in matter, the possible nuclear interactions can be classified into two main categories: an interaction, or collision, is called inelastic if new particles are produced and/or the structure of the projectile and/or the target nucleus is changed, while it is labelled elastic otherwise. With the only exception of radiative capture by low-energy neutrons, all the inelastic reactions are threshold reactions.

Elastic interactions are important up until a few MeV. For example, elastic scattering can be a process in which a large energy transfer is possible for neutrons with energy below few MeV: for instance, one-half of the incident neutron energy is on average lost in elastic collisions with hydrogen nuclei.

In order to describe inelastic interactions of hadrons with nuclei, it can be useful to consider inelastic interactions of hadrons with single nucleons first. Figure 2.5 shows the measured values for the total and elastic $p-p$ interaction cross section and the measured values of the total $p-n$ interaction cross section. At momenta below 1 GeV/c, the total and elastic cross sections tend to be equal, but at higher momenta the inelastic contribution becomes dominant and the differences between the $p-p$ and $p-n$ cross sections disappear. The phenomenology of hadron-nucleon interactions is quite complex and the physics models that are used to describe them strongly depend on the energy of the primary projectile: detailed reviews of these phenomena are for

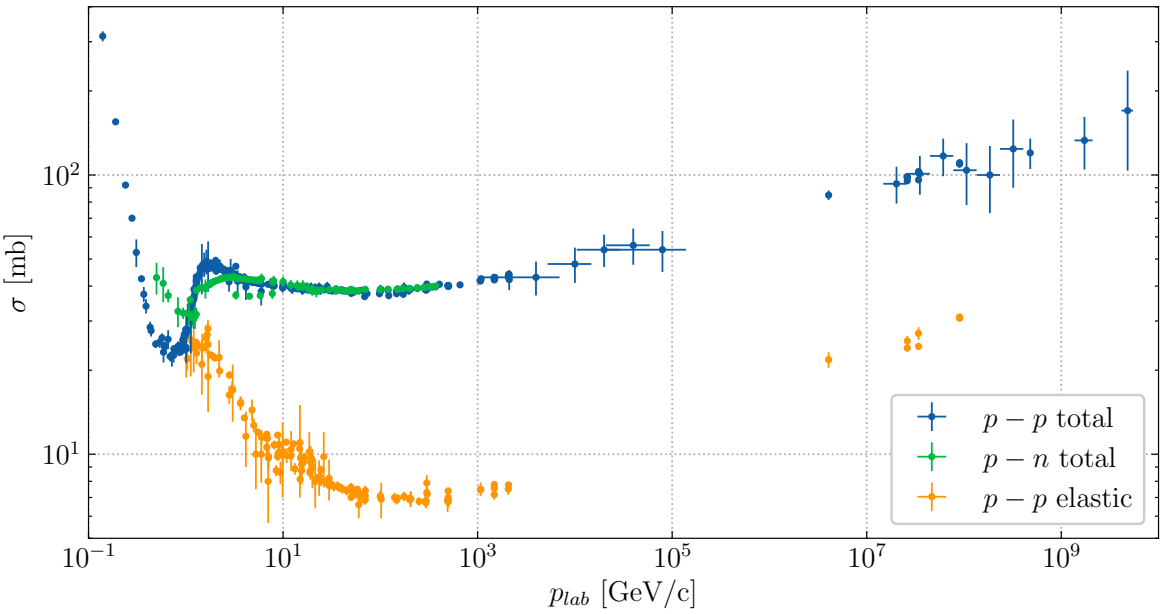

Figure 2.5: Measured total and elastic cross sections for $p-p$ interactions and measured total cross section for $p-n$ interactions: the data are from Ref. [33].

example given by Cerutti [42] and Ferrari [44], but for the purposes of this thesis work a qualitative description would suffice. The inelastic interaction of a hadron with a nucleon will lead to the production of new particles: the first inelastic channel that opens is the single pion production (with a threshold of 290 MeV) which becomes dominant above 700 MeV. As is the case for the single pion production, below few GeV the description of hadron-nucleon reactions is still feasible in terms of the production of resonances and their decay: dedicated models, like the Dual Parton Model (DPM), have instead to be used to accurately describe the experimental features of high-energy strong interactions above this energy range [42].

For hadron-nucleus inelastic interactions, also known as spallation reactions, it is possible to distinguish between three phases. During the fast reaction stage (1×10^{-22} s), called intra-nuclear cascade, the hadron interacts with a group of nucleons of the nucleus: fast-generated particles have a high probability of escaping the system without triggering a further cascade process within the nuclear system, while slower particles can further interact with other nucleons. The particles emitted at this stage are mostly forward-directed and their number approximately scales with the logarithm of the initial particle energy. At the end of the intra-nuclear cascade the nucleus is left with an excess of energy that is shared among the remaining nucleons: during this phase, called pre-equilibrium, intermediate energy nucleons and light ions formed by coalescence can be emitted. Finally, the last stage of the reaction is a de-excitation phase (1×10^{-18} s–1×10^{-16} s) in which the remaining excess energy of the system is dissipated by an evaporation process consisting of the emission of lower energy neutrons, protons and light ions: the yield of the particles emitted in the evaporation process is essentially independent of the direction of the initial particle and thus tends to be isotropic in

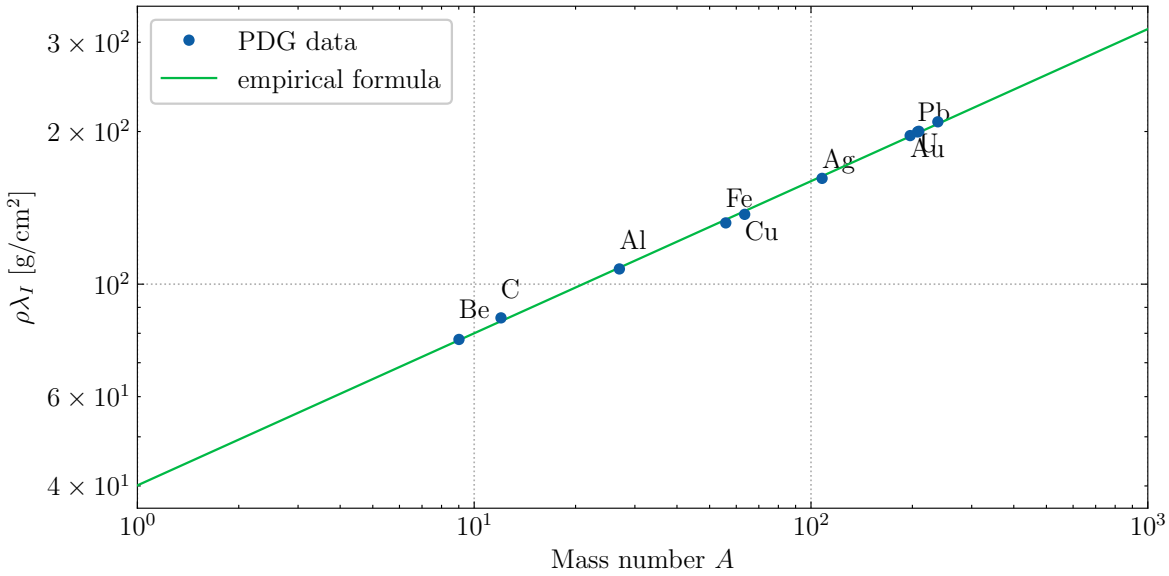

Figure 2.6: Mass inelastic scattering length $\rho\lambda_I$ as a function of the mass number. The data points are from Ref. [33], the solid line is the empirical law from Sullivan [45].

contrast to the yield of particles emitted in the fast stage of the reaction [42]. If the element is heavy, the evaporation process can be complemented by the fission of the nucleus: the remaining fragments, most likely in an excited state, will in turn undergo a similar de-excitation process. The completion of the de-excitation process is accompanied by the emission of prompt photons corresponding to the transition between the specific levels of the residual nucleus: the residual nucleus that is left at the end of the reaction is often an unstable one.

Due to its practical consequences in the operation and design of shielding installations at high-energy accelerators, it is due to comment on a very important feature of the spallation reaction. As it can be partially inferred from figure 2.5, the energy dependence of the inelastic cross section over a wider energy range is very little: furthermore, once the 1 GeV/c momentum threshold is passed (approximately few hundreds of MeV in kinetic energy), protons and neutrons behave in the same way. An excellent approximation of the total inelastic cross section is the one in which the latter is estimated with the geometric cross section of the nucleus: the total cross section will then have a dependence on the mass number as $A^{2/3}$ [40, 45]. It is customary to refer to the mean free path for inelastic interactions as inelastic scattering length, λ_I. Figure 2.6 shows the mass inelastic scattering length $\rho\lambda_I$ [g/cm^{-2}] as a function of the mass number A. The solid line corresponds to the empirical formula by Sullivan [45]

$$\rho\lambda_I = 40.1A^{0.3} \tag{2.8}$$

and gives visual proof of the goodness of the aforementioned approximation. In an analogous way to the radiation length for the electromagnetic cascade, the inelastic scattering length is the quantity that is naturally suited to describe the spatial evolution of hadronic showers.

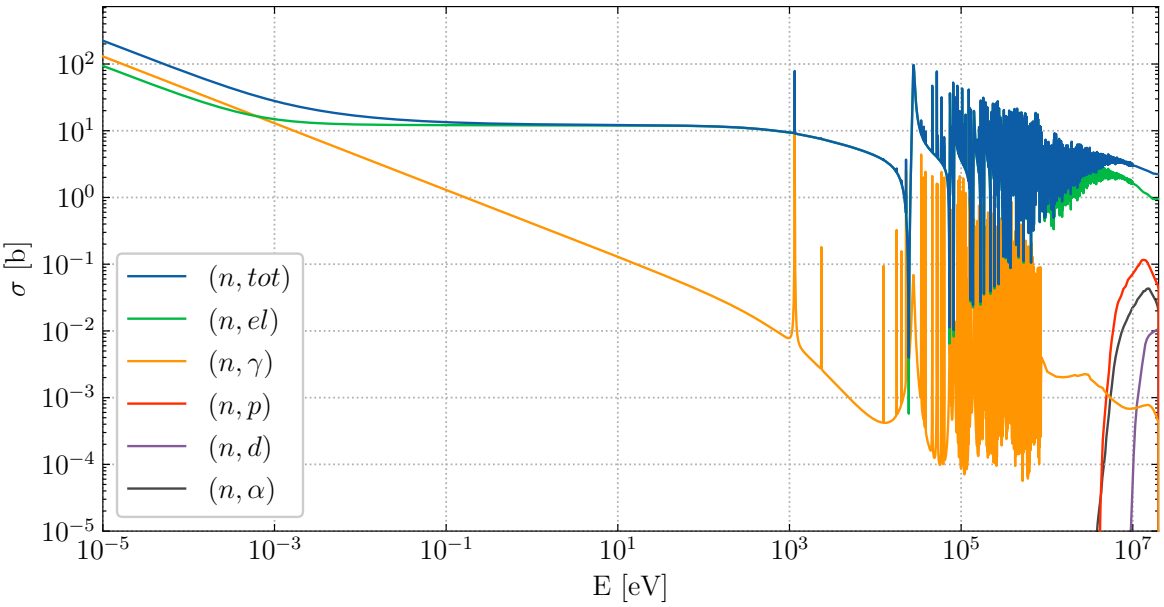

Figure 2.7: Cross sections of neutron interactions in ^{56}Fe below 20 MeV: (n, tot), (n, el) and (n, γ) indicate respectively the total, elastic and capture cross sections. The data shown are extracted from the JEFF-3.3 nuclear data library [46].

Inelastic interactions of low-energy neutrons

Neutrons are rather special particles: being neutral, they can travel significant distances before interacting and in the low-energy regime, that is approximately below 20 MeV, their interactions with nuclei can strongly be influenced by the nuclear structures of the latter. Additionally, their mean lifetime is of the order of 15 minutes, but despite being unstable they are essentially stable neutral hadrons when compared to the typical time scales of the processes described so far.

According to their energy (E_n), neutrons below 20 MeV can be classified into thermal neutrons ($E_n < 0.5\,\text{eV}$), which diffuse in materials, thermalize and can be captured via (n, γ) reactions, epithermal neutrons ($0.5\,\text{eV} < E_n < 100\,\text{keV}$), which mostly undergo nuclear elastic scattering, and fast (or evaporation) neutrons ($100\,\text{keV} < E_n < 20\,\text{MeV}$) which can interact via nuclear scattering or inelastic reactions.

As an example, various cross sections of neutron interactions in ^{56}Fe below 20 MeV are shown in figure 2.7. At thermal energies, the elastic and capture cross sections are smooth and inversely proportional to the neutron velocity ($1/\sqrt{E_n}$ dependence), but, depending on the specific nuclear structure of the target nucleus, they can exhibit characteristic resonances already from fractions of eV. In the epithermal region, the cross sections usually exhibit a large number of resonances and, above a certain threshold that is specific to each nucleus and reaction, these resonances cannot be experimentally resolved anymore: for example, the resonances of the capture cross section for ^{56}Fe are not resolved approximately above 1 MeV.

Figure 2.7 also shows some examples of inelastic reactions that entail the production of hadrons or light nuclei such as (n, p), (n, d) and (n, α). These threshold reactions

are often explained via the formation of a compound nucleus in an excited state and its consequent de-excitation [47]: from simple and qualitative considerations a 1 MeV neutron will have a de Broglie wavelength of approximately 4 fm and it is unlikely to interact with individual nucleons. Instead, neutrons with energy above 20 MeV will have a de Broglie wavelength that is smaller than 1 fm and thus more likely to engage in spallation reactions.

2.1.5 Hadronic cascade

As it was previously described, several energetic and forward-directed hadrons can be emitted from the nucleus during the fast stage of a hadron-nucleus interaction. If the secondary products have enough energy to interact with another nucleus, a multiplication process can start: this process is known as hadronic cascade or hadronic shower. In a way analogous to what the critical energy is to the electromagnetic shower, the multiplication process in the hadronic cascade roughly ends when the energy of the secondary hadrons drops below the pion production threshold.

Since nuclear processes are involved, a significant fraction of the initial particle energy can be lost into binding energy. Thanks to the production of neutral pions which quickly decay into photons, the hadronic shower is also often accompanied by an electromagnetic component. The fraction of energy that is lost to the electromagnetic shower is highly energy-dependent: for instance, it is approximately 30 % and 64 % respectively for 10 GeV and 1 TeV protons impacting on copper [40]. Alongside the electromagnetic component, a muon component is also present as a consequence of the decay of pions and kaons produced during the shower. It is important to note that the coupling of the electromagnetic shower to the hadronic shower is instead very weak due to the much lower photonuclear cross sections: nonetheless, this mechanism is still the main source of neutrons in electron accelerators.

The spatial development of the hadronic shower can be described with the inelastic scattering length λ_I. The 95% of the shower longitudinal development is approximately contained within 6 to $10\lambda_I$ while 95% of the shower is laterally limited within an effective radius of one λ_I. Since it is often the case that the inelastic interaction length is up to 30 times larger than the radiation length, hadronic showers are much harder to contain: additionally, the spatial profile of the hadronic shower is less defined since the neutrons, the de-excitation photons and the possibly present muons can deposit their energy away from the shower core.

2.2 Radiation damage

One of the unwanted consequences of the interaction of particles with matter is surely radiation-induced damage which can cause, among others, ageing in gaseous detectors and severely compromise the performances of solid state particle detectors exposed to very harsh conditions such as those that are typical in the LHC environment. The consequences of radiation damage can be distinguished between cumulative and

instantaneous effects and the causes of these effects can be different. The cumulative effects of radiation can be further distinguished between bulk damage and surface damage.

Particles that are traversing matter are not only ionizing but may also interact with lattice atoms via the electromagnetic and strong force: the energy that is lost in collisions with nuclei and does not lead to ionization is called nuclear stopping power or non-ionising energy loss (NIEL). If the energy transferred to the recoiling nucleus is higher than a certain threshold which is material-dependent, the lattice atom can be displaced from its initial position and can create bulk defects: vacancies and interstitials are the most common but more complex structures are possible [48].

The number and type of the created defects will be surely different for different particle species and energies but, under the so-called NIEL scaling hypothesis according to which the amount of bulk defects scales with the NIEL, the bulk radiation damage induced by different particle species can be compared. It is customary to scale the damage caused by a given particle at a given energy with that of 1 MeV neutrons in silicon [48, 49]: converting particle fluences to the 1 MeV-neutron equivalent fluence in silicon, Φ_{eq}, allows an efficient and useful comparison between different radiation environments as far as radiation damage is concerned. The NIEL scaling is not a strict principle since the real damage may also depend on the specificities of the energy transfer mechanisms not entirely accounted for by the NIEL: its application is nonetheless extremely useful to cancel out most of the particle and energy dependencies of the observed damage in silicon detectors.

The induced lattice displacements populate new levels in the band gap and these ultimately result in macroscopic property changes which are briefly described below.

Increase of leakage current The increase in the leakage current is due to the production of mid-gap levels which are efficient electron-hole pair generators. Many experiments have shown that there is a linear behaviour between the increase in leakage current per unit sensor volume $\Delta I/V$ and Φ_{eq} over several orders of magnitude [48]: the proportionality coefficient α is the current-related damage rate. Since the leakage current has an exponential dependence on temperature ($I \propto \exp[-E_g/2k_BT]$, where E_g is the energy band gap and k_B the Boltzmann constant) silicon sensors have to be operated at low temperature. The increase in leakage current is the main problem from $\Phi_{eq} \approx 1 \times 10^{13}\,\mathrm{cm}^{-2}$.

Change of effective doping concentration $\mathbf{N_{eff}}$ Creation of donors in the upper half of the band and acceptors in the lower half of the band contributes to a change in the effective space charge [48]. With increasing radiation, the sign of the space charge can change (Space Charge Sign Inversion, SCSI): for instance, starting with an n-type-doped silicon bulk, a removal of donors and an increase of acceptors with increasing radiation will first shift the space charge to an intrinsic level and then to a p-like substance. The depletion voltage V_{FD}, which depends on the effective doping concentration N_{eff} will therefore change: in the previous example V_{FD} will go positive with increasing radiation. The high resulting

depletion voltage is the main problem from $\Phi_{eq} \approx 1 \times 10^{14}\,\mathrm{cm}^{-2}$.

Decrease of charge collection efficiency Defects can act as trapping centres for electrons and holes: if the de-trapping time is larger than the electronics peaking time, the Charge Collection Efficiency (CCE) is degraded. Trapping becomes relevant for $\Phi_{eq} \approx 1 \times 10^{15}\,\mathrm{cm}^{-2}$ and above.

It is also important to add that the distribution of defects in sensors can evolve with time due to diffusion, migration, and recombination: these processes are globally summarized in the term annealing. The evolution with time of the different macroscopic effects is different and, in addition, macroscopic changes deriving from diffusion are highly temperature dependent. Leakage current always decreases with time (and it does so faster with higher temperature), while the trapping probability increases for electrons and decreases for holes [48]. The evolution with time of the effective doping concentration (and therefore the depletion voltage) is a bit more complex and in the so-called Hamburg model is usually parametrized by three terms: the stable damage (time-independent) which is the most relevant in a high-radiation environment, the short-term annealing due to the decay of the introduced acceptors (beneficial), and the long-term annealing (reverse annealing). The annealing time constants define the running and maintenance conditions of experiments in high-radiation environments: operation below 0 °C completely freezes the reverse annealing, while during maintenance periods the detector temperatures should be increased in a controlled way to benefit from the beneficial annealing for the depletion voltage and leakage current and to absolutely avoid the reverse annealing.

Contrary to bulk damage summarized so far, surface damage is introduced by ionization in the silicon oxide layer and at the interface between bulk and oxide: surface damage is therefore associated with the total ionising dose (TID) and not with NIEL. In an insulator, the creation of electron-hole pairs is not fully reversible and, with insufficient recombination and trapping of positive charge at the interface between silicon bulk and oxide, the sensor functionality is deteriorated, for instance, by an increase of inter-strip capacitance and a decrease of inter-strip resistance. Static charge centres have additional effects on electronics, particularly the increase of transistor threshold voltages and leakage currents.

Instantaneous effects, referred to as Single Events Effects (SEE), may severely impact the performance of electronics. Ionizing particles may deposit a charge in a device's sensitive node that is sufficient to disrupt its normal function: the simplest example is the change from "1" to "0" (or vice versa) in a logic circuit or memory cell. When transient and not critical on a short time frame, it is customary to speak of soft SEEs, also known as Single Events Upsets (SEUs): examples of SEUs are the already mentioned bit flips in memories. On the contrary one speaks of hard SEEs when their effect is permanent or critical: these are also known as Single Events Latch-ups (SEL). Contrary to effects induced by NIEL and total ionising dose that can be quantified in terms of the 1 MeV-neutron equivalent fluence in silicon or the absorbed dose, the failure of electronic components can only be characterized in terms of probability of occurrence.

The probability of occurrence of SEU scales with the fluence of the particles that are triggering them: the quantity that is often used as reference is the high-energy hadron equivalent fluence Φ_{HEH} which is the sum of the fluence of hadrons above 20 MeV and the low-energy neutron fluence weighted according to the ratio of their SEU cross section to that of high-energy hadrons: this weighting reflects in practice the profile of the (n, α) reaction cross section in silicon [42].

2.3 Induced radioactivity

As it was previously discussed, unstable radionuclides can be produced as a result of nuclear inelastic interactions in materials exposed to prompt radiation. For particle accelerators it is customary to refer to as prompt radiation the radiation owing to the operation of the accelerator itself: this could be the radiation produced by the impact of a beam on a target or on a beam-intercepting device, by a beam loss or by colliding beams. The defining feature of prompt radiation is that it vanishes within a small time frame once the primary source responsible for generating the radiation also vanishes (e.g. the beam is dumped). By contrast, residual or delayed radiation is the radiation due to the decay of the unstable radionuclides that have been created during operation: residual radiation can remain for a much longer time and may impose access restrictions and dedicated measures during maintenance and decommissioning operations.

Being unstable, the produced radionuclides can decay and the most common decay modes include α decay, β decay and electron capture (EC), γ decay or isomeric transition (IT), and internal conversion (IC). To complete the overall picture, one should also consider the decay channels that are typical of heavy radionuclides (transuranic elements) or exotic radionuclides that are far from the stability line: these entail spontaneous fission, and delayed particle emission (protons, neutrons) following a β decay. The decay of an unstable nucleus is a random process which is characterized by a decay constant specific to that radionuclide and which historically has been indicated with the symbol λ. The expectation value of the number of disintegrations per unit time of a given radionuclide concentration is the radionuclide activity, whose unit is the becquerel [$1\,\mathrm{Bq} = 1\,\mathrm{s}^{-1}$]: the activity per unit mass and the activity per unit volume are also commonly used and are referred to as mass-specific and volume-specific activity respectively.

Induced radioactivity can be present at nearly all kinds of accelerators and experimental facilities. Protons above 10 MeV can easily engage in nuclear reactions and neutrons, either coming from sources, reactors, light-ion accelerators or produced as secondaries in an inelastic reaction, can thermalize and be captured other than initiating nuclear reactions themselves. At the same time, the operation of electron accelerators often results in a copious production of photons which, above a threshold of few MeV in heavy materials, can generate neutrons via photonuclear reactions.

The kind and quantity of radionuclides present at any given time in an irradiated object will strongly depend on the combination of these factors:

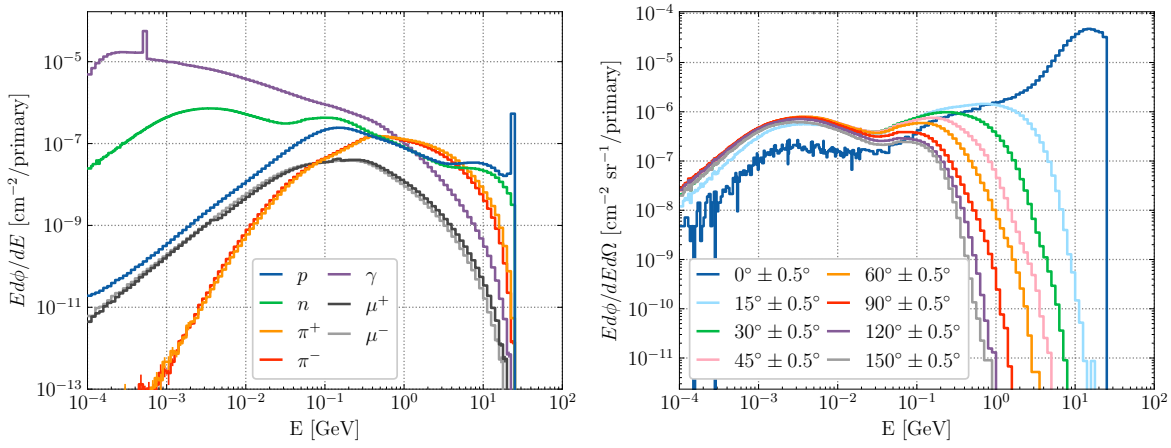

(a) (b)

Figure 2.8: Monte Carlo simulation with the FLUKA code of the fluence energy spectra of particles emitted from a 50 cm copper target hit by 24 GeV/c proton beam: (a) fluences integrated over the whole solid angle; (b) double differential neutron fluence at selected angles with respect to the beam direction.

- the material composition of the object being irradiated;
- the production cross section of the concerned radionuclides;
- the radionuclide half-life ($T_{1/2} = \ln 2/\lambda$);
- the intensity of the primary source, for example the primary beam intensity, the intensity of the loss or the collision rate;
- the irradiation history, that is the number of irradiation intervals and their duration and the time that the induced activity has had to decay (cooling time);
- the fluence energy spectrum of the particles at the irradiation location.

As an example in relation to the very last point, figure 2.8(a) shows the fluence energy spectra of the particles being emitted from a 50 cm copper target hit by a 24 GeV/c proton beam. As discussed in this chapter, the radiation fields at high-energy accelerators can indeed have components from various particle species (figure 2.8(a)) whose energy can extend up to the primary beam energy. Significant variations can also be observed at different angles with respect to the direction of the primary beam: as discussed in Section 2.1.4, the double differential (in energy and solid angle) neutron fluence spectra shown in figure 2.8(b) allow to appreciate that the high-energy component of the neutron spectrum, the so-called spallation shoulder, has a strong angular dependence, while the evaporation component around few MeV is more or less isotropic. Owing to the reasons detailed above, the computation of activity can be a very challenging task.

Table 2.1 summarises the most important medium and long-lived radionuclides that can be produced in typical accelerator materials. To be more precise, the first column of the table indicates elements that can be commonly found in compounds either as

Material	**Radionuclides**							
Carbon	^{3}H	(12.32 y)						
	^{7}Be	(53.22 d)						
	^{11}C	(20.364 min)	^{14}C	(5700 y)				
Aluminium	all the above							
	^{22}Na	(2.6018 y),	^{24}Na	(14.997 h)				
Iron	^{44}Sc	(58.61 h),	^{46}Sc	(83.79 d),	^{48}Sc	(43.67 h)		
	^{48}V	(15.9735 d)						
	^{51}Cr	(27.7025 d)						
	^{52}Mn	(5.591 d),	^{54}Mn	(312.20 d)				
	^{55}Fe	(2.744 y),	^{59}Fe	(44.495 d)				
	^{55}Co	(17.53 h),	^{56}Co	(77.236 d),	^{57}Co	(271.74 d),	^{58}Co	(70.86 d)
Steel alloys	all the above							
	^{60}Co	(5.27 y)						
	^{57}Ni	(35.60 h)						
Copper	all the above							
	^{63}Ni	(101.2 y)						
	^{61}Cu	(3.339 h),	^{64}Cu	(12.701 h)				
	^{65}Zn	(243.93 d)						

Table 2.1: Most important radiologically relevant radionuclides produced in typical accelerator materials. The corresponding half-lives are given in parentheses.

almost pure or with a mass fraction of at least tens of %: owing to their wide usage and their importance for this thesis work, an additional entry for steel alloys has been added. For other common materials, concrete and electronic components in primis, the typical radionuclide inventory is not reported since it would be quite extensive and strongly influenced by the presence of impurities: although substantially different, a general rule for these two classes of materials is that activation at short and long cooling time is dominated respectively by ^{24}Na and ^{22}Na which can be produced by spallation on silicon or, for the specific case of concrete, by low-energy neutron interaction on sodium and spallation on calcium. Especially if they are responsible for the production of long-lived radionuclides, trace elements may be very important even down to mass fractions of few ‰ or less: it is for example the case of cobalt impurities in aluminium alloys, cast iron, steel alloys and concrete, europium and caesium traces in standard concrete compositions, and a series of elements (most notably silver) in electronic components and cables.

2.3.1 The activation formalism

Studying the generation and the time evolution of the induced radioactivity can quickly become complex as soon as one deviates from an idealised textbook case. The simplest and probably most known case is the one in which a target material is irradi-

ated by a monoenergetic particle beam characterized by a flux[1] ϕ that is constant over a single irradiation interval of duration t_{irr}. Assuming that the target thickness is small compared to the mean free path before any interaction of the primary particle (thin target approximation), one can neglect the fluence attenuation in the target itself and the possible energy degradation of the primary beam. As consequence, it is possible to consider a single-valued radionuclide production cross section.

The number of radionuclides present at any given time, $N(t)$, is governed by the first-order differential equation:

$$\frac{dN(t)}{dt} = -\lambda N(t) + \left(\frac{M}{M^{mol}} N_{AV}\right) \sigma\phi(t) \tag{2.9}$$

where M and M^{mol} are the mass and molar mass of the material being irradiated, and N_{AV} the Avogadro's number: the term in parentheses is none other than the number of target atoms. With the initial condition $N(t = 0) = 0$, the number of radionuclides after a time t_{irr} is given by:

$$N(t_{irr}) = e^{-\lambda t_{irr}} \int_0^{t_{irr}} \frac{M N_{AV}}{M^{mol}} \phi(t) e^{\lambda t}\, dt \tag{2.10}$$

and the radionuclide activity $A(t)$ can be then computed from the relation $dN(t)/dt = -A(t)$. If, as stated before, we assume that the fluence rate is constant and for example equal to ϕ_0 over the full irradiation period, the activity at the end of the irradiation can be expressed with the commonly known formula

$$A(t_{irr}) = \frac{M N_{AV} \sigma \phi_0}{M^{mol}} \left(1 - e^{-\lambda t_{irr}}\right) \tag{2.11}$$

where the term appearing in front of the parentheses is the saturation activity. Although extremely valuable, this case is far from reality and some of the approximations introduced hardly ever hold in the radiation environment of high-energy accelerators. For a more general formulation, the formalism has to be substantially modified.

Consider for example a compound material of mass M and let m_e and M_e^{mol} be respectively the mass fraction[2] and the atomic weight of the element e. The material is exposed to a radiation field characterized by different particle species with fluence rate energy spectra $\phi_i(E, t)$. In this generalized case, the production rate of a radionuclide r from the element e per unit compound material mass $P_{r,e}(t)$ (nuclides $\mathrm{g}^{-1}\,\mathrm{s}^{-1}$) can be expressed as

[1] For consistency with most of the literature, the fluence of a given particle species is defined as the total particles' track length per unit volume, or equivalently the total number of particles hitting a sphere of unitary cross section area. The fluence rate or flux is instead the total track length per unit volume and per unit time. Conventional units for flux and fluence are $\mathrm{cm}^{-2}\,\mathrm{s}^{-1}$ and cm^{-2} respectively.

[2] Despite the unfortunate clash of conventionally adopted notation, from this moment onwards m_e will be used to indicate the mass fraction of an element e in a given compound material and not the mass of the electron.

$$P_{r,e}(t) = \frac{N_{AV}}{M_e^{mol}} \sum_{\substack{i=p,n,\\ \pi^{\pm},\gamma,...}} \int_0^{+\infty} \sigma_{r,e,i}(E)\phi_i(E,t)dE \tag{2.12}$$

where $\sigma_{r,e,i}$ is the production cross section of radionuclide r from element e due to particle i: unless stated otherwise, the radionuclide production cross sections are intended to be weighted on the natural isotopic abundance of the considered element. The summation has to be intended over all the particle species present at a given location and that can contribute to activation. The fluence rate spectra, hence the production rates, generally depend on the position as well: the explicit dependence from $\vec{\mathbf{r}}$ has and will be omitted for brevity. The total production rate of radionuclide r (nuclides s^{-1}) will be then $\sum_e M\, m_e P_{r,e}(t)$.

Other than the direct production from the particles interacting with a material, a radionuclide can also be generated by the decay of the parent nucleus. To take into account the build-up and decay of the produced nuclides during irradiation, the time evolution matrix has to be introduced and the final expression of the activity of a radionuclide b (Bq) will be

$$\begin{aligned} A_b(t) &= \sum_r T_{b,r} \sum_e M\, m_e P_{r,e}(t) \\ &= \sum_r T_{b,r} \sum_e \frac{M\, m_e N_{AV}}{M_e^{mol}} \sum_{\substack{i=p,n,\\ \pi^{\pm},\gamma,...}} \int_0^{+\infty} \sigma_{r,e,i}(E)\phi_i(E,t)dE \end{aligned} \tag{2.13}$$

where the first sum is extended over the possible radionuclides r that can decay to radionuclide b. The coefficients $T_{b,r}$ are the coefficients of the so-called time evolution matrix and depend on the irradiation history and on the possible cooling time from the end of the irradiation. A more in-depth discussion on the radionuclide build-up and decay and the derivation of the expression of these coefficients for a very useful case is given in the section below.

Radionuclide build-up and decay

The time evolution of the concentration of nuclides forming a decay and build-up chain is ruled by a system of first-order differential equations named after Harry Bateman, the first to give an analytical solution for a linear case [50]. The Bateman equations for a linear chain of length b take the form

$$\begin{aligned} \frac{dN_1(t)}{dt} &= -\lambda_1 N_1(t) + P_1(t) \\ \frac{dN_b(t)}{dt} &= -\lambda_b N_b(t) + \widetilde{\lambda}_{b-1} N_{b-1}(t) + P_b(t) \end{aligned} \tag{2.14}$$

where $P_b(t)$ is the production rate of radionuclide b having decay constant λ_b, and $\widetilde{\lambda}_{b-1} = \beta_{b-1,b}\lambda_b$ the partial decay constant of the b-th radionuclide to the $b-1$-th radionuclide accounting for the possible decay branching ratio $\beta_{b-1,b}$.

Thanks to the linearity of the system, in order to understand the form of the final solution it is useful and sufficient to consider without loss of generality the case in which $N_1(0) = N_0 \neq 0$ and zero for every other radionuclide, and $P_1(t) = P_0 H(t)$ and zero for every other radionuclide: $H(t)$ is here the Heaviside step function and thus a constant irradiation from $t > 0$ is assumed. The solution can be found by applying the Laplace transform to each equation of the system yielding

$$\begin{aligned} s\widetilde{N}_1(s) &= N_0 - \lambda_1 \widetilde{N}_1(s) + \frac{P_0}{s} \\ s\widetilde{N}_b(s) &= -\lambda_b \widetilde{N}_b(s) + \widetilde{\lambda}_{b-1} \widetilde{N}_{b-1}(s) \end{aligned} \tag{2.15}$$

where $\widetilde{N}_b(s)$ is the Laplace transform of $N_b(t)$. Exploiting the recursive relation between the abundances of adjacent radionuclides on the chain, one can easily find

$$\widetilde{N}_b(s) = \frac{\prod_{j=1}^{b-1} \widetilde{\lambda}_j}{\prod_{j=1}^{b} (s + \lambda_j)} \left(N_0 + \frac{P_0}{s} \right) \tag{2.16}$$

By expressing the solution in the Laplace domain using partial fractions, the inverse transform can easily be computed and the abundance of radionuclide b after an irradiation period t_{irr} followed by a cooling time t_{cool} will be given by

$$N_b(t_{irr} + t_{cool}) = \sum_{j=1}^{b} \frac{\prod_{k=1}^{b-1} \widetilde{\lambda}_k}{\prod_{\substack{k=1 \\ k \neq j}}^{b} (\lambda_k - \lambda_j)} \left(N_0 e^{-\lambda_j (t_{irr} + t_{cool})} + P_0 \frac{1 - e^{-\lambda_j t_{irr}}}{\lambda_j} e^{-\lambda_j t_{cool}} \right) \tag{2.17}$$

which allows introducing the Bateman coefficients $c_{b,j}$ as

$$c_{b,j} = \frac{\prod_{k=1}^{b-1} \widetilde{\lambda}_k}{\prod_{\substack{k=1 \\ k \neq j}}^{b} (\lambda_k - \lambda_j)} \tag{2.18}$$

The solution as of equation 2.17 was obtained for a single chain of length b in which only the initial nuclide has non-zero initial abundance and non-zero production rate. The general solution can be obtained as a linear superposition of the solutions in which other radionuclides have initial abundances and production rates different from zero.

Only linear chains have been discussed so far, but it is often the case that complex chains entail branching, meaning that a given radionuclide can have more than one direct parent. The general approach in this case [51] consists in breaking down the non-linear chain in sets of linear chains and the general solution will be obtained by summing the various contributions: for this very reason, the partial decay constant

accounting for the possible decay branching ratio where already introduced in the previous formulation.

Equation 2.13 gave the generalized expression of the activity of a radionuclide b being produced by activation and introduced the time evolution matrix whose coefficients $T_{b,r}$ relate the production rate of radionuclide r to the activity of radionuclide b. Exploiting what was obtained in equations 2.17 and 2.18, for zero initial abundances and for a constant irradiation period of duration t_{irr} followed by a cooling time t_{cool}, the coefficient $T_{b,r}$ will then assume the form

$$T_{b,r} = \sum_{\substack{c \\ r \to b}} \sum_{j=1}^{b} c_{b,j}^{c} \left(\frac{1 - e^{-\lambda_j^c t_{irr}}}{\lambda_j^c} \right) e^{-\lambda_j^c t_{cool}} \tag{2.19}$$

where the first summation has been introduced to account for all the (linearised) decay chains c (hence the superscript) starting from a radionuclide r and leading to radionuclide b. The results here discussed will be reprised in Chapter 4.

At this stage, it is of paramount importance to comment on the validity of the solutions obtained. The solving procedure adopted tacitly assumes that all the decay constants in the decay chain are different from each other: although improbable, there are exotic short-lived nuclides far away from the stability valley having half-lives either estimated only from theory or known within a certain experimental limit of few hundreds of ns. Examples can be the decay of ^{86}Ga in ^{86}Ge among nuclides of intermediate mass and the decay of ^{188}Lu into ^{188}Hf among heavier nuclides, but many more can be found. Although generally of little importance for safety considerations, they can occur while assessing the radiological inventory at high-energy accelerators and must be taken into account. The workaround generally adopted in such cases is to artificially modify the decay constants by a small increment and use the same formulas: the solution would be approximate, but the error on the numerical results is generally contained [51] and within the accuracy acceptance range for most of the applications.

Finally, an important consideration should be made on the production term: the production rate appearing in the equations 2.14 has to be intended as an external source term. In reality one should consider that the products of a nuclear reaction can in turn be activated: if one accounted for the transmutation process, additional source and depletion terms should be added to the equations 2.14 and they would depend on the radionuclide abundances themselves. If this aspect is considered, the possible decay chains can now present loops, something that is clearly impossible if only the decay and direct production are accounted for: the equations are further complicated and general solving algorithms, beyond the scopes of this work, are for example given by Cetnar [51] and Dreher [52]. Although transmutation is crucial, for example, if uranium and transuranic elements are involved, these cases are generally beyond the practical applications in the high-energy accelerators domain in the present day.

2.4 Radiation protection aspects

As already stated, prompt and residual radiation may have radiological consequences impacting the operation of accelerator facilities. This section introduces the basic principles of radiation protection and emphasises the key concepts that are of paramount importance for the Monte Carlo calculation performed for the LHC experiments as detailed in Chapter 5 and 6.

Unfortunately, the effects of ionising radiation on tissue are not correlated to the energy deposited in them through a very simple dependence, but these effects are also connected to the particle type and energy. Physical quantities, like fluence or absorbed dose, cannot be used to express legal protection limits since they do not allow quantifying the biological effects of the exposure of the human body to ionising radiation and the resulting detriment. International bodies like the International Commission on Radiological Protection (ICRP), the International Commission on Radiation Units and Measurements (ICRU), and the International Atomic Energy Agency (IAEA) have developed radiological standards to promote occupational and environmental radiological health that have been progressively incorporated or adopted into the laws and regulations of individual nations.

For the purpose of quantifying the external irradiation and the irradiation from the intake of radionuclides, the quantity of the effective dose E has been introduced in ICRP Publication 60 [53] and is recommended in the ICRP Publication 103 [54] as the fundamental quantity to be used in the regulatory framework to set dose limits. The effective dose E is defined as the weighted sum of the equivalent doses H_T in the organs or tissues T

$$E = \sum_T w_T H_T = \sum_T w_T \sum_R w_R D_{T,R} \tag{2.20}$$

where w_T is the tissue weighting factor chosen to represent the contributions of individual organs and tissues to the overall radiation detriment ($\sum_T w_T = 1$), $D_{T,R}$ is the mean absorbed dose in an organ or tissue T from radiation R, and w_R is a radiation weighting factor. The unit of the effective dose is the sievert (Sv).

The effective dose is a quantity that cannot be directly measured: for a specific irradiation configuration, its estimation from physical quantities (particle fluences) is possible using conversion coefficients that are a function of the particle type and energy. These coefficients are based on Monte Carlo simulations in which the dose to organs and tissues for a given irradiation configuration is computed with the aid of anthropomorphic phantoms. Figure 2.9 shows the ICRP Publication 116 [55] fluence to effective dose conversion coefficients for various particles for an anterior-posterior irradiation configuration, meaning that a broad parallel beam is assumed to be irradiating the human body from the front: the coefficients shown in figure 2.9 imply an extrapolation above 10 GeV up to LHC energies.

Because the effective dose is calculable but not measurable, the so-called protection quantities are introduced aiming to provide conservative estimates of the effective

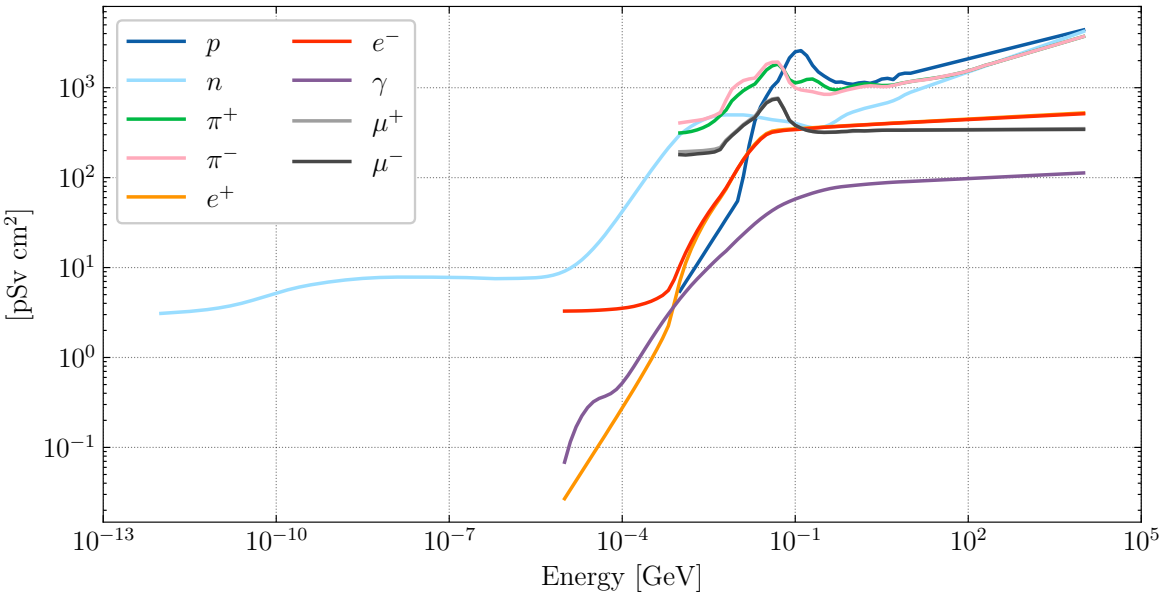

Figure 2.9: ICRP Publication 116 [55] fluence to effective dose conversion coefficients for an anterior-posterior irradiation configuration.

dose and to demonstrate compliance with the dose limits: radiation area monitors and dosimeters can be then calibrated in terms of these protection quantities. The operational quantity used for area monitoring is the ambient dose equivalent $H^*(10)$ (Sv), that is the dose equivalent that would be produced by a corresponding expanded and aligned field in a 30 cm diameter sphere of tissue of unit density at a depth of 10 mm, on the radius vector opposite to the direction of the aligned field [53]. The operational quantity for the monitoring of individuals is instead the personal dose equivalent [53] $H_p(d)$ (Sv) defined as the dose equivalent in standard tissue at an appropriate depth d below a specified point on the human body: this point depends on the position where an individual dosimeter is worn, and the considered depth is usually 10 mm for the assessment of the effective dose, and 0.07 mm for the assessment of doses to the skin and extremities.

As formulated in ICRP Publication 60 [53], radiation protection should be based on the principles of *justification*, that is any practice involving ionising radiation should not be carried out unless it gives a net benefit, *limitation*, meaning that the doses received by persons involved in a given practice have to be kept below legal limits, and *optimization*. The optimization principle is also known as ALARA principle and it implies that the exposure of persons to radiation and also the radiological impact on the environment should be kept as low as reasonably achievable taking into account economic and social factors. For radiation protection at high-energy physics accelerators, ALARA practices may range from simple and common-sense-based operational measures to more complex cost-benefit analyses involving budget and dose constraints, for instance as is the case for the installation of new components or the design of new shielding structures.

Among the various aspects of radiation protection at accelerators, clearance and

decommissioning activities are particularly relevant for this thesis work focused on radiological characterization studies of the LHC experiments. As defined within the IAEA Safety Glossary [56], with the term clearance it is meant the removal of radioactive materials or radioactive objects within notified or authorized facilities and activities from any further regulatory control. Owing to its particular status of international organization, CERN has to homologate its regulations in matters of radiation protection with the two Host States, ASN (Autorité de Sûreté Nucléaire) for France and OFSP (Office Fédéral de la Santé Publique) or BAG (Bundesamt für Gesundheit) for Switzerland, as well as International and European safety policies: among others, the management and disposal of radioactive waste are regulated by the Tripartite Agreement [57] which establishes a principle of fair share based on the volume eliminated, the radiotoxicity, and the elimination costs.

The clearance of materials is a possibility not contemplated within French regulations: by consequence, clearance at CERN follows Swiss regulations [58, 59]. According to the CERN and Swiss regulations [58, 59], a material has to be considered radioactive if at least one of the following criteria is fulfilled:

- the ambient dose equivalent rate measured at a 10 cm distance from the item is larger than 0.1 µSv/h after subtraction of the background;
- the mass-specific activity in Bq/g is above the clearance limits;
- the total activity in Bq is above the clearance limits;
- the surface activity concentration in Bq/cm^2 is above the limits for surface contamination (CS).

For a material containing a mixture of N_R radionuclides of artificial origin, the multiples of clearance limits (LL) is introduced as

$$LL = \sum_{i}^{N_R} \frac{A_i}{LL_i} \tag{2.21}$$

where A_i and LL_i denote respectively the mass-specific activity (Bq/g) and the clearance limit (Bq/g) of radionuclide i in the mixture. The clearance limits of each radionuclide are defined within the pertinent legal framework: the reference document for CERN is the Swiss Radiation Protection ordinance [59].

Chapter 3

Monte Carlo codes for radiation transport calculations

As outlined in the previous chapter, particles can interact with matter through a wide variety of mechanisms, each characterized by its own cross section: due to its nature, the problem of radiation transport is ultimately described in terms of probabilities and easily lends itself to be simulated using the Monte Carlo method. After an introduction to the basics of radiation transport calculations, this chapter summarises the most important aspects of the two Monte Carlo codes used for this work, FLUKA and PHITS.

3.1 Radiation transport calculations

Initially developed by John von Neumann, Nicholas Metropolis and Stanislaw Ulam and, independently, by Enrico Fermi, the Monte Carlo method was used to solve multi-dimensional integro-differential equations describing physical processes not necessarily of stochastic nature. While studying neutron diffusion phenomena described with the random walk model, it was soon realized that the Monte Carlo method applied to equations describing a stochastic process corresponded to an actual simulation: each step of the simulation had an exact equivalent in the physical process studied [60, 61].

In order to describe a radiation field, that is an ensemble of particles (possibly of different species) at a position $\vec{\mathbf{r}}$, with an energy E and moving along the direction $\vec{\mathbf{\Omega}}$, the fundamental quantity that should be used is the angular flux $\Psi(\vec{\mathbf{r}}, E, \vec{\mathbf{\Omega}}, t)$: the angular flux is related to the already introduced particle flux energy spectrum by an integration over the solid angle. The angular flux satisfies a phase space balance equation named after Ludwig Boltzmann who initially formulated it to describe gases. Albeit most of the historical development on the Boltzmann equation and of the Monte Carlo method is focused on low energy neutron and photon transport, the equation can be extended to the transport of any kind of particle: to the terms that describe the change in the particle population due to uniform translation, collision, and absorption, one can add terms that describe particle decay an energy loss [60, 62].

The analytical solution of the transport equation is possible for a very restricted

number of cases and under several simplifying assumptions. At the same time, numerical integration quickly becomes inefficient when the number of dimensions is greater than two. Monte Carlo calculations for transport problems work by following N particle histories (particle trajectories in phase space) and their great advantage is that their convergence is proportional to $1/\sqrt{N}$ and independent of the number of dimensions.

Any physical observable in a radiation transport problem will always be expressed as an integral of the angular flux over a suitable phase space volume: due to the stochastic nature of the underlying process, this integral will ultimately be an expectation value of a random variable whose probability distribution is, in general, the result of a convolution of different probability distributions. An estimation of the observable can then be obtained by drawing several random samples from the distributions and estimating the mean value. The mathematical foundation of the Monte Carlo method is the central limit theorem which ultimately states that the probability distribution of the mean of N independent random variables having the same distribution (provided that mean and variance are finite) tends to a Gaussian distribution having the same mean and a standard deviation that is $1/\sqrt{N}$ the initial standard deviation.

The typical workflow of a Monte Carlo calculation reflects the random walk model: each particle is followed through its path in matter and, at each step, the occurrence of an event and its aftermath are decided by randomly sampling from the appropriate distributions. It is often said that the Monte Carlo calculations are mathematical experiments and it is true that aspects of a real-life experiment have their Monte Carlo equivalent. A Monte Carlo estimator is a way in which a certain radiometric quantity can be computed and is equivalent to an experimental technique of choice. A Monte Carlo detector, which can be seen as a concrete application of an estimator to a phase space region, is instead the equivalent of the instrument. Repeated measurements correspond to the action of adding up the contributions to the "score", or "tally", when a particle enters the phase space volume of the defined detectors. As the result of a real-life experiment will be expressed as the average of several measured values with its associated uncertainty, the final outcome of a Monte Carlo calculation is obtained by a statistical estimation of the average between all the scores with its associated statistical uncertainty which is obtained by running several independent calculations. This uncertainty is only of statistical origin and one should keep in mind that the result of the Monte Carlo calculation is also affected by systematic contributions owing to the adopted physics models, the transport algorithms, the cross section data used, simplifications in the description of the geometry and materials of the problem.

So far, the expressions Monte Carlo calculation and Monte Carlo simulation have been used interchangeably. Strictly speaking, this is rigorous only for analogue calculations in which not only the mean of the estimators converges to the actual mean of their distributions, but also the higher moments are preserved: this means that partial distributions, fluctuations and correlations are correctly estimated.

For some problems the user may wish to accelerate the statistical convergence and this goal can be achieved using biasing techniques, also generally known as variance reduction techniques: some techniques aim at reducing the variance for the same com-

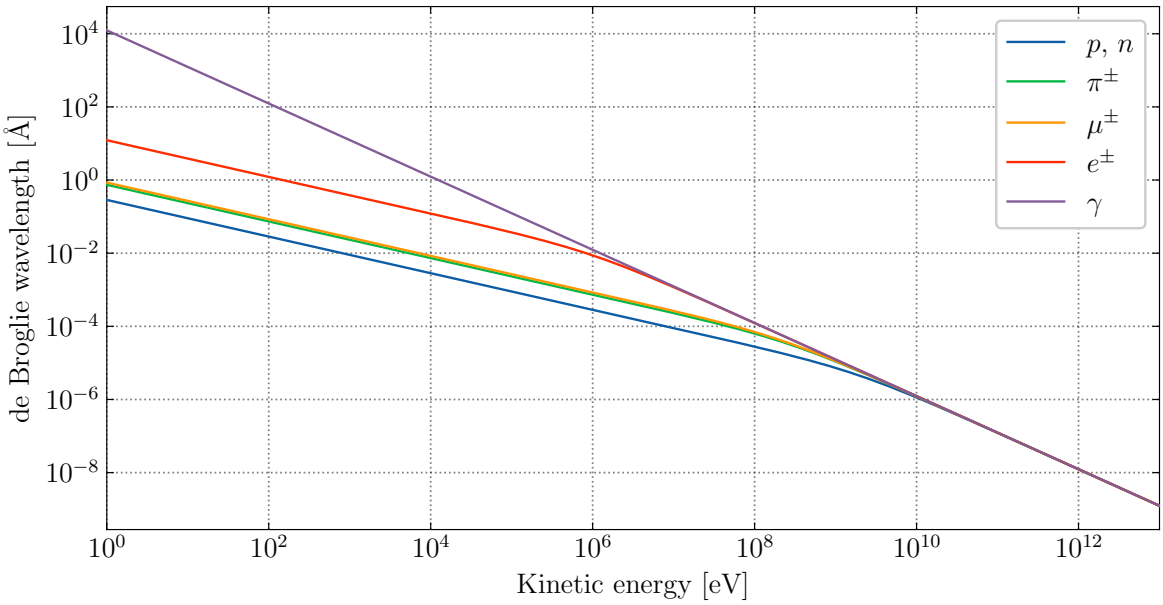

Figure 3.1: De Broglie wavelength for different particles as a function of their kinetic energy: due to the small difference in their rest mass, the curves for protons and neutrons overlap.

puting time, while others may aim at reducing the computing time for a target variance. Biased Monte Carlo calculations work by sampling from modified distributions that have the same mean as the non-biased one and/or by applying statistical weights to the transported particles: correlations and fluctuations cannot be exactly reproduced in this case.

It is very important to explicitly state the fact that most of the Monte Carlo codes work under some assumptions: the materials are assumed to be homogeneous and static, all the processes are Markovian (i.e. the fate of the particles is not influenced by previous histories), that the particles being transported do not interact with themselves (e.g. no beam-beam effects can be accounted), and that they interact with individual atoms, electrons, nuclei. In relation to the last point in particular, the picture of the random walk and of the particle trajectory is suitable as long as the de Broglie wavelength is small when compared to the distance between the particle's obstacles. Figure 3.1 shows the de Broglie wavelength for various particles as a function of their kinetic energy: for example, for electrons of 100 eV the wavelength is already of the same order of inter-atomic distances and the application of the random walk model becomes questionable.

3.2 Monte Carlo codes for radiation transport

3.2.1 FLUKA

FLUKA (FLUktuierende KAskade) [63, 64] is a general purpose Monte Carlo code for interaction and transport of particles in matter, covering domains of application

ranging from shielding design at accelerators, radiation protection, detector and instrumentation design, high-energy physics, dosimetry, and radiotherapy. The code is built and maintained with the aim of including the best possible physical models in terms of completeness and accuracy: results can therefore be obtained with a minimal set of free parameters which are normally related to a global optimization of the calculations, such as the adjustment of transport thresholds. FLUKA is capable of treating almost 60 different types of particles including photons, electrons, and positrons from the lower limit of fractions of 1 keV to thousands of TeV, optical photons, neutrinos, muons, neutrons down to thermal energies, heavy ions, and hadrons up to 20 TeV: this upper limit is 10 PeV when the DPMJET-III [65, 66] event generator is linked to the code. The code also allows to simulate the generation of radioactive nuclei produced in inelastic interactions and to transport the α, β and γ radiation emitted in their decay within the same run (one-step approach): radioactive decay can be treated in a semi-analogue way, which means that each single radioactive nucleus is handled like an unstable particle and a random decay time, random daughters, random radiation are selected and tracked, or in the so-called "activation study" mode, in which the time evolution following an irradiation profile is calculated analytically and all daughter nuclei and all associated radiations are considered at a fixed cooling time.

As far as the main models implemented are concerned, hadron-hadron interactions below few GeV are simulated by resonance production and decay while hadron-nucleus interactions up to momenta of 5 GeV/c are handled by the PEANUT (Pre-Equilibrium Approach to Nuclear Thermalisation) model which includes a refined Generalized Intra-Nuclear Cascade (GINC) and a pre-equilibrium stage: for energies up to 20 TeV, the Dual Parton Model (DPM) is used instead. A de-excitation package takes care of the nuclear evaporation, fission, Fermi break-up, and gamma de-excitation. Nucleus-nucleus interactions are instead dealt with the BME [67, 68, 69] event generator below 0.125 GeV/n, the modified RQMD [70, 71] event generator between 0.125 GeV/n and 5 GeV/n and DPMJET-III above the latter threshold. FLUKA can also simulate photonuclear and electronuclear interactions, photomuon production and electromagnetic dissociation.

For neutrons with energy below 20 MeV, two treatments are now possible. The first one is the established multigroup approach for which the energy range between 0.01 meV and 20 MeV is subdivided into 260 intervals, or energy groups, which have approximately the same size on a logarithmic scale. Elastic and inelastic reactions are simulated using transfer probabilities from one group to another, and the angular probabilities are obtained considering an expansion in Legendre polynomials of the actual scattering distribution truncated to five terms. The library of neutron cross sections contains information for different materials and in some cases at different temperatures to account for the Doppler broadening. The multigroup treatment has some shortcomings which may lead to artefacts: due to discrete angular distributions, unphysical results may arise when neutrons are likely to scatter only once, while, unless special corrections are made, self-shielding effects in some materials may be lost in the process of cross section averaging owing to the necessary coarse group structure

with respect to resonances. In the latter case, corrected cross sections for important elements (Al, Fe, Cu, Au, Pb, Bi) have been included in the code. Although in the vast majority of the cases the group-wise approach is sufficient, a full point-wise treatment has recently been made available to overcome the shortcomings of the former approach: the point-wise treatment allows a correlated generation of all reaction products for event-by-event studies, Doppler broadening of cross sections at any temperature, and the treatment of molecular binding effects for very low-energy neutrons.

Thanks to the Combinatorial Geometry (CG) package, FLUKA is able to handle extremely complex geometries such as those of the LHC experiments or even several hundreds of meters of the LHC tunnel [72]. Regions are defined using the Boolean operations of union, subtraction, and intersection to combine elementary bodies, for instance spheres, infinite cylinders, planes, parallelepipeds, and even generic quadric surfaces. Each region must be assigned a homogeneous material composition and the ensemble of all the regions has to be contained within an outermost boundary region, in jargon "blackhole region", that collects particles exiting the geometry and ends their tracking. Thanks to its lattice capabilities, FLUKA also allows for avoiding implementing repetitive structures in detail: a single module can be described and then replicated as many times as the user wishes in different portions of space using dedicated geometry transformations.

Particle tracking can be performed in presence of magnetic and electric fields with adaptive stepping algorithms to solve the equation of motions: these take into account the variation of the particle's energy during the step due to acceleration or energy loss and, for transport in vacuum, due to synchrotron radiation emission.

FLUKA uses as input a standard ASCII input file consisting of a variable number of commands, each consisting of one or more lines. For historical reasons, the lines of the commands are known as cards: the cards contain one keyword identifying the command, six numerical values (in jargon called WHATs) that specify some command parameters, for instance coordinates, energies, indices of a given region or material, and finally one character string referred to as SDUM. For editing the input file in a human-readable way without hiding the inner functionalities of the code, the FLAIR (FLUKA Advanced Interface) [73] code is available to users: among many features, it also provides means to debug the geometry and inspect and visualise the output of the calculations.

Scoring

As previously introduced, any result in a Monte Carlo calculation is obtained by summing contributions to the score, or tally, of a detector defined by the user. In FLUKA there are different types of scoring options available and in some cases there are different types of estimators for the same radiometric quantity. The most relevant options for the present thesis work are here summarised.

USRBIN This scoring option allows to estimate the spatial distribution of several radiometric quantities in a regular mesh (Cartesian, 2D-cylindrical, 3D-cylindrical

and even more complex phase space structures) that is independent of the simulation geometry. Among the many radiometric quantities that can be scored, one can find for instance energy density, dose, fluence (estimated as track length density), activity per unit volume, NIEL, 1 MeV-neutron equivalent fluence in silicon, high-energy hadron equivalent fluence and thermal-neutron equivalent fluence.

USRTRACK It is a track-length estimator allowing to score fluence energy spectra (energy differential fluence) on a region basis. Manual normalisation by the region volume is required.

USRBDX This option allows to define a boundary crossing detector to calculate fluence or current, averaged over the boundary between two geometry regions. The result will be in the form of a double differential fluence spectrum in energy and solid angle, where the solid angle considered is $2\pi(1-\cos\theta)$ and θ is the angle between the particle trajectory and the normal to the boundary at the point of crossing.

USRYIELD USRYIELD allows to score a double differential yield d^2Y/dx_1dx_2 of particles crossing a given boundary between surfaces or, for instance, emerging from an inelastic interaction. This is a multipurpose option in which the variables x_1 and x_2 can be energy, momentum, polar angle with respect to the beam direction, particle charge or even pseudorapidity.

RESNUCLEi This scorer allows to obtain information on residual nuclei on a region basis and is an event-based estimator, meaning that residual nuclei are scored after they have been produced as a result of an interaction and once they have been fully de-excited. With the appropriate commands indicating the irradiation history and the desired cooling time, the output of RESNUCLEi will be an activity instead of a production yield. Manual normalization by the region volume or region mass is required.

Another useful option immediately available to the user is the possibility to estimate different dose equivalent quantities using fluence to dose conversion coefficients: the radiation protection quantities that can be estimated are ambient dose equivalent, effective dose based on ICRP Publication 74 coefficients [74], effective dose based on the more recent ICRP Publication 116 coefficients [55], and several radiometric quantities defined in ICRU Report 95 [75].

For specific applications or for more complex problems, the built-in scoring options can be further extended with dedicated user routines to obtain the desired information: these routines have to be written in the FORTRAN programming language on which FLUKA is largely based and have then to be compiled and linked to the standard FLUKA library to produce a custom executable with which simulations should be run[1].

[1]The interface to FLUKA of the fluence conversion coefficients code developed for this thesis work (see Chapter 4 and, for more details, Sections 4.3 and 4.5) exploits this possibility.

Biasing

For applications in which fluctuations and correlations are not of interest and only quantities averaged over many events are, it can be extremely useful to set up biasing techniques to reduce the CPU time or the variance on the estimated quantities (or both). FLUKA comes with many options available but only two of the most relevant for this thesis work will be illustrated.

Based on the two techniques of surface splitting and Russian roulette, one of the simplest and most effective biasing options is importance biasing which can be independently set and tuned for different particle species. Importance biasing operates by assigning a numerical importance to each region of the simulation geometry. When a particle moves from a region of lower importance to a region of higher importance, replicas of the particle are created based on the relative importance (> 1.0) of the adjacent regions and the particle statistical weight, normally equal to 1.0 at the start of calculations, is reduced. When a particle moves instead from a region of higher importance to a region of lower importance, a random number is drawn and based on the relative importance of the adjacent regions (< 1.0) the particle can be killed: if the particle survives, its weight is increased. The weight adjustment in surface splitting and Russian roulette is always such that the total weight is conserved. To avoid excessive over-biasing or under-biasing, FLUKA internally limits the ratio of the importances between two regions traversed by a particle between 0.2 and 5.0. This form of biasing is best suited for shielding calculations in which particle fluences may be attenuated by several orders of magnitude: the importances of the regions are normally selected based on the inverse of the expected attenuation so that the particle populations remain approximately constant.

Instead of acting directly on the particle weight, one may want to bias directly certain probability distributions: in some cases, for instance in presence of very thin objects or for processes that intrinsically have a very low cross section, an analogue sampling would be inefficient. The option that FLUKA offers in this case is to bias the inelastic interaction probability of selected particles and selected materials by multiplying the corresponding inelastic scattering length by a given factor: by comparing the physical and the biased survival probabilities, the survival of the parent particle is decided via Russian roulette and the weight of the generated secondary particles will be adjusted. For example, in the case of objects whose thickness t is much smaller than the inelastic scattering length λ_I of the particle of interest, the typical and most simple choice of the biasing factor is of the order of t/λ_I, such that the biased inelastic scattering length is shorter and at least one inelastic interaction occurs on average in the thin target.

3.2.2 PHITS

PHITS (Particle and Heavy Ion Transport code System) [76, 77] is a Monte Carlo particle transport simulation code mostly tailored to studies in accelerator technology and radiation protection, but that finds applications also in the field of radiotherapy,

instrumentation design, and space radiation. The code can handle around 40 different types of particles up to the energy of 1 TeV (1 TeV/n in case of heavy ions), but at present cannot handle interactions involving two or more opposite-moving particles as in collision experiments.

PHITS comes with different physics models and the user is left with a lot of flexibility in departing from the default settings: with judgement, and often experience, it is not only possible to choose among different ones, but also to select the thresholds at which the code switches from the usage of one model to another depending on the particle energy. Although not transported by default for CPU time savings, electrons, positrons, and photons can be treated with the EGS5 (Electron Gamma Shower) algorithm from the lower limit of 1 keV up to the highest handled energy. Interaction of hadrons in the intermediate energy range, by default from 1 MeV to 3 GeV, are treated by the Intra Nuclear Cascade model (INCL4.6), while at higher energies the JAM hadronic cascade model is used. The JQMD and JAMQMD deal instead with hadron-nucleus and nucleus-nucleus interactions in the intermediate (1 MeV/n to 3 GeV/n by default) and high-energy range respectively. In all the above cases, a generalized evaporation model GEM takes care of the full de-excitation of the remnants of the inelastic interactions. The treatment of low-energy neutrons, photons and electrons is fully handled using nuclear and atomic data libraries: for this reason, photonuclear reactions can be treated only for the lower energy regions in which the giant dipole resonance is the dominant mechanism. Activation calculations in PHITS are possible but have to be performed in two steps. First one has to estimate the spectra of neutrons with energy below 20 MeV and the nuclear production yields by protons, heavy ions, mesons, and neutrons with energy above 20 MeV. Then, the DCHAIN code distributed with PHITS can combine these pieces of information to evaluate residual activity, decay heat, and residual radiation spectra for a given cooling time.

The geometrical configuration of a simulation is defined by geometry cells, jargon for regions, to which a homogeneous material composition is assigned: cells are described as the combination of elementary surfaces through Boolean operations with many resemblances with respect to FLUKA. In a similar fashion to the latter code, each point of space must belong to one and only one region and an outer boundary must be defined. Both surfaces and cells (at least by default), are identified by a number, not by a user-defined name. PHITS offers the possibility to change the material assigned to a certain cell as a function of the elapsed time since the start of a primary history: this feature allows for example the modelling of shutters and choppers in neutron beamlines.

The tracking of particles can be performed in presence of electric and magnetic fields of arbitrary complexity and even time-varying, and, for extremely refined calculations and accurate design of long beamlines, it is also possible to account for the presence of a gravitational field for neutrons below 1 eV.

PHITS uses as input a standard ASCII file which consists of a series of sections identified by a name included in square brackets: sections are used, for instance, to define the primary source, to describe the materials and geometry and to specify the

tallying[2] options. Each section can consist of several lines which normally contain a one-word string identifying a parameter of that particular section: each parameter or option is specified by a value or a list of values. The input file, the geometry in particular, is almost entirely number based: this means that options are selected using numerical values instead of text keywords interpreted by the code at runtime. A GUI for editing the input file is not available at present, but the FLAIR code allows to export simulation geometries in FLUKA format to the PHITS format and vice versa. PHITS also supports the execution of runs with two kinds of parallel computing. In distributed-memory parallel computing, primary histories are distributed to each CPU core in batch units: each batch unit is a job and, when all the assigned jobs to each core are finished, the main core collects and processes their results. In shared-memory parallel computing, instead, single histories are distributed to each CPU core.

Tallying

The PHITS Monte Carlo code comes with many different tally options which, to a certain degree, allow for a more flexible estimation of the desired quantities with respect to FLUKA. Each type of tally is defined within the dedicated section of the input file but there are certain features common to all. All the radiometric quantities and energy deposition quantities can be estimated on regular meshes (Cartesian, 2D-cylindrical or 3D-cylindrical) or on a region basis: in the latter case, a normalization by the region volume is required. Additional freedom is granted by the possibility of filtering the contributions to the desired quantity by the particles' angle, time since the start of the primary history, and energy: this feature can be for example exploited not only to obtain fluence energy spectra on a region basis but to also obtain in an easy way the fluence spatial distribution of selected particles having energy within defined energy ranges. The most important tally options are described below.

T-Track This tally can be used to obtain fluence and fluence spectra on a user-defined mesh or on a region basis. Fluence is estimated as total track-length per unit volume and, in the case of region-based scoring, manual normalization is needed.

T-Cross T-Cross is also a track-length estimator but is used to obtain the current or fluence at the boundary between two surfaces.

T-Deposit With this option it is possible to estimate energy deposition quantities. A variation of this tally allows to score the energy distribution in two selected regions for correlation studies.

T-Yield and T-Product Particles and nuclei produced by nuclear reactions can be estimated by means of this tally allowing to filter by the parent particle which underwent a reaction or its generation (i.e. a source particle or any other secondary particle). The latter tally allows for estimating the energy distribution of the generated particles as well.

[2]Instead of the term scoring, the wording tallying is conventionally used for PHITS.

To extend the flexibility of the different tally options, PHITS comes with the possibility to apply user-defined factors that depend on the particle energy and that can be directly defined in the input file in a dedicated section called Multiplier section[3]. For instance, this functionality can be used for dose equivalent estimations or damage calculations.

Biasing

Among the different variance reduction techniques available in PHITS, there is certainly importance biasing whose principles are exactly as described for the FLUKA code. However, there is virtually no internal restriction on the value that the relative importance between two regions crossed by a particle: to avoid possible over-biasing or under-biasing, weight windows should be concomitantly used when setting an importance-based variance reduction scheme. Another useful biasing technique is the forced collision which, on average, has the net effect of reducing the mean free path between inelastic collisions. A particle entering a region where this technique is applied is split into two particles: one is forced to engage in an inelastic interaction and the remaining passes through uncollided. If w is the statistical weight of the incoming particle and p is the penetration probability, the weight of the uncollided particle will be wp and the weight of the particle forced to interact will instead be $w(1-p)$: the interaction point is randomly determined along the particle track.

[3]The interface to PHITS of the fluence conversion coefficients code developed for this thesis work (see Chapter 4 and, for more details, Sections 4.3 and 4.5) exploits this possibility.

Chapter 4

The fluence conversion coefficients method for radiological characterization studies

The calculation of induced radioactivity is essential in all the stages of the life cycle of any accelerator component: during the design phase it is very relevant in the choice of materials, during the operation period is necessary for the estimation of residual dose rates and for establishing operational radiation protection measures, and finally the knowledge of the radionuclide inventory is of paramount importance for the decommissioning phase of the accelerator and detectors themselves.

Owing to the challenging radiation environment at most of the CERN facilities, Monte Carlo codes are necessarily used for the estimation of induced radioactivity. There are different ways in which such computations can be performed, each one with its own advantages and disadvantages: for each problem under examination, one technique may also be more efficient than another one.

This chapter is dedicated to a detailed explanation of the fluence conversion coefficients method applied to the radiological characterization of materials which was developed and maintained as part of this thesis work performed within the Radiation Protection group at CERN: its principles, operation, and proof of concept will be here illustrated. The discussion will be complemented by the code benchmarks illustrated in Chapter 5 and by a selection of relevant practical applications for the LHC experiment in Chapter 6: these include studies for the reinforcement of the CMS shielding and for the assessment of the effect of cobalt impurities on the activation of the CMS HGCal steel, simulations for establishing a zoning for clearance operations in ALICE for the Long Shutdown (LS) 3 and the possible decommissioning of the present ALICE detector in LS 4, and the calculations for ATLAS and CMS in preparation to the LHC pilot beam in 2021[1].

[1]As better contextualized in Section 6.4, the 2021 LHC pilot beam run was conducted between October 18 and November 1, 2021, for an early commissioning of the LHC machine and experiments in preparation to the restart of the LHC in early 2022.

4.1 Introduction and practical needs

An aspect of paramount importance in radiation protection is the radiological characterization of components that have been exposed to a radiation environment. From an operational point of view, this is required to establish the needed protection measures during the maintenance and handling of such components, to define their appropriate transport conditions and to distinguish, for instance, between conventional and radioactive waste thus determining the appropriate disposal pathways (and related costs). When performing a radiation protection assessment, one is often confronted with the task of estimating one or several radiological hazard factors. In the most general sense, a radiological hazard factor is a quantity, typically defined within European or national regulations in matter of radiation protection, that has to be evaluated for the specific case under examination and then compared with legally defined thresholds which will, for instance, determine possible actions to be taken. Very simple examples of hazard factors could be the total activity in Bq or the total specific activity in Bq/g of an activated object, while less trivial cases could be the total committed effective dose in mSv following the accidental inhalation or ingestion of a mixture of radionuclides. Particularly relevant for this thesis work is the multiples of (Swiss) clearance limits (LL, already introduced in equation 2.21), which is a radiological hazard factor with a crucial role in differentiating between conventional and radioactive waste (see for instance Section 2.4).

In almost the entirety of situations, a generic radiological hazard factor H can be expressed as a weighted sum of the mass-specific activities A_b of the radionuclides that are present in a given mixture, with weights w_b that depend on the particular radionuclide:

$$H = \sum_b \frac{A_b}{w_b} \tag{4.1}$$

The radionuclide weighting coefficients are case specific. Using the same examples provided before, the w_b will all be equal respectively to $1/M$ (where M is the mass of the component) and 1 if the hazard factors considered are the total activity and the total mass-specific activity. For the accidental ingestion of a volume of liquid V with density ρ, the weighting coefficients will instead be $1/(\rho V e_b)$ where e_b is the dose coefficient in mSv/Bq for the committed effective dose resulting from the ingestion of a unitary activity of a radionuclide b. Finally, in the case of the multiples of clearance limits, the weighting coefficients are none other than the clearance limits in Bq/g of considered radionuclides.

4.2 Traditional methods for radiological characterization

It is now clear that the computation of a hazard factor reduces to the computation of mass-specific activities. As it was extensively explained in Chapter 2, once one deviates

from extremely simple cases, the calculation of induced activity has to rely on Monte Carlo radiation transport codes. Traditionally, two standard methods are available and usually implemented in most of the Monte Carlo codes. These two methods are event-based methods and fluence-based methods and will be presented in the following sections in light of the brief description of the FLUKA and PHITS codes offered in Chapter 3.

4.2.1 Event-based methods

Event-based methods for the estimation of activities rely on the events of creation of radionuclides during interaction in the radiation transport calculation. Event-based estimation can be achieved, for instance, with the RESNUCLEi scoring in FLUKA and the T-Yield tally in PHITS: while in the case of FLUKA the time evolution of the estimated radionuclide inventory can be directly performed at run time, an offline calculation is necessary for PHITS.

In these two cases, the scoring/tallying has also to be based on the regions that are defined in the geometry of the simulation: this automatically implies that the normalization of results to specific activity[2] has to be manually performed. For complex problems of large extension, for instance almost the entirety of the facilities at CERN, this quickly becomes cumbersome to handle and very error prone: an additional consequence is that the result will be an average over the considered region and if more granularity is required, for instance to identify portions of an object in which the total specific activity is within a certain range, the only solution is to segment the concerned regions, thus maybe significantly increasing the number of regions in the simulation geometry.

The output of these event-based methods is often a list of radionuclide activities or production yields for the selected regions: although this might be sufficient in some cases, in many situations it is not only more practical but also necessary to have a visualization of the estimated quantity over the geometry of the problem. A possible solution would be to use mesh-based scorings, like USRBIN in FLUKA or again T-yield in PHITS, with even some possibilities of filtering for the produced radionuclide by means of dedicated user routines that extend the standard scoring/tallying capabilities. Even in this case, however, the estimation of the radionuclide inventory relies on the geometry description of the problem and, as explained in the following section, this can often be a limiting factor.

In all the cases presented above, it remains however the fact that the convergence[3] of the result can be very slow in regions that are far away from the main interaction zone unless extensive biasing techniques are implemented: this is not always an ideal solution since the implementation of variance reduction techniques often requires expert

[2]Unless differently stated, from this moment onwards all specific activities have to be intended as mass-specific activities.

[3]In the context of Monte Carlo calculations, the term convergence is often used to indicate the CPU time required to reach the desired level of statistical uncertainty on the estimated quantity.

knowledge and cannot be easily generalized from one problem to another one as far as high-energy transport phenomena are concerned.

4.2.2 Fluence-based methods

The second traditional class of methods with which one can estimate radionuclide activities are fluence-based methods: particle fluence spectra are calculated with Monte Carlo codes and in an offline post-processing step are first folded with radionuclide production cross sections to obtain production yields which are then used to compute the time evolution of the radionuclide inventory. Fluence spectra can be estimated, for instance, with the USRTRACK scoring in FLUKA or the T-Track tally in PHITS. The post-processing can be done with various codes such as JEREMY [78] or ActiWiz [79].

As the first kind of event-based methods previously explained, also fluence-based methods rely on scorings/tallies that are based on the regions of the simulation geometry and have all the consequences that this implies, namely the manual region normalization not feasible for complex problems, difficulty in obtaining more granular results, and the limited visualization capabilities.

Fluence-based methods offer nonetheless a series of non-negligible advantages. Since they necessarily require a post-processing step, they introduce the possibility of performing sensitivity studies of the estimated quantity with respect to input variables, for example with respect to the considered irradiation history or the presence of impurities in the irradiated materials. The post-processing step also decouples the radionuclide production cross section used in the computation of the radiological inventory from the Monte Carlo code used for the simulation: this aspect could be very useful in particular in assessing the sensitivity of the final results with respect to the used cross sections by, for instance, repeating the post-processing step using different databases and without the need of re-running the full Monte Carlo calculation. While this point clearly introduces some advantages, at the same time it implies that suitable databases for the problem under study have to be found in literature or obtained by other means, such as ad hoc Monte Carlo simulations efficiently set up for the direct estimation of radionuclide production cross sections.

A second great convenience of fluence-based methods is intimately connected to the way fluence estimators work in Monte Carlo codes. Fluence is estimated as a total track-length per unit volume and this essentially implies that, for the same number of primary histories simulated, the estimation of particle fluence spectra within a given region will converge faster (i.e. will have a much lower statistical uncertainty) with respect to the estimation of the radionuclide inventory performed within the same volume on an event basis: in much simpler terms, the probability that a radionuclide is generated in an inelastic interaction is often much lower than the probability that the particle will cross the volume, lose energy or interact in other ways.

Last but surely not least, fluence-based methods may be applied in situations in which the usage of event-based ones would be highly impractical and inefficient. This particular aspect will be fully developed and clarified in the next section, which in-

troduces the working principles of a method based on fluence conversion coefficients, and will be complemented by the presentation of practical applications for the LHC experiments in Chapter 6.

4.3 The fluence conversion coefficients method

From the discussion made so far clearly emerges the need of a valid complementary approach that is a good compromise between the advantages and disadvantages of event-based and fluence-based methods. This method should be efficient even for complex problems, such as radiological characterization studies at the LHC experiments, and its main requirements are fast convergence, automatic normalization, and most importantly good visualization capabilities.

For these reasons, the novel approach based on fluence conversion coefficients was developed [80, 81]. This method is based on the already mentioned fact that a radiological hazard factor H can often be expressed as a weighted sum of radionuclide specific activities. By dividing equation 2.13 by the object mass, one obtains the generalized expression of the specific activity of a radionuclide produced in a component being exposed to a radiation field. Combining this result with the definition of the generic hazard factor H of equation 4.1 one obtains the following complete expression[4]:

$$H = \sum_b \frac{1}{w_b} \left(\sum_r T_{b,r} \sum_e \frac{m_e N_{AV}}{M_e^{mol}} \sum_{\substack{i=p,n,\\ \pi^{\pm},\gamma,...}} \int_0^{+\infty} \sigma_{r,e,i}(E)\phi_i(E)dE \right) \tag{4.2}$$

By approximating the integral over the particle's energies with discrete sums and re-organizing all the terms in a convenient way, it is easy to find:

$$\begin{aligned} H &= \sum_{\substack{i=p,n,\\ \pi^{\pm},\gamma,...}} \sum_{E_j} \Phi_{i,E_j} \left(\sum_{b,r,e} \frac{1}{w_b} T_{b,r} \frac{m_e N_{AV}}{M_e^{mol}} \sigma_{r,e,i,E_j} \right) \\ &= \sum_{\substack{i=p,n,\\ \pi^{\pm},\gamma,...}} \sum_{E_j} \Phi_{i,E_j} C_{i,E_j} \end{aligned} \tag{4.3}$$

where E_j is the average energy over the energy bin j, Φ_{i,E_j} is the integral of the fluence energy spectrum of particle i over the j-th energy bin, and σ_{r,e,i,E_j} is the production cross section of radionuclide r due to element e by particle i averaged over the j-th energy bin.

Equation 4.3 gives the fundamental result for which the radiological hazard factor can now be computed as the sum of the particles fluences contributions weighted with

[4]It is worth reminding that, despite the unfortunate clash of conventionally adopted notation, from Section 2.3 onwards m_e will be used to indicate the mass fraction of an element e in a given compound material and not the mass of the electron.

Method	Advantages	Disadvantages
Event-based	• Fully integrated in the Monte Carlo code of choice. • Very efficient for a reduced number of regions close to the main interaction zone. • If a mesh scoring/tally is feasible, it gives margin for a visualization of the results.	• If region based, it requires manual normalization. • Cumbersome for a large number of regions. • If region based, the visualization capabilities and the granularity of the results are limited. • Convergence can be very slow in regions away from the main interaction zone. • It cannot be applied for objects that are not or cannot be described in the simulation geometry.
Fluence-based	• Overall better convergence properties with respect to event-based methods*. • Easier with respect to event-based methods to perform sensitivity studies of the estimated result with respect to any input variable. • Applicable to objects that are not or cannot be described in the simulation geometry.	• It is region based so a manual normalization is required. • Cumbersome for a large number of regions. • Limited visualization capabilities. • It requires a post-processing step and a suitable cross section database.
Fluence conversion coefficients based	• Overall better convergence properties with respect to event-based methods*. • Automatic normalization. • Very good visualization over a large number of regions. • Applicable to objects that are not or cannot be described in the simulation geometry.	• It requires a pre-processing step and a suitable cross section database. • It is less trivial to perform sensitivity analysis of the estimated result with respect to any input variable.

* The reduction in CPU time achievable clearly depends on the particular problem under examination and on the quantity being estimated, but it can even be up to a factor of 100 or more (see Section 4.6 and Chapter 6, Section 6.2 in particular).

Table 4.1: Comparison of the advantages and disadvantages of traditional methods employed in radiological characterization studies (event-based and fluence-based) as described in Section 4.2 with those of the fluence conversion coefficients method whose principles are detailed in Section 4.3.

particle- and energy-dependent coefficients C_{i,E_j} and yields at the same time their definition. The coefficients C_{i,E_j} depend on the radionuclide weighting coefficients that define the hazard factor, on the material composition of the irradiated object via the elemental mass fractions and the production cross section, and on the irradiation history and cooling time via the time evolution matrix: for a given radiological characterization, these terms are all fixed and thus the coefficients can be pre-computed and applied directly during Monte Carlo transport calculation either employing simple user routines or by exploiting built-in code functionalities.

Table 4.1 summarises the advantages and disadvantages of the traditional methods previously described and of the novel method just presented. Being intimately connected to a fluence scoring, the fluence conversion coefficients method will have better convergence properties with respect to event-based methods and, since it operates by directly weighting particle fluences, it can be applied to fluence scorings on a user-defined mesh that is decoupled from the geometry of the simulation: this means that the normalization is automatic and the visualization capabilities offered by the method

are good even for large problems. For a similar reason and as explained in the following section, the fluence conversion coefficients method inherits from the fluence-based methods many of the conditions of applicability and range of validity, in particular the fact that it can be applied in cases in which event-based methods would be impractical. Finally, owing to the decoupling between the pre-computation of the coefficients and the Monte Carlo calculations, the pre-processing step requires a suitable cross section database and makes it less obvious to perform sensitivity analysis of the estimated result with respect to any input variable.

4.4 Applicability and assumptions

The fluence conversion coefficients method as described and formulated in this chapter is based on some assumptions that are also common to fluence-based methods and that are discussed in the following.

- **Irradiation history** The irradiation history, or irradiation profile, is a crucial parameter that is needed in the computation of induced activity and enters in the definition of the fluence conversion coefficients through the time evolution matrix $T_{b,r}$. In order to compute the induced activity for an arbitrary time dependent irradiation profile, the general approach is to approximate the irradiation profile with an irradiation histogram, that is by considering a series of smaller time intervals in which the source intensity can be considered constant: the number of time intervals and their length should clearly be adapted and be fine enough for each specific case.

  The activity at the end of the complete irradiation history and after a cooling time t_{cool} will be then calculated as the summation of various contributions in which each addendum is the induced activity over a slice of constant irradiation with duration Δt_{irr} followed by a cooling time $t_{cool} + \Delta t_{cool}$ and computed with the time evolution matrix $T_{b,r}(\Delta t_{irr}, t_{cool} + \Delta t_{cool})$ whose expression is exactly the one already introduced with equation 2.19. It should be noted that Δt_{cool} represents the cooling time between the end of the considered irradiation slice and the end of the full irradiation history.

  Due to its crucial role in any calculations, general considerations on the strategies adopted in histogramming the irradiation profile are outlined in Section 4.8, in particular for what concerns predictive studies for the LHC experiments for Run 3 and HL-LHC.

- **Particle fluence spectra** The fluence energy spectra of the particles that are inducing the activation have to be the same over the considered irradiation intervals: a variation of the energy dependence of the particle spectra could be due, for instance, to a change in the primary beam composition or primary beam energy. The relative intensity of the particle fluence spectra, which scales with the primary source intensity, is instead already taken into account by the suitable binning of the irradiation profile.

If the condition just introduced on the fluence spectra energy dependence is not met, either the irradiation period has to be further subdivided into smaller parts, or the arising uncertainty for the non-uniformity of the particle spectra has to be taken into account. For the LHC experiments this is obviously the case in which the energy of the colliding beams is different (for instance 8 TeV c.o.m. in the last year of Run 1 and 13 TeV in Run 2), or when the colliding beams are different (lead-lead collisions instead of proton-proton collisions): luckily enough these periods are very well defined and, as explained in Section 4.8, small approximations can be taken if the objective is to have results that are overall conservative.

It was once introduced the fact that fluence-based methods that are also region-based, that is those relying on the estimation of particle fluence spectra on a region basis, provide results that are an average over the whole region. In reality, particle fluences may vary within the considered object, for instance simply due to attenuation: it was explained that, for a higher granularity of the result, the workaround in these cases is the segmentation of the concerned regions of the simulation geometry at the price of increased complexity. The fluence conversion coefficients method can be applied to mesh scorings/tallies and this issue is considerably attenuated: the results will then be an average over the bin of the defined mesh which can be suitably refined according to the user needs and specific problems.

Last but not least, it was mentioned several times that both fluence-based methods and the fluence conversion coefficients method can be applied in situations in which the usage of event-based ones would be not at all possible or highly inefficient and this is very relevant for high-energy physics problems more than anywhere else. Consider, for instance, the frequent practical case in which a radiological assessment is needed in the periphery of a high-energy physics detector, such as CMS or ATLAS, where many infrastructures can be present: this could be for example a study for an intervention requiring destructive works in a radiation area. The typical Monte Carlo simulation geometries for high-physics experiments must clearly be detailed enough to perform radiation studies in the inner detector elements, but a high level of detail cannot be maintained up to elements in the very periphery: these components are typically described in the simulation geometry in a much more simplified way or not described at all. The estimation of activity with the event-based methods would require that the actual objects are well represented in the geometry because they rely on the events of creation of radionuclides at the end of particle cascades or inelastic interactions: even if this were the case, the CPU time required to obtain a relative uncertainty on the final result below at least 10% would be considerate. Under the hypothesis that the size of the concerned components is small compared to the interaction length of the particle types and energies that are dominant in the activation process, one can expect that particle fluence spectra are at most slightly perturbed and can thus be estimated in dedicated air volumes making it possible to apply a fluence-based or the fluence conversion coefficients based approach. Different practical

applications of the method that exploit this fact will be presented in Chapter 6, in particular the design studies for the reinforcement of the CMS forward shield in Section 6.1 and the preparatory studies for CMS and ATLAS for the 2021 LHC pilot beam run in Section 6.4. In the case in which the above condition on the size of the irradiated object is not met, fluence-based methods and the fluence conversion coefficients method will give at least conservative results due to the fact that the attenuation of fluences in the object is not properly accounted for. This typically occurs only for the low-energy part of neutron fluence spectra and only in the presence of elements having a high neutron capture cross section (for instance europium isomers) which in reality would act as a neutron sink.

- **Material composition** The assumptions on the material composition are a consequence of how both Monte Carlo codes and the fluence conversion coefficients method handle this aspect. In the simulation geometry, all regions have a uniform and static material composition. Following what was discussed when the general activation formalism was introduced in Section 2.3.1, no interaction between the generated radionuclides and the radiation field inducing the activation is taken into account: as a consequence, no depletion of the initial material is considered and no breeding reaction, such as the transmutation of minor and major actinides, can be correctly described. The above conditions are essentially always met for applications at particle accelerators and colliders.

4.5 Implementation

Before running a Monte Carlo simulation for a given radiological study, the fluence conversion coefficients have to be pre-computed. Their calculation is performed by a dedicated code which has been developed and maintained as part of this thesis work performed within the Radiation Protection group at CERN [80, 81, 82]. The code is fully written in the Python programming language and has been tailored to be as much user-friendly as possible: since Python is a scripting language, the fluence conversion coefficients code naturally provides a scripting interface to the user. The minimum input parameters required for the calculation of the coefficients and their specificities are listed below, while a pseudo-code description is provided in the subsequent paragraph.

- **Material composition** The elemental composition of the object to be characterized can be specified via a standard Python dictionary data structure having for keys the element symbols and for values the corresponding mass fractions. If not done already at the input level, the mass fractions will be normalized.
- **Weighting factors** As previously explained, the weighting factors depend on the radiological hazard quantity that one wishes to compute. These can be provided as a Python dictionary data structure having for keys a character string identifying the radionuclides and for values the corresponding weights that one wishes to apply. Radionuclides for which a weight is not provided will not be considered in the final summation unless default values are set by the user.

- **Irradiation histogram and cooling time** The irradiation histogram can virtually be as complex as the user wishes. It can be represented by a single value interpreted as the irradiation time in seconds or it can be a nested Python list in which each sub-list has two items, the first being the duration of the irradiation interval in seconds and the second the source intensity per unit time. In the first case, a final normalization of the result by the source intensity will be required, while no further normalization is necessary in the latter situation. For the specific case of the LHC experiments, the way in which the irradiation profile is normally computed from real or forecast luminosity data is discussed in more detail in Section 4.8. The cooling time in seconds is instead simply provided as a floating point value.

- **Decay data** The knowledge of the decay constants and decay modes of each radionuclide is essential for the computation of the elements of the time evolution matrix. The decay engine, that is the part of the code that specifically performs the computation of the time evolution and which is a standalone Python package, is distributed with a decay database initially employed for the JEREMY code and that was extracted from the JEFF-3.1.1 database [83]. For advanced applications, the user can in principle employ decay databases from other sources.

- **Cross sections and energy binning** Particle- and energy-dependent cross sections are the last, but surely not least, piece of information required in the computation of the coefficients. Cross sections are treated via a dedicated Python class and the cross section database is essentially constituted by a dictionary where each reaction is unequivocally determined by a tuple formed by strings indicating the particle projectile, the target element, and the product radionuclide. For each reaction entry, the cross section data is stored as a list of energy bin borders in eV and the corresponding bin-averaged cross section values in b. The user can virtually use cross sections from any database if appropriately formatted as described before, but for multipurpose applications, a generic cross section database was specifically compiled. Low-energy neutron data (i.e. below 20 MeV) are derived from the JEREMY database, which in turn consisted of data extracted from the JEFF-3.1.1 database and re-binned to 260 energy groups of approximately equal width in logarithmic scale corresponding to those used for the multigroup neutron treatment in FLUKA. The isotope production cross sections for protons, charged pions, neutrons above 20 MeV, and photons were instead estimated with both FLUKA and PHITS as discussed in more detail in Section 4.7.

  The energy binning that is used in the computation of the coefficients is represented by a dictionary in which each particle is associated with the corresponding list of energy bin borders in eV: this also allows the user to select if the computation of the conversion coefficients should be made for a reduced group of particle species or for the standard set which entails protons, charged pions, neutrons and photons. By default, the energy binning provided with the code corresponds to

the one over which the cross sections of the compiled database are tabulated: the user has in any case the possibility to provide any other desired binning and, in this case, the fluence conversion coefficients code will take care of performing a re-binning of the radionuclide production data accordingly.

The coding knowledge and actions required by the user are minimal and the computation of the coefficients ultimately reduces to a simple call to a function receiving as arguments all the above parameters, properly defined according to the needed case. At the function call, the fluence conversion coefficients code will first start an iteration over the particles for which an energy binning was provided. For each specified particle, the mid value of each energy bin is computed as the geometric average of the bin edges and an iteration over each energy point commences. Then, for each energy point, a reduced cross section data set is extracted from the provided cross section database: each entry of this reduced set will now contain the available cross sections for the production of all radionuclides that can be created from the elements listed in the specified compound, by the selected particle, and for the given energy in the iteration step.

With this information, it is then possible to compute the vector of the produced radionuclides which is stored as a dictionary data structure where each key is a radionuclide r that can be produced by one or more of the elements e in the specified compound, and each value correspond exactly to the production-yield-like term $m_e N_{AV} \sigma_{r,e,i,E_j} / M_e^{mol}$ as in equation 4.3.

At this stage, the decay engine is called passing the provided information on the irradiation history, cooling time and the just computed production yield term: the decay engine will compute the build-up and decay of the initial radionuclide inventory (i.e. the coefficient of the time evolution matrix as in equation 2.19 and as explained in Section 4.4) and return the final inventory. At the end of this stage, one is left with a dictionary data structure in which each key representing a radionuclide of the final inventory is associated with a value that exactly corresponds to the term $\sum_r T_{b,r} m_e N_{AV} \sigma_{r,e,i,E_j} / M_e^{mol}$ as in equation 4.3.

Finally, the fluence conversion coefficients code applies the specified weights for each radionuclide in the inventory and the results are summed to have, at last, the coefficients C_{i,E_j} as in equation 4.3. This procedure is repeated for each energy point, then for the remaining selected particle species contributing to the activation.

The way in which these conversion coefficients are computed is totally independent of the Monte Carlo code for which they will be used, only the way they are formatted and handled does: only interfaces with FLUKA and PHITS have been implemented at the time of writing, but it would be easy the extend their application to other Monte Carlo codes provided that these either support user-defined extensions of scoring/tallies, or for which energy-dependent weights can be applied with built-in functionalities. As it is clear from the above description, a different set of conversion coefficients is produced for each provided combination of input arguments, that is material composition, irradiation history, cooling time, and radionuclide weights: the interface to FLUKA and PHITS was conceived in such a way to exploit as much as possible the flexibility

of the fluence conversion coefficients method. At least within the intrinsic limits of the Monte Carlo codes themselves, different fluence conversion coefficients' sets can be applied within a single simulation run, thus allowing the simultaneous assessment of different quantities: this can be very useful, for instance, to evaluate the activation of different materials, to examine the radionuclide inventories at different cooling times or even to consider different irradiation scenarios.

4.5.1 Interfacing with FLUKA

The FLUKA code doesn't currently support the possibility of directly specifying energy-dependent coefficients in the input file to weight the desired scored quantities. For this reason, the interface to the fluence conversion coefficients code has to be made through an auxiliary file and a user routine which was specifically coded in FORTRAN for the application. The auxiliary file is a simple ASCII file produced by the fluence conversion coefficients code in which the sets of coefficients are tabulated with a fixed format: based on the order in which it was computed, each set of coefficients is assigned an index running from 1 to virtually 999. The detailed structure of the auxiliary file is presented in detail in Ref. [81].

As far as the preparation of the simulation input file is concerned, the user can add all the desired fluence estimators (e.g. USRBIN, USRTRACK, USRBDX, and USRYIELD) and should issue the additional command USERWEIG in order to activate the calls to the user routine at scoring time. The weighting coefficients will be applied only to the scorings which have the SDUM parameter equal to the keyword FCS (standing for *Fluence conversion Coefficients Set*) followed by the three-digit, zero-padded number that selects the conversion coefficients set (e.g. FCS001 to apply the first tabulated set): the other free characters of the SDUM efficiently and effectively allow for the application of the same set of coefficients to different estimators, for instance for different user-defined meshes or geometry sections. Normally one should account for all particles that contribute to activation: in order to ensure this, the generalized FLUKA particle kind ALL-PART should be estimated and the routine will take care of applying the correct coefficients for each particle species. It is nonetheless possible to assess the separate contributions of the different particles by issuing different detectors, each associated with the same set of coefficients and each scoring the fluence of a given particle kind.

To effectively apply the coefficients, the user is simply required to compile the FORTRAN routine and link it to the standard FLUKA library generating a custom executable. At runtime, the routine will first read the auxiliary file, initialize the coefficients, and echo them to standard output. When track-length counters for the estimation of fluence are being updated, the routine will intercept the properties of the particle being tracked, namely the identity and the kinetic energy, identify the number of the set associated with the scoring counter being updated and then, based on the particle energy, apply the corresponding weighting coefficient: if the particle is not among those for which the coefficients are tabulated it will be discarded by applying a

weight equal to zero.

4.5.2 Interfacing with PHITS

Contrary to FLUKA, PHITS allows to directly specify energy dependent weighting factors, in jargon multipliers, through the dedicated Multiplier section. For each set, also identified by a number, one should have as many Multiplier sections as the particles for which the weighting has to be applied. The Multiplier sections for the same set of coefficients will be associated with the same numerical identifier: PHITS currently allows for a maximum of 99 different sets. Through the various parameters of the T-Track tallies, the user can then easily associate the tally with the desired Multiplier, hence to the conversion coefficients set.

In this case, the fluence conversion coefficients code will directly format the coefficients as Multiplier sections and save them in an ASCII file that can either be treated as an auxiliary file, or integrated into the text-based PHITS input file.

4.6 A toy model for the code testing

To test the fluence conversion coefficients code from the computation of the coefficients to its interface with the Monte Carlo codes, a simple toy model was first implemented and used. A pencil beam of 1 GeV protons impacts on a copper target of 5 cm in radius and 80 cm in length. The target is surrounded by air and is placed within a cylindrical shielding structure consisting of 40 cm of standard concrete, 40 cm of cast iron, and finally again 40 cm of standard concrete. The schematic view of the simulation geometry is offered in figure 4.1: for scoring purposes, the target has been segmented into four different regions, labelled from T1 to T4, and the shielding laterally to the target is also segmented into three regions, labelled instead from Sh1 to Sh3.

For consistency, the cast iron and concrete standard compositions used in the simulation have also been used in the computation of fluence conversion coefficients. The test irradiation profile, consisting of 10 years of continuous irradiation with cooling times of 2 days and 2 years, has been used for the same reason for the direct estimation of radionuclide activities with event-based methods and their calculation via fluence conversion coefficients.

The most relevant results of the test with FLUKA will be here discussed: the results of the testing with PHITS and an overall more extensive discussion are offered in a dedicated report [81]. Several quantities ranging from specific activity of selected radionuclides to multiples of Swiss clearance limits (LL) were estimated both using FLUKA built-in methods (event-based) and the fluence conversion coefficients method. Figure 4.2 shows the spatial distribution of the specific activity of ^{22}Na, ^{54}Mn, ^{56}Co, ^{60}Co, and of the multiples of LL as a function of the longitudinal coordinate in the copper target: the symbols (method 1) corresponds to FLUKA built-in scoring, the lines (method 2) correspond to the fluence conversion coefficient method. In the

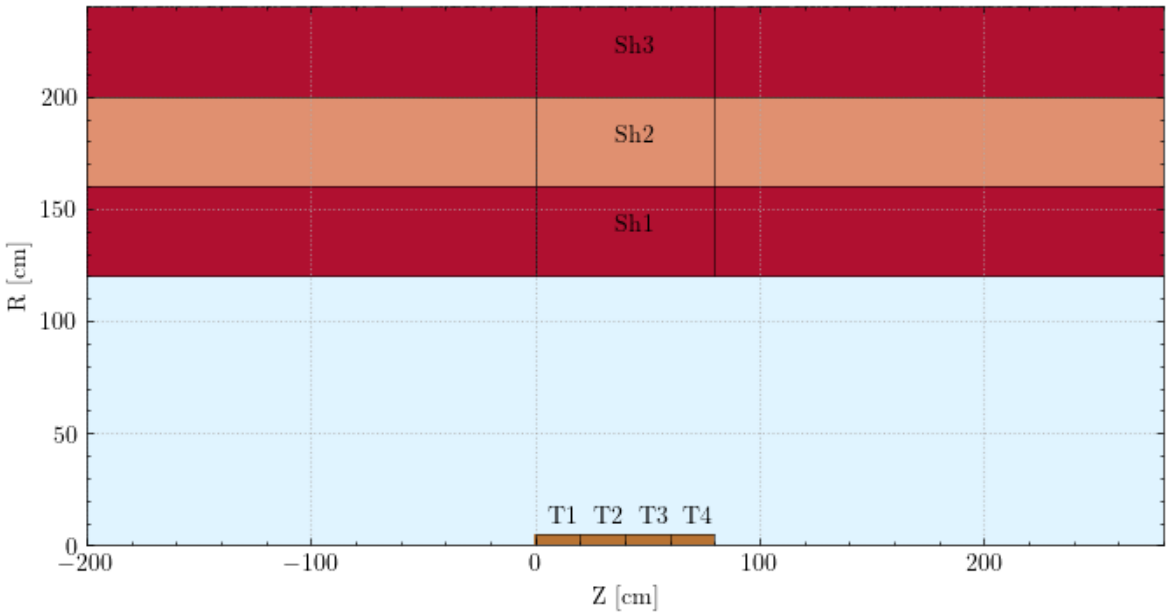

Figure 4.1: Simulation geometry of the toy model used for the testing of the fluence conversion coefficients code: the scoring regions for volume averaged quantities are indicated with their corresponding labels.

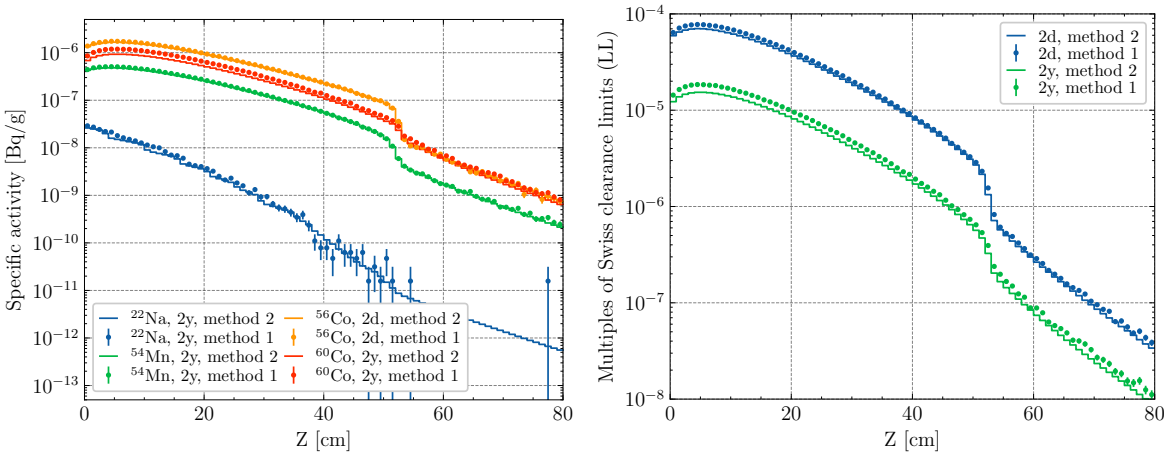

(a) (b)

Figure 4.2: Comparison of radionuclide specific activities (a) and multiples of Swiss clearance limits (b) for different cooling times estimated in the copper target of figure 4.1 with a FLUKA event-based method (symbols, method 1) and with the fluence conversion coefficients method (lines, method 2). A continuous irradiation period of 10 years is assumed, and all results are normalized per primary source intensity.

considered toy example, the copper target is the region where the interaction of the primary beam occurs and therefore the convergence is expected to be rather fast even with a reduced number of primary histories simulated (of the order of few hundreds of thousands). Despite this fact, it is still possible to appreciate that the convergence is much faster with the fluence conversion coefficients method even in the last centimetres of the target: this is particularly evident when considering the uncertainty on the ^{22}Na specific activity.

As previously precised, stating that the convergence is faster means in general that, for the same number of primary histories simulated (i.e. for the same CPU time), the statistical uncertainty on the estimated quantity is smaller: equivalently this means that in order to achieve a given level of statistical uncertainty for a given quantity, less CPU time is required. The reduction in CPU time that can in general be achieved with the fluence conversion coefficients method with respect to event-based methods clearly has a strong dependence on the particular problem under examination and on the quantity being estimated: whenever pertinent, some case-specific estimates will be provided in Chapter 6 to further stress the advantages of the method contextualizing them in the discussed studies. In this simple case, for instance, the relative statistical uncertainty on the ^{22}Na specific activity in the copper target in the range $40\,\text{cm} < Z < 60\,\text{cm}$ is of the level of few or fractions of % for the fluence conversion coefficients method (figure 4.2(a)) while is approximately 50 % for the event-based method: approximately 100 to 150 times more primary histories would need to be simulated in order for the above quantity estimated with the event-based method to reach the same accuracy as presently obtained with the fluence conversion coefficients.

Table 4.2 provides a summary of the most relevant volume-averaged quantities in the scoring region described before and labelled in figure 4.1. The considerations on the convergence of the results made in the previous paragraph are here more evident, particularly when considering the relative statistical uncertainties in the shielding regions where fluence can be significantly attenuated.

As it can be deduced from figure 4.2 and table 4.2, the agreement between a standard FLUKA simulation and a FLUKA simulation employing the fluence conversion coefficients method is rather good. As of the present status of the code, these comparisons can never be intended as an exact numerical validation: as stated before, the low energy cross sections included in the fluence conversion coefficients code are indeed derived from JEFF-3.1.1, while those in FLUKA are not. It is very important to stress that, albeit these small differences, the outcome of the code performance testing was quite satisfactory, particularly in regards to radionuclides that dominate the activation in ferrous materials (e.g. ^{54}Mn, ^{60}Co) and concrete (e.g. ^{24}Na, ^{22}Na). Finally, this very simple toy model was meant only to illustrate the overall code operation and give a glimpse at the code capabilities: important applications to the LHC experiments will be exhaustively presented in Chapter 6.

Specific Activity [Bq/g]	Material	Region	FLUKA	Flu. Conv. Coef.	FLUKA/Flu. Conv. Coef.
^{56}Co, 2 d	Copper	T1	1.42×10^{-6} (0.39%)	1.16×10^{-6} (0.01%)	1.22 (0.39%)
		T4	2.47×10^{-9} (9.94%)	1.87×10^{-9} (1.09%)	1.32 (10.00%)
^{60}Co, 2 y	Copper	T1	9.69×10^{-7} (0.39%)	8.00×10^{-7} (0.03%)	1.21 (0.39%)
		T4	2.93×10^{-9} (6.79%)	2.32×10^{-9} (1.00%)	1.26 (6.87%)
	Cast Iron	Sh2	1.44×10^{-10} (0.71%)	1.43×10^{-10} (0.18%)	1.01 (0.73%)
^{59}Fe, 2 d	Cast Iron	Sh2	3.35×10^{-11} (2.01%)	2.00×10^{-11} (0.14%)	1.68 (2.02%)
	Std Concrete	Sh1	1.60×10^{-11} (6.00%)	1.58×10^{-11} (0.07%)	1.01 (6.00%)
		Sh3	4.98×10^{-13} (26.92%)	4.90×10^{-13} (0.33%)	1.02 (26.92%)
^{54}Mn, 2 y	Copper	T1	4.12×10^{-7} (0.34%)	3.48×10^{-7} (0.01%)	1.18 (0.34%)
		T4	7.35×10^{-10} (8.34%)	5.92×10^{-10} (1.12%)	1.24 (8.41%)
	Cast Iron	Sh2	1.36×10^{-10} (0.47%)	1.38×10^{-10} (0.23%)	0.99 (0.53%)
	Std Concrete	Sh1	1.24×10^{-11} (2.99%)	1.26×10^{-11} (0.10%)	0.99 (2.99%)
		Sh3	2.17×10^{-13} (17.31%)	2.29×10^{-13} (0.70%)	0.94 (17.32%)
^{24}Na, 2 d	Std Concrete	Sh1	2.59×10^{-10} (0.46%)	2.53×10^{-10} (0.07%)	1.03 (0.47%)
		Sh3	7.53×10^{-12} (2.19%)	7.62×10^{-12} (0.32%)	0.99 (2.21%)
^{22}Na, 2 y	Cast Iron	Sh2	2.30×10^{-12} (5.48%)	2.45×10^{-12} (0.27%)	0.94 (5.49%)
	Std Concrete	Sh1	1.09×10^{-10} (1.64%)	1.26×10^{-10} (0.12%)	0.87 (1.64%)
		Sh3	2.39×10^{-12} (8.11%)	2.74×10^{-12} (0.67%)	0.87 (8.14%)

LL	Material	Region	FLUKA	Flu. Conv. Coef.	FLUKA/Flu. Conv. Coef.
2 d	Copper	T1	6.32×10^{-5} (0.17%)	5.19×10^{-5} (0.01%)	1.22 (0.17%)
		T4	1.25×10^{-7} (3.88%)	9.87×10^{-8} (1.03%)	1.27 (4.02%)
	Cast Iron	Sh2	9.03×10^{-9} (0.39%)	9.05×10^{-9} (0.20%)	1.00 (0.44%)
	Std Concrete	Sh1	7.83×10^{-9} (0.59%)	8.01×10^{-9} (0.07%)	0.98 (0.59%)
		Sh3	2.17×10^{-10} (2.55%)	2.20×10^{-10} (0.31%)	0.99 (2.57%)
2 y	Copper	T1	1.50×10^{-5} (0.27%)	1.24×10^{-5} (0.02%)	1.21 (0.27%)
		T4	3.84×10^{-8} (5.43%)	3.04×10^{-8} (1.00%)	1.26 (5.53%)
	Cast Iron	Sh2	2.83×10^{-9} (0.43%)	2.83×10^{-9} (0.17%)	1.00 (0.46%)
	Std Concrete	Sh1	5.65×10^{-9} (0.55%)	5.73×10^{-9} (0.07%)	0.99 (0.56%)
		Sh3	1.64×10^{-10} (2.45%)	1.65×10^{-10} (0.30%)	0.99 (2.47%)

Table 4.2: Comparison of radionuclide specific activities and multiples of Swiss clearance limits (LL) for different cooling times estimated with a standard FLUKA event-based method and with fluence conversion coefficients method for the toy model shown in figure 4.1. The relative statistical uncertainty is shown in parentheses.

4.7 Preparation of a database for the fluence conversion coefficients code

The computation of conversion coefficients from fluence to any quantity that is derived from radionuclides' activities relies on the knowledge and availability of energy- and particle-dependent radionuclide production cross sections. Although many evaluated nuclear data libraries are available, these libraries are often not best suited for generic applications at high-energy accelerator facilities like the ones at CERN: in most cases, this is due to the fact that they lack data above a certain energy, typically around hundreds of MeV, or they lack data for a set of particles, typically charged pions. A way to overcome these limitations is to compute radionuclide production cross sections using Monte Carlo codes so that they can be used at a later stage for a large variety of applications involving the assessment of induced radioactivity.

The cross section database initially available with the fluence conversion coefficients code was derived from the database employed by the JEREMY code, in turn initially compiled with calculations from previous versions of the FLUKA code. Due to the evolution of the FLUKA code [63] in recent years, it clearly emerged the necessity to substantially update and extend the cross section database. Therefore, this section presents the general calculation methodology adopted and the large efforts undertaken to prepare an updated version of this database. Despite the fact that a systematic cross-check between different Monte Carlo codes at the single interaction level is beyond the objective of the task, the computations of radionuclide production data were at the same time performed with both FLUKA and PHITS in view of possible cross-comparisons in the near future.

The calculation of the energy-dependent cross sections has been tailored to CERN and LHC applications: for this reason, the particles considered are the ones responsible for almost the entirety of the residual activity production, namely protons, charged pions, and neutrons. Despite the fact that the situations in which photonuclear reactions contribute significantly to activation are limited, photons were also considered in addition to these particle species already included in the initial version of the database.

As far as the energy binning is concerned, it was opted to divide the energy range of interest into sub-intervals as detailed in table 4.3 and to consider a uniform binning in logarithmic scale for each of these sub-intervals. It is indeed reasonable to adopt a more refined energy grid up to fractions of GeV where cross sections typically exhibit

Energy Interval	**Number of bins**	**Bin width factor**	**Particles**
1 MeV-3 MeV	10	1.11612	n, γ
3 MeV-20 MeV	20	1.09950	p, π^+, π^-, n, γ
20 MeV-10 GeV	60	1.10913	p, π^+, π^-, n, γ
10 GeV-10 TeV	10	1.99526	p, π^+, π^-, n, γ

Table 4.3: Overview of the adopted binning structure for the calculation of radionuclide production data.

peaks while implementing a coarser mesh in the high-energy range where no significant changes are expected. In contrast to what originally available, the cross section database for charged hadrons has been extended from 20 MeV down to 3 MeV. Data for low-energy neutrons (below 20 MeV) was still kept as in the JEREMY database, that is cross section extracted from JEFF-3.1.1: calculations for neutrons were nonetheless performed in the range between 1 MeV and 20 MeV only as an additional check for reactions that might haven't been included.

The list of target elements considered for the calculations is also tailored to CERN and LHC applications and covers essentially all the light and medium weight elements from H to Se (this clearly includes important elements such as Al, Si, Mn, Fe, Co, Ni, Cu, and Zn), plus medium weight and heavy elements of radiological importance that can be found either in traces or essentially as pure elements: notable items in this second list are Zr, Nb, Mo, Ag, Cd, Sn, Eu, Ta, W, Hg, Pb, and Bi. All the calculations were performed assuming that the element is in its natural isotopic composition such that the resulting estimated cross sections are to be intended as isotopically averaged as described in the section on the activation formalism.

As far as the FLUKA calculations are concerned, a dedicated executable was employed: this executable is directly interfaced with the interaction models and allows, for a given combination of target element, projectile, and energy grid, to directly obtain an estimation of the radionuclide production cross sections without performing a full transport simulation. A dedicated simulation has to be performed separately for each combination of target, projectile and energy grid: the FLUKA calculations were performed with the code version 4-1.0 as hosted by the FLUKA.CERN Collaboration.

In the case of the PHITS simulations, the simulation geometry used is extremely minimal and optimized for the computation of radionuclide production yields: a pencil and monoenergetic beam of a given particle of species i at energy E_j impacts on a very thin target of thickness l and transverse area S made of element e (with molar mass M_e^{mol}) having density ρ. The production cross section of radionuclide r from element e by particle i at energy E_j can be computed from the estimated yield per unit primary fluence of such radionuclide Y_{r,e,i,E_j}, obtained using the T-Yield tally in PHITS, and using the simple formula

$$\sigma_{r,e,i,E_j} = Y_{r,e,i,E_j} \frac{M_e^{mol}}{N_{AV}\,\rho\,S\,l} \tag{4.4}$$

A separate simulation needs to be performed for each combination of target, projectile and, in this case, for each energy point: with the particle species listed before and the chosen energy binning, this amounts to a total of 520 different simulation inputs, each with a number of primary histories to be simulated kept between 1×10^8 and 1×10^9. The PHITS simulations were performed with the code version 3.20.

In both the FLUKA and PHITS cases, dedicated Python scripts were written to automatically prepare all the needed input files for each selected element starting from a common template. It was also clear since the beginning of the task that the amount of simulations jobs to be managed would have been substantial and for this reason Python

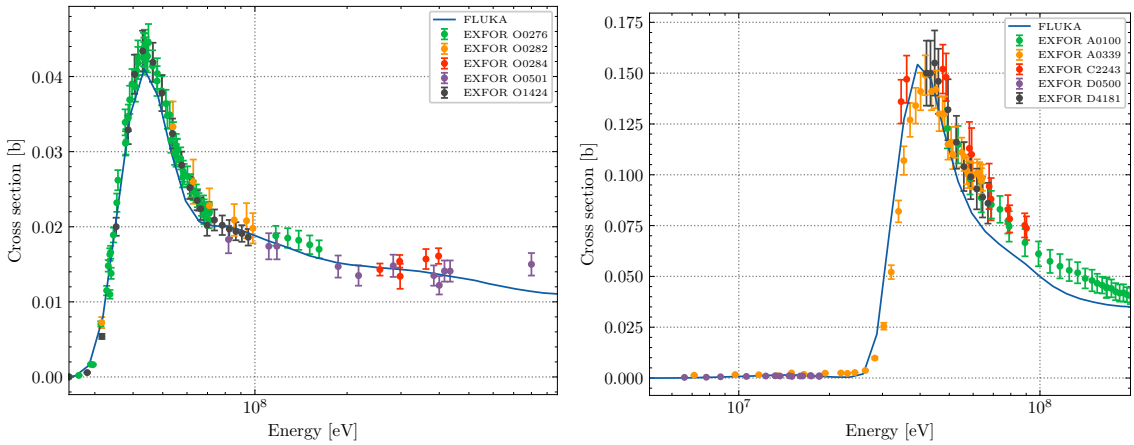

(a) $^{27}\mathrm{Al}(p,x)^{22}\mathrm{Na}$ (b) $^{\mathrm{nat}}\mathrm{Fe}(p,x)^{54}\mathrm{Mn}$

Figure 4.3: Qualitative comparison of the proton-induced production of (a) ^{22}Na from ^{27}Al, and (b) ^{54}Mn from $^{\mathrm{nat}}$Fe computed with FLUKA and with available experimental data. The experimental points are referenced via the corresponding EXFOR [84, 85] entries.

scripts were also implemented to submit the simulation jobs on the CERN Batch Service (LXBATCH) and on the Radiation Protection computing cluster. For the PHITS calculations, a dedicated executable allowing to perform distributed memory parallel computing was also used: depending on the element, the computation time required to complete the full particle and energy sweep varied from few days to approximately a week and a half. To further automatize the process and digest the large amount of data produced, another set of Python scripts was coded to post-process the results for a given target element once all the related simulation jobs were completed: after merging the results, these scripts ultimately converted the computed energy-dependent production cross sections into the data format adopted by the fluence conversion coefficients code.

Albeit not covering the full periodic table, the produced databases are adequate for almost the entirety of the needed radiological assessments at the LHC experiments and can, if necessary, be easily extended with results for the required elements. In its current status, the cross section database contains more than 100 000 entries: a direct and systematic comparison with experimental data on radionuclide production cross sections, which is beyond the scope of this thesis work, would be challenging.

In the vast majority of the situations, experimental data up to very high energies are limited to proton-induced reactions only due to the larger availability of monoenergetic proton beams: at the same time, if data is available for a given reaction, the number of experimental points may be in some cases scarce or limited to a specific energy range. Without claiming to be a rigorous analysis, some qualitative comparisons with experimental data were made for a reduced set of reactions involving relevant target materials (mostly Al, Fe and Cu) and selected radionuclides. Figure 4.3 shows a qualitative comparison of the $^{27}\mathrm{Al}(p,x)^{22}\mathrm{Na}$ and $^{\mathrm{nat}}\mathrm{Fe}(p,x)^{54}\mathrm{Mn}$ reactions as computed with FLUKA with available experimental data extracted from the EXFOR [84,

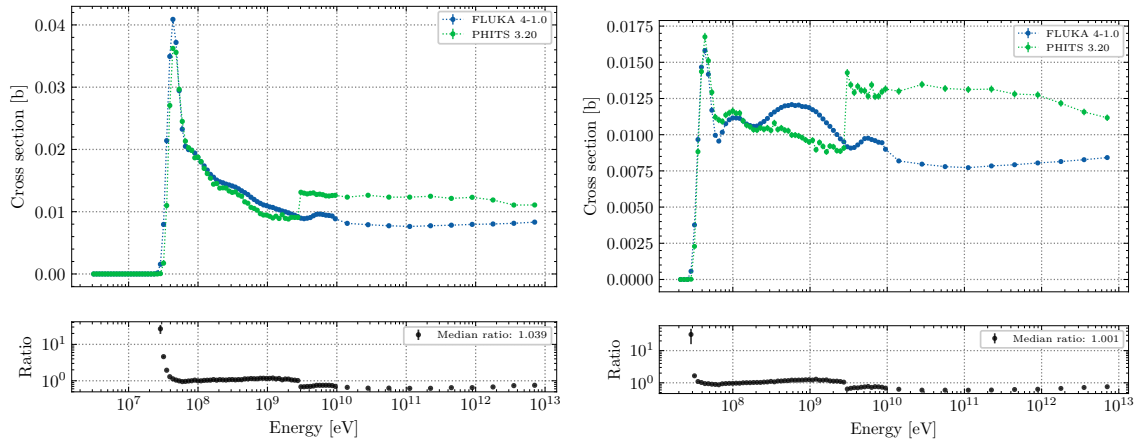

(a) $^{27}\mathrm{Al}(p,x)^{22}\mathrm{Na}$

(b) $^{27}\mathrm{Al}(n,x)^{22}\mathrm{Na}$

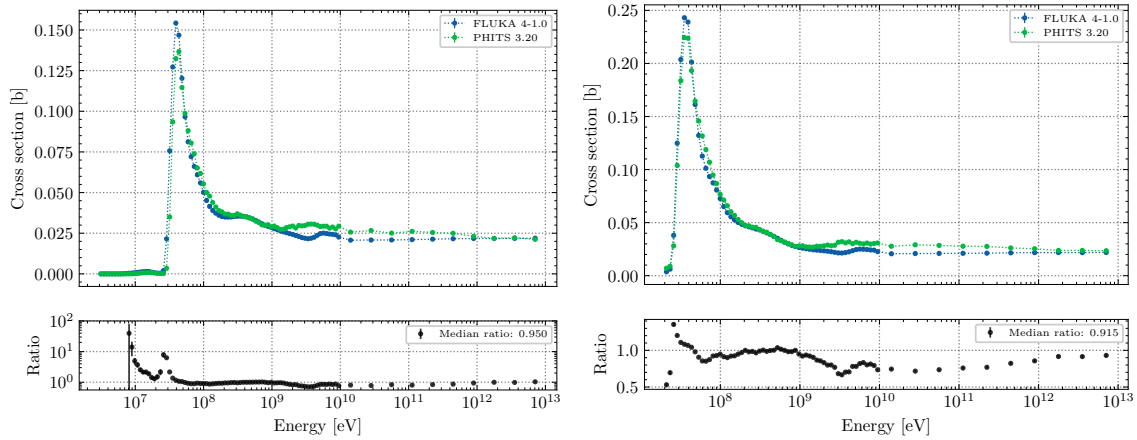

(c) $^{\mathrm{nat}}\mathrm{Fe}(p,x)^{54}\mathrm{Mn}$

(d) $^{\mathrm{nat}}\mathrm{Fe}(n,x)^{54}\mathrm{Mn}$

Figure 4.4: Comparison of the cross sections of proton- and neutron-induced production of ^{22}Na from ^{27}Al and ^{54}Mn from $^{\mathrm{nat}}$Fe as computed with FLUKA and PHITS.

85] database: the comparison is limited only to the data sets with at least five experimental points and each data set is referenced via the corresponding EXFOR entry. Further examples of proton-induced reactions on Al, Si, Mn, Fe and Cu can be found in Appendix A.

For the same very reason on the extent of the database, systematic comparisons between the different codes are also not at all trivial and would require a dedicated work on their own. Figure 4.4 shows a simple comparison of the cross sections for proton- and neutron-induced production of ^{22}Na from ^{27}Al and of ^{54}Mn from $^{\mathrm{nat}}$Fe. Despite the fact that in these cases comparisons with projectiles other than protons are possible and that, thanks to the choice of a common energy grid, ratios can be computed without adding additional systematic uncertainties owing to any attempted fitting procedure, the outcome of these comparisons cannot be definitive. Indeed, the ratios shown in figure 4.4 and all the additional plots in Appendix A are computed giving the same importance to each value of the cross sections. For any final conclusion, for instance on the sensitivity of the computed activity with respect to the variation in the cross sections used, it would be necessary to fully take into account the energy-

dependent spectra of the particles inducing activation in the specific irradiated object to properly weight these ratios.

In conclusion to this section, it is also worth mentioning the effort made in optimizing the database in view of its applications in the fluence conversion coefficients code. As outlined in the previous paragraphs, the raw database contains a large amount of cross section data: a non-negligible fraction of it is for the production of radionuclides whose half-life is much shorter even than that of the shortest cooling times at which accesses and interventions in the radiation areas can occur after the beam is stopped. For radioactive waste characterization studies, one would be typically interested in considering cooling times of several months, years, or even decades.

In specific cases, a reduced cross section database would be more efficient: to effectively reduce the size of the raw database without loss of information, databases with cumulative cross section were also computed with an iterative procedure. By looping over each reaction entry of the database[5], the half-life of the product radionuclide is compared to a pre-defined time cut-off: if the radionuclide half-life is shorter than this threshold and all the daughter radionuclides are in turn unstable, the production cross section for that radionuclide is attributed to the direct production of the daughters based on the decay branching ratios. Since the daughters can be short-lived as well, this procedure is repeated until no further change can be made.

4.8 Strategies for computing irradiation profiles

This short and yet necessary section placed in conclusion to the explanation of the fluence conversion coefficients method aims to present the various strategies with which irradiation profiles can be computed for practical applications. Although the discussion could certainly be more general, it will be tailored to radiological studies for the LHC experiments and the LHC machine: for the latter, the considerations will be valid only in cases in which the main source of radiation is due to the collision debris, such as for the Long Straight Sections (LSS) neighbouring the experiments, and not due to the interaction of beams with residual gas or beam intercepting devices. It is possible to start by stating that the need of computing an irradiation profile may come from either a posteriori assessments or predictive studies.

In situations of the first kind, the real data on the instantaneous luminosity delivered to an experiment is available and can be retrieved from the CERN Accelerator Logging Service profiting from the dedicated web-based interface TIMBER [86]: data can be obtained at fixed timestamps, generally each 1.2 s, or can be averaged over fixed time intervals of one or more minutes or even over the fill duration. The latter possibility is particularly useful if one has to consider an irradiation history that extends over several years and for which a granularity of seconds or minutes would be excessive. Then, for each specific case/assessment, the instantaneous luminosity data can be

[5]To recall, each reaction entry is unequivocally identified by the tuple of the projectile particle, the target element, and the produced nuclide

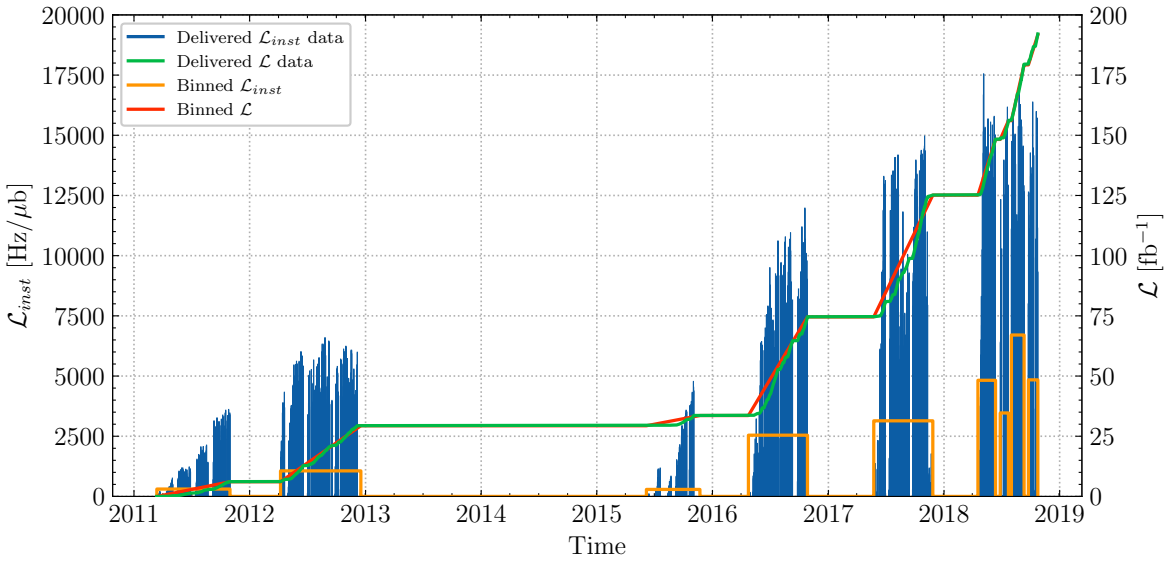

Figure 4.5: Comparison of the instantaneous fill-averaged luminosity delivered to CMS during proton physics in Run 1 and Run 2 as retrieved from the CERN Accelerator Logging Service with respect to the binned data used in standard radiation protection calculations: the corresponding integrated luminosities for the two cases are shown on the second axis. The yearly marks on the abscissa always refer to January 1st.

further averaged over user-defined time intervals: the corresponding average collision rate over the periods of choice will be then obtained by multiplying the computed average instantaneous luminosity by the appropriate cross section.

A typical example is illustrated in figure 4.5 in which the instantaneous fill-averaged luminosity delivered to CMS during proton physics and as retrieved with TIMBER is shown against the corresponding luminosity profile obtained with a coarser binning which is adequate for the vast majority of radiation protection assessments that concern LS 2. This standardly binned profile consists of one irradiation period for each year from 2011 to 2017 and four irradiation periods for 2018 which account for the presence of Technical Stops (TS): this differentiation is in some cases necessary because it is true that the radionuclide activities will be less influenced by the time structure of the irradiation history in the initial years, but they may be more sensitive to the last months or last weeks of irradiation, particularly in the case of short-lived radionuclides and short cooling times.

The corresponding integrated luminosities for the two cases are shown on the second axis of the plot in figure 4.5: irrespective of the choice of the binning, the integrated luminosities at the end of the considered irradiation period must be the same. All the above considerations remain valid also for fixed target experimental facilities in which the quantity to be suitably binned is the intensity of the delivered beam on target: examples from dedicated benchmarks are extensively presented in Chapter 5.

A quite different situation is that of predictive studies, such as those related to the full Run 3 or HL-LHC: the detailed time structure of the delivered instantaneous luminosity is obviously not known a priori and some assumptions have to be made

with the ultimate goal of computing an irradiation profile that leads to conservative and yet somewhat realistic estimates. For radiation protection studies, a dedicated methodology [87] was developed with the aim of introducing standardized approaches here described.

Starting from the foreseen yearly integrated luminosities and considering the presence of (Extended) Year End Technical Stops ((E)YETS) and Long Shutdowns (LS), one possibility is to fix a number of effective operational days, compute with this assumption an average instantaneous luminosity, and finally consider one single irradiation period placed at the end of each year. The number of effective operational days is estimated based on forecasts from the LHC Program Coordination or, in absence of information, from extrapolation of past LHC machine performances: for reference, 160 operational days scheduled for proton physics are usually considered [6, 88, 87].

Another possibility is instead to take into account the expected yearly integrated luminosities and the presence of (E)YETSs and LSs, then fix an average luminosity for each calendar year, and finally compute the duration of the time interval required to reach the targeted integrated luminosity in that year. As in the previous case, one single irradiation period is considered at the end of the operational year. In this case, the average luminosity for each year is computed by multiplying the expected maximum peak luminosity by a global efficiency parameter. The maximum peak luminosity is typically known together with the yearly integrated luminosity from the initial machine performance forecast parameters and the efficiency parameter represents an average measure of the fraction of time spent in physics operation with respect to the total operational time. This parameter depends, among others, on the machine availability and on the number of successful fills and can vary from approximately 20% in the first years of a Run period to approximately 50% towards its end as it was for Run 2 [88]: mostly based on the experience gained during Run 1 and Run 2, the global performance parameter used in computing irradiation profiles with this second method is assumed to be approximately 45% [88, 87] and, for simplicity, it is considered to be the same for every year.

As a pertinent example in view of the simulations presented in Chapter 6, it is useful to consider the irradiation profile for the ATLAS and CMS proton physics operation beyond LS 2 [87]: this irradiation profile is based on the best available estimates of the expected yearly integrated luminosities and peak luminosities at the time of writing as summarized in table 4.4. Figure 4.6 graphically presents the average instantaneous luminosities that result from the application of the two described methodologies using the data of table 4.4. It is possible to notice that the second approach results in generally shorter irradiation periods with higher average luminosities: this is particularly evident in the first years of a Run period in which the global efficiency is expected to be less than the assumed 45%. To quantify the degree of conservativeness of the second approach, the activity of a list of radiologically relevant radionuclides was analytically computed using the two derived irradiation profiles and the results of the comparison are summarised in table 4.5: as expected, the second method is slightly more conservative and the differences between the two remain around few % for short-

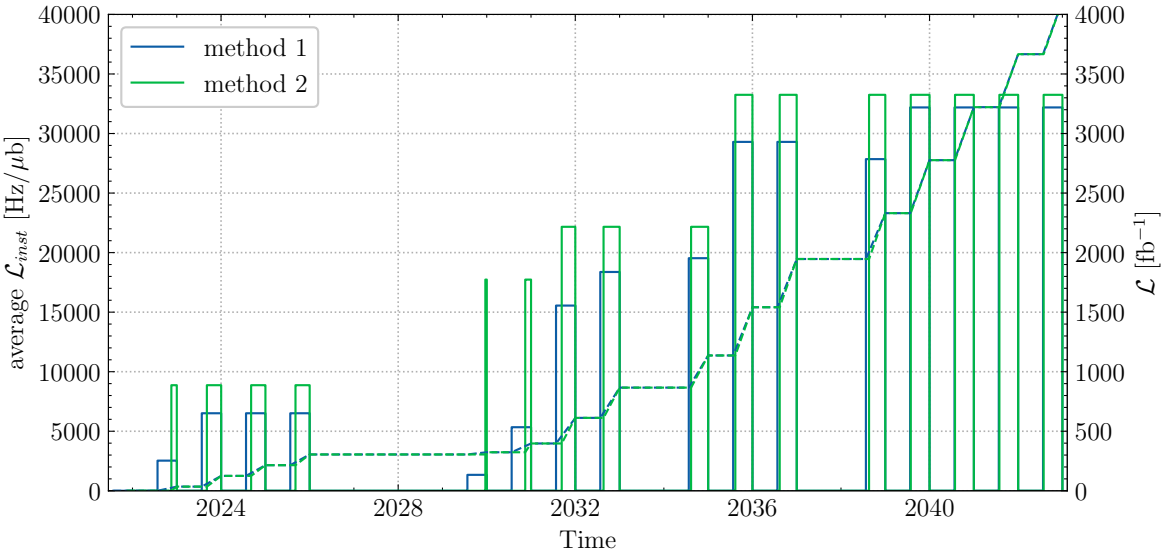

Figure 4.6: Comparison of Run 3 and HL-LHC luminosity profiles for proton physics in ATLAS and CMS obtained by fixing the number of operational days in one case (method 1) and by evaluating an average instantaneous luminosity from a global efficiency parameter in the other case (method 2). The yearly marks on the abscissa refer to January 1st and, for the two cases, the dashed lines indicate the integrated luminosity. The currently foreseen HL-LHC schedule [6] is just shifted to accommodate the changes to Run 3.

Run	**Year**	**Integrated luminosity per year** [fb^{-1}]	**Peak luminosity** [Hz/µb]
Run 3	2022	35	2.0×10^4
	2023	90	2.0×10^4
	2024	90	2.0×10^4
	2025	90	2.0×10^4
Long Shutdown 3			
Run 4	2029	18.5	4.0×10^4
	2030	73.8	4.0×10^4
	2031	215	5.0×10^4
	2032	254	5.0×10^4
Long Shutdown 4			
Run 5	2034	270	5.0×10^4
	2035	405	7.5×10^4
	2036	405	7.5×10^4
Long Shutdown 5			
Run 6	2038	385	7.5×10^4
	2039	445	7.5×10^4
	2040	445	7.5×10^4
	2041	445	7.5×10^4
	2042	445	7.5×10^4

Table 4.4: Expected yearly integrated luminosities and peak luminosities [6] used for the calculation of standard irradiation profiles for ATLAS and CMS proton physics for Run 3 and HL-LHC. The currently foreseen HL-LHC schedule [6] is just shifted to accommodate the recent changes to Run 3.

Nuclide	Half-life	Method 1 / 2
^{11}C	20.37 min	0.9681
^{41}Ar	1.827 h	0.9681
^{61}Cu	3.333 h	0.9681
^{44}Sc	3.97 h	0.9681
^{64}Cu	12.7 h	0.9681
^{24}Na	14.96 h	0.9681
^{55}Co	17.53 h	0.9681
^{57}Ni	1.496 d	0.9681
^{52}Mn	5.595 d	0.9681
^{32}P	14.27 d	0.9682
^{48}V	15.97 d	0.9684
^{51}Cr	27.7 d	0.9706
^{7}Be	53.22 d	0.9777
^{58}Co	70.86 d	0.9814
^{56}Co	77.31 d	0.9825
^{65}Zn	244.2 d	0.9930
^{57}Co	271.8 d	0.9937
^{54}Mn	312.1 d	0.9942
^{22}Na	2.603 y	0.9967
^{55}Fe	2.735 y	0.9968
^{60}Co	5.271 y	0.9977
^{3}H	12.33 y	0.9987
^{63}Ni	100.6 y	0.9998

Table 4.5: Comparison of the activities of radiologically relevant radionuclides computed using the collision profile obtained by fixing the number of operation days in one case (method 1) and by evaluating an average instantaneous luminosity from a global efficiency parameter in the other case (method 2) as shown in figure 4.6.

lived nuclides and below 1% for the long-lived ones. Unless specified otherwise, the second method is the one adopted in applications of the fluence conversion coefficients method in predictive studies discussed in Chapter 6.

The discussion made so far on irradiation profiles for the LHC experiments hasn't explicitly mentioned the heavy-ion physics program. With the only exception of the ALICE experiment, a case that due to its specificities will be treated directly in Section 6.3 while presenting a radiological study for clearance and decommissioning operations, the heavy-ion operation has a negligible impact on the activation of materials and residual dose rates during shutdown periods. The first reason is that the period dedicated to heavy-ion physics is much shorter than the one dedicated to proton physics, typically four weeks with respect to the majority of the operational year. The second reason is that the nominal instantaneous luminosity achievable with the LHC ion scheme design parameters is almost seven orders of magnitude lower than the nominal luminosity achievable with the LHC proton scheme design parameters [1]. In most cases, the heavy-ion run is then neglected and the irradiation period corresponding to the proton operation is placed directly at the end of the year for slightly more conservative final estimates.

Chapter 5

Activation benchmarks for the fluence conversion coefficients method

As it emerged from the discussion in the previous chapters, the calculation of induced radioactivity is a crucial point in all the steps of the life cycle of high-energy accelerators: the calculation of the radionuclide inventory is necessary for the choice of materials during the design phase, it is needed during operational periods and maintenance to estimate residual dose rates for planned exposure situations and to establish suitable protection measures, and is mandatory in the decommissioning phase to determine the appropriate disposal pathways.

The applicability and the numerical consistency of the fluence conversion coefficients method were presented in Chapter 4 with a simplified test case. To fully test the code and ultimately better understand the required safety margins that should be applied in radiation protection assessments, dedicated activation benchmarks have been performed. Since this thesis focuses on the LHC experiments, CMS in particular, the activation benchmarks would have been ideally fully performed with dedicated activation samples directly irradiated in the experiment radiation environment. Owing to the shift in the Run 3 restart due to the Covid-19 pandemic, this possibility soon became non-viable based on rule of thumb estimates for good gamma spectroscopy results: for locations in the LHC experiment that are easily accessible during shutdown periods and where samples can be installed, irradiation times of the order of several months or years are typically required to build-up a sufficient amount of activity for long-lived radionuclides.

However, at least for the studies that will be discussed in Chapter 6 and that represent a significant fraction of typical practical applications, suitable substitutes were found. This chapter will first present benchmarks conducted at CERN experimental facilities which, in virtue of their design, mimic the LHC radiation environment but permit at the same time to reach much higher intensities allowing for shorter irradiation. Finally, a benchmark exploiting activation samples installed in LHCb during Run 1 and Run 2 and that were never systematically analysed before will be discussed. For each case, the most relevant conclusions in relation to the studies of Chapter 6 will be highlighted.

5.1 Activation benchmarks at the CERN High energy AcceleRator Mixed field (CHARM) facility and the CERN Shielding Benchmark Facility (CSBF)

5.1.1 Introduction and overview of the facility

The CHARM (CERN High energy AcceleRator Mixed field) facility [89, 90] was specifically designed and established at CERN with the aim to test the performances of electronic devices and systems in high-energy and mixed radiation fields that are not only representative of particle accelerators, but also ground-level, atmospheric, and space environments. CHARM is located at the CERN East Experimental Area whose aerial view and relative position with respect to the PS complex are shown in figure 5.1. The facility receives a 24 GeV/c proton beam from the PS accelerator via the T08 beamline which also serves the IRRAD facility located upstream: the details of the horizontal layout of IRRAD and CHARM are better shown in the figure 5.2. While IRRAD is used for direct in-beam irradiation of electronics and calorimeter material, in CHARM the beam is directed onto a target to generate a secondary radiation field whose intensity and relative particle composition can be modulated in a variety of ways.

The first way in which the irradiation conditions can be varied is through the choice of the target. Mounted on a remotely controlled revolver, three different targets, all 50 cm long and 8 cm in diameter, are available: one is made out of copper, one out of aluminium, and the last one (the so-called aluminium sieve target) consists of several aluminium disks arranged to achieve an effective density which is about one-third of that of aluminium. There is also a fourth slot in the target revolver which is left empty and in that case the beam is directly sent to the downstream iron dump. For the same primary beam intensity, the secondary field is stronger when the copper target is selected: the secondary particle energy and angular spectra are less affected by the target choice [90]. The target revolver is itself mounted onto a movable table which, during access to the facility, can be retracted into a dedicated alcove that is then closed by a 20 cm marble wall.

Within the CHARM target room, which has a volume of approximately 70 m^3, it is possible to place the equipment to be tested in thirteen different locations for which the irradiation conditions have been extensively characterized. Some of these are in direct view of the beam or at small angles with respect to it, while others are at larger distances and in more shielded locations. Depending on the position, the energy spectrum and relative particle composition of the radiation field will be different [90].

Another degree of flexibility in adapting the irradiation conditions is offered by four shielding blocks of 20 cm thickness that, with a remotely controlled motor, can be moved into the irradiation room: in the standard configuration, the outermost blocks are made out of concrete while the two innermost are in steel. With the insertion of one or more of these shielding walls, one can tune the intensity, energy spectrum and relative particle composition of the radiation field, particularly at the locations that

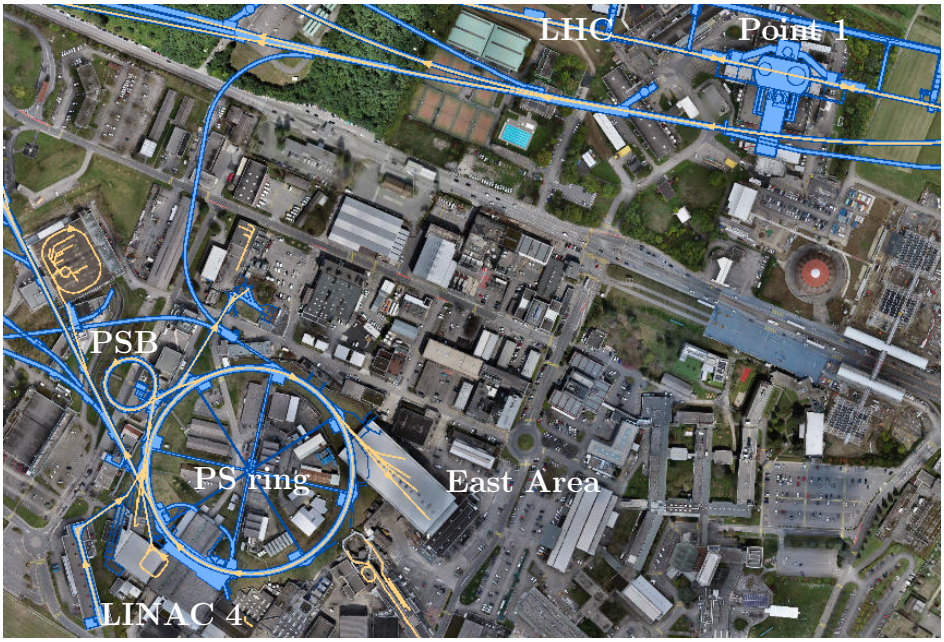

Figure 5.1: Aerial view of the CERN Meyrin site showing the location of the East Experimental Area with respect to the PS complex.

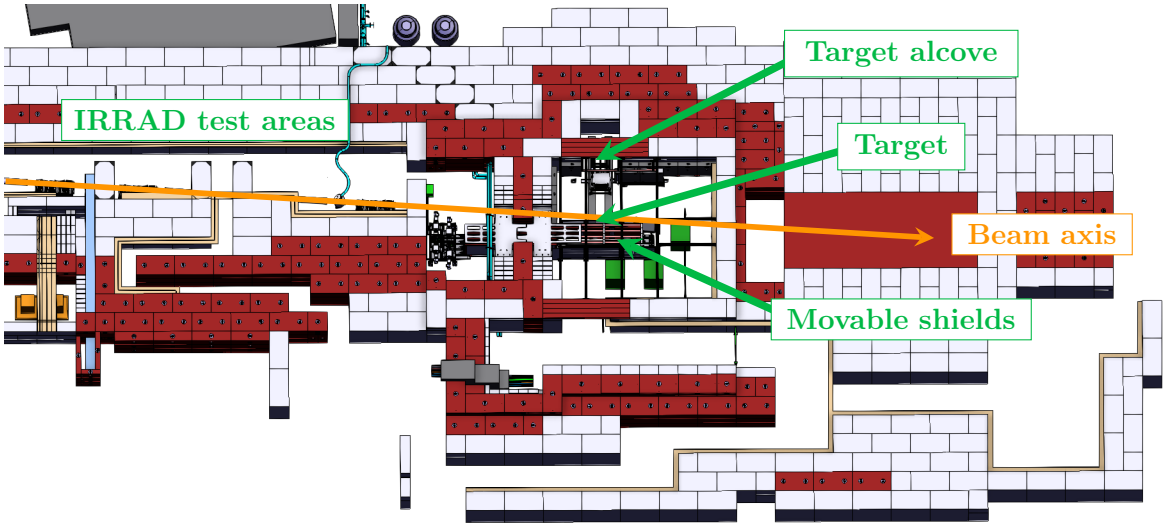

Figure 5.2: Top view of the 3D rendering of the layout of the IRRAD and CHARM facilities at the CERN East Experimental Area: iron and concrete shielding blocks are indicated respectively in red and light grey.

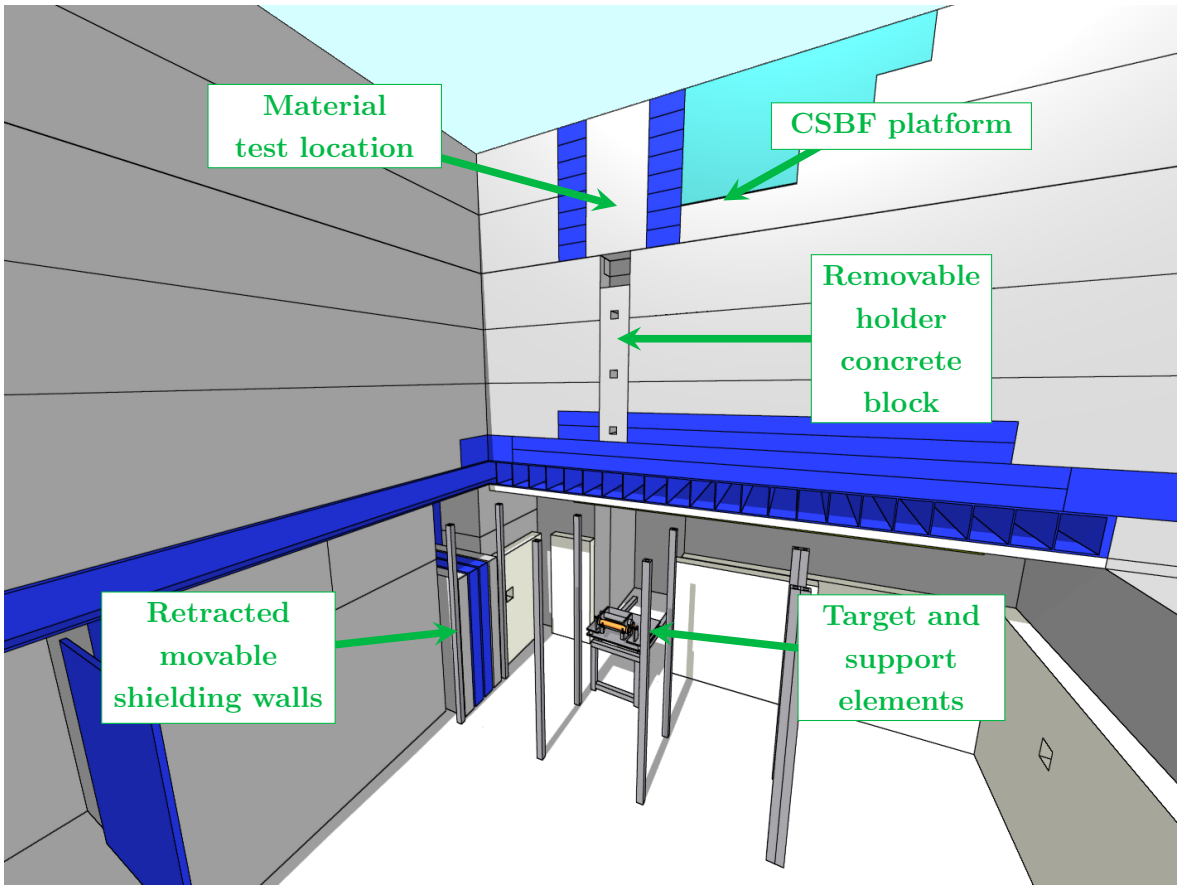

Figure 5.3: Perspective view of the CHARM target area and standard roof shielding configuration as implemented in the FLUKA simulation geometry: some elements have been made transparent to allow a better view of the CERN Shielding Benchmark Facility (CSBF). Standard concrete is in grey, barite concrete in cyan and cast iron in blue.

are lateral to the target.

The proton beam that serves IRRAD and CHARM is structured in spills, or pulses: each spill has a duration of 350 ms and a maximum intensity of 5×10^{11} protons per spill. The spills are separated by at least 1.2 seconds and, in nominal conditions, the T08 beamline can receive two pulses over 45.6 s, a typical length of the PS cycle: if in the East Experimental Area the beam is requested only by the T08 line, up to six spills can be sent to IRRAD and CHARM over the duration of a PS cycle. Therefore, the nominal average beam intensity is 2.2×10^{10} p/s, while the maximum average beam intensity is 6.6×10^{10} p/s [91].

The beam intensity is measured using two Secondary Emission Counters (SEC1 and SEC2) which are placed respectively upstream and downstream of IRRAD: since the signal from SEC2 can be influenced by the presence of material placed in the test stations of IRRAD, SEC1 should be used to determine the number of protons that reach the target [92, 93]. The absolute calibration of these devices is periodically performed using the thin aluminium activation-foils technique and independently with the fast

beam current transformer located after the extraction from the PS: the systematic uncertainty on the beam intensity from the calibration of the two SEC devices is estimated to be 7 % [92]. The beam position with respect to the target and the beam size are measured by Beam Position Monitors (BPMs): the proton beam is Gaussian and typically has a FWHM of 1.2 cm in both directions of the transverse plane. The data from the two SECs, the BPMs and facility configuration (target configuration, target material, movable shield configuration) are all logged to the CERN Accelerators Logging Service and can be retrieved with the online interface TIMBER [86].

Part of the experimental campaign that will be here described was conducted at a dedicated installation within CHARM. Laterally above the target and incorporated within the roof shielding of the facility, lies the CERN Shielding Benchmark Facility (CSBF) [90]: it makes parasitic use of the beam conditions at CHARM and its main purpose is to allow for activation measurements in high-energy neutron fields, deep shielding penetration studies, and more generally characterization of shielding materials [94, 95, 96]. An overview of the CHARM irradiation room and the CSBF in its nominal configuration is shown in figure 5.3.

The present configuration of the CSBF consists of a 10 cm thick marble board[1] and a 40 cm thick layer of cast iron shielding that are followed by a 400 cm thick shielding which employs blocks of standard concrete (in grey in figure 5.3), barite concrete (in cyan in figure 5.3), and again cast iron (in blue in figure 5.3).

Exactly above the target and in a 40 cm×40 cm×240 cm shaft within the shielding structure, it is possible to place a removable sample-holder concrete block (hereafter removable holder concrete block, RHCB) which allows the insertion of activation samples and passive detectors at various depths within the shielding. This block is 200 cm long, 37 cm×37 cm wide, and is equipped with three slots each having a 10 cm×10 cm cross section area: conventionally, the first position is the one closest to the target, while the fourth additional position is on top of the block. Thanks to a remotely controlled hook, the installation and retrieval of samples can be performed within less than half an hour. A photo of the block is shown in figure 5.8.

If the removable holder concrete block is not inserted, the shaft allows to obtain a collimated high-energy neutron field which is directed towards the so-called material test location. Shielding material can be located in a 80 cm×80 cm×160 cm shaft with the primary aims of measuring the spectrum-averaged neutron attenuation length or performing activation measurements. Finally, by removing a custom-shaped barite concrete block, the CSBF platform becomes accessible: this zone can be used in parallel with any other measurement and can be exploited for shielding studies, testing of radiation detectors and measurements of neutron spectra.

[1] Marble poses fewer constraints related to residual activation with respect to concrete and is used not only to reduce the induced activation in the concrete and steel blocks surrounding the target, but also to effectively reduce the residual radiation levels in the target room owing to the activation of the shielding structures [94].

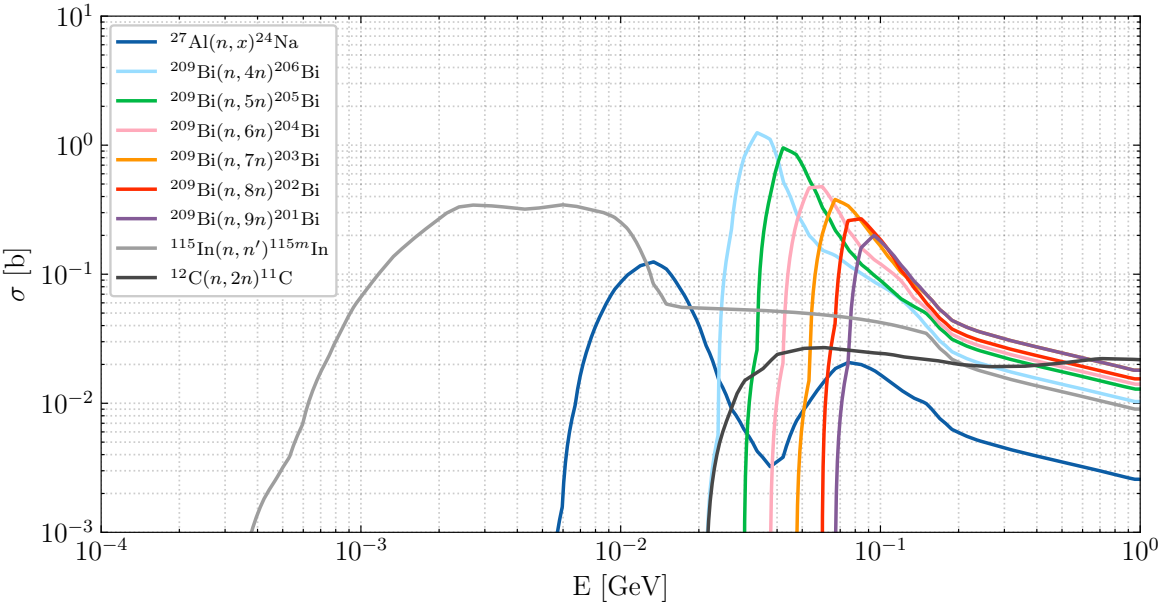

Figure 5.4: Radionuclide production cross sections for high-energy neutron reactions in C, Al, In, and Bi as evaluated by Meakawa et al. [102].

5.1.2 Activation benchmark with C, Al, In, and Bi samples at the CERN Shielding Benchmark Facility (CSBF)

Motivations

The first comparison presented involves the use of activation samples of C, Al, In and Bi which are effective at monitoring the fluence of medium to high energy neutrons [95, 97]. The experimental results for various shielding configurations were obtained during dedicated measurement campaigns in 2022, 2018, 2017, and 2016: here are presented the recently performed FLUKA Monte Carlo simulations for the activation benchmarks which are part of a wider experimental and code inter-comparison campaign [98, 99] with the PHITS and Geant4 [100, 101] Monte Carlo codes.

As illustrated in figure 5.4, the energy-dependent reaction cross sections for the ^{27}Al$(n, 2n2p)^{24}$Na, the ^{209}Bi$(n, xn)^{210-x}$Bi (with $x = 4 - 9$), the ^{115}In$(n, n')^{115m}$In, and the ^{12}C$(n, 2n)^{11}$C reactions all exhibit a threshold energy which is of the order of few to several tens of MeV. The main purpose of this benchmark is to test the overall code infrastructure of the fluence conversion coefficient method using a set of established reactions and in a well characterized facility.

Experimental setup

Shielding experiments were conducted with mainly two different kinds of setups. In the first case, samples were installed on top and in the three available slots of the removable holder concrete block: after the sample holder was inserted into its shaft, the shaft of the material test location was sealed with concrete blocks for a total thickness of 160 cm. In the second case, the shaft of the sample holder remained empty

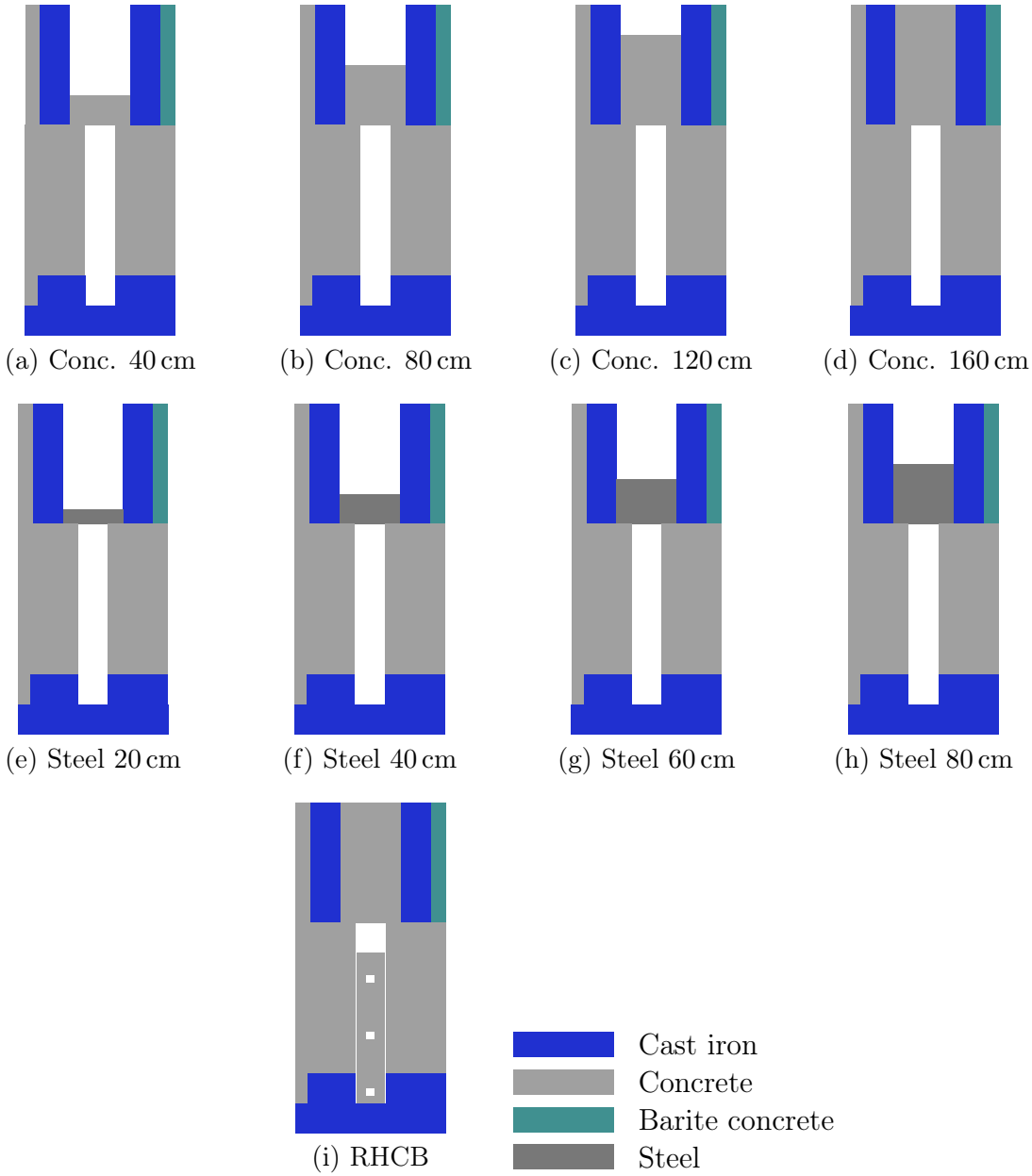

Figure 5.5: Summary of the various CSBF shielding configurations for the activation experiments with C, Al, In, and Bi samples: for the configurations (a) to (h) the samples are installed at the bottom and on top of the shielding block in the material test location; for the configuration (i) the samples are installed in the holes of the concrete bar and on top of it.

Concrete	Density: 2.23 g/cm^3 (0.93 %)				
Element	**Mass fraction [%]**	**Element**	**Mass fraction [%]**	**Element**	**Mass fraction [%]**
O	48.204	Al	2.113	H	0.561
Ca	23.929	Mg	1.512	Na	0.446
Si	16.175	Fe	1.263	S	0.414
C	4.377	K	0.833	Ti	0.173

Steel	Density: 7.77 g/cm^3 (0.15 %)				
Element	**Mass fraction [%]**	**Element**	**Mass fraction [%]**	**Element**	**Mass fraction [%]**
Fe	97.793	C	0.170	N	0.012
Mn	1.400	P	0.035	Co	0.005
Cu	0.550	S	0.035		

Table 5.1: Measured density (and relative uncertainty) and material composition of the shielding blocks used in the CSBF experiments.

and samples were installed at the bottom and top surfaces of concrete and steel blocks of various thicknesses which were then inserted in the material test location shaft. A schematic overview of the various CERN Shielding Benchmark Facility (CSBF) shielding configurations for the measurements over the various experimental campaigns is presented in figure 5.5. During all the experiments, the beam was sent to the copper target and the movable shielding walls were retracted.

Depending on the expected intensity of the radiation field at a given location, the activation samples were prepared in two sizes: 8 cm in diameter and 1 cm thick disks were used for less intense irradiation conditions, while 4 cm in diameter and 0.4 cm thick disks for more intense conditions [98]. Owing to the specific application, the purity of the samples materials was very high (greater than 99.99 % [103]): additionally, there are no competing reactions for the production of the selected radionuclides listed in figure 5.4.

With the aim of reducing the systematic uncertainty on the final result associated with the density of the blocks, the mass and dimensions of the shielding blocks were measured during summer 2022: the crane scale that was used had a $\pm$ 2 kg systematic uncertainty up to 6000 kg (the heaviest block is approximately 1000 kg), while the accuracy achieved in the size measurement with a laser meter was $\pm$ 1 mm. Table 5.1 summarizes the measured densities (and the resulting uncertainty) and the chemical composition (from the manufacturer) of the shielding block materials used for the experiments here discussed: these pieces of information were all taken into account in the implementation of the simulation geometry.

Production yield measurement

The beam intensity and profile were monitored by the T08 beamline instrumentation and are discussed in more detail by Nakao et al. [98]. Once the irradiation ended and the samples were removed, they were analyzed by gamma spectroscopy with a High-Purity Germanium (HPGe) detector: Bi and Al samples were measured from

3 to 24 hours depending on the peak count rates, while the In and C samples were measured for 4 hours and 30 minutes respectively. The production rate of the selected radionuclides in the activation samples was computed from the measured net peak count rate for the selected photon lines, the energy-dependent efficiency of the HPGe detector, and the beam irradiation history with a procedure that is described in detail by Nakao et al. [98].

FLUKA Monte Carlo calculations

Monte Carlo calculations were performed with the FLUKA code[2]. The simulation geometry reproduces the full experimental setup with a high level of detail: the primary source consists of a 24 GeV/c proton beam with a FHMW of 1.2 cm in both directions of the transverse plane and that starts upstream IRRAD to account for the presence of electronic samples located in the IRRAD test locations and the beam passage in air inside the IRRAD facility.

To optimize the simulation, importance biasing was used in order to compensate for the attenuation of particle fluences in the shielding: the geometry of the bulk shielding was further segmented in slabs of 20 cm and the importances were set based on the expected attenuation in concrete and steel. For each configuration, approximately 50 million primary histories were simulated.

Particles were transported down to 1 MeV with the exception of electrons, positrons, and photons which were not transported, and of neutrons which were followed down to 0.01 meV. For each activation sample location, neutron energy spectra were estimated from thermal energies up to 10 GeV. With the fluence conversion coefficients method, the estimated particle spectra were folded online with the radionuclide production cross sections illustrated in figure 5.4 to obtain the desired production yields.

Discussion of the results

The estimated neutron fluence energy spectra at the various sample locations are shown in figure 5.6 for energies greater than the lowest threshold energy of the considered production cross sections. For the samples installed in the removable holder concrete block (RHCB) and at the material test location, figure 5.7 shows the production yields of ^{24}Na, $^{206-201}$Bi, ^{115m}In, and ^{11}C as measured and as simulated with FLUKA using the fluence conversion coefficients code. For visual clarity, the results have been multiplied by a multiplicative factor and, when possible, a fit for the attenuation trend has been added: for the purposes of the present benchmark, the fit serves only to guide the eye. The numerical values are summarized in tables 5.2, 5.3, and 5.4.

The uncertainties that are reported in the first columns of the tables only correspond to the statistical uncertainty of the Monte Carlo calculation (between 0.2 % and 1.6 %) and to the counting statistics of the gamma spectroscopy (between 1.2 % and 47.3 %). The ratio between the computed quantities and the experimental results (C/E ratio) includes, instead, additional contributions to the systematic uncertainties. As far as the

[2]The calculations employed the code version 4-3.0 as hosted by the FLUKA.CERN Collaboration

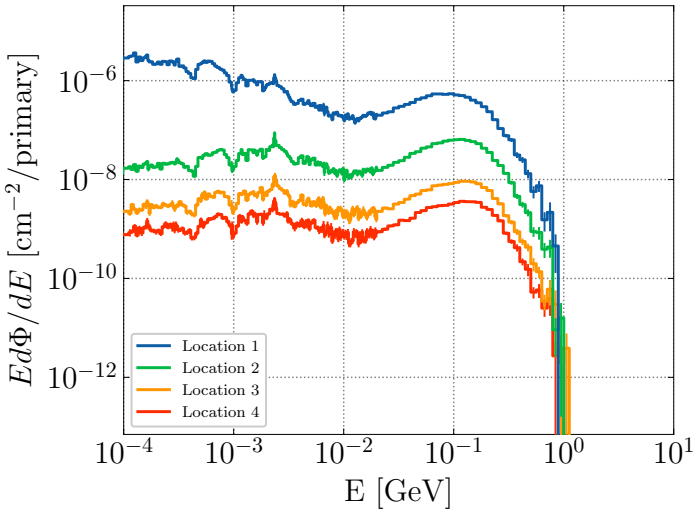

(a) Removable holder concrete block.

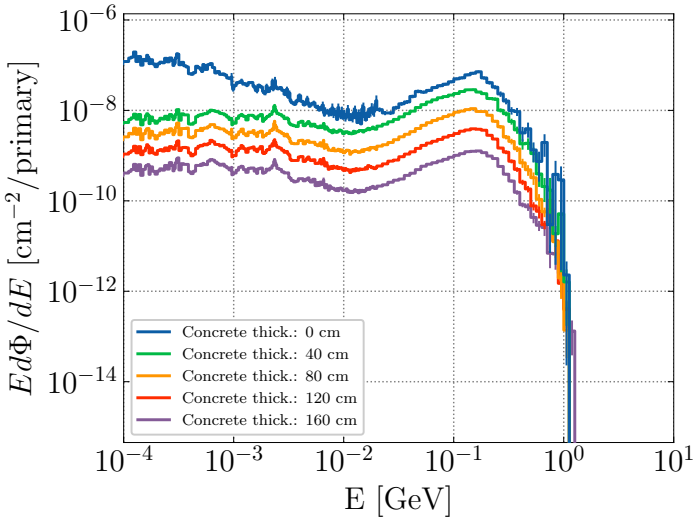

(b) Material test location (concrete).

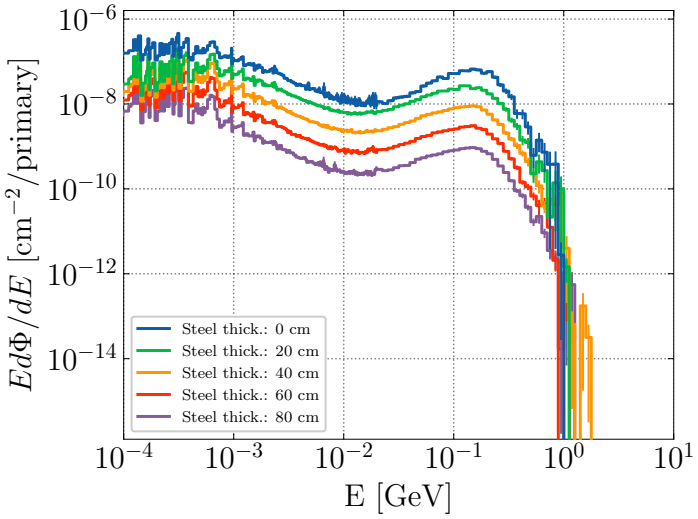

(c) Material test location (steel).

Figure 5.6: High-energy neutron fluence energy spectra for the various CSBF shielding configuration as estimated with FLUKA.

Monte Carlo calculations are concerned, the largest source of systematic uncertainty is linked to the uncertainty in the density of shielding material. A change in the shielding density implies a variation of the slope of the attenuation profile: for small variations (at least less than 1 % as in this case), the variation in the production yield is directly proportional to the density variation and this effect would increase with increasing shielding thickness [95]. Owing to the first 40 cm of cast iron shielding, there is then a systematic contribution of 4 % from the uncertainty on the cast iron density [95]. The uncertainties on the concrete and steel densities then add a systematic contribution that can be respectively up to 1 % and 4 %. As verified in dedicated calculations, the systematic contribution owing to the sample positions, the beam size, and the exact positioning of the materials in IRRAD have instead a negligible impact on the simulated results. As far as the experimental data is concerned, one should account for a systematic uncertainty contribution of 7 % owing to the calibration of the SEC1 that has to be used to monitor the beam intensity: the uncertainty on the sample mass and dimension is instead negligible.

As it is evident from tables 5.2, 5.3, and 5.4, the differences with the experimental data are within 20 % with a very limited number of exceptions. In many cases the C/E ratios are very close to 1.0, making the comparison with FLUKA satisfactory as far as high-energy neutrons are concerned. Since the evaluated cross section data used are well established and the simulation geometry is also well characterized and relatively simple, these results can be an indication of the overall goodness of the simulation setup. Additionally, as presented by Nakao et al. [98], for the same simulation geometry and analysis procedure, the calculation results from PHITS and Geant4 show the same trends albeit being on average 1.5 to 2 times larger than those obtained with FLUKA.

In conclusion, these results constitute a valuable set of benchmark data for activation and deep-shielding penetration studies at accelerators. They also provide further proof that the C, Al, In, and Bi activation samples are an efficient solution in monitoring the neutron component of a radiation field above few MeV. Due to their simplicity and relatively low cost, they could be even employed in the future for dedicated benchmarks and/or neutron radiation monitoring at the LHC experiments.

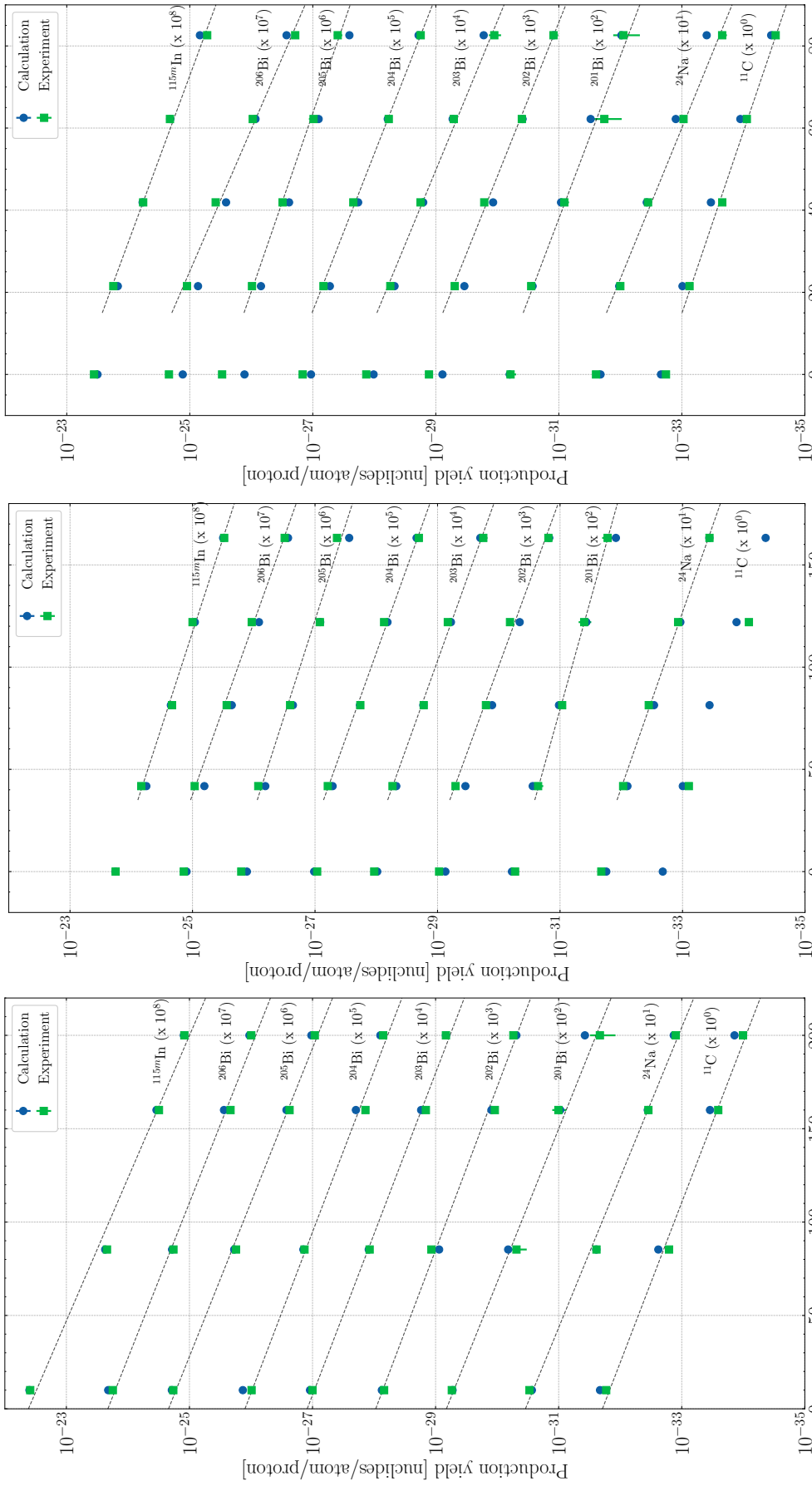

(a) Removable holder concrete block. (b) Material test location (concrete). (c) Material test location (steel).

Figure 5.7: Production yield of ^{24}Na, $^{206-201}$Bi, ^{115m}In, and ^{11}C as a function of various shielding thicknesses as calculated with FLUKA using the fluence conversion coefficients method and as experimentally measured.

Radionuclide	Location	FLUKA [nucl./atom/p] (Rel. unc. %)*		Experiment [nucl./atom/p] (Rel. unc. %)†		C/E Ratio (Rel. unc. %)‡	
^{115m}In	1	3.98e-31	(0.31%)	3.87e-31	(7.20%)	1.03	(10.82%)
	2	2.34e-32	(0.44%)	2.19e-32	(1.30%)	1.07	(8.41%)
	3	3.43e-33	(0.62%)	3.13e-33	(7.00%)	1.10	(11.32%)
	4	1.23e-33	(0.77%)	1.21e-33	(4.50%)	1.02	(10.36%)
^{206}Bi	1	2.09e-31	(0.70%)	1.76e-31	(1.40%)	1.19	(8.22%)
	2	1.91e-32	(0.68%)	1.82e-32	(1.90%)	1.05	(8.54%)
	3	2.75e-33	(0.97%)	2.15e-33	(2.70%)	1.28	(9.32%)
	4	1.06e-33	(1.10%)	9.91e-34	(1.90%)	1.07	(9.55%)
^{205}Bi	1	1.93e-31	(0.66%)	1.83e-31	(2.90%)	1.06	(8.60%)
	2	1.87e-32	(0.59%)	1.75e-32	(3.70%)	1.07	(9.11%)
	3	2.65e-33	(0.90%)	2.36e-33	(5.20%)	1.12	(10.32%)
	4	1.04e-33	(0.97%)	9.20e-34	(3.80%)	1.13	(10.09%)
^{204}Bi	1	1.36e-31	(0.61%)	9.78e-32	(1.90%)	1.39	(8.31%)
	2	1.41e-32	(0.52%)	1.35e-32	(1.70%)	1.04	(8.49%)
	3	1.97e-33	(0.74%)	1.38e-33	(2.70%)	1.43	(9.30%)
	4	7.90e-34	(0.86%)	7.11e-34	(1.70%)	1.11	(9.49%)
^{203}Bi	1	1.10e-31	(0.62%)	1.00e-31	(5.30%)	1.10	(9.67%)
	2	1.22e-32	(0.51%)	1.18e-32	(4.90%)	1.03	(9.65%)
	3	1.72e-33	(0.70%)	1.44e-33	(6.80%)	1.19	(11.20%)
	4	6.79e-34	(0.81%)	6.79e-34	(4.60%)	1.00	(10.40%)
^{202}Bi	1	7.47e-32	(0.68%)	6.87e-32	(3.90%)	1.09	(8.98%)
	2	8.77e-33	(0.53%)	1.17e-32	(5.80%)	0.75	(10.14%)
	3	1.24e-33	(0.74%)	1.09e-33	(8.90%)	1.14	(12.59%)
	4	4.87e-34	(0.84%)	5.45e-34	(7.70%)	0.89	(12.10%)
^{201}Bi	1	5.30e-32	(0.71%)	5.45e-32	(11.80%)	0.97	(14.31%)
	2	6.62e-33	(0.54%)	4.85e-33	(31.10%)	1.36	(32.19%)
	3	9.44e-34	(0.73%)	1.01e-33	(24.80%)	0.93	(26.35%)
	4	3.75e-34	(0.82%)	2.14e-34	(43.60%)	1.75	(44.59%)
^{24}Na	1	2.73e-32	(0.58%)	2.98e-32	(1.50%)	0.91	(8.22%)
	2	2.45e-33	(0.59%)	2.43e-33	(2.30%)	1.01	(8.63%)
	3	3.57e-34	(0.88%)	3.48e-34	(3.40%)	1.02	(9.54%)
	4	1.35e-34	(0.97%)	1.25e-34	(4.30%)	1.08	(10.29%)
^{11}C	1	2.13e-32	(0.46%)	1.69e-32	(0.90%)	1.26	(8.13%)
	2	2.40e-33	(0.41%)	1.61e-33	(3.20%)	1.49	(8.91%)
	3	3.47e-34	(0.54%)	2.55e-34	(4.90%)	1.36	(10.15%)
	4	1.39e-34	(0.60%)	1.01e-34	(12.80%)	1.37	(15.83%)

* Only statistical uncertainty is reported.
† Only gamma spectroscopy uncertainty is reported.
‡ Systematic uncertainty sources included as discussed in Section 5.1.2.

Table 5.2: Production yield of ^{24}Na, $^{206-201}$Bi, ^{115m}In, and ^{11}C as calculated with FLUKA using the fluence conversion coefficients method and experimentally measured for the samples in the removable holder concrete block.

Radionuclide	Shield thickness [cm]	FLUKA [nucl./atom/p] (Rel. unc. %)*		Experiment [nucl./atom/p] (Rel. unc. %)†		C/E Ratio (Rel. unc. %)‡	
^{115m}In	0	1.81e-32	(0.63%)	1.80e-32	(6.70%)	1.00	(10.50%)
	40	5.67e-33	(0.33%)	6.87e-33	(4.10%)	0.83	(9.10%)
	80	2.26e-33	(0.30%)	2.16e-33	(2.80%)	1.05	(8.74%)
	120	9.17e-34	(0.32%)	1.00e-33	(5.40%)	0.92	(10.10%)
	160	3.16e-34	(0.36%)	3.04e-34	(8.20%)	1.04	(12.10%)
^{206}Bi	0	1.25e-32	(1.58%)	1.39e-32	(2.10%)	0.90	(8.48%)
	40	6.41e-33	(0.52%)	9.21e-33	(4.00%)	0.70	(9.06%)
	80	2.29e-33	(0.42%)	2.77e-33	(1.70%)	0.83	(8.46%)
	120	8.22e-34	(0.48%)	1.08e-33	(6.10%)	0.76	(10.50%)
	160	2.76e-34	(0.50%)	3.13e-34	(5.40%)	0.88	(10.42%)
^{205}Bi	0	1.30e-32	(1.61%)	1.60e-32	(3.10%)	0.81	(8.79%)
	40	6.48e-33	(0.58%)	8.45e-33	(9.40%)	0.77	(12.43%)
	80	2.30e-33	(0.40%)	2.55e-33	(4.00%)	0.90	(9.20%)
	120	8.23e-34	(0.42%)	8.33e-34	(12.20%)	0.99	(14.89%)
	160	2.77e-34	(0.49%)	4.38e-34	(9.20%)	0.63	(12.80%)
^{204}Bi	0	1.03e-32	(1.36%)	9.23e-33	(1.20%)	1.12	(8.26%)
	40	5.16e-33	(0.72%)	6.19e-33	(2.00%)	0.83	(8.39%)
	80	1.85e-33	(0.44%)	1.82e-33	(1.20%)	1.01	(8.37%)
	120	6.56e-34	(0.39%)	7.45e-34	(3.60%)	0.88	(9.27%)
	160	2.20e-34	(0.48%)	2.02e-34	(4.00%)	1.09	(9.76%)
^{203}Bi	0	9.64e-33	(1.34%)	1.08e-32	(2.80%)	0.89	(8.64%)
	40	4.71e-33	(0.91%)	5.43e-33	(5.90%)	0.87	(10.08%)
	80	1.71e-33	(0.53%)	1.68e-33	(3.50%)	1.02	(9.00%)
	120	6.04e-34	(0.43%)	6.79e-34	(10.70%)	0.89	(13.69%)
	160	2.00e-34	(0.45%)	1.79e-34	(12.80%)	1.12	(15.59%)
^{202}Bi	0	7.43e-33	(1.42%)	9.42e-33	(3.40%)	0.79	(8.86%)
	40	3.51e-33	(1.08%)	5.08e-33	(3.50%)	0.69	(8.91%)
	80	1.29e-33	(0.63%)	1.62e-33	(3.00%)	0.79	(8.82%)
	120	4.56e-34	(0.48%)	6.56e-34	(6.20%)	0.69	(10.56%)
	160	1.50e-34	(0.47%)	1.55e-34	(10.50%)	0.97	(13.77%)
^{201}Bi	0	6.10e-33	(1.42%)	5.42e-33	(12.60%)	1.13	(15.03%)
	40	2.79e-33	(1.27%)	2.28e-33	(16.10%)	1.23	(18.08%)
	80	1.04e-33	(0.78%)	9.23e-34	(10.40%)	1.13	(13.31%)
	120	3.72e-34	(0.58%)	4.03e-34	(22.20%)	0.92	(23.79%)
	160	1.22e-34	(0.52%)	1.67e-34	(21.70%)	0.73	(23.46%)
^{24}Na	0	1.76e-33	(1.09%)	2.12e-33	(1.90%)	0.83	(8.35%)
	40	7.94e-34	(0.60%)	9.33e-34	(4.20%)	0.85	(9.16%)
	80	2.92e-34	(0.45%)	3.56e-34	(1.00%)	0.82	(8.35%)
	120	1.09e-34	(0.42%)	1.18e-34	(3.90%)	0.92	(9.39%)
	160	3.65e-35	(0.47%)	3.63e-35	(9.30%)	1.00	(12.88%)
^{11}C	0	2.10e-33	(1.07%)				
	40	9.90e-34	(1.07%)	7.89e-34	(3.90%)	1.26	(9.07%)
	80	3.62e-34	(0.78%)				
	120	1.31e-34	(0.62%)	8.25e-35	(9.00%)	1.59	(12.42%)
	160	4.40e-35	(0.55%)				

* Only statistical uncertainty is reported.
† Only gamma spectroscopy uncertainty is reported.
‡ Systematic uncertainty sources included as discussed in Section 5.1.2.

Table 5.3: Production yield of ^{24}Na, $^{206-201}$Bi, ^{115m}In, and ^{11}C as calculated with FLUKA using the fluence conversion coefficients method and experimentally measured for the samples in the material test location with concrete slabs of various thicknesses.

Radionuclide	Shield thickness [cm]	FLUKA [nucl./atom/p] (Rel. unc. %)*		Experiment [nucl./atom/p] (Rel. unc. %)†		C/E Ratio (Rel. unc. %)‡	
^{115m}In	0	3.16e-32	(0.35%)	3.60e-32	(3.10%)	0.88	(8.64%)
	20	1.48e-32	(0.20%)	1.75e-32	(0.80%)	0.85	(8.11%)
	40	5.84e-33	(0.23%)	5.72e-33	(1.30%)	1.02	(8.18%)
	60	2.08e-33	(0.32%)	2.10e-33	(4.00%)	0.99	(9.02%)
	80	6.84e-34	(0.45%)	5.21e-34	(7.70%)	1.31	(11.17%)
^{206}Bi	0	1.30e-32	(1.47%)	2.18e-32	(5.10%)	0.60	(9.65%)
	20	7.34e-33	(0.59%)	1.11e-32	(1.70%)	0.66	(8.26%)
	40	2.57e-33	(0.56%)	3.79e-33	(2.90%)	0.68	(8.59%)
	60	8.54e-34	(0.72%)	9.46e-34	(7.70%)	0.90	(11.18%)
	80	2.67e-34	(1.06%)	1.93e-34	(9.80%)	1.38	(12.75%)
^{205}Bi	0	1.29e-32	(1.45%)	2.98e-32	(10.60%)	0.43	(13.40%)
	20	6.96e-33	(0.65%)	9.73e-33	(3.60%)	0.72	(8.85%)
	40	2.43e-33	(0.52%)	3.10e-33	(7.40%)	0.78	(10.96%)
	60	8.04e-34	(0.69%)	9.71e-34	(17.70%)	0.83	(19.47%)
	80	2.54e-34	(1.09%)	3.93e-34	(13.90%)	0.65	(16.12%)
^{204}Bi	0	1.07e-32	(1.36%)	1.46e-32	(2.50%)	0.73	(8.55%)
	20	5.28e-33	(0.75%)	6.70e-33	(0.90%)	0.79	(8.15%)
	40	1.83e-33	(0.49%)	2.19e-33	(1.60%)	0.84	(8.24%)
	60	6.03e-34	(0.57%)	5.82e-34	(4.10%)	1.04	(9.07%)
	80	1.90e-34	(0.89%)	1.76e-34	(5.80%)	1.08	(9.99%)
^{203}Bi	0	1.03e-32	(1.36%)	1.35e-32	(7.30%)	0.76	(10.96%)
	20	4.69e-33	(0.92%)	5.49e-33	(2.70%)	0.85	(8.55%)
	40	1.60e-33	(0.54%)	1.77e-33	(4.80%)	0.91	(9.40%)
	60	5.32e-34	(0.58%)	5.10e-34	(12.40%)	1.04	(14.81%)
	80	1.66e-34	(0.85%)	1.12e-34	(21.30%)	1.49	(22.80%)
^{202}Bi	0	7.79e-33	(1.44%)	1.29e-32	(4.80%)	0.60	(9.49%)
	20	3.43e-33	(1.08%)	4.92e-33	(2.10%)	0.70	(8.40%)
	40	1.17e-33	(0.61%)	1.63e-33	(3.90%)	0.72	(8.98%)
	60	3.88e-34	(0.60%)	3.99e-34	(9.60%)	0.97	(12.56%)
	80	1.22e-34	(0.94%)	1.22e-34	(14.50%)	1.00	(16.63%)
^{201}Bi	0	6.28e-33	(1.41%)	6.09e-33	(17.70%)	1.03	(19.50%)
	20	2.67e-33	(1.25%)	2.81e-33	(7.10%)	0.95	(10.82%)
	40	9.19e-34	(0.71%)	8.14e-34	(14.60%)	1.13	(16.70%)
	60	3.04e-34	(0.62%)	1.82e-34	(47.30%)	1.67	(47.99%)
	80	9.59e-35	(0.87%)	8.92e-35	(45.60%)	1.08	(46.32%)
^{24}Na	0	2.10e-33	(0.89%)	2.48e-33	(4.00%)	0.85	(9.04%)
	20	1.04e-33	(0.49%)	1.00e-33	(1.40%)	1.04	(8.20%)
	40	3.72e-34	(0.47%)	3.54e-34	(3.60%)	1.05	(8.85%)
	60	1.25e-34	(0.63%)	9.38e-35	(5.00%)	1.34	(9.52%)
	80	3.94e-35	(0.93%)	2.21e-35	(14.70%)	1.78	(16.80%)
^{11}C	0	2.18e-33	(1.06%)	1.81e-33	(3.00%)	1.21	(8.67%)
	20	9.75e-34	(0.95%)	7.49e-34	(1.90%)	1.30	(8.34%)
	40	3.37e-34	(0.63%)	2.20e-34	(4.00%)	1.53	(9.03%)
	60	1.12e-34	(0.53%)	8.77e-35	(10.20%)	1.27	(13.02%)
	80	3.53e-35	(0.64%)	2.98e-35	(10.10%)	1.18	(12.95%)

* Only statistical uncertainty is reported.
† Only gamma spectroscopy uncertainty is reported.
‡ Systematic uncertainty sources included as discussed in Section 5.1.2.

Table 5.4: Production yield of ^{24}Na, $^{206-201}$Bi, ^{115m}In, and ^{11}C as calculated with FLUKA using the fluence conversion coefficients method and experimentally measured for the samples in the material test location with steel slabs of various thicknesses.

5.1.3 Activation benchmark with copper and steel samples at the CERN Shielding Benchmark Facility (CSBF)

Motivations

As demonstrated in the previous section, the activation of C, Al, In, and Bi samples by high-energy neutrons is predicted by the FLUKA Monte Carlo code with satisfactory agreement to experimental data. The configurations of the experimental setup are rather simple and can be easily controlled: this also allows to better estimate the various sources of systematic uncertainty.

In addition to the above reasons, it is important to stress that the environment to which activation samples and passive detectors can be exposed to is representative of the radiation conditions which can typically be found at the LHC experiments laterally to forward shielding structures or, more generally, at particle accelerators behind bulk shieldings (see Section 6.1 and 6.1.5). To perform an activation benchmark on an important class of materials widely employed at the LHC experiments and machine, activation samples of copper and two steel alloys were irradiated at the CERN Shielding Benchmark Facility (CSBF) to benchmark the predictions of FLUKA Monte Carlo simulations with the fluence conversion coefficients code applied to radiological characterization studies. A second, but surely not less important, goal was also to better understand the safety margins which should be in general applied when performing this kind of studies, for instance as the ones discussed in Section 6.1.

Contrary to the previously discussed benchmark, the main interest of this study was the activity of the long-lived radionuclides commonly produced in steel alloys and copper (such as ^{54}Mn and Co isotopes) and which, in the majority of the cases, determine the radiological procedures to be applied to activated components of these materials. For this experimental campaign an extended irradiation period was foreseen in order to build-up an amount of specific activity reasonably above the minimum detectable activity (MDA) of the High-Purity Germanium (HPGe) detector.

Experimental setup

The experiments had to be conducted at the CSBF exploiting parasitically a high-intensity run at CHARM to achieve an irradiation lasting more than one month. For these reasons, only one configuration could be chosen. Samples were installed on top and in the three available slots of the removable holder concrete block which was then inserted into its shaft: the shaft of the material test location was later closed by barite concrete blocks for a total thickness of 160 cm. The CSBF shielding configuration is then similar to the one depicted in figure 5.5(i). Figure 5.8 shows instead photographs of the removable holder concrete block during the installation of the activation samples: the samples installed on top of the block are visible in the second photo. Owing to the more intense secondary field that can be produced, the copper target was selected for the experiments and the movable walls in the CHARM target room were retracted: the CERN Accelerator Logging Service was used to also check that the configuration

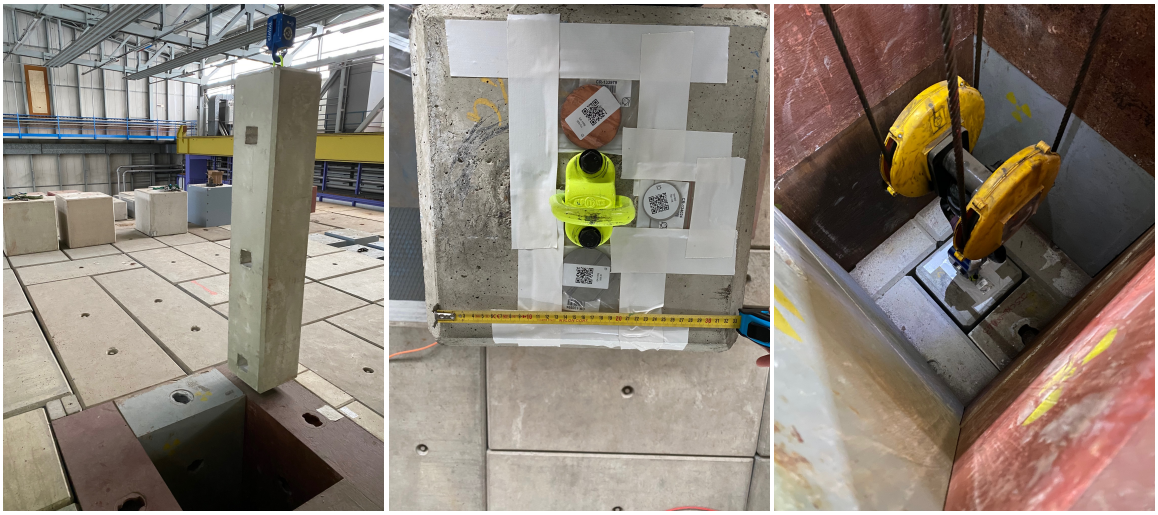

(a) (b) (c)

Figure 5.8: Photographs of the removable holder concrete block during the installation of the activation samples: (a) extraction of the block; (b) activation samples on top of the block; (c) re-insertion of the block into its shaft.

of the facility was not changed during the full period of irradiation.

Two steel alloys were chosen for the activation experiments: one has a composition similar to that of the austenitic stainless steel alloy 304L and is representative of a class of austenitic steels widely employed in components of the LHC machine and experiments, while the second is a kovar steel (a steel with an enriched cobalt content) and is, therefore, more sensitive to the activation by thermal neutrons. Steel samples of the first alloy came as disks of 6 cm diameter and 0.5 cm thickness, while those of the second alloy as disks of 4 cm diameter and 0.1 cm thickness. Similarly, the copper samples were disks of 6 cm diameter and 0.5 cm thickness.

Prior to their installation, the samples were all weighted with a precision scale having a resolution of 1 mg and were subsequently labelled with a code for their easier tracing in the CERN application for the traceability of radioactive equipment. All the samples were installed on August 31, 2022, and were retrieved on October 12, 2022. A summary of the irradiated samples is given in table 5.5 while table 5.6 lists the composition of the samples as obtained by glow discharge mass spectroscopy (GDMS) performed by an external analysis laboratory.

Beam conditions and activity measurements

The experiments were conducted from August 31, 2022, to October 12, 2022, during which a high-intensity run at CHARM took place. The beam intensity was monitored using the Secondary Emission Counter 1 (SEC1) located upstream of IRRAD. The counts per spill were retrieved from the CERN Accelerator Logging Service and were converted to protons per spill using the latest SEC1 calibration factor of 5.46×10^6 p/count [92]. Data was then binned into 20-minute-long intervals to obtain an average beam intensity in p/s which was later used for the Monte Carlo calculations:

Location	Sample name	Sample ID	Material	Mass [g]	Analysis live time [s]	
1st	EA-100g-003-Cu	CR-133976	Copper	126.483	21000.0	(from 13/10/2022 08:18:06)
	EA-100g-003-St	CR-133991	Steel	113.317	7200.0	(from 13/10/2022 08:18:23)
	EA-10g-003-Ko	CR-134021	Kovar	10.401	10000.0	(from 13/10/2022 10:25:09)
2nd	EA-100g-004-Cu	CR-133977	Copper	126.646	50000.0	(from 12/10/2022 16:31:10)
	EA-100g-004-St	CR-133992	Steel	113.257	50000.0	(from 12/10/2022 16:32:38)
	EA-10g-004-Ko	CR-134022	Kovar	10.351	27682.3	(from 13/10/2022 08:39:40)
3rd	EA-100g-005-Cu	CR-133978	Copper	126.656	54000.0	(from 13/10/2022 14:39:56)
	EA-100g-005-St	CR-133993	Steel	113.021	54000.0	(from 13/10/2022 16:23:24)
	EA-10g-005-Ko	CR-134023	Kovar	10.375	54000.0	(from 18/10/2022 11:23:38)
4th	EA-100g-006-Cu	CR-133979	Copper	126.025	86400.0	(from 14/14/2022 15:31:49)
	EA-100g-006-St	CR-133994	Steel	113.177	86400.0	(from 14/10/2022 16:24:17)
	EA-10g-006-Ko	CR-134024	Kovar	10.435	86400.0	(from 17/10/2022 09:42:14)

Table 5.5: Description of the copper and steel samples used for the experiments at the CSBF from August 31, 2022, to October 12, 2022.

Steel	Density: 7.95 g/cm^3 (0.02 %)				
Element	**Mass fraction [%]**	**Element**	**Mass fraction [%]**	**Element**	**Mass fraction [%]**
Fe	7.19×10^{1}	V	7.38×10^{-2}	Al	1.02×10^{-3}
Cr	1.77×10^{1}	Cu	2.60×10^{-2}	W	1.75×10^{-4}
Ni	8.10×10^{0}	P	2.44×10^{-2}	Mg	1.18×10^{-4}
Mn	1.33×10^{0}	Mo	4.20×10^{-3}	Na	5.00×10^{-7}
Si	5.20×10^{-1}	S	3.35×10^{-3}		
Co	2.48×10^{-1}	Ca	1.13×10^{-3}		

Kovar	Density: 8.24 g/cm^3 (0.02 %)				
Element	**Mass fraction [%]**	**Element**	**Mass fraction [%]**	**Element**	**Mass fraction [%]**
Fe	5.41×10^{1}	Mn	2.60×10^{-1}	Cr	5.55×10^{-2}
Ni	2.88×10^{1}	Si	8.35×10^{-2}	Cu	5.00×10^{-2}
Co	1.66×10^{1}	Mo	5.70×10^{-2}		

Copper	Density: 8.96 g/cm^3 (0.02 %)				
Element	**Mass fraction [%]**	**Element**	**Mass fraction [%]**	**Element**	**Mass fraction [%]**
Cu	9.992×10^{1}	Zn	3.39×10^{-4}	Hg	4.71×10^{-6}
S	1.41×10^{-1}	Pb	7.11×10^{-5}	Cd	7.84×10^{-7}
Si	1.66×10^{-3}	Bi	4.89×10^{-5}		

Table 5.6: Measured density (and relative uncertainty) and expected material composition of the activation samples used in the CSBF experiments in 2022.

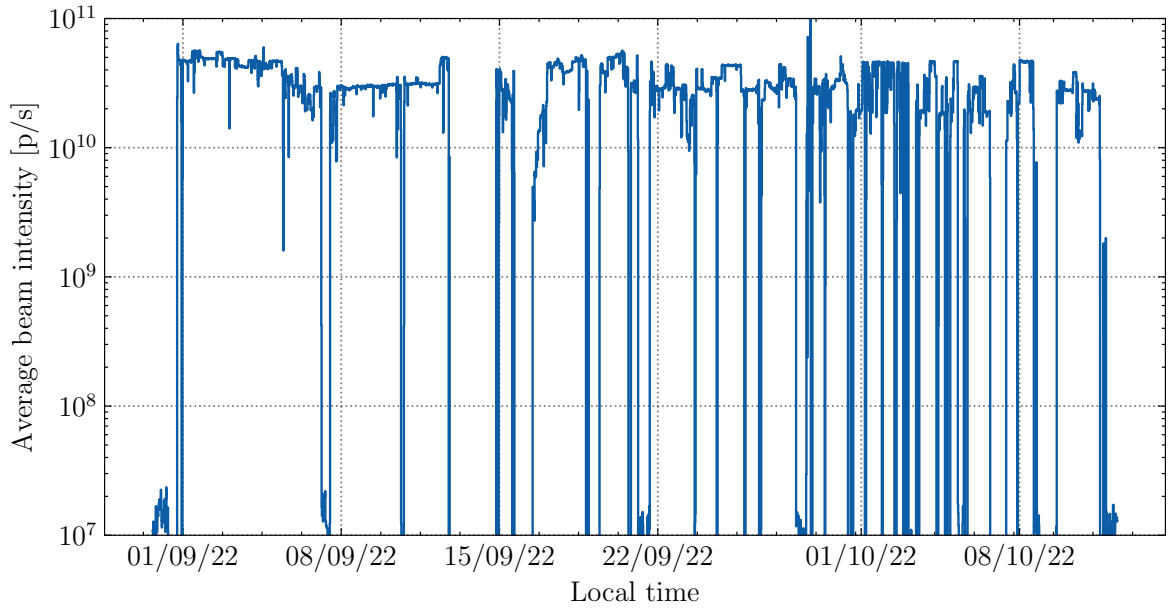

Figure 5.9: Average beam intensity sent to the CHARM target during the activation experiments from August 31, 2022, to October 12, 2022, as monitored with the Secondary Emission Counter 1 (SEC1). The intensity is binned in 20-minute-long intervals.

the beam intensity over the full period binned in 20 minutes long intervals is shown in figure 5.9.

Once removed, the samples were left for approximately one day in a dedicated storage area for radioactive materials within the CHARM facility: this cooling time was enough to appreciably reduce the activity of the short-lived radionuclides which were not of interest and, by consequence, decrease the residual dose rates from the samples themselves which would have otherwise increased the MDAs of the relevant radionuclides in the gamma spectroscopy due to the high dead-time. The activation samples were then transported to the CERN Radiation Protection Analytical Laboratory where they were each analyzed with a HPGe detector to determine the residual activity inventory: depending on the sample locations, the counting times ranged from 2 to 24 hours. The final activity inventory refers to the start of the measurement as detailed in table 5.5 since the analysis software takes into account a correction for the decay during the acquisition.

FLUKA Monte Carlo calculations

Monte Carlo calculations were performed with the FLUKA code[3] using the same simulation geometry and source settings as described in Section 5.1.2.

As previously discussed, an importance biasing scheme was used to compensate for the attenuation of the particle fluences: more than 100 million primary histories were simulated. With the exception of electrons, positrons, and photons (not transported) and neutrons (followed down to thermal energies), the transport threshold of 1 MeV

[3]The calculations employed the code version 4-3.0 as hosted by the FLUKA.CERN Collaboration

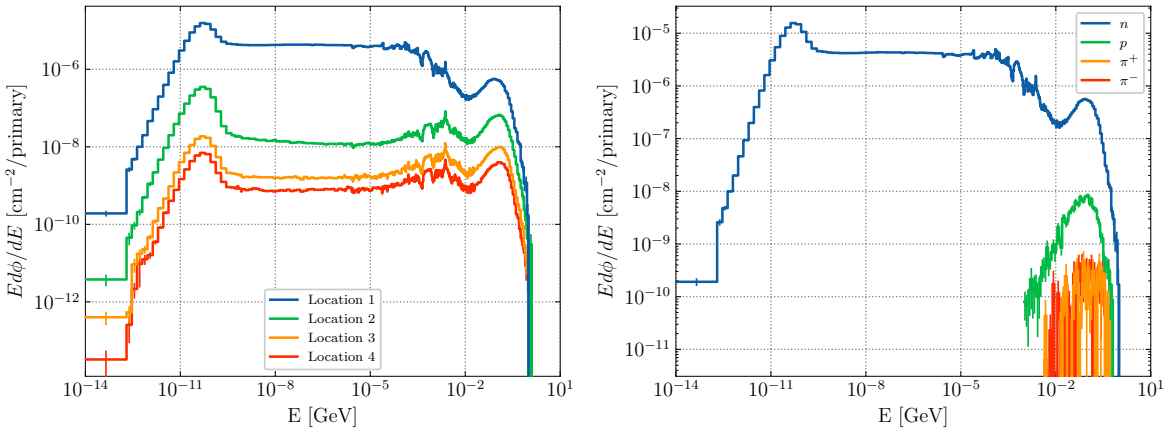

(a) (b)

Figure 5.10: Particle fluence energy spectra in the removable holder concrete block locations as estimated with the FLUKA Monte Carlo code: (a) neutron fluence energy spectra at the four locations; (b) neutron, proton, and charged pions fluence spectra at the location of the first sample.

was applied to the other particles. Particle fluence spectra were estimated for each activation sample location: neutron fluence energy spectra were estimated from thermal energies up to 10 GeV, while those of protons and charged pions from 1 MeV to 10 GeV. In the previously discussed benchmark, which was focused on high-energy neutron activation and attenuation, the selected radionuclides were such that their production cross section exhibited a reasonably high threshold. In the present case, instead, the general activation of steel and copper is under study: low-energy neutron interactions are therefore very relevant (notably for the production of ^{60}Co from ^{59}Co) and, albeit they may contribute in a very small fraction, reactions induced by charged hadrons should be considered as well.

The irradiation profile with a 20-minute binning as shown in figure 5.9 and the sample-specific cooling times were used, together with the material compositions in table 5.6, to compute fluence conversion coefficients which served for the final estimation of the radionuclide specific activities.

Discussion of the results

Figure 5.10(a) shows the neutron fluence energy spectra for the various locations within the removable holder concrete block, while figure 5.10(b) is an example of the particle fluence energy spectra for the first location: as previously mentioned, the contribution from charged hadrons is already very small for the first and less shielded location.

Although the discussion will be tailored to relevant radionuclides, the numerical values of the comparison for the full radionuclide inventory are all reported in table 5.7 together with the multiples of the Swiss clearance limits (LL). The uncertainties that are listed in the first columns of table 5.7 only correspond to the statistical uncertainty

of the Monte Carlo calculation (approximately between 0.2 % and 1.0 %) and to the counting statistics of the gamma spectroscopy (approximately between 2 % and 30 %). The ratio between the computed quantities and the experimental results (C/E ratio) includes instead additional systematic uncertainty contributions as discussed for Section 5.1.2: these entail a 4 % contribution from the uncertainty on the cast iron density, a contribution up to 1 % for the concrete density, and a 7 % contribution owing to the calibration of the SEC1. As per the previous comparison, the uncertainties due to the sample positioning, their mass, the beam size, and the positioning of the material in IRRAD are much lower than the ones already considered and it is safe to neglect them.

For the discussion of the results, it could be valuable to start from a global overview. By computing the uncertainty-averaged C/E ratios over all the estimated radionuclides for each location, it is possible to observe that the agreement with the experiments is within a factor 1.2 for the first two locations, and a factor 1.7 and 1.4 for the third and fourth ones. It is then very useful to look in more detail at some relevant radionuclides: for a better picture, figure 5.11 offers a plot of the ratios between the computed and measured specific activities as reported in table 5.7 for ^{57}Co, ^{58}Co, ^{60}Co, ^{54}Mn, and, additionally, for the multiples of Swiss clearance limits (LL).

For ^{57}Co, ^{58}Co and ^{54}Mn in the steel and copper samples the agreement is in general within a factor of 1.5 and, for this kind of experimental configuration, the calculated results tend to be conservative since the calculated quantity is overestimating the experimental results (C/E $>$ 1.0): a similar trend is observed for radionuclides predominantly produced in reactions at higher energy. The same holds true for the radionuclides produced in kovar samples (with the only exception of the second location) and for the production of ^{60}Co in copper, in which case the simulation is instead slightly underestimating the measured values. The calculated specific activities of ^{60}Co in steel and kovar show instead higher discrepancies, within a factor often between 2.5 and 3.0. One of the possible sources of these discrepancies may come from the material composition of the concrete (its hydrogen content in particular) or of the samples: additional independent chemical analysis would be needed to refine them.

It is of paramount importance to also consider the overall predictions for the multiples of Swiss clearance limits (LL), which, as it follows from equation 2.21, may be seen as a sum of radionuclide specific activities weighted on the radiological relevance of each radionuclide. For this deep shielding case, the results are conservative and the agreement is better than a factor between 1.5 and 2.0 for the copper and steel samples, while for the kovar samples higher discrepancies are observed: the C/E ratios for the multiples of Swiss clearance limits then reflect the general trends previously discussed.

In conclusion, one of the most relevant results is the following: the first and less shielded location in the removable holder concrete block, is characterized by particles spectra that are very similar to those that can be for instance found at CMS laterally to the existing forward shield (see Section 6.1). The overall agreement for the multiples of LL is better than a factor 1.5 and so is the production of ^{60}Co, while the production of ^{54}Mn differs by less than 20 %. For this kind of activation studies, the agreement of the experimentally measured activity of long-lived radionuclides with the Monte Carlo

simulations is very satisfactory and very valuable. These considerations will be very important and will be reprised in the context of the studies on the reinforcement of the existing CMS forward shield (Section 6.1 and 6.1.5).

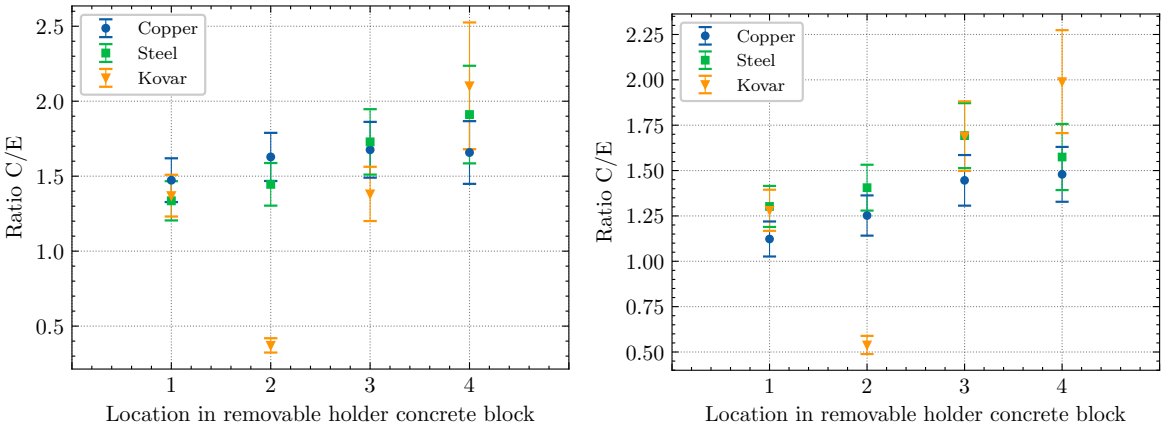

(a) ^{57}Co

(b) ^{58}Co

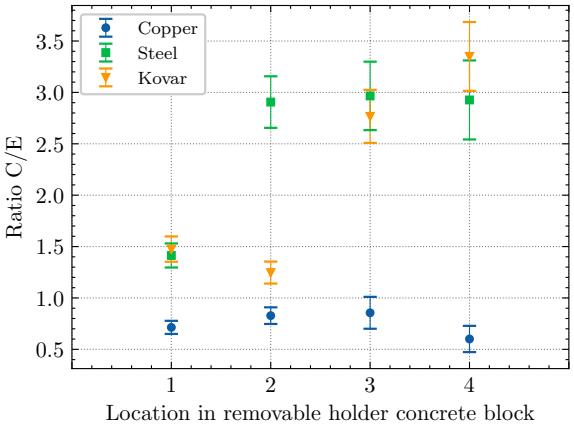

(c) ^{60}Co

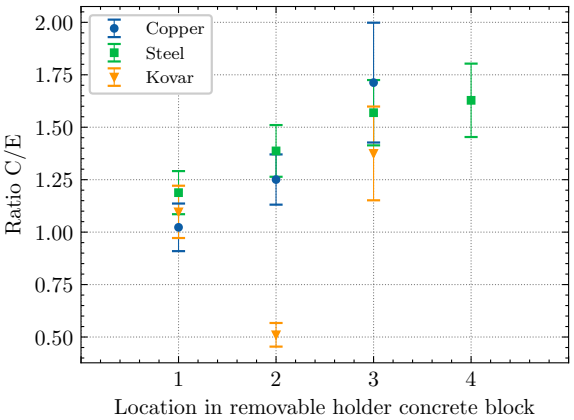

(d) ^{54}Mn

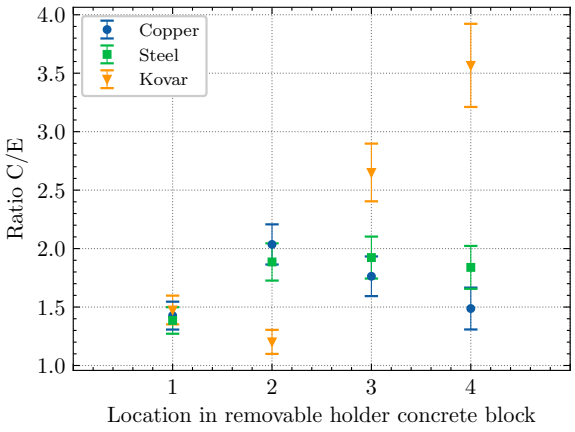

(e) Multiples of Swiss clearance limits (LL)

Figure 5.11: Ratio between the computed and measured specific activities (C/E ratio) in the copper and steel samples in the removable holder concrete block for selected radionuclides and for the multiples of Swiss clearance limits (LL).

Table 5.7: Mass-specific activities in the copper, steel and kovar samples in the removable holder concrete block as calculated with FLUKA using the fluence conversion coefficients method and as experimentally measured.

* Only statistical uncertainty is reported.
† Only gamma spectroscopy uncertainty is reported.
‡ Systematic uncertainty sources included as discussed in Section 5.1.3.

Location	Material	Radionuclide	FLUKA [Bq/g] (Rel. unc. %)*		Experiment [Bq/g] (Rel. unc. %)†		C/E Ratio (Rel. unc. %)‡	
1	Copper	^{46}Sc	1.21×10^{-2}	(0.92 %)	7.38×10^{-3}	(30.20 %)	1.64	(31.27 %)
		^{48}Sc	4.40×10^{-3}	(0.77 %)	2.38×10^{-2}	(16.00 %)	0.18	(17.93 %)
		^{48}V	9.57×10^{-2}	(0.91 %)	4.14×10^{-2}	(10.85 %)	2.31	(13.55 %)
		^{52}Mn	1.32×10^{-1}	(0.65 %)	1.47×10^{-1}	(2.75 %)	0.90	(8.55 %)
		^{54}Mn	1.54×10^{-1}	(0.47 %)	1.51×10^{-1}	(7.60 %)	1.02	(11.09 %)
		^{55}Co	1.91×10^{-2}	(0.51 %)	1.63×10^{-2}	(19.25 %)	1.17	(20.88 %)
		^{56}Co	4.33×10^{-1}	(0.43 %)	2.39×10^{-1}	(2.20 %)	1.81	(8.37 %)
		^{57}Co	6.43×10^{-1}	(0.37 %)	4.36×10^{-1}	(5.75 %)	1.47	(9.91 %)
		^{57}Ni	5.18×10^{-2}	(0.47 %)	2.57×10^{-2}	(12.60 %)	2.02	(14.97 %)
		^{58}Co	2.90×10^{0}	(0.32 %)	2.58×10^{0}	(2.95 %)	1.12	(8.59 %)
		^{59}Fe	1.45×10^{-1}	(0.34 %)	2.54×10^{-1}	(6.30 %)	0.57	(10.24 %)
		^{60}Co	5.70×10^{-2}	(0.32 %)	7.98×10^{-2}	(3.85 %)	0.71	(8.94 %)
		LL	3.23×10^{1}	(0.09 %)	2.26×10^{1}	(2.20 %)	1.43	(8.36 %)
	Steel	^{44}Sc	2.36×10^{-1}	(0.37 %)	1.36×10^{-1}	(6.30 %)	1.73	(10.24 %)
		^{44m}Sc	2.23×10^{-1}	(0.37 %)	1.35×10^{-1}	(7.80 %)	1.65	(11.23 %)
		^{46}Sc	2.95×10^{-1}	(0.29 %)	2.44×10^{-1}	(3.40 %)	1.21	(8.76 %)
		^{47}Sc	3.59×10^{-1}	(0.27 %)	3.35×10^{-1}	(6.85 %)	1.07	(10.59 %)
		^{48}Sc	8.09×10^{-2}	(0.25 %)	4.02×10^{-2}	(22.30 %)	2.01	(23.72 %)
		^{48}V	3.09×10^{0}	(0.28 %)	1.45×10^{0}	(2.10 %)	2.13	(8.34 %)
		^{51}Cr	6.44×10^{2}	(0.07 %)	4.58×10^{2}	(4.80 %)	1.40	(9.39 %)
		^{52}Mn	2.32×10^{0}	(0.32 %)	1.52×10^{0}	(1.80 %)	1.52	(8.27 %)
		^{54}Mn	2.11×10^{0}	(0.29 %)	1.77×10^{0}	(3.10 %)	1.19	(8.65 %)
		^{56}Co	5.64×10^{-1}	(0.46 %)	3.38×10^{-1}	(2.55 %)	1.67	(8.47 %)
		^{57}Co	4.99×10^{-1}	(0.39 %)	3.74×10^{-1}	(5.55 %)	1.34	(9.80 %)
		^{57}Ni	2.70×10^{-1}	(0.33 %)	1.75×10^{-1}	(8.95 %)	1.54	(12.05 %)
		^{58}Co	1.60×10^{0}	(0.40 %)	1.23×10^{0}	(3.20 %)	1.30	(8.69 %)
		^{59}Fe	9.21×10^{0}	(0.07 %)	7.30×10^{0}	(2.75 %)	1.26	(8.52 %)
		^{60}Co	1.28×10^{1}	(0.08 %)	9.07×10^{0}	(1.90 %)	1.41	(8.29 %)
		LL	1.81×10^{2}	(0.07 %)	1.31×10^{2}	(1.40 %)	1.39	(8.19 %)
	Kovar	^{48}V	1.56×10^{0}	(0.52 %)	7.92×10^{-1}	(7.15 %)	1.97	(10.79 %)
		^{51}Cr	7.60×10^{0}	(0.30 %)	5.45×10^{0}	(11.50 %)	1.39	(14.05 %)
		^{52}Mn	2.23×10^{0}	(0.39 %)	1.52×10^{0}	(3.65 %)	1.46	(8.86 %)
		^{54}Mn	1.78×10^{0}	(0.41 %)	1.62×10^{0}	(8.00 %)	1.10	(11.37 %)
		^{56}Co	2.10×10^{0}	(0.48 %)	1.24×10^{0}	(5.40 %)	1.69	(9.72 %)
		^{57}Co	2.15×10^{0}	(0.55 %)	1.57×10^{0}	(6.15 %)	1.37	(10.16 %)
		^{58}Co	8.33×10^{0}	(0.58 %)	6.51×10^{0}	(3.60 %)	1.28	(8.85 %)
		^{59}Fe	7.30×10^{0}	(0.13 %)	6.55×10^{0}	(3.95 %)	1.11	(8.98 %)
		^{60}Co	8.59×10^{2}	(0.14 %)	5.82×10^{2}	(2.15 %)	1.48	(8.35 %)
		LL	8.66×10^{3}	(0.14 %)	5.87×10^{3}	(2.13 %)	1.47	(8.34 %)
2	Copper	^{46}Sc	1.85×10^{-3}	(0.84 %)	2.17×10^{-3}	(13.25 %)	0.85	(15.66 %)
		^{48}V	1.50×10^{-2}	(0.82 %)	8.79×10^{-3}	(4.65 %)	1.70	(9.55 %)
		^{52}Mn	2.09×10^{-2}	(0.58 %)	2.05×10^{-2}	(2.60 %)	1.02	(8.72 %)
		^{54}Mn	2.08×10^{-2}	(0.42 %)	1.66×10^{-2}	(4.75 %)	1.25	(9.57 %)
		^{55}Co	4.92×10^{-3}	(0.45 %)	2.94×10^{-3}	(16.75 %)	1.67	(18.70 %)
		^{56}Co	5.66×10^{-2}	(0.38 %)	2.80×10^{-2}	(2.70 %)	2.02	(8.74 %)
		^{57}Co	7.79×10^{-2}	(0.33 %)	4.78×10^{-2}	(5.30 %)	1.63	(9.86 %)
		^{57}Ni	9.47×10^{-3}	(0.41 %)	5.12×10^{-3}	(14.40 %)	1.85	(16.63 %)
		^{58}Co	3.31×10^{-1}	(0.29 %)	2.64×10^{-1}	(3.05 %)	1.25	(8.85 %)
		^{59}Fe	1.71×10^{-2}	(0.31 %)	2.39×10^{-2}	(4.70 %)	0.71	(9.55 %)
		^{60}Co	6.15×10^{-3}	(0.29 %)	7.43×10^{-3}	(5.15 %)	0.83	(9.77 %)
		LL	2.32×10^{0}	(0.15 %)	1.14×10^{0}	(1.49 %)	2.04	(8.44 %)

Table 5.7 (continued)

Location	Material	Radionuclide	FLUKA [Bq/g] (Rel. unc. %)*		Experiment [Bq/g] (Rel. unc. %)†		C/E Ratio (Rel. unc. %)‡	
2	Steel	^{44}Sc	3.96×10^{-2}	(0.33 %)	1.97×10^{-2}	(5.15 %)	2.01	(9.78 %)
		^{44m}Sc	3.70×10^{-2}	(0.33 %)	1.87×10^{-2}	(6.10 %)	1.98	(10.31 %)
		^{46}Sc	3.75×10^{-2}	(0.26 %)	2.89×10^{-2}	(3.10 %)	1.30	(8.87 %)
		^{47}Sc	5.02×10^{-2}	(0.24 %)	3.81×10^{-2}	(6.05 %)	1.32	(10.28 %)
		^{48}Sc	1.23×10^{-2}	(0.22 %)	5.34×10^{-3}	(14.65 %)	2.30	(16.84 %)
		^{48}V	4.00×10^{-1}	(0.25 %)	1.71×10^{-1}	(2.05 %)	2.34	(8.56 %)
		^{51}Cr	1.42×10^{1}	(0.21 %)	4.84×10^{0}	(4.85 %)	2.94	(9.62 %)
		^{52}Mn	2.94×10^{-1}	(0.27 %)	1.63×10^{-1}	(1.80 %)	1.80	(8.50 %)
		^{54}Mn	2.08×10^{-1}	(0.27 %)	1.50×10^{-1}	(3.15 %)	1.39	(8.88 %)
		^{56}Co	6.08×10^{-2}	(0.54 %)	3.13×10^{-2}	(2.95 %)	1.94	(8.83 %)
		^{57}Co	4.74×10^{-2}	(0.38 %)	3.28×10^{-2}	(5.25 %)	1.45	(9.83 %)
		^{57}Ni	3.84×10^{-2}	(0.31 %)	1.77×10^{-2}	(9.05 %)	2.17	(12.29 %)
		^{58}Co	1.19×10^{-1}	(0.49 %)	8.49×10^{-2}	(3.40 %)	1.41	(8.99 %)
		^{59}Fe	1.86×10^{-1}	(0.23 %)	6.36×10^{-2}	(3.75 %)	2.92	(9.11 %)
		^{60}Co	2.17×10^{-1}	(0.23 %)	7.48×10^{-2}	(2.35 %)	2.91	(8.63 %)
		LL	6.46×10^{0}	(0.13 %)	3.43×10^{0}	(1.53 %)	1.89	(8.44 %)
	Kovar	^{48}V	2.00×10^{-1}	(0.44 %)	2.21×10^{-1}	(7.15 %)	0.91	(10.97 %)
		^{51}Cr	6.89×10^{-1}	(0.32 %)	1.42×10^{0}	(11.80 %)	0.49	(14.43 %)
		^{52}Mn	2.36×10^{-1}	(0.33 %)	3.38×10^{-1}	(5.00 %)	0.70	(9.70 %)
		^{54}Mn	1.81×10^{-1}	(0.37 %)	3.54×10^{-1}	(7.25 %)	0.51	(11.03 %)
		^{56}Co	2.21×10^{-1}	(0.44 %)	2.99×10^{-1}	(8.85 %)	0.74	(12.14 %)
		^{57}Co	2.07×10^{-1}	(0.54 %)	5.57×10^{-1}	(9.80 %)	0.37	(12.86 %)
		^{58}Co	6.54×10^{-1}	(0.64 %)	1.21×10^{0}	(4.15 %)	0.54	(9.30 %)
		^{59}Fe	1.64×10^{-1}	(0.36 %)	1.46×10^{-1}	(16.00 %)	1.13	(18.03 %)
		^{60}Co	1.44×10^{1}	(0.41 %)	1.15×10^{1}	(2.15 %)	1.25	(8.59 %)
		LL	1.49×10^{2}	(0.40 %)	1.24×10^{2}	(2.02 %)	1.20	(8.55 %)
3	Copper	^{48}V	2.25×10^{-3}	(0.90 %)	1.28×10^{-3}	(13.85 %)	1.76	(16.48 %)
		^{52}Mn	2.90×10^{-3}	(0.66 %)	2.73×10^{-3}	(6.60 %)	1.06	(11.08 %)
		^{54}Mn	3.16×10^{-3}	(0.50 %)	1.84×10^{-3}	(14.10 %)	1.71	(16.67 %)
		^{56}Co	8.52×10^{-3}	(0.46 %)	3.93×10^{-3}	(7.40 %)	2.17	(11.57 %)
		^{57}Co	1.17×10^{-2}	(0.41 %)	6.97×10^{-3}	(6.65 %)	1.68	(11.10 %)
		^{58}Co	4.90×10^{-2}	(0.38 %)	3.39×10^{-2}	(3.75 %)	1.45	(9.65 %)
		^{59}Fe	2.52×10^{-3}	(0.39 %)	3.64×10^{-3}	(11.40 %)	0.69	(14.46 %)
		^{60}Co	9.17×10^{-4}	(0.39 %)	1.07×10^{-3}	(15.80 %)	0.86	(18.13 %)
		LL	2.16×10^{-1}	(0.23 %)	1.22×10^{-1}	(3.71 %)	1.76	(9.63 %)
	Steel	^{44}Sc	4.57×10^{-3}	(0.37 %)	2.46×10^{-3}	(13.95 %)	1.86	(16.54 %)
		^{44m}Sc	4.31×10^{-3}	(0.37 %)	1.67×10^{-3}	(18.80 %)	2.58	(20.79 %)
		^{46}Sc	5.65×10^{-3}	(0.31 %)	3.85×10^{-3}	(7.65 %)	1.47	(11.72 %)
		^{47}Sc	6.22×10^{-3}	(0.30 %)	4.75×10^{-3}	(10.10 %)	1.31	(13.45 %)
		^{48}V	5.83×10^{-2}	(0.30 %)	2.31×10^{-2}	(3.00 %)	2.52	(9.38 %)
		^{51}Cr	8.88×10^{-1}	(0.42 %)	3.43×10^{-1}	(5.15 %)	2.58	(10.27 %)
		^{52}Mn	3.90×10^{-2}	(0.36 %)	1.88×10^{-2}	(2.75 %)	2.07	(9.30 %)
		^{54}Mn	3.11×10^{-2}	(0.39 %)	1.98×10^{-2}	(4.40 %)	1.57	(9.92 %)
		^{56}Co	9.17×10^{-3}	(0.98 %)	3.61×10^{-3}	(13.30 %)	2.54	(16.02 %)
		^{57}Co	7.16×10^{-3}	(0.57 %)	4.14×10^{-3}	(8.95 %)	1.73	(12.62 %)
		^{57}Ni	3.68×10^{-3}	(0.43 %)	2.31×10^{-3}	(18.00 %)	1.59	(20.08 %)
		^{58}Co	1.79×10^{-2}	(0.69 %)	1.06×10^{-2}	(5.70 %)	1.69	(10.57 %)
		^{59}Fe	1.02×10^{-2}	(0.51 %)	3.30×10^{-3}	(13.25 %)	3.10	(15.96 %)
		^{60}Co	1.25×10^{-2}	(0.52 %)	4.23×10^{-3}	(6.85 %)	2.97	(11.23 %)
		LL	7.30×10^{-1}	(0.23 %)	3.79×10^{-1}	(2.86 %)	1.92	(9.33 %)
	Kovar	^{48}V	2.52×10^{-2}	(0.54 %)	1.37×10^{-2}	(12.85 %)	1.83	(15.63 %)
		^{52}Mn	2.09×10^{-2}	(0.44 %)	1.53×10^{-2}	(9.45 %)	1.37	(12.97 %)
		^{54}Mn	2.66×10^{-2}	(0.53 %)	1.94×10^{-2}	(13.60 %)	1.38	(16.25 %)
		^{56}Co	3.16×10^{-2}	(0.59 %)	1.27×10^{-2}	(23.05 %)	2.50	(24.71 %)
		^{57}Co	3.01×10^{-2}	(0.68 %)	2.18×10^{-2}	(9.60 %)	1.38	(13.09 %)
		^{58}Co	9.54×10^{-2}	(0.93 %)	5.64×10^{-2}	(7.00 %)	1.69	(11.34 %)
		^{60}Co	8.24×10^{-1}	(0.90 %)	2.98×10^{-1}	(2.75 %)	2.77	(9.34 %)
		LL	9.03×10^{0}	(0.82 %)	3.41×10^{0}	(2.67 %)	2.65	(9.31 %)

Table 5.7 (continued)

Location	Material	Radionuclide	FLUKA [Bq/g] (Rel. unc. %)*		Experiment [Bq/g] (Rel. unc. %)†		C/E Ratio (Rel. unc. %)‡	
4	Copper	^{46}Sc	1.16×10^{-4}	(1.02 %)	1.04×10^{-3}	(30.55 %)	0.11	(31.95 %)
		^{48}V	8.84×10^{-4}	(1.00 %)	7.01×10^{-4}	(15.90 %)	1.26	(18.45 %)
		^{52}Mn	1.05×10^{-3}	(0.72 %)	7.54×10^{-4}	(16.95 %)	1.39	(19.35 %)
		^{54}Mn	1.29×10^{-3}	(0.55 %)	6.48×10^{-4}	(25.75 %)	1.99	(27.39 %)
		^{56}Co	3.45×10^{-3}	(0.51 %)	1.44×10^{-3}	(12.10 %)	2.39	(15.27 %)
		^{57}Co	4.75×10^{-3}	(0.46 %)	2.87×10^{-3}	(8.50 %)	1.66	(12.61 %)
		^{58}Co	1.97×10^{-2}	(0.41 %)	1.33×10^{-2}	(4.20 %)	1.48	(10.22 %)
		^{60}Co	3.72×10^{-4}	(0.43 %)	6.19×10^{-4}	(19.10 %)	0.60	(21.25 %)
		LL	8.20×10^{-2}	(0.26 %)	5.51×10^{-2}	(7.64 %)	1.49	(12.04 %)
	Steel	^{46}Sc	2.29×10^{-3}	(0.35 %)	1.59×10^{-3}	(11.40 %)	1.44	(14.72 %)
		^{47}Sc	2.06×10^{-3}	(0.34 %)	1.44×10^{-3}	(18.85 %)	1.43	(21.03 %)
		^{48}V	2.27×10^{-2}	(0.34 %)	8.37×10^{-3}	(3.90 %)	2.71	(10.10 %)
		^{51}Cr	3.32×10^{-1}	(0.52 %)	1.29×10^{-1}	(5.40 %)	2.57	(10.77 %)
		^{52}Mn	1.39×10^{-2}	(0.40 %)	6.83×10^{-3}	(3.55 %)	2.03	(9.97 %)
		^{54}Mn	1.23×10^{-2}	(0.43 %)	7.58×10^{-3}	(5.35 %)	1.63	(10.74 %)
		^{56}Co	3.55×10^{-3}	(0.68 %)	2.29×10^{-3}	(12.15 %)	1.55	(15.32 %)
		^{57}Co	2.82×10^{-3}	(0.59 %)	1.48×10^{-3}	(14.25 %)	1.91	(17.03 %)
		^{57}Ni	9.22×10^{-4}	(0.46 %)	1.28×10^{-3}	(24.00 %)	0.72	(25.75 %)
		^{58}Co	6.96×10^{-3}	(0.75 %)	4.42×10^{-3}	(6.85 %)	1.57	(11.58 %)
		^{59}Fe	3.84×10^{-3}	(0.64 %)	1.15×10^{-3}	(25.55 %)	3.34	(27.20 %)
		^{60}Co	4.87×10^{-3}	(0.70 %)	1.67×10^{-3}	(9.25 %)	2.93	(13.14 %)
		LL	2.85×10^{-1}	(0.24 %)	1.55×10^{-1}	(3.55 %)	1.84	(9.96 %)
	Kovar	^{52}Mn	9.39×10^{-3}	(0.48 %)	6.12×10^{-3}	(88.25 %)	1.53	(88.74 %)
		^{57}Co	1.18×10^{-2}	(0.81 %)	5.62×10^{-3}	(17.80 %)	2.10	(20.10 %)
		^{58}Co	3.72×10^{-2}	(1.03 %)	1.87×10^{-2}	(10.75 %)	1.99	(14.26 %)
		^{60}Co	3.15×10^{-1}	(1.08 %)	9.41×10^{-2}	(3.50 %)	3.35	(10.00 %)
		LL	3.46×10^{0}	(0.98 %)	9.71×10^{-1}	(3.44 %)	3.57	(9.97 %)

5.1.4 Activation benchmark with copper and steel samples at the CERN High energy AcceleRator Mixed field (CHARM) facility

Motivations

Owing to the design of the CERN Shielding Benchmark Facility (CSBF), the neutron and charged hadron particle spectra expected at the locations of the removable sample holder concrete block can be representative of the irradiation conditions found at particle accelerators laterally to the impact point of high-energy particles on massive components and behind medium-thick or bulky shielding elements. An equally important and common situation is the one in which objects are in less shielded conditions.

Activation samples of copper and steel alloys of the same kind as those employed at the CSBF were irradiated inside the CERN High energy AcceleRator Mixed field (CHARM) facility to benchmark the predictions of the FLUKA Monte Carlo code and the fluence conversion coefficients method and to better understand the safety margins which should be generally applied when performing activation studies. As for the previous benchmark, the main interest of this study was the activation of long-lived radionuclides commonly produced in steel and copper and that determine, in the vast majority of the situations, the radiological procedures to be applied to activated components made out of such materials.

Experimental setup

The measurements were part of a series of campaigns conducted at CHARM during a beam time of one week allocated to radiation protection experiments. Two sets of activation samples were installed on August 26, 2022, and both retrieved on August 29, 2022: one was placed directly in the CHARM target room at beam height at the grid enclosing the movable shielding walls and at approximately 90° from the target, while the second one was still located at approximately 90° from the target but approximately at 20 cm above the beam level and at the wall in the access maze facing the target room (thus at a greater distance with respect to the target).

Figure 5.12 shows a photo of the CHARM target room when the movable shielding walls are retracted, while figure 5.13 represents the horizontal cut of the IRRAD and CHARM FLUKA simulation geometry and provides a schematic overview of the approximate sample locations. The selected CHARM target was the copper one and the movable shielding walls were retracted for the whole duration of the experiment such that one could maximise the intensity of the irradiation field for the two installation locations: in this way it was possible to irradiate the samples for two days only while still keeping the specific activities of the radionuclides of interest well above the minimum detectable activity (MDA) of a standard gamma spectroscopy analysis.

The copper, steel and kovar samples were of the same kind and sizes as those described in 5.1.3 and, prior to their installation, they were all weighted with a precision scale with a 1 mg resolution and consequently labelled for their easier tracing. A

Figure 5.12: Photo of the CHARM target room with the movable shielding walls retracted [104].

Location	Sample name	Sample ID	Material	Mass [g]	Analysis live time [s]	
1 ("Grid")	EA-100g-001-Cu	CR-133974	Copper	126.695	7200.0	(from 07/09/2022 09:16:30)
	EA-100g-001-St	CR-133989	Steel	113.123	3000.0	(from 06/09/2022 15:08:33)
	EA-10g-001-Ko	CR-134019	Kovar	10.405	3600.0	(from 07/09/2022 08:02:35)
2 ("Wall")	EA-100g-002-Cu	CR-133975	Copper	126.810	15000.0	(from 06/09/2022 16:31:10)
	EA-100g-002-St	CR-133990	Steel	112.992	10000.0	(from 06/09/2022 10:43:34)
	EA-10g-002-Ko	CR-134020	Kovar	10.437	8000.0	(from 06/09/2022 08:26:48)

Table 5.8: Description of the copper and steel samples used for the experiments at CHARM from August 26, 2022, to August 29, 2022.

summary of the irradiated samples is given in table 5.8 while the composition of the irradiated samples was already provided in table 5.6.

Beam conditions and activity measurements

The experiments were conducted from August 26, 2022, to August 29, 2022: the beam was very stable throughout the whole period and the intensity was monitored using the Secondary Emission Counter 1 (SEC1) located upstream of IRRAD. The counts per spill were retrieved from the CERN Accelerator Logging Service and converted to protons per spill using the latest SEC1 calibration factor of 5.46×10^6 p/count [92]. The data was then binned into intervals of 1 minute to obtain an average beam intensity in p/s, later used for the Monte Carlo calculations: the average beam intensity over the full period is shown in figure 5.14.

The samples were retrieved at the end of the allocated irradiation time and, owing to the high residual dose rates, they were left for approximately one week in a dedicated

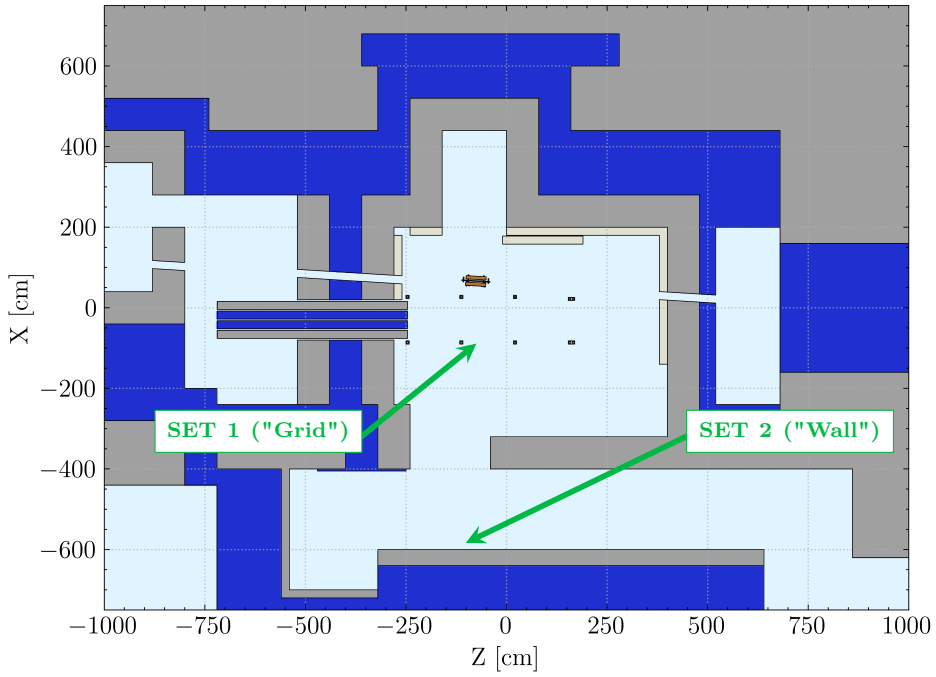

Figure 5.13: Cut at beam height of the FLUKA simulation geometry of IRRAD and CHARM showing the target room and the access maze: the locations of the activation samples are also indicated.

storage area for radioactive materials within the CHARM facility. This cooling time was needed to considerably reduce the activity of the short-lived radionuclides which were not of interest and, as consequence, decrease the residual dose rates from the samples themselves: this later allowed to keep the dead-time losses during the gamma spectroscopy below 0.5 %[4]. The activation samples were then transported to the CERN Radiation Protection Analytical Laboratory where they were each analyzed with a High-Purity Germanium (HPGe) detector to determine the residual activity inventory: due to the high-intensity field to which they were exposed to, the counting times ranged from 50 minutes to 4.2 hours. The final activity inventory refers to the start of the measurement as detailed in table 5.8 since a correction for the decay during acquisition is taken into account by the analysis software.

FLUKA Monte Carlo calculations

Monte Carlo calculations were performed with the FLUKA code[5]. The simulation geometry fully reproduces IRRAD and CHARM with a significant level of detail: as for the previous benchmarks, the primary source consists of a 24 GeV/c proton beam with a FHMW of 1.2 cm in both directions of the transverse plane and that starts upstream

[4]As briefly mentioned in Section 5.1.3, high-activity of γ-emitting radionuclides means high counting rates during gamma spectroscopy, therefore high dead-time counting losses. High dead-time counting losses imply higher minimum detectable activities (MDAs).

[5]The calculations employed the code version 4-3.0 as hosted by the FLUKA.CERN Collaboration

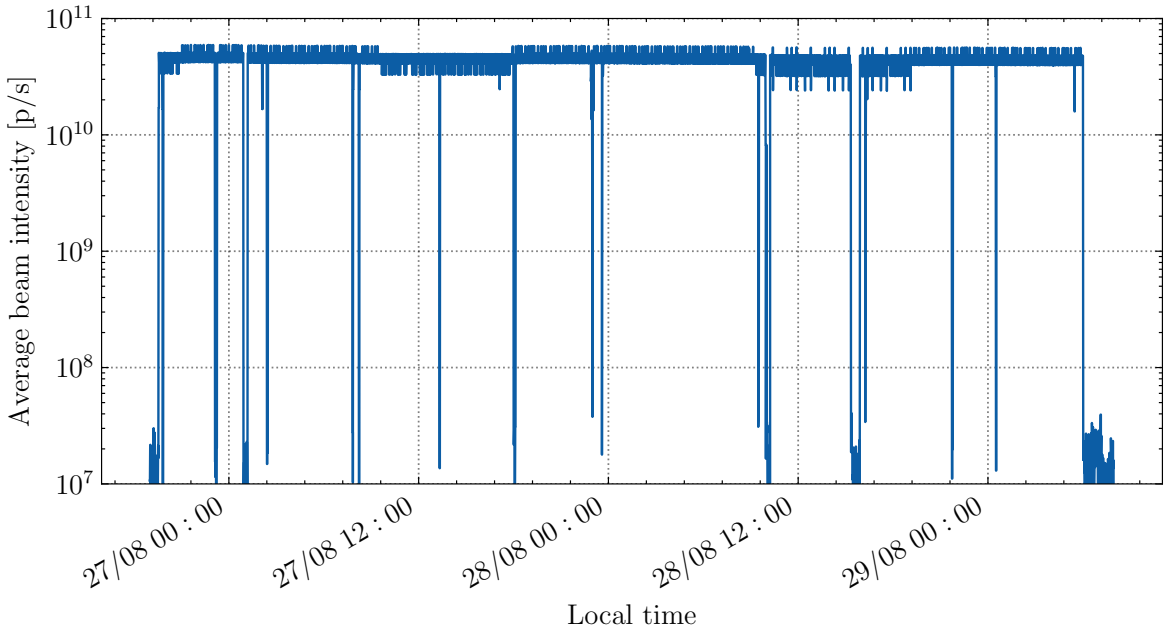

Figure 5.14: Average beam intensity sent to the CHARM facility during the activation experiments from August 26, 2022, to August 29, 2022, as monitored with the Secondary Emission Counter 1 (SEC1). The intensity is binned in intervals of 1 minute.

IRRAD to account for the presence of electronic samples located in the IRRAD test locations. The cut at beam height of the FLUKA simulation geometry was already shown in figure 5.13: the beam axis is at an angle of $-3.5°$ with respect to the z-axis in the reference frame adopted in the simulations.

Particles were transported down to 1 MeV with the exception of electrons, positrons, and photons which were transported down to 100 keV, and of neutrons which were followed down to 0.01 meV. Particle fluence spectra were estimated for each activation sample location: neutron fluence energy spectra were estimated from thermal energies up to 10 GeV, while those of protons and charged pions from 1 MeV to 10 GeV. In this case, there was no need to compensate for the attenuation of particle fluences so no biasing scheme was used: approximately 20 million primary histories were simulated.

The computation of radionuclide activities from particle fluences was performed with the information on the irradiation profile with a 1-minute binning as shown in figure 5.14, the sample-specific cooling times as in table 5.8, and the samples material compositions as in table 5.6.

Discussion of the results

Figure 5.15 shows the simulated particle fluence energy spectra at the first ("Grid") and second ("Wall") location in CHARM. It can be noticed that, at the location that is closer to the target, the contribution from charged hadrons is smaller than that of neutrons and even smaller in the proximity of the walls in front of the access to the target room. Apart from the differences in the evaporation region, the neutron fluence energy spectra qualitatively show the same dependency on overall and the spectral

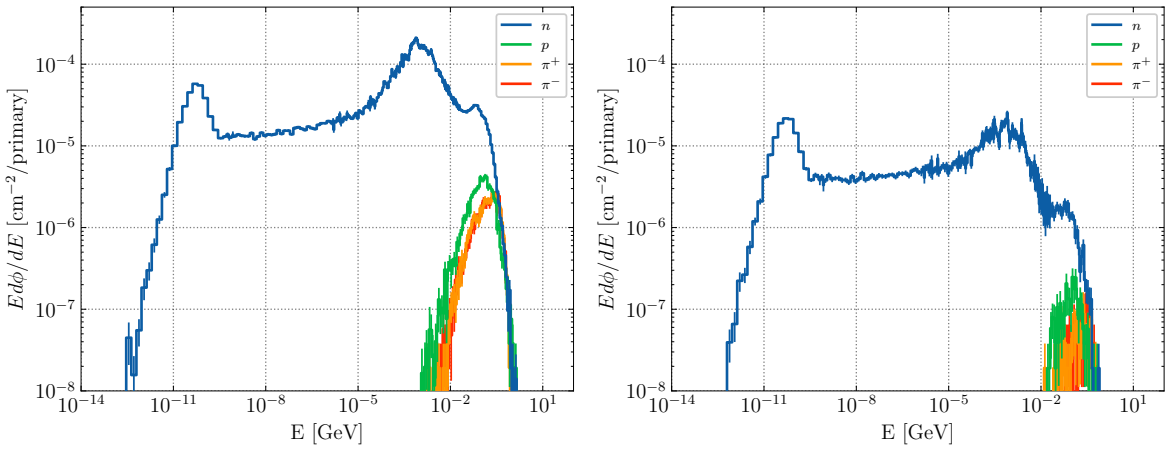

(a) Fluence energy spectra at the first location ("Grid").

(b) Fluence energy spectra at the second location ("Wall").

Figure 5.15: Particle fluence energy spectra as estimated with the FLUKA Monte Carlo code in correspondence of the installation locations of the activation samples in CHARM.

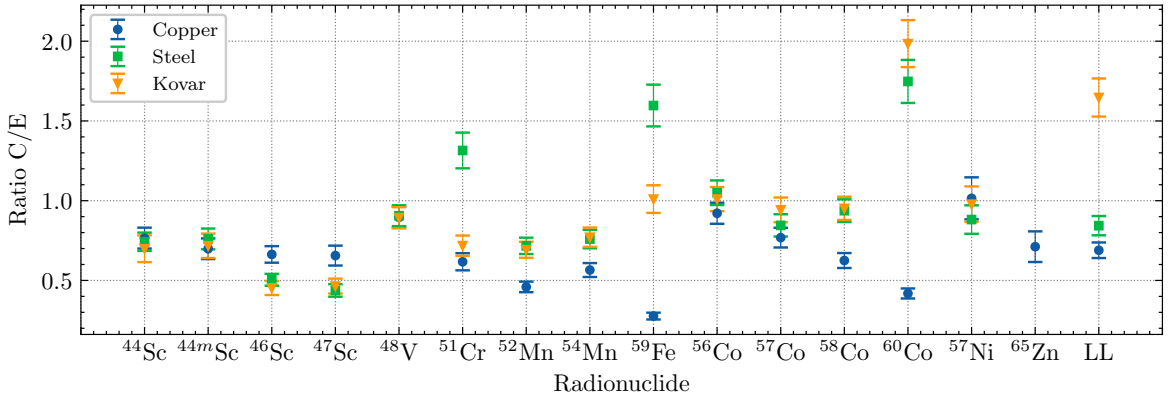

(a) First location ("Grid").

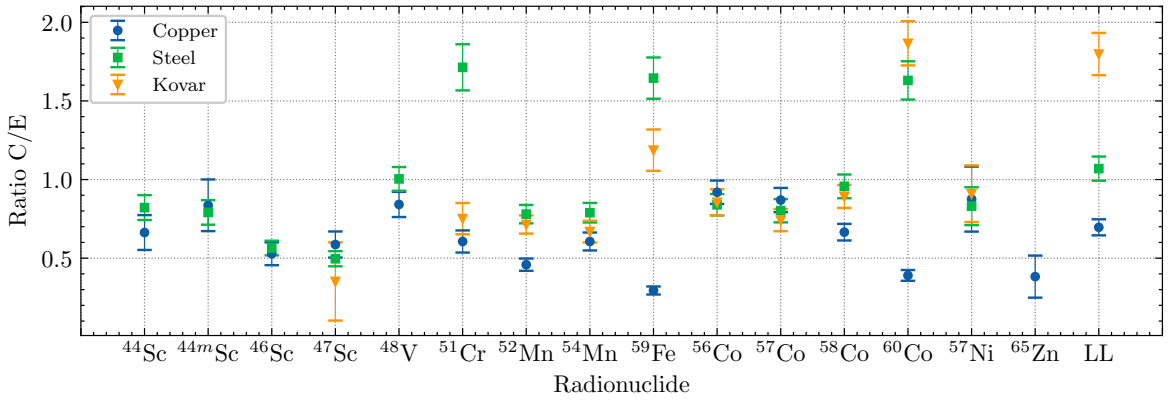

(b) Second location ("Wall").

Figure 5.16: Ratio between the computed and measured specific activities and multiples of Swiss clearance limits (LL) in the copper, steel, and kovar samples in CHARM.

fluence at the wall is obviously less intense[6].

Although the discussion will be tailored on relevant radionuclides, the numerical values of the comparison are all reported in table 5.9: in addition to the radionuclide specific activities, additional entries have been added for the multiples of the Swiss clearance limits (LL). The uncertainties that are listed in the first columns of the tables only correspond to the statistical uncertainty of the Monte Carlo calculation (approximately between 0.4 % and 7.0 % excluding ^{65}Zn in one case) and to the counting statistics of the gamma spectroscopy (approximately between 2 % and 25 % excluding ^{47}Sc in one case). The ratio between the computed quantities and the experimental results (C/E ratio) includes instead a 7 % contribution owing to the calibration of the SEC1. As per the previous comparison, the uncertainties due to the sample positioning and their mass, the beam size, and the positioning of materials in IRRAD are much lower than the ones already considered and is safe to neglect them.

For the discussion of the results, it could be valuable to start from a global overview. By computing the uncertainty averaged C/E ratios over all the estimated radionuclides for each location, it is possible to observe that the agreement with the experiments is within a factor of 0.73 and 0.75 for both locations. For a graphical overview of the results for the two locations, figure 5.16 illustrates the ratios between the computed and measured specific activities as reported in table 5.9 for all the measured radionuclides and additionally for the multiples of Swiss clearance limits (LL): with a limited number of exceptions, the agreement is very satisfactory and it sets within a factor between 0.6 and 1.2.

For ^{57}Co, ^{58}Co the agreement is in general better than a factor 0.8, while for ^{54}Mn the agreement is within a factor 0.7: for this experimental configuration the calculated results tend to be slightly underestimating the measurements (C/E < 1.0) and a similar trend is observed for radionuclides predominantly produced in reactions at higher energy. The estimation of ^{60}Co is better than a factor 2.0 for the steel and kovar samples, while it is underestimated by a factor 0.4 in copper.

It is fundamental to consider the prediction for the multiples of Swiss clearance limits (LL) which represent a result weighted on the radiological relevance of each radionuclide. For kovar samples the results tend to be reasonably conservative within a factor of 2.0 while for both the copper sample and the steel sample located near the target a slight underestimation is observed, still better than a factor of 0.7. The FLUKA predictions at the wall facing the entrance of the CHARM target room are instead in excellent agreement with the experimental result.

In conclusion, one of the most valuable results is the following. Both the considered locations, particularly the one at the walls, are characterized by a radiation field that is very similar to the one that can be found in the CMS experimental cavern (see Section 6.1): the satisfactory and valuable results for the LL, ^{60}Co, and ^{54}Mn are very important for considerations on the studies on the reinforcement of the existing CMS forward shield (Section 6.1 and 6.1.5).

[6]The evaporation (or fast) region of neutron fluence energy spectra is approximately between 100 keV to 20 MeV (see Section 2.1.4).

Table 5.9: Mass-specific activities in the copper, steel and kovar samples in CHARM as calculated with FLUKA using the fluence conversion coefficients method and as experimentally measured.

* Only statistical uncertainty is reported.
† Only gamma spectroscopy uncertainty is reported.
‡ Systematic uncertainty sources included as discussed in Section 5.1.4.

Location	Material	Radionuclide	FLUKA [Bq/g] (Rel. unc. %)*		Experiment [Bq/g] (Rel. unc. %)†		C/E Ratio (Rel. unc. %)‡	
"Grid"	Copper	^{44}Sc	3.28×10^{-1}	(1.21 %)	4.29×10^{-1}	(4.75 %)	0.77	(8.54 %)
		^{44m}Sc	3.09×10^{-1}	(1.21 %)	4.43×10^{-1}	(5.95 %)	0.70	(9.27 %)
		^{46}Sc	2.86×10^{-1}	(1.08 %)	4.32×10^{-1}	(3.30 %)	0.66	(7.81 %)
		^{47}Sc	5.23×10^{-1}	(1.07 %)	7.98×10^{-1}	(6.35 %)	0.66	(9.51 %)
		^{48}V	3.14×10^{0}	(1.02 %)	3.50×10^{0}	(2.00 %)	0.90	(7.35 %)
		^{51}Cr	6.66×10^{0}	(0.84 %)	1.08×10^{1}	(5.10 %)	0.62	(8.70 %)
		^{52}Mn	3.29×10^{0}	(0.84 %)	7.16×10^{0}	(1.55 %)	0.46	(7.22 %)
		^{54}Mn	1.33×10^{0}	(0.66 %)	2.35×10^{0}	(3.20 %)	0.57	(7.73 %)
		^{56}Co	3.94×10^{0}	(0.61 %)	4.28×10^{0}	(1.45 %)	0.92	(7.17 %)
		^{57}Co	4.79×10^{0}	(0.54 %)	6.23×10^{0}	(3.90 %)	0.77	(8.03 %)
		^{57}Ni	1.90×10^{-1}	(0.69 %)	1.88×10^{-1}	(10.90 %)	1.01	(12.97 %)
		^{58}Co	2.27×10^{1}	(0.46 %)	3.64×10^{1}	(2.65 %)	0.62	(7.50 %)
		^{59}Fe	1.10×10^{0}	(0.52 %)	3.97×10^{0}	(3.15 %)	0.28	(7.69 %)
		^{60}Co	4.34×10^{-1}	(0.48 %)	1.04×10^{0}	(2.70 %)	0.42	(7.52 %)
		^{65}Zn	1.65×10^{-1}	(5.20 %)	2.32×10^{-1}	(10.30 %)	0.71	(13.50 %)
		LL	9.71×10^{1}	(0.31 %)	1.41×10^{2}	(1.04 %)	0.69	(7.08 %)
	Steel	^{44}Sc	3.73×10^{0}	(0.51 %)	5.02×10^{0}	(3.20 %)	0.74	(7.71 %)
		^{44m}Sc	3.52×10^{0}	(0.51 %)	4.63×10^{0}	(4.90 %)	0.76	(8.56 %)
		^{46}Sc	2.63×10^{0}	(0.42 %)	5.22×10^{0}	(2.30 %)	0.50	(7.38 %)
		^{47}Sc	4.90×10^{0}	(0.40 %)	1.12×10^{1}	(5.60 %)	0.44	(8.97 %)
		^{48}V	3.91×10^{1}	(0.39 %)	4.32×10^{1}	(1.65 %)	0.91	(7.20 %)
		^{51}Cr	4.35×10^{2}	(0.54 %)	3.31×10^{2}	(4.80 %)	1.31	(8.50 %)
		^{52}Mn	3.57×10^{1}	(0.45 %)	4.98×10^{1}	(1.45 %)	0.72	(7.16 %)
		^{54}Mn	1.87×10^{1}	(0.38 %)	2.46×10^{1}	(3.00 %)	0.76	(7.63 %)
		^{56}Co	5.96×10^{0}	(1.10 %)	5.67×10^{0}	(1.90 %)	1.05	(7.34 %)
		^{57}Co	5.25×10^{0}	(0.56 %)	6.21×10^{0}	(4.35 %)	0.85	(8.26 %)
		^{57}Ni	1.44×10^{0}	(0.46 %)	1.64×10^{0}	(7.30 %)	0.88	(10.12 %)
		^{58}Co	3.16×10^{1}	(0.44 %)	3.37×10^{1}	(2.90 %)	0.94	(7.59 %)
		^{59}Fe	4.07×10^{0}	(0.72 %)	2.55×10^{0}	(4.20 %)	1.60	(8.19 %)
		^{60}Co	4.63×10^{0}	(0.84 %)	2.65×10^{0}	(3.15 %)	1.75	(7.72 %)
		LL	4.41×10^{2}	(0.24 %)	5.23×10^{2}	(1.48 %)	0.84	(7.16 %)
	Kovar	^{44}Sc	1.73×10^{0}	(0.91 %)	2.48×10^{0}	(9.70 %)	0.70	(12.00 %)
		^{44m}Sc	1.63×10^{0}	(0.91 %)	2.27×10^{0}	(8.00 %)	0.72	(10.67 %)
		^{46}Sc	1.15×10^{0}	(0.81 %)	2.54×10^{0}	(6.75 %)	0.45	(9.76 %)
		^{47}Sc	1.65×10^{0}	(0.81 %)	3.56×10^{0}	(7.15 %)	0.46	(10.04 %)
		^{48}V	2.16×10^{1}	(0.69 %)	2.42×10^{1}	(2.40 %)	0.89	(7.43 %)
		^{51}Cr	5.54×10^{1}	(0.54 %)	7.72×10^{1}	(5.45 %)	0.72	(8.89 %)
		^{52}Mn	3.10×10^{1}	(0.55 %)	4.48×10^{1}	(1.85 %)	0.69	(7.26 %)
		^{54}Mn	1.51×10^{1}	(0.56 %)	1.96×10^{1}	(3.55 %)	0.77	(7.87 %)
		^{56}Co	1.80×10^{1}	(0.73 %)	1.78×10^{1}	(2.50 %)	1.01	(7.47 %)
		^{57}Co	2.19×10^{1}	(0.77 %)	2.32×10^{1}	(4.25 %)	0.94	(8.23 %)
		^{57}Ni	3.61×10^{0}	(0.76 %)	3.70×10^{0}	(8.95 %)	0.98	(11.39 %)
		^{58}Co	1.44×10^{2}	(0.60 %)	1.51×10^{2}	(3.00 %)	0.95	(7.64 %)
		^{59}Fe	8.99×10^{0}	(0.67 %)	8.90×10^{0}	(4.90 %)	1.01	(8.57 %)
		^{60}Co	2.96×10^{2}	(1.53 %)	1.49×10^{2}	(1.95 %)	1.98	(7.43 %)
		LL	3.53×10^{3}	(1.29 %)	2.14×10^{3}	(1.43 %)	1.65	(7.26 %)

Table 5.9 (continued)

Location	Material	Radionuclide	FLUKA [Bq/g] (Rel. unc. %)*		Experiment [Bq/g] (Rel. unc. %)†		C/E Ratio (Rel. unc. %)‡	
"Wall"	Copper	^{44}Sc	1.24×10^{-2}	(6.42 %)	1.87×10^{-2}	(13.75 %)	0.66	(16.71 %)
		^{44m}Sc	1.17×10^{-2}	(6.42 %)	1.40×10^{-2}	(17.20 %)	0.84	(19.65 %)
		^{46}Sc	9.17×10^{-3}	(5.53 %)	1.74×10^{-2}	(10.45 %)	0.53	(13.74 %)
		^{47}Sc	1.95×10^{-2}	(5.41 %)	3.32×10^{-2}	(11.05 %)	0.59	(14.16 %)
		^{48}V	1.05×10^{-1}	(5.34 %)	1.24×10^{-1}	(3.60 %)	0.84	(9.51 %)
		^{51}Cr	2.38×10^{-1}	(4.21 %)	3.93×10^{-1}	(8.25 %)	0.61	(11.61 %)
		^{52}Mn	1.27×10^{-1}	(4.23 %)	2.76×10^{-1}	(2.30 %)	0.46	(8.50 %)
		^{54}Mn	5.38×10^{-2}	(3.10 %)	8.87×10^{-2}	(5.45 %)	0.61	(9.40 %)
		^{56}Co	1.66×10^{-1}	(2.87 %)	1.81×10^{-1}	(2.85 %)	0.92	(8.09 %)
		^{57}Co	2.23×10^{-1}	(2.48 %)	2.56×10^{-1}	(4.85 %)	0.87	(8.87 %)
		^{57}Ni	1.07×10^{-2}	(3.31 %)	1.22×10^{-2}	(22.30 %)	0.88	(23.61 %)
		^{58}Co	1.14×10^{0}	(2.15 %)	1.71×10^{0}	(3.05 %)	0.67	(7.93 %)
		^{59}Fe	5.54×10^{-2}	(2.28 %)	1.88×10^{-1}	(4.60 %)	0.29	(8.68 %)
		^{60}Co	2.34×10^{-2}	(2.13 %)	6.00×10^{-2}	(4.85 %)	0.39	(8.78 %)
		^{65}Zn	6.16×10^{-3}	(23.60 %)	1.61×10^{-2}	(24.85 %)	0.38	(34.98 %)
		LL	4.31×10^{0}	(1.37 %)	6.19×10^{0}	(1.68 %)	0.70	(7.33 %)
	Steel	^{44}Sc	1.40×10^{-1}	(2.49 %)	1.71×10^{-1}	(6.10 %)	0.82	(9.61 %)
		^{44m}Sc	1.33×10^{-1}	(2.49 %)	1.68×10^{-1}	(6.50 %)	0.79	(9.87 %)
		^{46}Sc	1.10×10^{-1}	(1.93 %)	1.96×10^{-1}	(3.90 %)	0.56	(8.24 %)
		^{47}Sc	2.25×10^{-1}	(1.82 %)	4.53×10^{-1}	(6.45 %)	0.50	(9.69 %)
		^{48}V	1.68×10^{0}	(1.79 %)	1.67×10^{0}	(2.10 %)	1.00	(7.52 %)
		^{51}Cr	1.22×10^{2}	(1.11 %)	7.12×10^{1}	(4.80 %)	1.71	(8.56 %)
		^{52}Mn	1.72×10^{0}	(2.02 %)	2.21×10^{0}	(1.80 %)	0.78	(7.50 %)
		^{54}Mn	1.10×10^{0}	(1.58 %)	1.40×10^{0}	(3.25 %)	0.79	(7.88 %)
		^{56}Co	2.69×10^{-1}	(2.55 %)	3.20×10^{-1}	(3.15 %)	0.84	(8.09 %)
		^{57}Co	2.91×10^{-1}	(2.74 %)	3.63×10^{-1}	(5.40 %)	0.80	(9.26 %)
		^{57}Ni	8.17×10^{-2}	(2.23 %)	9.84×10^{-2}	(12.50 %)	0.83	(14.50 %)
		^{58}Co	2.27×10^{0}	(1.77 %)	2.37×10^{0}	(3.15 %)	0.96	(7.88 %)
		^{59}Fe	1.52×10^{0}	(1.15 %)	9.24×10^{-1}	(3.65 %)	1.65	(7.98 %)
		^{60}Co	1.68×10^{0}	(1.19 %)	1.03×10^{0}	(2.30 %)	1.63	(7.46 %)
		LL	4.04×10^{1}	(0.70 %)	3.78×10^{1}	(1.43 %)	1.07	(7.18 %)
	Kovar	^{47}Sc	7.59×10^{-2}	(3.88 %)	2.16×10^{-1}	(70.20 %)	0.35	(70.65 %)
		^{51}Cr	2.96×10^{0}	(2.25 %)	3.93×10^{0}	(11.00 %)	0.75	(13.23 %)
		^{52}Mn	1.63×10^{0}	(2.57 %)	2.29×10^{0}	(3.20 %)	0.71	(8.11 %)
		^{54}Mn	8.45×10^{-1}	(2.27 %)	1.26×10^{0}	(7.25 %)	0.67	(10.33 %)
		^{56}Co	9.25×10^{-1}	(3.08 %)	1.08×10^{0}	(6.00 %)	0.86	(9.72 %)
		^{57}Co	1.16×10^{0}	(3.11 %)	1.57×10^{0}	(5.55 %)	0.74	(9.46 %)
		^{57}Ni	2.87×10^{-1}	(3.08 %)	3.15×10^{-1}	(18.30 %)	0.91	(19.83 %)
		^{58}Co	9.76×10^{0}	(2.46 %)	1.09×10^{1}	(3.40 %)	0.89	(8.16 %)
		^{59}Fe	1.49×10^{0}	(1.69 %)	1.26×10^{0}	(8.40 %)	1.19	(11.06 %)
		^{60}Co	1.08×10^{2}	(1.98 %)	5.81×10^{1}	(1.95 %)	1.87	(7.53 %)
		LL	1.12×10^{3}	(1.92 %)	6.21×10^{2}	(1.83 %)	1.80	(7.49 %)

5.2 Activation benchmark at LHCb

5.2.1 Introduction and motivation

Infrastructures, detector components, and electronics installed in the underground caverns of the LHC experiments are exposed to high-energy and mixed radiation fields and may therefore become radioactive after prolonged irradiation. As it was introduced in Section 2.4 and as it will be further discussed in Chapter 6, any material that leaves an area that is classified as a radiation area is subject to a radiological control which can range from a simple verification measurement to the full determination of the radionuclide inventory: the form of this control is defined in CERN operation rules in matter of radiation protection and depends on the expected levels of residual activation [105].

To help establishing a zoning for the radiological classification of components, several sets of activation samples of representative materials were installed in the LHCb experimental cavern (UX85B) [106]: a first batch of activation detectors was positioned before the start of Run 1, while a second batch was put in place in the middle of Run 2. These extensive sets of activation samples were retrieved during the past LS 2 and gamma spectroscopy was performed to determine the residual nuclide inventory. This set of data represented a unique and valuable opportunity to perform a benchmark of the FLUKA Monte Carlo simulation setup of the fluence conversion coefficients code directly in the complex conditions of an LHC experiment: indeed, prior to the present work, the gamma spectroscopy results had never been systematically compared with Monte Carlo calculations.

The benchmark here presented constitutes a study of non-negligible relevance since it allowed to build the analysis tools necessary for any future extensive activation campaign at the LHC experiments. Furthermore, based on the return of experience from this study, a large-scale activation campaign for ALICE, ATLAS, and CMS was also put in place for the upcoming shutdowns at CERN.

5.2.2 Overview of the activation samples

A total of 38 sets of activation samples are installed within the LHCb experimental cavern. The first 20 sets were installed prior to Run 1 and consist of aluminium, copper and steel disks of 2 cm diameter and 0.5 cm thickness: these are completed by a small cylindrical rod containing silver (approximately 0.5 cm diameter and 1 cm thickness), a small square plate containing lead (approximately 2 mm×2 cm×2 cm), and a small capacitor with tantalum impurities (approximately 0.5 cm).

During the Technical Stops of 2017, 18 additional sets were added. These new sets consist of copper and steel disks of 6 cm diameter and 0.5 cm thickness, aluminium disks of 6 cm diameter and 1.5 cm thickness, and small kovar disks of 4 cm diameter and 0.1 cm thickness. The samples in copper and the two types of steel are similar to those that have been used in the activation benchmarks at the CSBF (Section 5.1.3) and CHARM (Section 5.1.4).

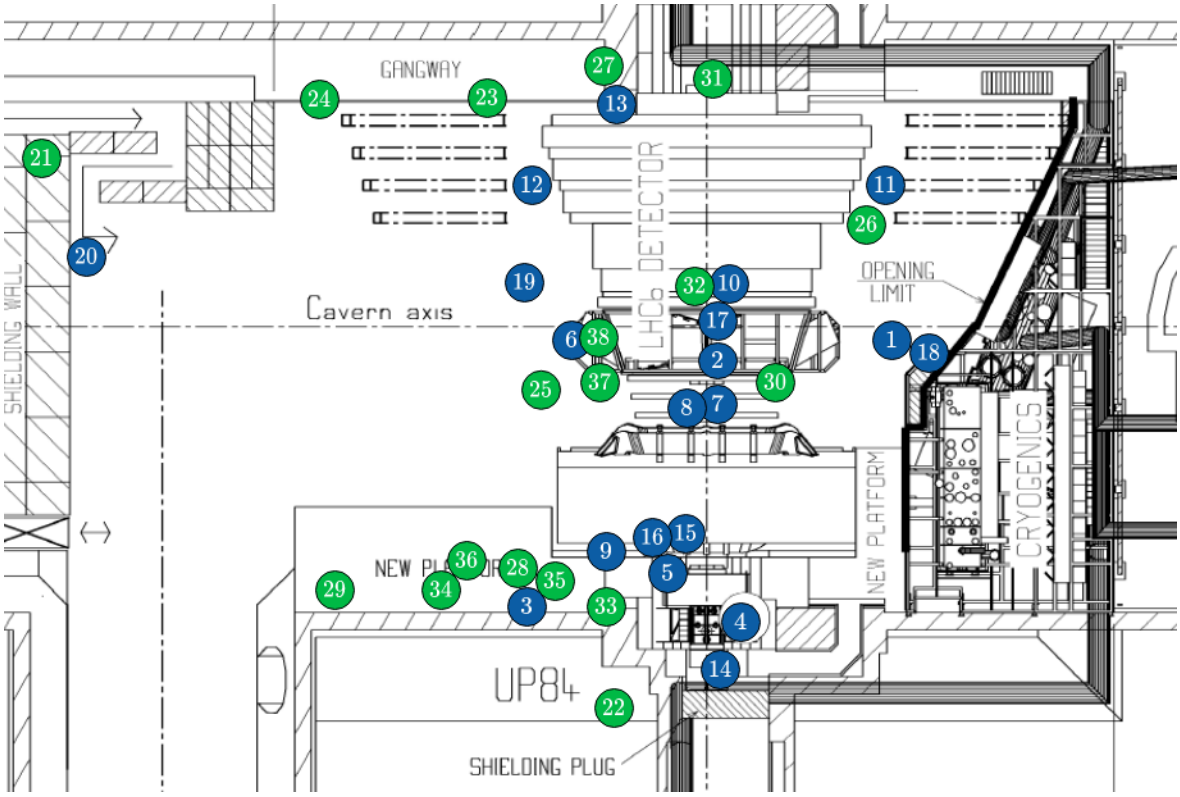

Figure 5.17: Top view of the qualitative location of the various sets of activation samples in the LHCb experimental cavern. Samples installed prior to Run 1 are indicated in blue, while samples installed during Run 2 are indicated in green.

The locations of the samples were chosen in order to have them close to equipment that is likely to be removed for maintenance [106]. An overview of their positioning is offered in figure 5.17 where the samples sets initially installed are indicated in blue, while the ones subsequently placed are indicated in green. This scheme is only qualitative since the samples are not placed at beam height, but in the vertical direction and at few or several meters from the beam axis: the only exception is set number 14 which is placed very close to the beam pipe and upstream the VELO detector. This choice is in line with the need of maintaining the material budget in the acceptance of the spectrometer as low as reasonably possible. It is important to note that sample set 22 is located in a side gallery that technically belongs to the LHC machine. All the samples are labelled for easier tracing and have been weighted with a precision scale having a resolution of 1 mg. A summary table describing the samples is given in Appendix B.1.

Aluminium, copper, and steel samples represent common materials used in detector components and infrastructures, while the other materials in the initially installed sets were mostly added for qualitative considerations on the activation of critical electronic equipment. Some spare aluminium, copper and steel samples were sent to an external contractor for chemical and radioanalytical analysis during the past LS 2 and the obtained elemental mass fractions for the compound material compositions are reported in table 5.10. It is important to mention that the samples that were sent for analysis

Aluminium	Density: 2.7 g/cm^3 (0.02 %)				
Element	**Mass fraction [%]**	**Element**	**Mass fraction [%]**	**Element**	**Mass fraction [%]**
Al	96.95	Fe	5.33×10^{-1}	Zn	1.01×10^{-1}
Mg	1.19	Cr	1.64×10^{-1}	Si	7.20×10^{-2}
Mn	0.83	Cu	1.12×10^{-1}	Ti	4.21×10^{-2}

Steel	Density: 7.95 g/cm^3 (0.02 %)				
Element	**Mass fraction [%]**	**Element**	**Mass fraction [%]**	**Element**	**Mass fraction [%]**
Fe	67.96	Mo	2.97×10^{-1}	Ca	5.19×10^{-3}
Cr	17.68	Si	2.37×10^{-1}	Al	3.01×10^{-3}
Ni	8.43	P	1.98×10^{-1}	Na	6.49×10^{-4}
V	2.98	Co	1.95×10^{-1}	Mg	5.02×10^{-4}
Mn	1.53	W	4.23×10^{-2}		
Cu	0.41	S	3.96×10^{-2}		

Kovar	Density: 8.24 g/cm^3 (0.02 %)				
Element	**Mass fraction [%]**	**Element**	**Mass fraction [%]**	**Element**	**Mass fraction [%]**
Fe	52.59	Mn	6.28×10^{-1}	Mo	8.02×10^{-2}
Ni	29.48	Cr	2.61×10^{-1}		
Co	16.73	Cu	2.32×10^{-1}		

Copper	Density: 8.96 g/cm^3 (0.02 %)				
Element	**Mass fraction [%]**	**Element**	**Mass fraction [%]**	**Element**	**Mass fraction [%]**
Cu	99.92	Zn	3.39×10^{-4}	Hg	4.71×10^{-6}
S	1.41×10^{-1}	Pb	7.11×10^{-5}	Cd	7.84×10^{-7}
Si	1.66×10^{-3}	Bi	4.89×10^{-5}		

Table 5.10: Measured density (and relative uncertainty) and expected material composition of the aluminium, steel, and copper activation samples installed in LHCb.

were large samples of the same kind as those installed during Run 2: it is almost certain that the Run 2 samples were laser-cut from metallic sheets produced in a different batch than those of the smaller samples placed prior to Run 1. Despite this, it is still reasonable to assume that the material compositions are very similar, if not equal for what concerns the elements with the highest mass fractions. As far as the samples that are representative of electronic components are concerned (rods with silver, plates with lead, and capacitors with tantalum), no non-irradiated spares were available and no chemical analysis could be performed: owing to the fact that the activation in this components is dominated by silver, lead, bismuth, and tantalum impurities but more precise information on their mass fractions is not available, they were excluded from the systematic comparison discussed in the following sections.

The various sets of activation samples were retrieved from the LHCb experimental cavern during LS 2 to be analysed with a HPGe detector. Even excluding some of the samples for the reason discussed above[7], a total of 132 samples had to be measured:

[7]The rods with silver, the plates with lead, and the capacitors with tantalum were in any case analysed with the HPGe detector: it is because of the more qualitative analysis results that they were excluded from the final comparison.

considering the primary and operational need of obtaining the residual radionuclide inventory for establishing a radiological zoning, the availability of the measuring device, and the number of samples, a counting time of 1 hour had to be chosen as a reasonable compromise.

5.2.3 FLUKA Monte Carlo simulations

Monte Carlo calculations were performed with the FLUKA Monte Carlo code[8]. This section illustrates the main features and updates of the simulation input file and geometry, presents the main settings, and describes the irradiation conditions.

The simulation input file

The FLUKA simulation input file for the Phase I LHCb detector configuration was initially received from the LHCb Radiation Simulation Working Group. To allow compatibility with the latest released versions of the FLUKA code, an extensive work was carried out to remove legacy statements both in the input file and the FORTRAN routines needed to run the calculation. As described in the following paragraphs, the simulation settings were optimized for activation calculations and tuned to best match the run conditions.

The activation samples installed in 2009 were also exposed to the radiation environment caused by proton-proton collisions at 7 TeV and 8 TeV centre of mass energy. Considering that the first two years of irradiation (2011 and 2012) give a small contribution to the activity levels remaining in LS 2 with respect to the full Run 2 irradiation, it was opted to set an energy of 6.5 TeV for the two colliding beams in the source settings, thus allowing to reduce the number of simulations to be performed.

Referring to the local coordinate system described in Section 1.3[9], collisions in LHCb occurred in the horizontal plane for the whole Run 2: owing to the small crossing angle and following the convention for which the first and second beam circulate respectively clockwise and anti-clockwise in the LHC machine, the two beams collide pointing outwards the LHC ring. From a practical point of view, this means that the angle to be used in the FLUKA source settings to describe the collision plane is 180° instead of the default 0°.

The beam half-crossing angle depends on the running conditions and is the sum of an "external" half-crossing angle of 250 µrad [107] and of an "internal" half-crossing angle of ± 135 µrad [107] depending on whether the LHCb main dipole has a positive or negative polarity respectively. Following the LHCb convention [30], the polarity is positive/negative if the dipole magnetic field is along the positive/negative direction of the y-axis.

[8]The calculations employed the code version 4-2.2 as hosted by the FLUKA.CERN Collaboration

[9]The origin of the right-handed local coordinate system is the IP, the $x-$axis points from the IP towards the centre of the LHC ring, the $y-$axis points from the IP upwards, and the $z-$axis, whose orientation is determined in relation to the other two, lies on the beam-pipe axis

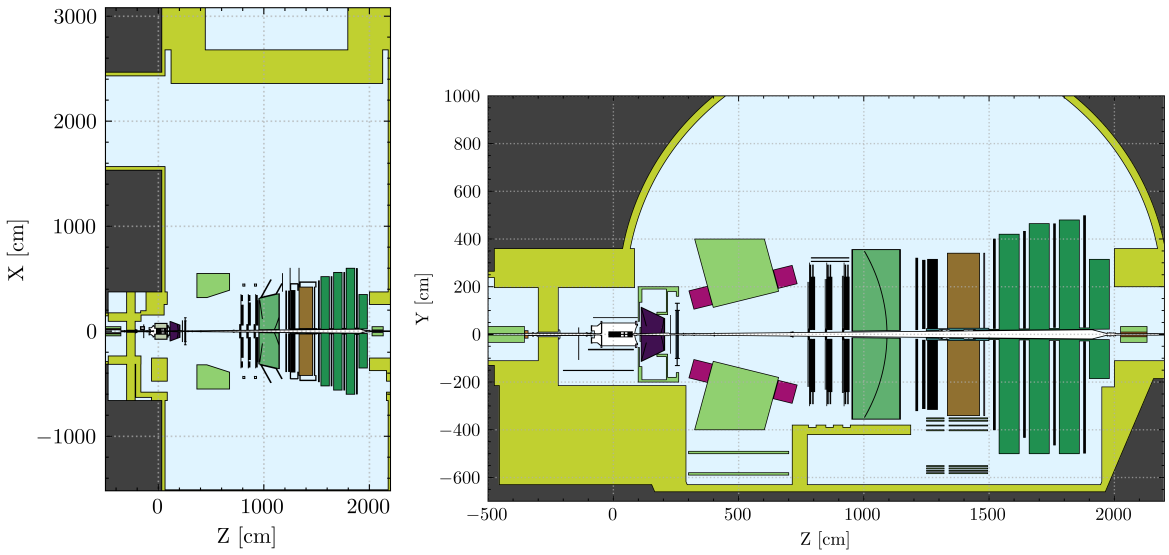

(a) (b)

Figure 5.18: Updated FLUKA simulation geometry of the LHCb experimental cavern and Phase I detector configuration: (a) horizontal cut; (b) vertical cut.

As far as the simulation geometry is concerned, legacy bodies were substituted with infinite planes and the concerned regions were automatically updated with FLAIR, the FLUKA Advanced Interface. Several elements of the UX85B experimental cavern were included based on engineering drawings with the aim of better describing the neutron radiation environment of the activation samples placed closest to the walls and shielding elements. The notable additions encompass the addition of the PX84 shaft, of service passages, of the shielding wall between the underground caverns UX85A and UX85B with its access maze, and the revision of the shape of the experimental cavern side walls. No modifications were made to the geometry implementation of the LHCb sub-detectors. The horizontal and vertical cuts of the FLUKA simulation geometry are shown in figure 5.18: the coordinate system used in FLUKA and displayed in figure 5.18 corresponds to the one conventionally adopted by the LHC experiments (see Section 1.3 or the previous footnote).

An important aspect of the Monte Carlo simulations is connected to the transport of particles in the presence of a magnetic field. Dedicated FORTRAN routines were modified so that the magnetic field maps for the two polarities of the LHCb dipole would be treated as auxiliary simulation files and read at initialization. The initializing routine is controlled by a dedicated FLUKA card which also allows to pass some parameters during the call: the routine was adjusted so that the magnetic field configuration could be selected by the user directly from the input file in a less error-prone way, instead of having the chosen magnet polarity hard-coded in the FORTRAN code. This allowed also to automatically select the polarity of the upstream and downstream dipoles (compensators) based on the polarity of the LHCb main dipole.

The general transport settings were optimized for activation calculations: all particles were transported down to 1 MeV with the exception of neutrons which were

followed down to thermal energies (0.01 meV). For some of the samples, for instance those located close to the beamline such as the set 14 upstream of the VELO, photonuclear reactions may give a contribution: therefore photons (and by consequence electrons and positrons for consistency) were also transported down to 1 MeV, well below the typical thresholds for the giant dipole resonance mechanism.

Particle spectra were scored in correspondence of the locations where the sets of activation samples had been installed with the aim to then fold them with radionuclide production cross sections and computing residual activities using the information on the irradiation history and material composition. For the same simulation settings, two sets of calculations were performed, one for each magnetic field configuration: in each case, more than one million primary histories were simulated. Although not the main focus of the discussion, figure 5.19 shows three valuable examples of the particle fluence spectra estimated. Figure 5.19(a) and 5.19(b) show the spectra computed for the sample set 11 which is located laterally to the muon stations and for which the different magnet configuration is clearly significant. Figure 5.19(c), instead, represents the spectra scored in correspondence of the set 14 installed upstream of the VELO and close to the beam pipe: this plot allows to show the prominent contribution of charged hadrons and photons to the local radiation field.

Irradiation conditions

A key parameter in the computation of induced activity is the time dependent irradiation profile. Data for the instantaneous luminosity delivered at LHCb in proton-proton collisions from 2011 till the end of 2018 was extracted from the CERN Accelerator Logging Service and is shown in figure 5.20(a) with the corresponding trend of the integrated luminosity.

As it was introduced in the general description of LHCb (Section 1.3.4) and mentioned in the previous paragraphs, the polarity of the LHCb dipole is switched several times during operation and this impacts the activation of infrastructures. Albeit for first-order calculations it would be reasonable to assume a 50 %−50 % sharing of the run time between positive and negative polarity, it was opted to consider this aspect in more detail. The history of the magnet polarity as retrieved from the online LHCb Run Database [108] was employed to further refine the irradiation history. As an example, figure 5.20(b) shows the detail of the instantaneous luminosity delivered to LHCb in 2018 with an overlay of the magnet polarity in arbitrary units. With these additional pieces of information to filter the instantaneous luminosity data, two different data sets were produced, one for each magnet polarity, or equivalently one for each set of calculations.

Finally, with a procedure as the one described in Section 4.8 and taking into account the extensive cool-down from the end of irradiation, the luminosity data sets were binned to compute, for each time interval, an average instantaneous luminosity. A coarser binning was adopted for the first two years, while a more refined one was used for Run 2, in particular for the last periods of irradiation: the binning procedure resulted in a total of 59 irradiation periods. The corresponding average collision rate was computed

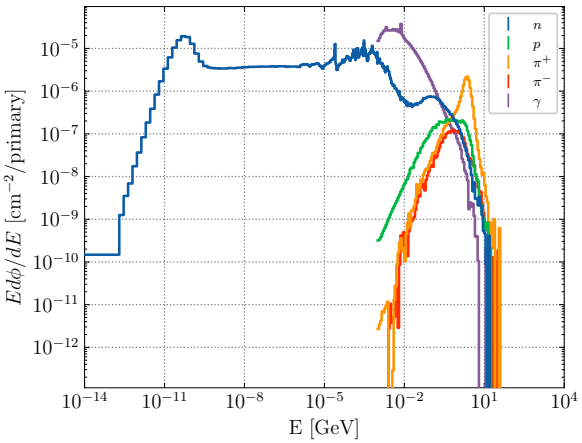

(a)

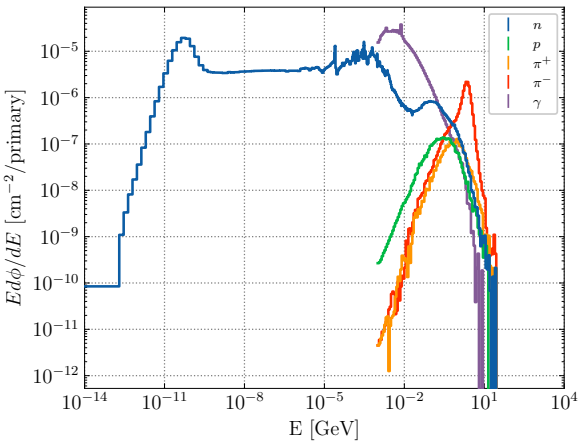

(b)

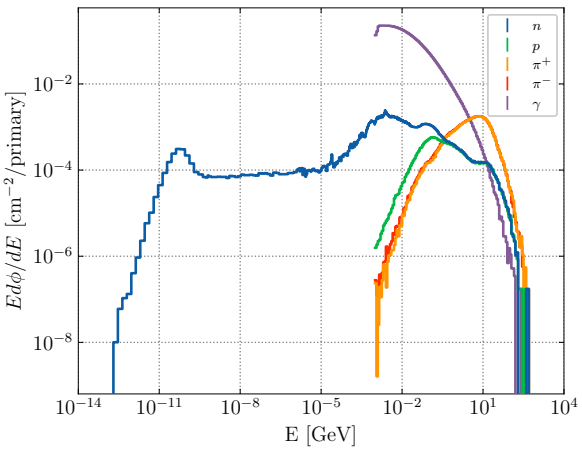

(c)

Figure 5.19: Example of particle spectra estimated with FLUKA for the samples installed in the LHCb experimental cavern: (a) and (b) are the spectra for the location of set 11 as in figure 5.17 for positive and negative polarity of the LHCb dipole; (c) particle spectra upstream the VELO and close to the beam pipe (set 14 as in figure 5.17) for positive polarity of the LHCb dipole.

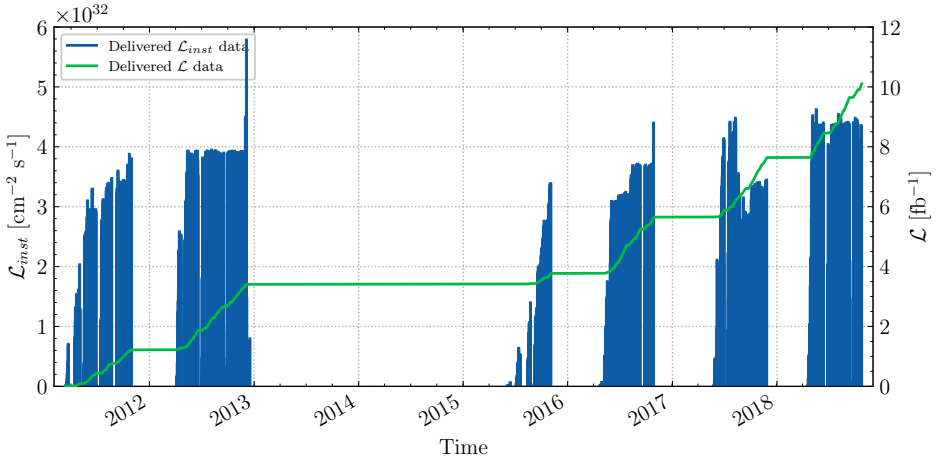

(a)

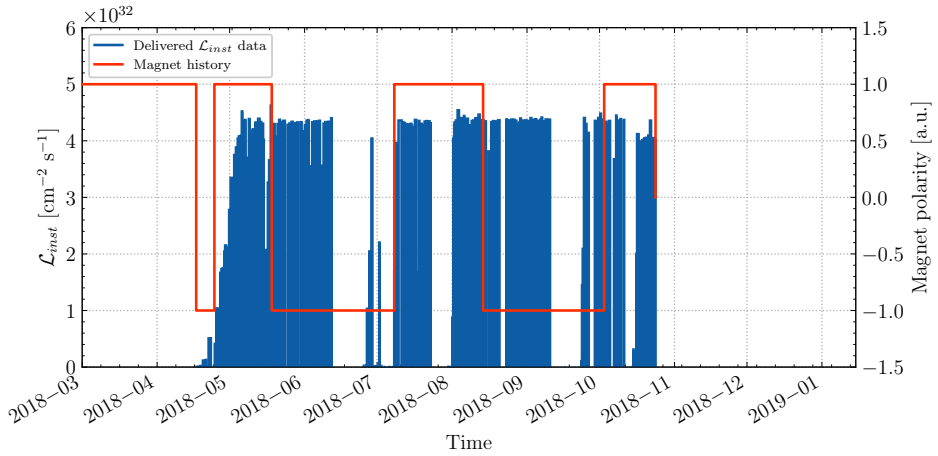

(b)

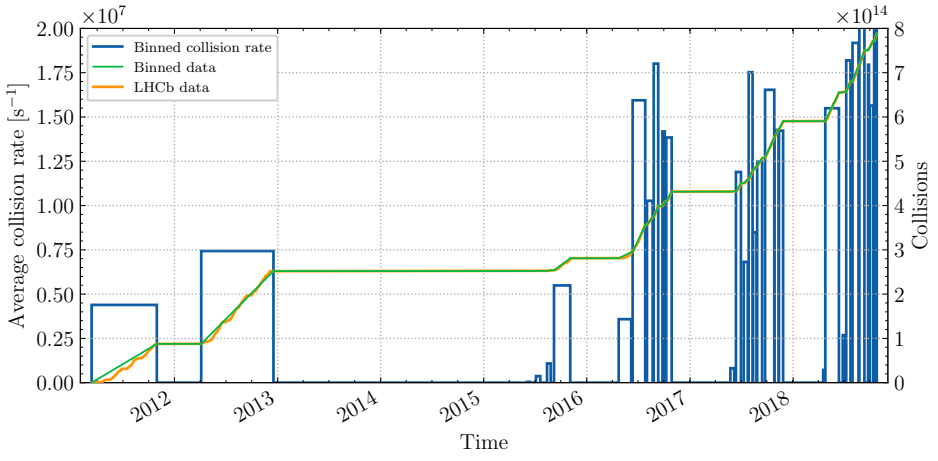

(c)

Figure 5.20: Instantaneous luminosity ($\mathcal{L}_{inst}$) delivered to LHCb and computed collision profile for the residual activity calculation: (a) delivered $\mathcal{L}_{inst}$ data as retrieved from the CERN Accelerator Logging Service; (b) detail of the delivered $\mathcal{L}_{inst}$ in 2018 with the change in magnet polarity in overlay; (c) collision profile resulting from the binning of the luminosity data. The marks on the abscissa always refer to the beginning of the year or of the month.

by multiplying the estimated average luminosity by the appropriate inelastic interaction cross section: the values of 72 mb, 75 mb, and 80 mb were used for the irradiation intervals of 2011, 2012 and Run 2 respectively. Figure 5.20(c) illustrates the resulting full collision profile (i.e. with no differentiation between the magnet polarities) and the corresponding trend of the integrated number of collisions: the dashed green line represents the number of collisions over time as directly computed by the raw un-binned data and allows to clearly illustrate that the obtained collision profiles are suitable and still well represent the reality of the irradiation conditions.

For the actual computation of radionuclide activities, the irradiation profile was adjusted for each set of activation samples according to its installation date: the irradiation intervals prior to the installation date of a given set were simply neglected. Finally, a specific cooling time was computed for each activation sample in virtue of the different analysis dates. The installation dates and the analysis times for each sample are listed, together with other pieces of information, in the overview table in Appendix B.1.

5.2.4 Discussion of the results

For each location and for each sample material, the radionuclide specific activities computed with FLUKA with the previously described methodology were compared with what experimentally measured. Although the discussion will be tailored to relevant radionuclides, the ratios between the computed and measured specific activities are reported in table 5.11 at the end of this chapter. As previously mentioned, samples for which the material composition is not known, or for which no activity was measured (set 20), or which belong to the LHC machine (set 22), are not reported in the table. In addition to the radionuclide specific activities, additional entries have been added for the multiples of Swiss clearance limits (LL).

The statistical uncertainty on the FLUKA simulation is contained below 0.1 % and thus is not reported in the table for brevity. The uncertainty shown for the experimental results accounts for the gamma spectroscopy only and is the major source of uncertainty in the final result. With respect to the previous benchmarks for which the whole experimental setup and geometry were simpler and easier to control, a detailed examination of the various systematic uncertainty contributions to the final result is not a feasible solution in this case. For each variation of a simulation parameter, for instance the density of a component, its size, or its positioning, a new set of calculations would have to be performed and the whole procedure would have become very quickly extremely CPU time-consuming. The only possible exception would be the systematic uncertainty on the luminosity which in any case would amount to few %: in any case, considering the magnitude of the gamma spectroscopy uncertainty, it won't significantly change the uncertainty on the final result either. For these reasons, the benchmark here discussed has to be intended as a benchmark for the whole simulation setup and simulation geometry.

For the discussion of the results, it could be fruitful to start by addressing the

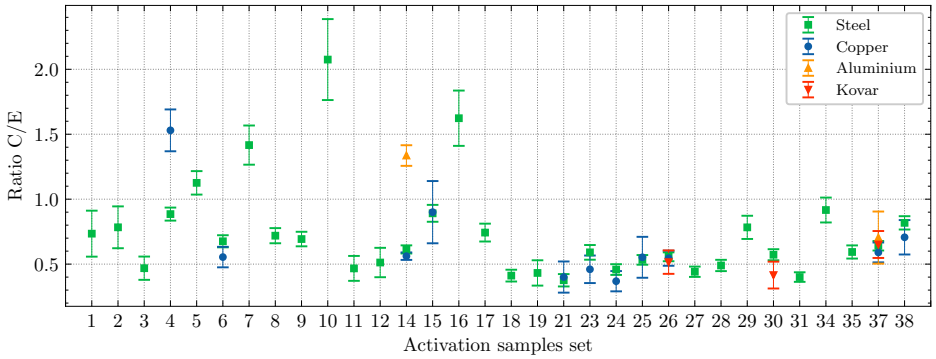

(a) ^{54}Mn in aluminium, copper, steel and kovar.

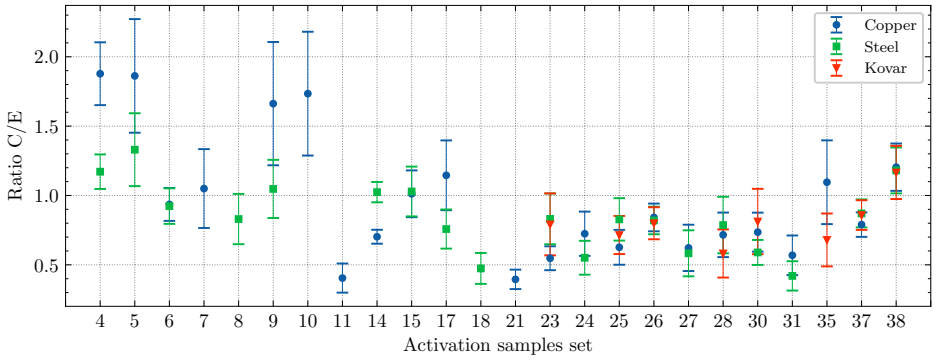

(b) ^{57}Co in copper, steel and kovar.

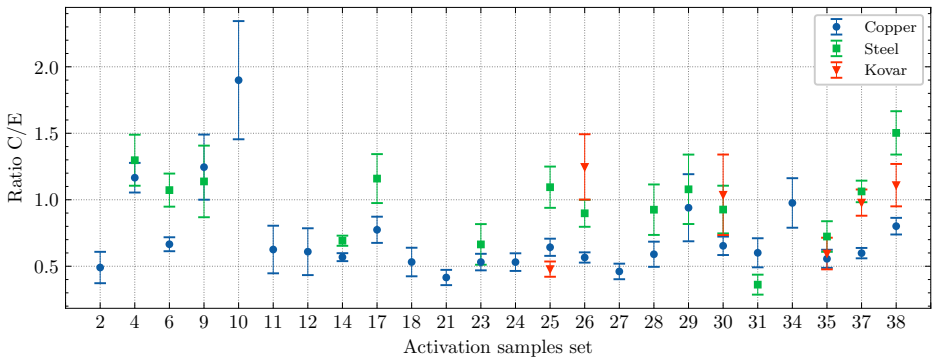

(c) ^{58}Co in copper, steel and kovar.

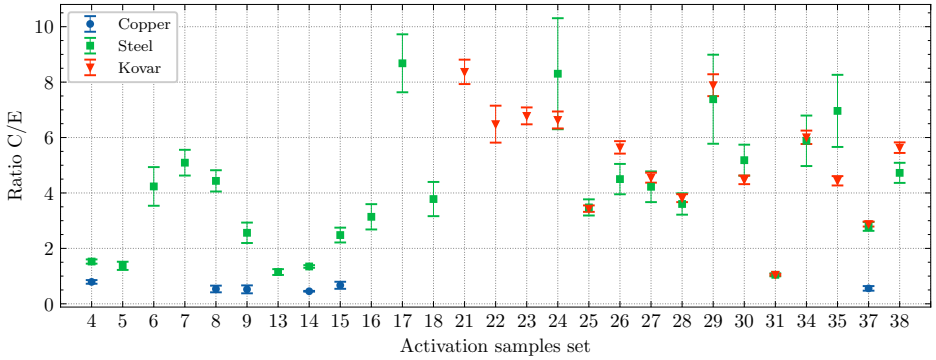

(d) ^{60}Co in copper, steel and kovar.

Figure 5.21: Ratio between the computed and measured specific activities in the aluminium, copper, steel and kovar samples installed in the LHCb experimental cavern for selected radionuclides.

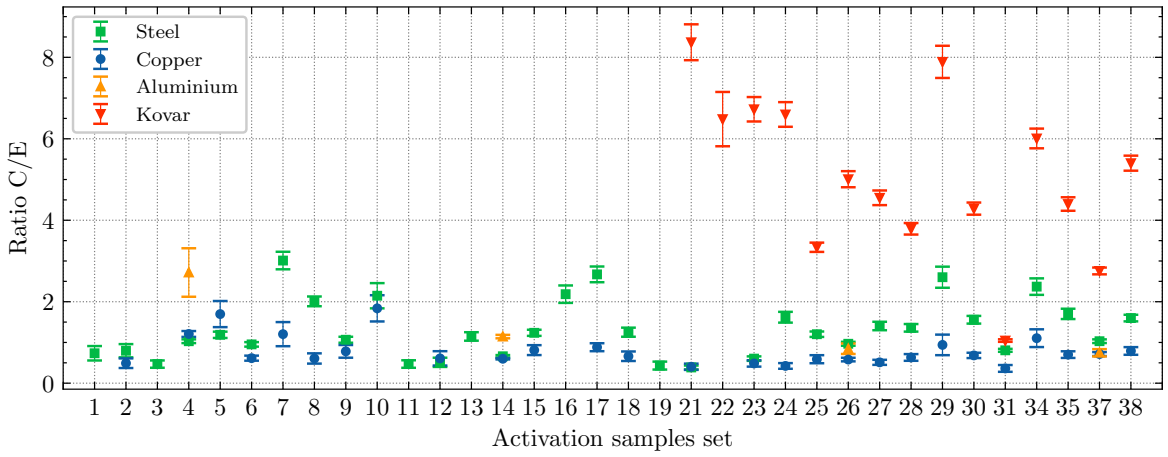

Figure 5.22: Ratio between the computed and measured multiples of Swiss clearance limits (LL) in the aluminium, copper, steel and kovar samples installed in the LHCb experimental cavern.

average agreement for each location. By computing the uncertainty averaged C/E ratios (ratio between the computed quantities and experimental results) over all the estimated radionuclides for each location, it is possible to observe that the average agreement with the experiments is in most cases within a factor that ranges from 0.7 to 2.2. The locations for which there is an overall larger discrepancy are those at the balconies in the proximity of the caver walls (for instance locations 29, 32, 33, 34 and 35) and for which the simulation geometry is less refined: in those cases, the simulation still tends to globally overestimate the results (C/E $>$ 1.0) by a factor ranging from 2.2 to 4.0 (5.3 for location 35).

It is then very useful to look in more detail at some relevant radionuclides: for an easier discussion, figure 5.21 offers a plot of the ratios between the computed and measured specific activities as reported in table 5.11 for ^{54}Mn, ^{57}Co, ^{58}Co, and ^{60}Co in aluminium, steel, copper and kovar samples, while figure 5.22 for the multiples of Swiss clearance limits (LL).

For ^{57}Co, ^{58}Co, ^{54}Mn in the steel, kovar and copper samples the agreement is in general between a factor 0.5 and 1.2, and, with very few exceptions, up to 2.0: the FLUKA calculations for LHCb have a general tendency to slightly underestimate these radionuclides for which the average C/E ratios settle respectively around 0.81, 0.71 and 0.65 respectively. This trend is in line with that observed at CHARM (see Section 5.1.4).

As it was also observed in the benchmarks of Section 5.1.3 and 5.1.4, the calculated specific activity of ^{60}Co in steel and kovar tends to be very conservative with differences on average between a factor 2.0 and 8.0 depending on the location. One of the reasons for this discrepancy was already pointed out and additional independent chemical analyses would be needed to refine the material composition of the samples.

The simulation geometry and material description are of the utmost importance and, as already remarked, they were much more difficult to control or implement in de-

tail in this case with respect to the ones previously analysed. Therefore, an additional source of discrepancy could reside in the geometry implementation of some components, in particular of materials with low atomic number, which may be incomplete or incorrect: this greatly affects the behaviour of thermal neutrons which are largely responsible for the production of ^{60}Co. In support to this point, for the locations which are almost in sight of the IP and for which the thermal part of the neutron spectrum is of smaller prominence such as locations 4, 5, and 14, the difference is indeed below 2.0 albeit being still conservative.

Finally, it is important to consider the overall predictions for the multiples of *LL*, which take into account the radiological relevance of each radionuclide in the considered material. Owing to the fact that ^{54}Mn, ^{57}Co, ^{58}Co, and ^{60}Co are among the isotopes of higher radiological relevance, the previously discussed trends are reflected in that of the multiples of Swiss clearance limits. For aluminium, copper, and steel samples the agreement is within a factor of 0.5 to 2.0 in most cases, while for kovar higher discrepancies are observed due to the overestimation of ^{60}Co.

In conclusion, the present benchmark has given valuable results and has illustrated the feasibility of a large-scale comparison between FLUKA Monte Carlo simulations and experimental measurements even in very complex conditions such as those of the LHC experiments. Based on the know-how and the code developed for this benchmark, large-scale activation campaigns were prepared and then put in place for CMS, ATLAS and ALICE: these have the twofold objective of allowing the establishment of a material-based radiological zoning for the upcoming shutdowns, and of assessing the overall goodness of the predictions of the radiation environment from Monte Carlo calculations.

Table 5.11: Summary of the computed and measured activities in the activation samples installed in the LHCb experimental cavern. Samples for which the material composition is not known or for which no activity was found above the minimum detectable activity are not reported in the table.

* The statistical uncertainty is below 0.1 % and thus not reported.
† Only gamma spectroscopy uncertainty is reported.
‡ Contributions from additional systematic uncertainty sources have been accounted for as discussed.

Location	Material	Radionuclide	FLUKA*	Experiment (Unc. %)†		C/E Ratio (Unc. %)‡	
1	Steel	^{54}Mn	2.01×10^{-2}	2.73×10^{-2}	(24.10 %)	0.73	(24.10 %)
		LL	2.01×10^{-1}	2.73×10^{-1}	(24.10 %)	0.73	(24.10 %)
2	Copper	^{58}Co	1.20×10^{-2}	2.46×10^{-2}	(24.05 %)	0.49	(24.05 %)
		LL	1.20×10^{-2}	2.46×10^{-2}	(24.05 %)	0.49	(24.05 %)
	Steel	^{51}Cr	5.76×10^{-1}	2.00×10^{-1}	(24.02 %)	2.88	(24.02 %)
		^{54}Mn	2.44×10^{-2}	3.12×10^{-2}	(20.56 %)	0.78	(20.56 %)
		LL	2.50×10^{-1}	3.14×10^{-1}	(20.43 %)	0.80	(20.43 %)
3	Steel	^{54}Mn	1.27×10^{-2}	3.21×10^{-2}	(19.13 %)	0.40	(19.13 %)
		LL	1.27×10^{-1}	3.21×10^{-1}	(19.13 %)	0.40	(19.13 %)
28	Copper	^{57}Co	2.26×10^{-3}	3.52×10^{-3}	(22.42 %)	0.64	(22.42 %)
		^{58}Co	3.57×10^{-3}	7.09×10^{-3}	(16.03 %)	0.50	(16.03 %)
		LL	5.83×10^{-3}	1.06×10^{-2}	(13.04 %)	0.55	(13.04 %)
	Steel	^{51}Cr	1.13×10^{-1}	4.20×10^{-2}	(25.66 %)	2.68	(25.66 %)

Table 5.11 (continued)

Location	Material	Radionuclide	FLUKA*	Experiment (Unc. %)†		C/E Ratio (Unc. %)‡	
		^{54}Mn	8.96×10^{-3}	2.16×10^{-2}	(8.88 %)	0.41	(8.88 %)
		^{57}Co	2.66×10^{-3}	3.87×10^{-3}	(25.91 %)	0.69	(25.91 %)
		^{58}Co	5.36×10^{-3}	6.09×10^{-3}	(20.51 %)	0.88	(20.51 %)
		^{60}Co	3.15×10^{-2}	8.56×10^{-3}	(10.71 %)	3.68	(10.71 %)
		LL	4.14×10^{-1}	3.12×10^{-1}	(6.84 %)	1.33	(6.84 %)
	Kovar	^{57}Co	1.11×10^{-2}	2.19×10^{-2}	(29.83 %)	0.51	(29.83 %)
		^{58}Co	2.48×10^{-2}	2.99×10^{-2}	(31.78 %)	0.83	(31.78 %)
		^{60}Co	2.70×10^{0}	6.94×10^{-1}	(3.75 %)	3.89	(3.75 %)
		LL	2.70×10^{1}	6.99×10^{0}	(3.73 %)	3.87	(3.73 %)
4	Copper	^{54}Mn	1.29×10^{-1}	8.40×10^{-2}	(10.53 %)	1.53	(10.53 %)
		^{57}Co	2.84×10^{-1}	1.51×10^{-1}	(12.06 %)	1.88	(12.06 %)
		^{58}Co	1.09×10^{-1}	9.38×10^{-2}	(9.56 %)	1.17	(9.56 %)
		^{60}Co	6.94×10^{-2}	8.78×10^{-2}	(8.34 %)	0.79	(8.34 %)
		LL	2.37×10^{0}	1.96×10^{0}	(5.94 %)	1.21	(5.94 %)
	Steel	^{54}Mn	7.53×10^{-1}	8.51×10^{-1}	(5.66 %)	0.89	(5.66 %)
		^{57}Co	2.04×10^{-1}	1.74×10^{-1}	(10.62 %)	1.17	(10.62 %)
		^{58}Co	8.27×10^{-2}	6.37×10^{-2}	(14.78 %)	1.30	(14.78 %)
		^{60}Co	3.67×10^{-1}	2.41×10^{-1}	(5.00 %)	1.53	(5.00 %)
		LL	1.15×10^{1}	1.12×10^{1}	(4.46 %)	1.03	(4.46 %)
	Aluminium	^{22}Na	2.24×10^{-1}	8.23×10^{-2}	(21.90 %)	2.72	(21.90 %)
		LL	2.24×10^{0}	8.23×10^{-1}	(21.90 %)	2.72	(21.90 %)
5	Copper	^{57}Co	5.51×10^{-2}	2.96×10^{-2}	(21.99 %)	1.86	(21.99 %)
		^{58}Co	2.35×10^{-2}	1.67×10^{-2}	(35.01 %)	1.40	(35.01 %)
		LL	7.86×10^{-2}	4.63×10^{-2}	(18.90 %)	1.70	(18.90 %)
	Steel	^{54}Mn	1.97×10^{-1}	1.75×10^{-1}	(8.03 %)	1.13	(8.03 %)
		^{57}Co	5.32×10^{-2}	4.00×10^{-2}	(19.74 %)	1.33	(19.74 %)
		^{60}Co	7.70×10^{-2}	5.62×10^{-2}	(10.79 %)	1.37	(10.79 %)
		LL	2.79×10^{0}	2.35×10^{0}	(6.51 %)	1.19	(6.51 %)
6	Copper	^{54}Mn	2.95×10^{-2}	5.32×10^{-2}	(14.23 %)	0.55	(14.23 %)
		^{57}Co	6.94×10^{-2}	7.42×10^{-2}	(12.68 %)	0.94	(12.68 %)
		^{58}Co	1.06×10^{-1}	1.60×10^{-1}	(7.88 %)	0.67	(7.88 %)
		LL	4.71×10^{-1}	7.66×10^{-1}	(10.10 %)	0.61	(10.10 %)
	Steel	^{46}Sc	2.12×10^{-2}	3.20×10^{-2}	(16.42 %)	0.66	(16.42 %)
		^{51}Cr	6.52×10^{-1}	3.88×10^{-1}	(17.87 %)	1.68	(17.87 %)
		^{54}Mn	1.90×10^{-1}	2.82×10^{-1}	(6.90 %)	0.68	(6.90 %)
		^{57}Co	5.99×10^{-2}	6.49×10^{-2}	(13.88 %)	0.92	(13.88 %)
		^{58}Co	8.13×10^{-2}	7.58×10^{-2}	(11.60 %)	1.07	(11.60 %)
		^{60}Co	1.11×10^{-1}	2.63×10^{-2}	(16.47 %)	4.24	(16.47 %)
		LL	3.38×10^{0}	3.54×10^{0}	(5.82 %)	0.95	(5.82 %)
	Aluminium	^{22}Na	4.11×10^{-2}	2.89×10^{-2}	(46.96 %)	1.42	(46.96 %)
		LL	4.11×10^{-1}	2.89×10^{-1}	(46.96 %)	1.42	(46.96 %)
7	Copper	^{57}Co	3.09×10^{-2}	2.94×10^{-2}	(27.07 %)	1.05	(27.07 %)
		^{58}Co	1.52×10^{-2}	8.88×10^{-3}	(56.56 %)	1.72	(56.56 %)
		LL	4.61×10^{-2}	3.83×10^{-2}	(24.58 %)	1.20	(24.58 %)
	Steel	^{54}Mn	1.65×10^{-1}	1.17×10^{-1}	(10.65 %)	1.42	(10.65 %)
		^{57}Co	4.45×10^{-2}	1.74×10^{-2}	(37.85 %)	2.56	(37.85 %)
		^{60}Co	4.57×10^{-1}	8.96×10^{-2}	(9.11 %)	5.09	(9.11 %)
		LL	6.26×10^{0}	2.08×10^{0}	(7.15 %)	3.01	(7.15 %)
8	Copper	^{57}Co	2.41×10^{-2}	1.82×10^{-2}	(38.21 %)	1.33	(38.21 %)
		^{60}Co	9.82×10^{-3}	1.83×10^{-2}	(22.48 %)	0.54	(22.48 %)
		LL	1.22×10^{-1}	2.02×10^{-1}	(20.74 %)	0.61	(20.74 %)
	Steel	^{54}Mn	1.29×10^{-1}	1.79×10^{-1}	(8.11 %)	0.72	(8.11 %)
		^{57}Co	3.41×10^{-2}	4.11×10^{-2}	(21.83 %)	0.83	(21.83 %)
		^{58}Co	2.08×10^{-2}	1.95×10^{-2}	(31.72 %)	1.07	(31.72 %)
		^{60}Co	4.35×10^{-1}	9.80×10^{-2}	(8.65 %)	4.44	(8.65 %)

Table 5.11 (continued)

Location	Material	Radionuclide	FLUKA*	Experiment (Unc. %)†		C/E Ratio (Unc. %)‡	
		LL	5.69×10^{0}	2.83×10^{0}	(5.95 %)	2.01	(5.95 %)
9	Copper	^{57}Co	4.22×10^{-2}	2.54×10^{-2}	(26.73 %)	1.66	(26.73 %)
		^{58}Co	4.59×10^{-2}	3.68×10^{-2}	(19.67 %)	1.25	(19.67 %)
		^{60}Co	7.90×10^{-3}	1.52×10^{-2}	(27.40 %)	0.52	(27.40 %)
		LL	1.67×10^{-1}	2.14×10^{-1}	(19.98 %)	0.78	(19.98 %)
	Steel	^{54}Mn	1.17×10^{-1}	1.70×10^{-1}	(8.08 %)	0.69	(8.08 %)
		^{57}Co	3.48×10^{-2}	3.32×10^{-2}	(20.00 %)	1.05	(20.00 %)
		^{58}Co	4.05×10^{-2}	3.56×10^{-2}	(23.67 %)	1.14	(23.67 %)
		^{60}Co	1.08×10^{-1}	4.22×10^{-2}	(14.37 %)	2.56	(14.37 %)
		LL	2.33×10^{0}	2.19×10^{0}	(6.87 %)	1.07	(6.87 %)
10	Copper	^{57}Co	2.60×10^{-2}	1.50×10^{-2}	(25.73 %)	1.73	(25.73 %)
		^{58}Co	4.77×10^{-2}	2.51×10^{-2}	(23.40 %)	1.90	(23.40 %)
		LL	7.37×10^{-2}	4.01×10^{-2}	(17.53 %)	1.84	(17.53 %)
	Steel	^{51}Cr	1.22×10^{0}	2.72×10^{-1}	(17.30 %)	4.47	(17.30 %)
		^{54}Mn	1.10×10^{-1}	5.31×10^{-2}	(15.02 %)	2.07	(15.02 %)
		^{58}Co	7.71×10^{-2}	2.10×10^{-2}	(30.03 %)	3.67	(30.03 %)
		LL	1.19×10^{0}	5.55×10^{-1}	(14.42 %)	2.15	(14.42 %)
11	Copper	^{54}Mn	3.59×10^{-3}	8.17×10^{-3}	(53.64 %)	0.44	(53.64 %)
		^{57}Co	7.50×10^{-3}	1.85×10^{-2}	(25.95 %)	0.40	(25.95 %)
		^{58}Co	1.08×10^{-2}	1.73×10^{-2}	(28.60 %)	0.63	(28.60 %)
		LL	5.42×10^{-2}	1.18×10^{-1}	(37.76 %)	0.46	(37.76 %)
	Steel	^{51}Cr	3.54×10^{-1}	1.40×10^{-1}	(34.56 %)	2.53	(34.56 %)
		^{54}Mn	1.55×10^{-2}	3.32×10^{-2}	(20.52 %)	0.47	(20.52 %)
		^{58}Co	5.52×10^{-3}	1.56×10^{-2}	(32.87 %)	0.35	(32.87 %)
		LL	1.64×10^{-1}	3.49×10^{-1}	(19.58 %)	0.47	(19.58 %)
12	Copper	^{58}Co	9.27×10^{-3}	1.52×10^{-2}	(28.88 %)	0.61	(28.88 %)
		LL	9.27×10^{-3}	1.52×10^{-2}	(28.88 %)	0.61	(28.88 %)
	Steel	^{54}Mn	1.45×10^{-2}	2.84×10^{-2}	(22.08 %)	0.51	(22.08 %)
		LL	1.45×10^{-1}	2.84×10^{-1}	(22.08 %)	0.51	(22.08 %)
13	Steel	^{51}Cr	3.51×10^{-1}	2.38×10^{-1}	(24.21 %)	1.47	(24.21 %)
		^{60}Co	7.86×10^{-2}	6.86×10^{-2}	(9.11 %)	1.15	(9.11 %)
		LL	7.89×10^{-1}	6.88×10^{-1}	(9.08 %)	1.15	(9.08 %)
14	Copper	^{7}Be	8.16×10^{-1}	1.02×10^{0}	(21.56 %)	0.80	(21.56 %)
		^{22}Na	5.81×10^{-1}	4.03×10^{-1}	(6.15 %)	1.44	(6.15 %)
		^{46}Sc	9.47×10^{-1}	1.21×10^{0}	(4.16 %)	0.78	(4.16 %)
		^{51}Cr	1.23×10^{-1}	3.81×10^{-1}	(40.87 %)	0.32	(40.87 %)
		^{54}Mn	8.65×10^{0}	1.54×10^{1}	(5.13 %)	0.56	(5.13 %)
		^{56}Co	2.07×10^{0}	1.52×10^{0}	(2.78 %)	1.36	(2.78 %)
		^{57}Co	1.58×10^{1}	2.25×10^{1}	(7.14 %)	0.70	(7.14 %)
		^{58}Co	5.68×10^{0}	9.99×10^{0}	(5.27 %)	0.57	(5.27 %)
		^{59}Fe	6.05×10^{-2}	3.06×10^{-1}	(10.16 %)	0.20	(10.16 %)
		^{60}Co	3.09×10^{0}	6.83×10^{0}	(2.90 %)	0.45	(2.90 %)
		^{65}Zn	4.23×10^{-1}	1.21×10^{0}	(6.64 %)	0.35	(6.64 %)
		LL	1.79×10^{2}	2.99×10^{2}	(2.81 %)	0.60	(2.81 %)
	Steel	^{22}Na	1.02×10^{0}	6.55×10^{-1}	(5.34 %)	1.56	(5.34 %)
		^{46}Sc	1.82×10^{0}	2.92×10^{0}	(3.21 %)	0.62	(3.21 %)
		^{51}Cr	9.64×10^{-1}	1.52×10^{0}	(20.35 %)	0.64	(20.35 %)
		^{54}Mn	3.56×10^{1}	5.81×10^{1}	(5.11 %)	0.61	(5.11 %)
		^{56}Co	1.86×10^{0}	1.37×10^{0}	(2.99 %)	1.36	(2.99 %)
		^{57}Co	2.01×10^{1}	1.96×10^{1}	(7.15 %)	1.02	(7.15 %)
		^{58}Co	1.71×10^{0}	2.47×10^{0}	(5.52 %)	0.69	(5.52 %)
		^{60}Co	1.22×10^{0}	9.06×10^{-1}	(3.51 %)	1.35	(3.51 %)
		LL	4.37×10^{2}	6.61×10^{2}	(4.49 %)	0.66	(4.49 %)
	Aluminium	^{7}Be	2.36×10^{0}	1.91×10^{0}	(20.75 %)	1.23	(20.75 %)
		^{22}Na	1.45×10^{1}	1.30×10^{1}	(4.15 %)	1.12	(4.15 %)
		^{54}Mn	2.49×10^{0}	1.86×10^{0}	(5.94 %)	1.34	(5.94 %)

Table 5.11 (continued)

Location	Material	Radionuclide	FLUKA*	Experiment (Unc. %)†		C/E Ratio (Unc. %)‡	
		LL	1.70×10^{2}	1.49×10^{2}	(3.70 %)	1.14	(3.70 %)
15	Copper	^{54}Mn	2.48×10^{-2}	2.75×10^{-2}	(26.62 %)	0.90	(26.62 %)
		^{57}Co	6.19×10^{-2}	6.12×10^{-2}	(16.66 %)	1.01	(16.66 %)
		^{60}Co	1.70×10^{-2}	2.54×10^{-2}	(19.05 %)	0.67	(19.05 %)
		LL	4.80×10^{-1}	5.91×10^{-1}	(14.97 %)	0.81	(14.97 %)
	Steel	^{54}Mn	1.92×10^{-1}	2.15×10^{-1}	(7.30 %)	0.89	(7.30 %)
		^{57}Co	5.24×10^{-2}	5.09×10^{-2}	(17.44 %)	1.03	(17.44 %)
		^{60}Co	1.51×10^{-1}	6.07×10^{-2}	(10.78 %)	2.48	(10.78 %)
		LL	3.48×10^{0}	2.81×10^{0}	(6.07 %)	1.24	(6.07 %)
16	Steel	^{54}Mn	1.22×10^{-1}	7.52×10^{-2}	(13.11 %)	1.62	(13.11 %)
		^{57}Co	3.31×10^{-2}	1.06×10^{-2}	(56.52 %)	3.11	(56.52 %)
		^{60}Co	1.36×10^{-1}	4.32×10^{-2}	(14.54 %)	3.14	(14.54 %)
		LL	2.61×10^{0}	1.19×10^{0}	(9.80 %)	2.19	(9.80 %)
17	Copper	^{57}Co	2.52×10^{-2}	2.20×10^{-2}	(21.96 %)	1.15	(21.96 %)
		^{58}Co	4.10×10^{-2}	5.29×10^{-2}	(12.72 %)	0.77	(12.72 %)
		LL	6.61×10^{-2}	7.49×10^{-2}	(11.06 %)	0.88	(11.06 %)
	Steel	^{51}Cr	1.51×10^{0}	3.46×10^{-1}	(19.74 %)	4.36	(19.74 %)
		^{54}Mn	8.80×10^{-2}	1.18×10^{-1}	(9.25 %)	0.74	(9.25 %)
		^{57}Co	2.37×10^{-2}	3.13×10^{-2}	(18.59 %)	0.76	(18.59 %)
		^{58}Co	4.83×10^{-2}	4.17×10^{-2}	(15.87 %)	1.16	(15.87 %)
		^{60}Co	3.47×10^{-1}	4.00×10^{-2}	(12.05 %)	8.68	(12.05 %)
		LL	4.44×10^{0}	1.66×10^{0}	(7.23 %)	2.67	(7.23 %)
18	Copper	^{57}Co	1.40×10^{-2}	1.42×10^{-2}	(35.68 %)	0.99	(35.68 %)
		^{58}Co	1.90×10^{-2}	3.58×10^{-2}	(20.19 %)	0.53	(20.19 %)
		LL	3.31×10^{-2}	5.00×10^{-2}	(17.65 %)	0.66	(17.65 %)
	Steel	^{51}Cr	4.29×10^{-1}	1.13×10^{-1}	(39.19 %)	3.78	(39.19 %)
		^{54}Mn	3.10×10^{-2}	7.54×10^{-2}	(11.02 %)	0.41	(11.02 %)
		^{57}Co	9.77×10^{-3}	2.06×10^{-2}	(23.50 %)	0.47	(23.50 %)
		^{58}Co	1.32×10^{-2}	1.60×10^{-2}	(38.54 %)	0.82	(38.54 %)
		^{60}Co	9.78×10^{-2}	2.59×10^{-2}	(16.33 %)	3.78	(16.33 %)
		LL	1.32×10^{0}	1.05×10^{0}	(8.91 %)	1.25	(8.91 %)
19	Steel	^{54}Mn	1.61×10^{-2}	3.73×10^{-2}	(22.55 %)	0.43	(22.55 %)
		LL	1.61×10^{-1}	3.73×10^{-1}	(22.55 %)	0.43	(22.55 %)
21	Copper	^{54}Mn	8.18×10^{-4}	2.04×10^{-3}	(29.95 %)	0.40	(29.95 %)
		^{57}Co	1.94×10^{-3}	4.91×10^{-3}	(17.72 %)	0.40	(17.72 %)
		^{58}Co	3.17×10^{-3}	7.62×10^{-3}	(13.82 %)	0.42	(13.82 %)
		LL	1.33×10^{-2}	3.30×10^{-2}	(19.02 %)	0.40	(19.02 %)
	Steel	^{51}Cr	9.67×10^{-2}	2.20×10^{-2}	(39.33 %)	4.40	(39.33 %)
		^{54}Mn	4.65×10^{-3}	1.24×10^{-2}	(12.66 %)	0.38	(12.66 %)
		^{57}Co	1.37×10^{-3}	2.62×10^{-3}	(36.64 %)	0.52	(36.64 %)
		LL	4.88×10^{-2}	1.27×10^{-1}	(12.40 %)	0.39	(12.40 %)
	Kovar	^{60}Co	2.17×10^{0}	2.60×10^{-1}	(5.26 %)	8.37	(5.26 %)
		LL	2.17×10^{1}	2.60×10^{0}	(5.26 %)	8.37	(5.26 %)
23	Copper	^{54}Mn	1.96×10^{-3}	4.26×10^{-3}	(23.04 %)	0.46	(23.04 %)
		^{57}Co	4.50×10^{-3}	8.22×10^{-3}	(15.74 %)	0.55	(15.74 %)
		^{58}Co	5.94×10^{-3}	1.12×10^{-2}	(11.70 %)	0.53	(11.70 %)
		LL	3.01×10^{-2}	6.20×10^{-2}	(16.11 %)	0.48	(16.11 %)
	Steel	^{51}Cr	1.01×10^{-1}	1.28×10^{-2}	(44.65 %)	7.85	(44.65 %)
		^{54}Mn	1.05×10^{-2}	1.77×10^{-2}	(9.58 %)	0.59	(9.58 %)
		^{57}Co	3.71×10^{-3}	4.46×10^{-3}	(22.02 %)	0.83	(22.02 %)
		^{58}Co	3.31×10^{-3}	4.98×10^{-3}	(23.00 %)	0.66	(23.00 %)
		LL	1.13×10^{-1}	1.87×10^{-1}	(9.12 %)	0.60	(9.12 %)
	Kovar	^{57}Co	1.53×10^{-2}	1.94×10^{-2}	(28.21 %)	0.79	(28.21 %)
		^{58}Co	1.91×10^{-2}	1.67×10^{-2}	(46.45 %)	1.14	(46.45 %)
		^{60}Co	2.49×10^{0}	3.67×10^{-1}	(4.50 %)	6.78	(4.50 %)

Table 5.11 (continued)

Location	Material	Radionuclide	FLUKA*	Experiment (Unc. %)†		C/E Ratio (Unc. %)‡	
		LL	2.49×10^{1}	3.70×10^{0}	(4.46 %)	6.72	(4.46 %)
24	Copper	^{54}Mn	1.74×10^{-3}	4.72×10^{-3}	(21.17 %)	0.37	(21.17 %)
		^{57}Co	3.85×10^{-3}	5.32×10^{-3}	(22.04 %)	0.72	(22.04 %)
		^{58}Co	4.94×10^{-3}	9.30×10^{-3}	(12.49 %)	0.53	(12.49 %)
		LL	2.62×10^{-2}	6.18×10^{-2}	(16.39 %)	0.42	(16.39 %)
	Steel	^{51}Cr	9.73×10^{-2}	3.44×10^{-2}	(29.87 %)	2.83	(29.87 %)
		^{54}Mn	8.65×10^{-3}	1.89×10^{-2}	(9.00 %)	0.46	(9.00 %)
		^{57}Co	2.84×10^{-3}	5.16×10^{-3}	(22.15 %)	0.55	(22.15 %)
		^{58}Co	3.09×10^{-3}	3.26×10^{-3}	(35.29 %)	0.95	(35.29 %)
		^{60}Co	2.82×10^{-2}	3.39×10^{-3}	(24.13 %)	8.30	(24.13 %)
		LL	3.75×10^{-1}	2.32×10^{-1}	(8.18 %)	1.62	(8.18 %)
	Aluminium	^{22}Na	1.72×10^{-3}	2.56×10^{-3}	(43.09 %)	0.67	(43.09 %)
		LL	1.72×10^{-2}	2.56×10^{-2}	(43.09 %)	0.67	(43.09 %)
	Kovar	^{58}Co	1.65×10^{-2}	2.29×10^{-2}	(36.83 %)	0.72	(36.83 %)
		^{60}Co	2.41×10^{0}	3.64×10^{-1}	(4.61 %)	6.63	(4.61 %)
		LL	2.42×10^{1}	3.66×10^{0}	(4.59 %)	6.60	(4.59 %)
25	Copper	^{54}Mn	1.88×10^{-3}	3.39×10^{-3}	(28.51 %)	0.55	(28.51 %)
		^{57}Co	6.34×10^{-3}	1.01×10^{-2}	(20.06 %)	0.63	(20.06 %)
		^{58}Co	9.99×10^{-3}	1.55×10^{-2}	(10.05 %)	0.64	(10.05 %)
		LL	3.51×10^{-2}	5.96×10^{-2}	(16.80 %)	0.59	(16.80 %)
	Steel	^{51}Cr	1.66×10^{-1}	3.86×10^{-2}	(28.40 %)	4.31	(28.40 %)
		^{54}Mn	2.30×10^{-2}	4.32×10^{-2}	(6.98 %)	0.53	(6.98 %)
		^{57}Co	6.37×10^{-3}	7.70×10^{-3}	(18.46 %)	0.83	(18.46 %)
		^{58}Co	1.16×10^{-2}	1.06×10^{-2}	(14.18 %)	1.09	(14.18 %)
		^{60}Co	4.46×10^{-2}	1.28×10^{-2}	(8.38 %)	3.48	(8.38 %)
		LL	6.96×10^{-1}	5.79×10^{-1}	(5.54 %)	1.20	(5.54 %)
	Kovar	^{54}Mn	2.01×10^{-2}	2.58×10^{-2}	(45.61 %)	0.78	(45.61 %)
		^{57}Co	2.68×10^{-2}	3.75×10^{-2}	(19.22 %)	0.71	(19.22 %)
		^{58}Co	5.47×10^{-2}	1.14×10^{-1}	(11.99 %)	0.48	(11.99 %)
		^{60}Co	3.83×10^{0}	1.11×10^{0}	(3.38 %)	3.43	(3.38 %)
		LL	3.85×10^{1}	1.15×10^{1}	(3.41 %)	3.34	(3.41 %)
26	Copper	^{54}Mn	7.15×10^{-3}	1.31×10^{-2}	(10.65 %)	0.55	(10.65 %)
		^{57}Co	1.64×10^{-2}	1.95×10^{-2}	(11.87 %)	0.84	(11.87 %)
		^{58}Co	2.18×10^{-2}	3.85×10^{-2}	(6.81 %)	0.57	(6.81 %)
		LL	1.10×10^{-1}	1.89×10^{-1}	(7.61 %)	0.58	(7.61 %)
	Steel	^{46}Sc	4.89×10^{-3}	7.26×10^{-3}	(12.29 %)	0.67	(12.29 %)
		^{51}Cr	1.45×10^{-1}	6.21×10^{-2}	(17.35 %)	2.33	(17.35 %)
		^{54}Mn	3.71×10^{-2}	6.67×10^{-2}	(6.15 %)	0.56	(6.15 %)
		^{56}Co	5.14×10^{-3}	3.49×10^{-3}	(24.86 %)	1.47	(24.86 %)
		^{57}Co	1.36×10^{-2}	1.66×10^{-2}	(12.12 %)	0.82	(12.12 %)
		^{58}Co	1.28×10^{-2}	1.43×10^{-2}	(11.30 %)	0.90	(11.30 %)
		^{60}Co	3.58×10^{-2}	7.95×10^{-3}	(12.16 %)	4.50	(12.16 %)
		LL	8.57×10^{-1}	8.86×10^{-1}	(4.97 %)	0.97	(4.97 %)
	Aluminium	^{22}Na	7.15×10^{-3}	8.45×10^{-3}	(15.26 %)	0.85	(15.26 %)
		LL	7.15×10^{-2}	8.45×10^{-2}	(15.26 %)	0.85	(15.26 %)
	Kovar	^{54}Mn	3.37×10^{-2}	6.54×10^{-2}	(17.51 %)	0.52	(17.51 %)
		^{57}Co	5.59×10^{-2}	7.00×10^{-2}	(14.43 %)	0.80	(14.43 %)
		^{58}Co	7.36×10^{-2}	5.91×10^{-2}	(19.71 %)	1.25	(19.71 %)
		^{60}Co	3.06×10^{0}	5.42×10^{-1}	(3.98 %)	5.64	(3.98 %)
		LL	3.11×10^{1}	6.21×10^{0}	(3.95 %)	5.01	(3.95 %)
27	Copper	^{57}Co	2.73×10^{-3}	4.39×10^{-3}	(26.83 %)	0.62	(26.83 %)
		^{58}Co	4.37×10^{-3}	9.48×10^{-3}	(12.70 %)	0.46	(12.70 %)
		LL	7.10×10^{-3}	1.39×10^{-2}	(12.14 %)	0.51	(12.14 %)
	Steel	^{51}Cr	1.08×10^{-1}	3.58×10^{-2}	(29.25 %)	3.01	(29.25 %)
		^{54}Mn	8.64×10^{-3}	1.96×10^{-2}	(9.00 %)	0.44	(9.00 %)
		^{57}Co	2.08×10^{-3}	3.57×10^{-3}	(28.46 %)	0.58	(28.46 %)

Table 5.11 (continued)

Location	Material	Radionuclide	FLUKA*	Experiment (Unc. %)†		C/E Ratio (Unc. %)‡	
		^{60}Co	2.86×10^{-2}	6.77×10^{-3}	(13.11 %)	4.22	(13.11 %)
		LL	3.76×10^{-1}	2.67×10^{-1}	(7.39 %)	1.40	(7.39 %)
	Kovar	^{60}Co	2.45×10^{0}	5.39×10^{-1}	(3.95 %)	4.55	(3.95 %)
		LL	2.45×10^{1}	5.39×10^{0}	(3.95 %)	4.55	(3.95 %)
3	Steel	^{54}Mn	1.50×10^{-2}	3.21×10^{-2}	(19.13 %)	0.47	(19.13 %)
		LL	1.50×10^{-1}	3.21×10^{-1}	(19.13 %)	0.47	(19.13 %)
28	Copper	^{57}Co	2.52×10^{-3}	3.52×10^{-3}	(22.42 %)	0.72	(22.42 %)
		^{58}Co	4.18×10^{-3}	7.09×10^{-3}	(16.03 %)	0.59	(16.03 %)
		LL	6.70×10^{-3}	1.06×10^{-2}	(13.04 %)	0.63	(13.04 %)
	Steel	^{51}Cr	1.12×10^{-1}	4.20×10^{-2}	(25.66 %)	2.68	(25.66 %)
		^{54}Mn	1.06×10^{-2}	2.16×10^{-2}	(8.88 %)	0.49	(8.88 %)
		^{57}Co	3.04×10^{-3}	3.87×10^{-3}	(25.91 %)	0.79	(25.91 %)
		^{58}Co	5.64×10^{-3}	6.09×10^{-3}	(20.51 %)	0.93	(20.51 %)
		^{60}Co	3.09×10^{-2}	8.56×10^{-3}	(10.71 %)	3.60	(10.71 %)
		LL	4.24×10^{-1}	3.12×10^{-1}	(6.84 %)	1.36	(6.84 %)
	Kovar	^{57}Co	1.27×10^{-2}	2.19×10^{-2}	(29.83 %)	0.58	(29.83 %)
		^{58}Co	2.66×10^{-2}	2.99×10^{-2}	(31.78 %)	0.89	(31.78 %)
		^{60}Co	2.65×10^{0}	6.94×10^{-1}	(3.75 %)	3.81	(3.75 %)
		LL	2.65×10^{1}	6.99×10^{0}	(3.73 %)	3.79	(3.73 %)
29	Copper	^{58}Co	2.77×10^{-3}	2.95×10^{-3}	(26.84 %)	0.94	(26.84 %)
		LL	2.77×10^{-3}	2.95×10^{-3}	(26.84 %)	0.94	(26.84 %)
	Steel	^{51}Cr	9.54×10^{-2}	2.82×10^{-2}	(26.21 %)	3.38	(26.21 %)
		^{54}Mn	7.65×10^{-3}	9.76×10^{-3}	(11.41 %)	0.78	(11.41 %)
		^{58}Co	4.18×10^{-3}	3.87×10^{-3}	(24.20 %)	1.08	(24.20 %)
		^{60}Co	2.83×10^{-2}	3.83×10^{-3}	(21.76 %)	7.38	(21.76 %)
		LL	3.65×10^{-1}	1.40×10^{-1}	(9.95 %)	2.60	(9.95 %)
	Kovar	^{60}Co	2.43×10^{0}	3.08×10^{-1}	(5.01 %)	7.89	(5.01 %)
		LL	2.43×10^{1}	3.08×10^{0}	(5.01 %)	7.89	(5.01 %)
30	Copper	^{57}Co	4.59×10^{-3}	6.24×10^{-3}	(19.12 %)	0.74	(19.12 %)
		^{58}Co	7.74×10^{-3}	1.18×10^{-2}	(10.61 %)	0.65	(10.61 %)
		LL	1.23×10^{-2}	1.81×10^{-2}	(9.58 %)	0.68	(9.58 %)
	Steel	^{51}Cr	1.65×10^{-1}	3.78×10^{-2}	(27.59 %)	4.36	(27.59 %)
		^{54}Mn	1.84×10^{-2}	3.22×10^{-2}	(7.42 %)	0.57	(7.42 %)
		^{57}Co	4.68×10^{-3}	7.95×10^{-3}	(15.27 %)	0.59	(15.27 %)
		^{58}Co	6.03×10^{-3}	6.51×10^{-3}	(19.36 %)	0.93	(19.36 %)
		^{60}Co	4.68×10^{-2}	9.03×10^{-3}	(10.78 %)	5.18	(10.78 %)
		LL	6.64×10^{-1}	4.27×10^{-1}	(6.06 %)	1.56	(6.06 %)
	Kovar	^{54}Mn	1.62×10^{-2}	3.89×10^{-2}	(24.86 %)	0.42	(24.86 %)
		^{57}Co	2.01×10^{-2}	2.48×10^{-2}	(29.00 %)	0.81	(29.00 %)
		^{58}Co	3.05×10^{-2}	2.94×10^{-2}	(29.18 %)	1.04	(29.18 %)
		^{60}Co	4.01×10^{0}	8.97×10^{-1}	(3.49 %)	4.47	(3.49 %)
		LL	4.04×10^{1}	9.42×10^{0}	(3.48 %)	4.29	(3.48 %)
31	Copper	^{54}Mn	6.27×10^{-4}	2.40×10^{-3}	(32.57 %)	0.26	(32.57 %)
		^{57}Co	2.48×10^{-3}	4.35×10^{-3}	(25.12 %)	0.57	(25.12 %)
		^{58}Co	3.89×10^{-3}	6.48×10^{-3}	(18.18 %)	0.60	(18.18 %)
		LL	1.26×10^{-2}	3.49×10^{-2}	(22.92 %)	0.36	(22.92 %)
	Steel	^{51}Cr	1.32×10^{-1}	1.24×10^{-1}	(11.83 %)	1.07	(11.83 %)
		^{54}Mn	8.26×10^{-3}	2.06×10^{-2}	(9.20 %)	0.40	(9.20 %)
		^{57}Co	2.00×10^{-3}	4.75×10^{-3}	(25.16 %)	0.42	(25.16 %)
		^{58}Co	2.37×10^{-3}	6.56×10^{-3}	(20.76 %)	0.36	(20.76 %)
		^{59}Fe	4.35×10^{-3}	7.24×10^{-3}	(20.92 %)	0.60	(20.92 %)
		^{60}Co	3.93×10^{-2}	3.76×10^{-2}	(5.16 %)	1.05	(5.16 %)
		LL	4.86×10^{-1}	6.02×10^{-1}	(4.52 %)	0.81	(4.52 %)
	Aluminium	^{22}Na	1.02×10^{-3}	1.60×10^{-3}	(52.19 %)	0.64	(52.19 %)
		LL	1.02×10^{-2}	1.60×10^{-2}	(52.19 %)	0.64	(52.19 %)

Table 5.11 (continued)

Location	Material	Radionuclide	FLUKA*	Experiment (Unc. %)†		C/E Ratio (Unc. %)‡	
	Kovar	^{58}Co	1.21×10^{-2}	2.39×10^{-2}	(43.18 %)	0.51	(43.18 %)
		^{60}Co	3.37×10^{0}	3.22×10^{0}	(3.01 %)	1.05	(3.01 %)
		LL	3.37×10^{1}	3.22×10^{1}	(3.01 %)	1.05	(3.01 %)
32	Copper	^{54}Mn	6.20×10^{-3}	3.15×10^{-3}	(38.64 %)	1.97	(38.64 %)
		^{57}Co	2.02×10^{-2}	1.18×10^{-2}	(13.31 %)	1.72	(13.31 %)
		^{58}Co	3.20×10^{-2}	1.75×10^{-2}	(9.42 %)	1.83	(9.42 %)
		LL	1.14×10^{-1}	6.07×10^{-2}	(20.37 %)	1.88	(20.37 %)
	Steel	^{51}Cr	4.48×10^{-1}	3.92×10^{-2}	(21.65 %)	11.45	(21.65 %)
		^{54}Mn	7.99×10^{-2}	4.63×10^{-2}	(6.80 %)	1.73	(6.80 %)
		^{57}Co	2.27×10^{-2}	1.04×10^{-2}	(15.24 %)	2.19	(15.24 %)
		^{58}Co	4.76×10^{-2}	1.14×10^{-2}	(11.03 %)	4.18	(11.03 %)
		^{60}Co	1.21×10^{-1}	9.06×10^{-3}	(10.58 %)	13.41	(10.58 %)
		LL	2.09×10^{0}	5.76×10^{-1}	(5.73 %)	3.63	(5.73 %)
	Kovar	^{57}Co	9.47×10^{-2}	4.49×10^{-2}	(16.51 %)	2.11	(16.51 %)
		^{58}Co	2.18×10^{-1}	6.73×10^{-2}	(16.65 %)	3.24	(16.65 %)
		^{60}Co	1.04×10^{1}	7.14×10^{-1}	(3.66 %)	14.56	(3.66 %)
		LL	1.04×10^{2}	7.25×10^{0}	(3.61 %)	14.38	(3.61 %)
33	Copper	^{54}Mn	1.13×10^{-2}	2.75×10^{-3}	(29.81 %)	4.13	(29.81 %)
		^{57}Co	3.16×10^{-2}	8.54×10^{-3}	(14.48 %)	3.70	(14.48 %)
		^{58}Co	6.15×10^{-2}	2.11×10^{-2}	(8.02 %)	2.91	(8.02 %)
		LL	2.07×10^{-1}	5.71×10^{-2}	(14.79 %)	3.61	(14.79 %)
	Steel	^{46}Sc	1.07×10^{-2}	3.05×10^{-3}	(23.44 %)	3.53	(23.44 %)
		^{51}Cr	1.67×10^{0}	4.59×10^{-1}	(8.45 %)	3.64	(8.45 %)
		^{54}Mn	9.58×10^{-2}	3.90×10^{-2}	(7.02 %)	2.45	(7.02 %)
		^{57}Co	2.99×10^{-2}	1.01×10^{-2}	(14.81 %)	2.95	(14.81 %)
		^{58}Co	7.06×10^{-2}	1.84×10^{-2}	(9.98 %)	3.83	(9.98 %)
		^{59}Fe	3.12×10^{-2}	9.51×10^{-3}	(14.39 %)	3.28	(14.39 %)
		^{60}Co	1.45×10^{-1}	2.73×10^{-2}	(5.30 %)	5.32	(5.30 %)
		LL	2.67×10^{0}	7.37×10^{-1}	(4.33 %)	3.62	(4.33 %)
	Kovar	^{54}Mn	8.43×10^{-2}	3.12×10^{-2}	(27.99 %)	2.71	(27.99 %)
		^{57}Co	1.25×10^{-1}	3.74×10^{-2}	(17.87 %)	3.33	(17.87 %)
		^{58}Co	3.38×10^{-1}	1.15×10^{-1}	(13.70 %)	2.93	(13.70 %)
		^{60}Co	1.25×10^{1}	2.05×10^{0}	(3.13 %)	6.09	(3.13 %)
		LL	1.26×10^{2}	2.09×10^{1}	(3.09 %)	6.02	(3.09 %)
34	Copper	^{57}Co	2.97×10^{-3}	2.12×10^{-3}	(47.73 %)	1.40	(47.73 %)
		^{58}Co	4.69×10^{-3}	4.81×10^{-3}	(19.08 %)	0.98	(19.08 %)
		LL	7.66×10^{-3}	6.93×10^{-3}	(19.72 %)	1.10	(19.72 %)
	Steel	^{51}Cr	1.07×10^{-1}	2.22×10^{-2}	(36.64 %)	4.82	(36.64 %)
		^{54}Mn	1.32×10^{-2}	1.44×10^{-2}	(10.45 %)	0.92	(10.45 %)
		^{58}Co	6.42×10^{-3}	3.26×10^{-3}	(36.90 %)	1.97	(36.90 %)
		^{60}Co	3.51×10^{-2}	5.97×10^{-3}	(15.49 %)	5.88	(15.49 %)
		LL	4.90×10^{-1}	2.07×10^{-1}	(8.54 %)	2.37	(8.54 %)
	Kovar	^{60}Co	3.01×10^{0}	5.01×10^{-1}	(4.03 %)	6.01	(4.03 %)
		LL	3.01×10^{1}	5.01×10^{0}	(4.03 %)	6.01	(4.03 %)
35	Copper	^{57}Co	4.15×10^{-3}	3.79×10^{-3}	(27.55 %)	1.10	(27.55 %)
		^{58}Co	5.71×10^{-3}	1.03×10^{-2}	(12.24 %)	0.56	(12.24 %)
		LL	9.86×10^{-3}	1.41×10^{-2}	(11.63 %)	0.70	(11.63 %)
	Steel	^{51}Cr	1.03×10^{-1}	5.10×10^{-2}	(19.03 %)	2.03	(19.03 %)
		^{54}Mn	1.23×10^{-2}	2.07×10^{-2}	(8.53 %)	0.59	(8.53 %)
		^{57}Co	3.53×10^{-3}	3.48×10^{-3}	(32.67 %)	1.01	(32.67 %)
		^{58}Co	5.38×10^{-3}	7.43×10^{-3}	(15.89 %)	0.72	(15.89 %)
		^{60}Co	3.16×10^{-2}	4.53×10^{-3}	(18.69 %)	6.96	(18.69 %)
		LL	4.48×10^{-1}	2.63×10^{-1}	(7.45 %)	1.70	(7.45 %)
	Kovar	^{57}Co	1.48×10^{-2}	2.18×10^{-2}	(28.05 %)	0.68	(28.05 %)
		^{58}Co	2.60×10^{-2}	4.37×10^{-2}	(19.97 %)	0.60	(19.97 %)
		^{60}Co	2.71×10^{0}	6.10×10^{-1}	(3.80 %)	4.44	(3.80 %)

Table 5.11 (continued)

Location	Material	Radionuclide	FLUKA*	Experiment (Unc. %)†		C/E Ratio (Unc. %)‡	
		LL	2.71×10^{1}	6.16×10^{0}	(3.77 %)	4.40	(3.77 %)
36	Copper	^{58}Co	4.17×10^{-3}	1.81×10^{-3}	(46.10 %)	2.30	(46.10 %)
		LL	4.17×10^{-3}	1.81×10^{-3}	(46.10 %)	2.30	(46.10 %)
	Steel	^{54}Mn	1.22×10^{-2}	7.04×10^{-3}	(19.38 %)	1.73	(19.38 %)
		^{58}Co	5.91×10^{-3}	1.59×10^{-3}	(47.40 %)	3.72	(47.40 %)
		^{60}Co	3.33×10^{-2}	2.79×10^{-3}	(26.57 %)	11.95	(26.57 %)
		LL	4.61×10^{-1}	9.98×10^{-2}	(15.57 %)	4.62	(15.57 %)
	Kovar	^{60}Co	2.86×10^{0}	3.48×10^{-1}	(4.55 %)	8.21	(4.55 %)
		LL	2.86×10^{1}	3.48×10^{0}	(4.55 %)	8.21	(4.55 %)
37	Copper	^{54}Mn	6.33×10^{-3}	1.07×10^{-2}	(12.96 %)	0.59	(12.96 %)
		^{56}Co	5.54×10^{-3}	4.21×10^{-3}	(20.67 %)	1.32	(20.67 %)
		^{57}Co	1.94×10^{-2}	2.45×10^{-2}	(11.17 %)	0.79	(11.17 %)
		^{58}Co	2.83×10^{-2}	4.72×10^{-2}	(6.51 %)	0.60	(6.51 %)
		^{60}Co	2.89×10^{-3}	5.20×10^{-3}	(14.87 %)	0.56	(14.87 %)
		LL	1.95×10^{-1}	2.73×10^{-1}	(6.81 %)	0.72	(6.81 %)
	Steel	^{46}Sc	4.68×10^{-3}	6.52×10^{-3}	(13.45 %)	0.72	(13.45 %)
		^{51}Cr	2.16×10^{-1}	1.43×10^{-1}	(11.76 %)	1.51	(11.76 %)
		^{54}Mn	7.42×10^{-2}	1.16×10^{-1}	(5.71 %)	0.64	(5.71 %)
		^{56}Co	7.33×10^{-3}	4.73×10^{-3}	(21.36 %)	1.55	(21.36 %)
		^{57}Co	2.14×10^{-2}	2.46×10^{-2}	(11.56 %)	0.87	(11.56 %)
		^{58}Co	3.46×10^{-2}	3.25×10^{-2}	(7.62 %)	1.06	(7.62 %)
		^{60}Co	7.10×10^{-2}	2.54×10^{-2}	(5.76 %)	2.79	(5.76 %)
		LL	1.63×10^{0}	1.58×10^{0}	(4.37 %)	1.03	(4.37 %)
	Aluminium	^{22}Na	9.00×10^{-3}	1.18×10^{-2}	(12.55 %)	0.76	(12.55 %)
		^{54}Mn	3.00×10^{-3}	4.26×10^{-3}	(28.48 %)	0.70	(28.48 %)
		LL	1.20×10^{-1}	1.61×10^{-1}	(11.92 %)	0.75	(11.92 %)
	Kovar	^{54}Mn	6.45×10^{-2}	9.91×10^{-2}	(15.92 %)	0.65	(15.92 %)
		^{57}Co	8.94×10^{-2}	1.04×10^{-1}	(12.44 %)	0.86	(12.44 %)
		^{58}Co	1.65×10^{-1}	1.69×10^{-1}	(10.08 %)	0.98	(10.08 %)
		^{60}Co	6.07×10^{0}	2.11×10^{0}	(3.12 %)	2.88	(3.12 %)
		LL	6.16×10^{1}	2.24×10^{1}	(3.03 %)	2.76	(3.03 %)
38	Copper	^{54}Mn	4.01×10^{-3}	5.68×10^{-3}	(18.75 %)	0.71	(18.75 %)
		^{57}Co	1.33×10^{-2}	1.11×10^{-2}	(14.17 %)	1.20	(14.17 %)
		^{58}Co	1.93×10^{-2}	2.41×10^{-2}	(7.81 %)	0.80	(7.81 %)
		LL	7.27×10^{-2}	9.19×10^{-2}	(11.88 %)	0.79	(11.88 %)
	Steel	^{51}Cr	2.12×10^{-1}	6.55×10^{-2}	(18.25 %)	3.23	(18.25 %)
		^{54}Mn	4.86×10^{-2}	5.95×10^{-2}	(6.28 %)	0.82	(6.28 %)
		^{57}Co	1.34×10^{-2}	1.14×10^{-2}	(14.02 %)	1.18	(14.02 %)
		^{58}Co	2.13×10^{-2}	1.42×10^{-2}	(10.85 %)	1.50	(10.85 %)
		^{60}Co	7.10×10^{-2}	1.50×10^{-2}	(7.67 %)	4.73	(7.67 %)
		LL	1.23×10^{0}	7.71×10^{-1}	(5.08 %)	1.60	(5.08 %)
	Aluminium	^{22}Na	5.98×10^{-3}	2.21×10^{-3}	(49.22 %)	2.70	(49.22 %)
		LL	5.98×10^{-2}	2.21×10^{-2}	(49.22 %)	2.70	(49.22 %)
	Kovar	^{54}Mn	4.25×10^{-2}	4.35×10^{-2}	(30.24 %)	0.98	(30.24 %)
		^{57}Co	5.64×10^{-2}	4.84×10^{-2}	(16.43 %)	1.17	(16.43 %)
		^{58}Co	1.00×10^{-1}	9.04×10^{-2}	(14.36 %)	1.11	(14.36 %)
		^{60}Co	6.07×10^{0}	1.08×10^{0}	(3.38 %)	5.63	(3.38 %)
		LL	6.13×10^{1}	1.14×10^{1}	(3.42 %)	5.40	(3.42 %)

Chapter 6

Applications of the fluence conversion coefficients method to studies for the LHC experiments

As it was extensively presented in Chapter 4, the fluence conversion coefficients method is based on the idea that radiological hazard factors can often be expressed as a weighted sum of radionuclide mass-specific activities with radionuclide-specific weights. The working principles of this method have been shown with a simplified and controlled example which also allowed to give a glimpse of the possibilities and versatility of this radiological assessment approach.

Several benchmarks of the FLUKA Monte Carlo code and of the fluence conversion coefficients code setup with activation detectors were then presented in Chapter 5. The experiments were conducted at CERN irradiation facilities which are designed to reproduce the irradiation conditions typically found at particle accelerators and at the LHC experiments: these were complemented by an extensive and complex benchmark of the LHCb radiation environment. These comparisons allowed to have a reasonable estimate of the overall goodness of the simulation codes and of the safety margins that should be taken into account in radiological assessments: the agreement between experimental measurements and simulation was satisfactory in most of the situations and better than a factor 2.0 or even 1.5.

With the objective of illustrating the capabilities and advantages of the method even in very complex cases, this chapter collects a selection of simulation studies for the LHC experiments that had important practical consequences. The examples here presented are dedicated to establishing a radiological zoning and designing a forward shield reinforcement for CMS (Section 6.1), to the assessment of residual activity in the stainless steel absorber plates of the CMS HGCal (Section 6.2), to establishing a preliminary zoning for clearance/decommissioning operations at ALICE (Section 6.3), and to radiation protection studies for ATLAS and CMS which significantly contributed to the preparation to the 2021 LHC pilot beam conducted as part of the commissioning of the LHC machine and experiments before the Run 3 restart in 2022 (Section 6.4).

6.1 Design studies for the CMS New Forward Shield

6.1.1 Introduction and motivations

All the areas that are within CERN's perimeter are classified in relation to the effective dose that a person can potentially receive during the stay in the area in normal working conditions: areas can be non-designated areas or radiation areas, the latter further classified depending on the levels of ambient dose equivalent rates, and of surface and airborne contamination [109].

Any material that leaves a radiation area is subject to a form of radiological control and two approaches are possible. Based on Monte Carlo simulations, ambient dose rate measurements, activation samples of representative materials, and surface contamination checks, the CERN Radiation Protection group can apply the so-called global control for radiation areas: in this case, the levels of stray radiation are sufficiently low so that materials can be considered a-priory as non-radioactive and equipment is subject to a simple verification measurement [110, 111]. If the activation of materials cannot be excluded by reasoning and measurements, the area is subject instead to the so-called individual control and any material has to be treated as potentially radioactive[1] and thus subject to measurements for its classification [110, 111]. As it was explained in Section 2.4, materials can be cleared from regulatory control if certain requirements are fulfilled and the most constraining one is often on the specific activity or the total activity. It may be useful to recall at this stage that for a mixture of radionuclides of artificial origin, the specific activity of each radionuclide must be compared with its clearance limits [59] and that the multiples of Swiss clearance limits (LL), as defined by the sum rule in equation 2.21, should not exceed 1.0.

With the only exception of the visitor platform that can normally be declassified after a certain cooling time during shutdown periods, the CMS experimental cavern (UXC55) is classified as a radiation area. During a past campaign conducted at approximately four months in Long Shutdown (LS) 2, gamma spectroscopy on steel samples close to the visitor platform had shown values slightly above 1.0. The analysis had shown that stainless steel (AISI 304L) was providing the highest activation levels and was the most penalizing material: the radionuclide having a larger radiological relevance was ^{54}Mn [112] ($T_{1/2}$ = 312.5 d) and it should also be noted that the present clearance limit for ^{54}Mn is 0.1 Bq/g, a factor 100 lower than the clearance limit prior to 2018 [59]. Particularly in all the areas not in the shadow of the yoke, these levels of residual activity may pose constraints to works in the CMS experimental cavern such as maintenance of air pads, destructive works and more generally works on steel structures. Considering that more luminosity will be integrated by the end of Run 3, the CMS Technical Coordination started investigating the possibility of reinforcing the existing forward shield[2] to reduce the levels of activation and ideally establish a

[1] This clearly excludes materials that were never exposed to the beam and that were not used for destructive works in a radiation area.

[2] The existing forward shield is also known as rotating shield. More details can be found in Section 6.1.3.

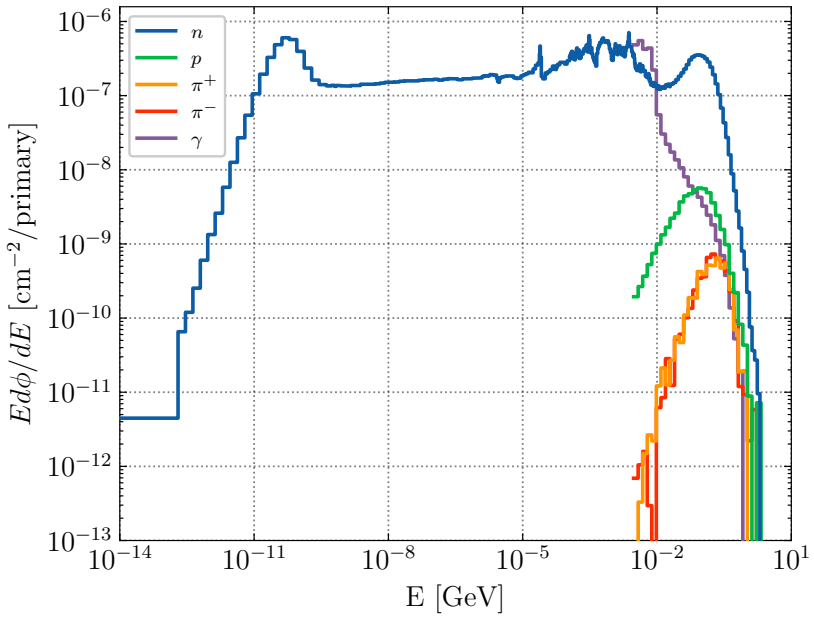

Figure 6.1: Typical particle spectra of neutrons, protons, charged pions, and photons in the proximity of the CMS experimental cavern walls laterally to the existing forward shield as estimated with the FLUKA Monte Carlo code.

global control in the periphery of the cavern. Although the radiation protection considerations were the first aspect considered, they are not the only argument driving the reinforcement of the shield: its installation could also be beneficial for the reduction of background radiation for the Muon Drift Tubes and would allow to compensate for the removal of two internal shells of the existing shield to house the new beam pipe support for Phase II.

6.1.2 Analysis of the problem

Several FLUKA Monte Carlo simulations were performed in iteration with the engineering design process and the main studies will be presented in the subsequent sections. Before entering into the details, it is of paramount importance to better frame the sources of the problem, something that will clearly allow to better explain why certain choices were made.

The aforementioned gamma spectroscopy performed at the beginning of LS 2 highlighted that at the CMS visitor platform, and in general laterally to the existing forward shield, steel is the most penalizing material for long cooling times. Some initial consideration had been drawn by estimating particle fluence spectra in the proximity of the CMS cavern walls, as shown in figure 6.1, and by computing the expected radionuclide inventory [112] with the ActiWiz code [79]. In these first examinations and in all subsequent studies, several typical representative materials were taken into account other than the stainless steel alloy 304L: this served to identify the worst case and/or to make sure that steel remained the most penalizing material in each considered scenario. These materials include pure iron, concrete (with europium traces), copper oxygen-free

Material	**LL**	**Top contributors to LL**
St. Steel 304L	1.06	^{54}Mn (70%), ^{60}Co (19%), ^{56}Co (6%), ^{46}Sc (2%), ^{57}Co (2%), ^{58}Co (1%)
Iron	1.04	^{54}Mn (98%), ^{46}Sc (1%)
Concrete	0.0045	^{22}Na (66%), ^{54}Mn (28%), ^{46}Sc (3%), ^{152}Eu (2%)
Cu OFE	0.197	^{54}Mn (29%), ^{60}Co (29%), ^{56}Co (17%), ^{58}Co (11%), ^{57}Co (11%)
Al6060	0.123	^{22}Na (86%), ^{65}Zn (10%), ^{54}Mn (3%)
Elec. Comp. 1	0.345	^{65}Zn (34%), ^{54}Mn(23%), ^{110m}Ag (20%), ^{46}Sc (6%), ^{60}Co (4%), ^{56}Co (3%), ^{57}Co (2%), ^{58}Co (2%), ^{125}Sb (2%), ^{22}Na (1%)
Elec. Comp. 2	0.217	^{65}Zn(36%), ^{54}Mn (28%), ^{110m}Ag (10%), ^{125}Sb (7%), ^{56}Co (5%), ^{60}Co (4%), ^{57}Co (3%), ^{22}Na (2%), ^{58}Co (2%)

Table 6.1: Preliminary estimates of the multiples of Swiss clearance limits for typical materials at the CMS visitor platform after 4 months cooling since the end of proton operation in LS 2. Table extracted from Ref. [112].

electronics (Cu OFE), the aluminium alloy 6060 (Al6060), and two compositions for electronic components: for completeness, the detailed composition of these materials is reported in Appendix C.1. Table 6.1 summarizes the preliminary estimates of multiples of Swiss clearance limits (LL) for the considered materials at the CMS visitor platform after 4 months since the end of proton operation in LS 2. As it can be seen, stainless steel and iron are the most penalizing materials and, unfortunately, they are quite ubiquitous in infrastructures in the CMS experimental cavern: the relative contribution to the total multiples of LL of ^{54}Mn is up to 70 % in the stainless steel and up to 98 % in iron.

To further break down the problem and to better identify possible solutions for the reduction of the activation levels in the CMS experimental cavern using a reinforcement of the forward shield, it is necessary to directly examine the production channels of ^{54}Mn. Owing to the elements present in the stainless steel 304L and steel alloys in general, ^{54}Mn can be produced from Fe, Ni, Co, Cr, and Mn itself. Considering the mass fractions of these elements in the material composition and the expected particle spectra at the CMS cavern walls, it is possible to estimate that the main source of ^{54}Mn is Fe for the 90.60 % of the total yield, while Mn itself is in second place with 6.15 %, and Ni in third with 3.20 %.

Once it is identified that Fe is almost the solely responsible for the overall high yield of ^{54}Mn, a further closer look can be given to the particles responsible for the activation. Figure 6.2 shows the ^{54}Mn production cross sections on ^{nat}Fe for neutrons, protons, charged pions and photons as estimated with the FLUKA Monte Carlo code: the details of the calculation are given in Section 4.7. The highest values for the cross sections are attained for neutrons and protons: the $^{nat}\mathrm{Fe}(n,x)^{54}\mathrm{Mn}$ exhibits a first broad peak of approximately 30 mb around 10 MeV due to the direct contribution of the $^{54}\mathrm{Fe}(n,p)^{54}\mathrm{Mn}$ reaction and a pronounced spallation peak of approximately 240 mb around 35 MeV. Considering the particle spectra at the location of interest, it is also

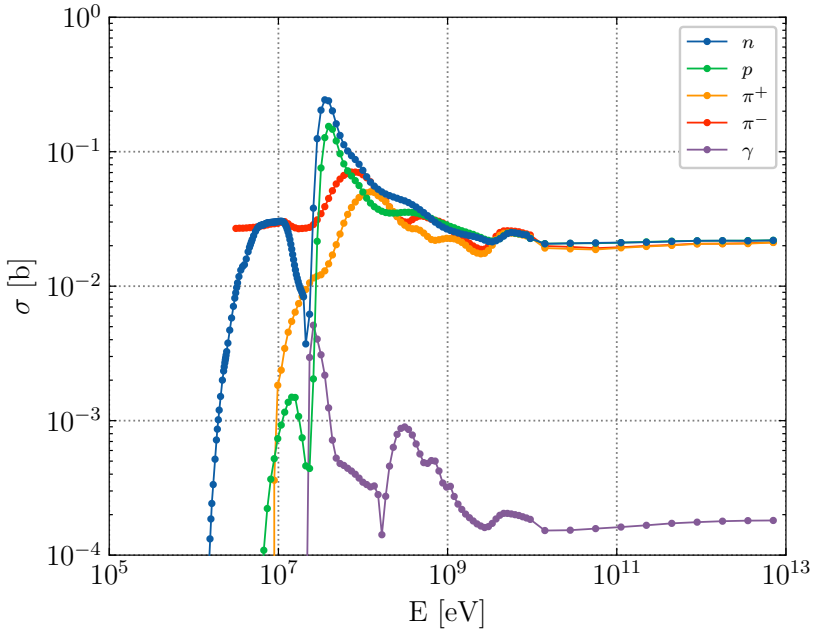

Figure 6.2: ^{54}Mn production cross sections on $^{\text{nat}}$Fe for neutrons, protons, charged pions and photons as estimated with the FLUKA Monte Carlo code.

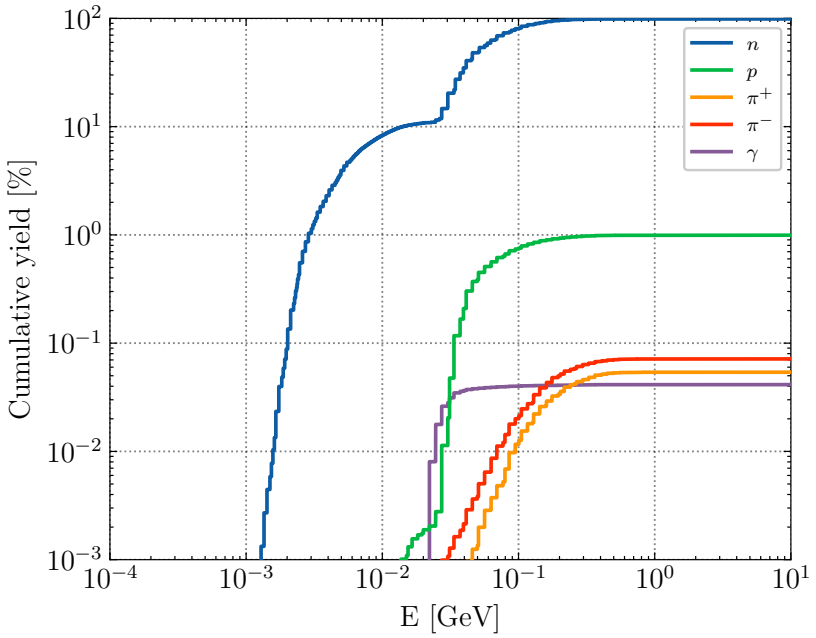

Figure 6.3: Cumulative ^{54}Mn production yield on $^{\text{nat}}$Fe as a function of the neutron, proton, charged pions, and photon energy at the CMS cavern walls laterally to the existing forward shield: the cumulative yield is normalized to the total yield.

possible to compute the cumulative ^{54}Mn production yield on ^{nat}Fe as a function of the energy of the incident neutrons, protons, charged pions and photons: the cumulative yield normalized to the total expected yield is shown in figure 6.3.

Despite the fact that the spectra of protons and charged pions extend above few GeV, their intensity is not enough to contribute significantly to activation. Instead, the energy spectrum of photons peaks around few MeV but the ^{nat}Fe$(\gamma, x)^{54}$Mn cross section not only has a smaller peak with respect to that of other particles, but it also occurs at an energy that is different from the energy at which the fluence reaches its maximum. As a result, the contribution of all these particles is less than 1.2 %, while more than 98.8 % of the ^{54}Mn production is owed to neutrons as illustrated in figure 6.3. Although it could qualitatively be inferred by looking at the particle spectra and the production cross section, if one considers the percentiles of the ^{54}Mn production by neutrons it is clear that low-energy neutrons contribute much less to the overall production than the rest of the spectrum. Indeed, only approximately 10 % of ^{54}Mn is due to neutrons with an energy below 33.6 MeV while for instance the 50 % and the 90 % are respectively attained at the energies of 56.3 MeV and 160 MeV approximately.

Summarizing the most important conclusions from the analysis of the problem, the residual activation levels in the CMS experimental cavern for cooling times between few weeks and few years[3] from the end of irradiation are mostly dominated by ^{54}Mn, a long-lived radionuclide with a 312.5 d half-life. The major source of this radionuclide is ^{nat}Fe, which is unfortunately a ubiquitous element in infrastructure materials, and it is almost entirely produced by high-energy neutrons in the quite narrow range from few tens of MeV to less than 200 MeV. This preliminary analysis was fundamental in order to start and support the design of a reinforcement of the existing CMS forward shield.

6.1.3 Overview of the proposed designs

The present design of the CMS forward shield, also known as rotating shield, is such that it allows a fast opening of the CMS detector and consists of two shells surrounding the forward beam pipe that can fold to the sides allowing for the CMS endcaps to be retracted for maintenance [114]: each shell consists of a steel casing with concrete and metal filling for a total of 18.5 tons of steel and 73 tons of concrete each. This concept avoids the need of heavy-lifting equipment in the cavern but imposes some restrictions. When opened, the shield is supported on the platform that constitutes the roof of the garage for the HF detector: the minimum garage height, the platform thickness and the complex geometry of the shells when folded on the platform all constrain the maximum radius of the shield. Since the shield is cantilevered from one end, the mass limit of each shell (approximately 160 tons) comes from the maximum allowed force that acts on the fixations at the cavern wall.

[3] For very long cooling times such as six or ten years the activation levels are then dominated by ^{60}Co ($T_{1/2} = 5.27$ y)

(a) Full closed CMS forward shield installed at present (in orange).

(b) CMS forward shield installed at present (in orange) during the full opening procedure [113].

Figure 6.4: Photos illustrating the presently installed forward shield (in orange) in CMS.

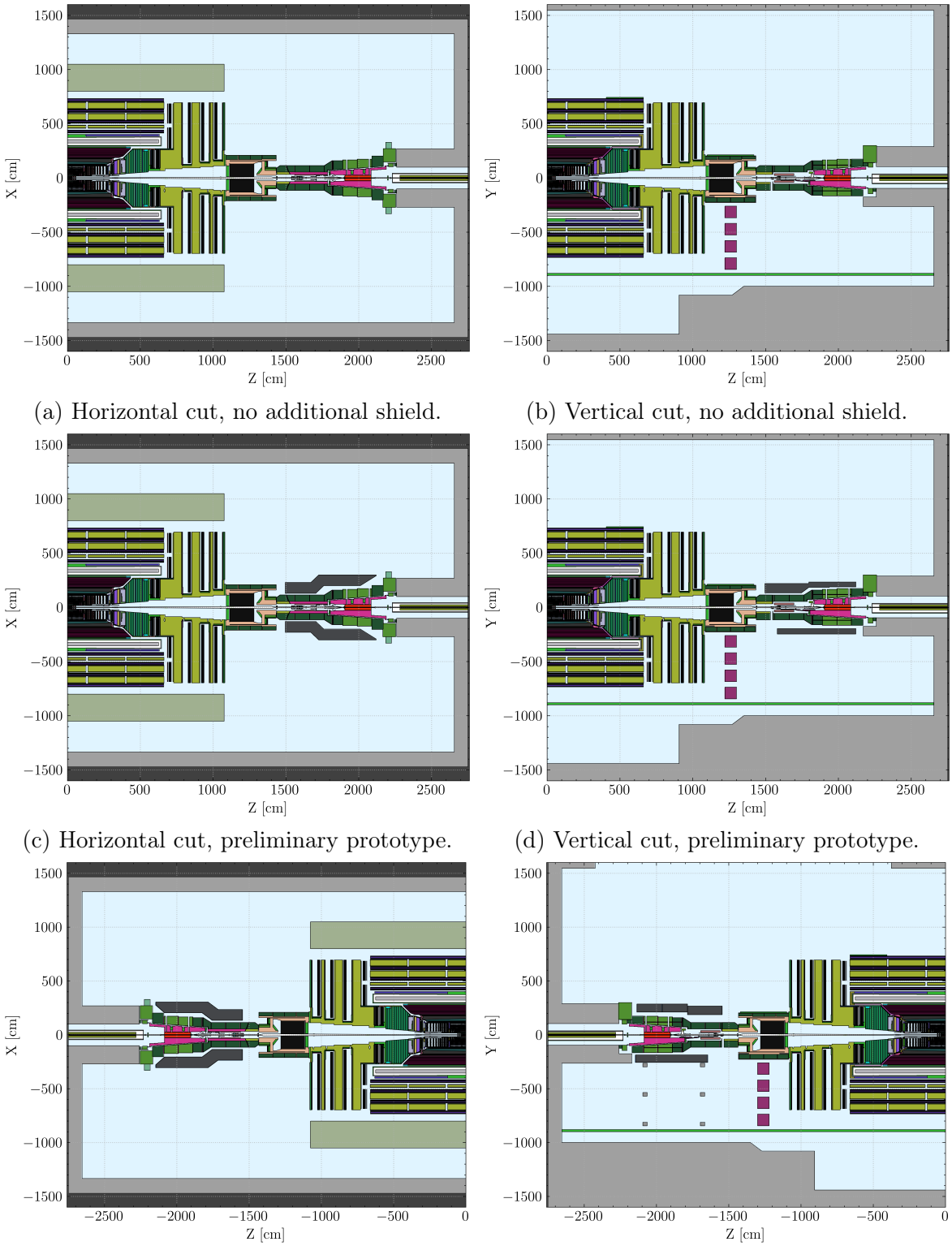

(a) Horizontal cut, no additional shield.

(b) Vertical cut, no additional shield.

(c) Horizontal cut, preliminary prototype.

(d) Vertical cut, preliminary prototype.

(e) Horizontal cut, final prototype.

(f) Vertical cut, final prototype.

Figure 6.5: Horizontal and vertical cut of the Run 3 FLUKA simulation geometries of CMS used for the calculations.

Designing a new shield is not always a simple task since several compromises have to be taken based on economic considerations and several practical constraints. Ideally, the same design should be used for both sides of the experimental cavern and the overall structure, that is the shield and its support, must allow for a relatively fast assembling and disassembling sequence. Other constraints come from the fact that one side of the experimental cavern ($Z > 0$) has no direct access to the surface, that the crane has a 20 tons lifting limit, and that the support structure must be able to fit through the passage to the PM54 shaft which is 3.5 m wide and only 7 m high.

Iteratively within the engineering design process, FLUKA Monte Carlo simulations were performed with the fluence conversion coefficients method to evaluate the expected residual levels of activation in the experimental cavern, thus assessing the effectiveness of the proposed shield solution. The various shield designs that will be briefly described are shown as implemented from engineering drawings in the FLUKA CMS Run 3 simulation geometry in figures 6.5(c) to 6.5(f), while figures 6.5(a) and (b) represent the reference Run 3 geometry with no additional shield installed.

Following the considerations on the ^{54}Mn production explained in Section 6.1.2 and the constraints briefly summarized in the previous paragraphs, a modular concrete shield was envisaged. In its preliminary design, the structure consisted of 12 blocks per side, each block being below the 20 tons limit, for a total of 206 tons: the material initially considered was heavy concrete (concrete barite) but, in view of a subsequent optimization, also the option of using ordinary concrete was evaluated for the same shield geometry. As represented in figure 6.5(c) and 6.5(d), the features of the supporting platform were not initially known with the same detail as the shield itself, but it was still reasonable to neglect them at least for the first round of calculations: at the same time it was also assumed that equal shields would be installed in both sides of the experimental cavern.

With the feedback from the first set of calculations, the design of the shield prototype was refined: albeit with a refined shape to best embrace the existing rotating shield and possibly reinforce previously weaker points, in its present status the structure still consists of 12 blocks in ordinary concrete with a steel casing for a total of 240 tons. Owing to several schedule constraints, the final prototype is scheduled to be installed in the YETS 2023/2024 in one side ($Z < 0$) of the CMS cavern only: the final prototype and its support structure as implemented in the FLUKA simulation geometry are shown in figure 6.5(e) and 6.5(f). With the experience from the years of Run 3 in which the shield will be installed and its efficiency will be assessed, it will be possible for the CMS Technical Coordination to evaluate the possibility of fully upgrading the overall forward shield in view of HL-LHC.

6.1.4 Application of the fluence conversion coefficients method for the evaluation of the shield effectiveness

Since one of the driving arguments in favour of an additional shield is the need to maintain the levels of residual activation in LS 3 low enough to establish a global

radiological control at the periphery of the CMS cavern not shaded by the barrel, Monte Carlo simulations were performed with FLUKA: the simulations were initially performed with the versions 4-1.1 and 4-2.0, but were recently re-run with the version 4-3.0 as distributed by the FLUKA.CERN collaboration.

The purpose of the assessment is to establish a conservative boundary outside which materials are expected to be a priori non-radioactive according to the Swiss legislation [59], provided that the additional, but normally less constraining, requirements on dose rate and residual contamination are met. To best assess the effectiveness of the shield from a radiation protection point of view, one must consider the activation of the infrastructure materials in the periphery of the CMS cavern by estimating the multiples of Swiss clearance limits (LL). The typical Monte Carlo simulation geometries for high-physics experiments are detailed enough to perform radiation studies in the inner detector elements, but a high level of detail cannot be feasibly maintained up to the very periphery: infrastructure elements are typically described in the simulation geometry in a much more simplified way or not described at all. Following these considerations and the extensive discussion in Chapter 4, the application of the fluence conversion coefficients method has in this case two unmatched advantages. First and foremost, the usage of an event-based method would not be possible at all since, relying on the events of creation of radionuclides, it would require that the concerned objects (i.e. the infrastructures in this case) are well represented in the simulation geometry. Second, the quantities of interest need to be estimated over extended regions of space and thus good visualization capabilities are fundamental (see Section 6.1.5 and figures therein).

From the initial considerations it was expected that a conservative picture would have been given by estimating the multiples of LL for stainless steel 304L since that material proved to represent the most penalizing case: to maintain a global overview, several compounds that are representative of common families of materials (see Section 6.1.2 and Appendix C.1) were nonetheless taken into account.

As far as the irradiation conditions are concerned, the revised calculations considered the full Run 3 proton operation with a collision profile computed assuming the yearly integrated luminosities of $30\,\mathrm{fb}^{-1}$, $90\,\mathrm{fb}^{-1}$, $90\,\mathrm{fb}^{-1}$, and $90\,\mathrm{fb}^{-1}$ for 2022, 2023, 2024, and 2025 as detailed in table 4.4: the duration of the irradiation for each year was computed as the time interval required to reach the targeted integrated luminosity in that year, assuming a continuous operation at a constant average luminosity estimated with the methodology explained in detail in Section 4.8. The installation schedule of the final prototype has now changed, but the calculation here presented all assumed that the shield element would be installed from the beginning of Run 3. Considering that the half-life of ^{54}Mn is 312.5 d and that the majority of the shutdown activities in the CMS experimental cavern begin after a couple of months after the end of the run period, the reference cooling time considered was 4 months in LS 3 after the end of proton operation: this also allowed to maintain consistency with the initial investigation conducted at the beginning of LS 2.

The simulation settings were optimized for activation calculations, namely charged

hadrons, photons (and electrons and positrons for consistency) were transported down to 1 MeV, while neutrons were transported down to thermal energies. The calculations were fully analogue, i.e. no biasing was implemented, and more than 300 000 primary collision events were simulated for each considered case.

For the described irradiation conditions, conversion coefficients from fluence to multiples of LL were computed for the selected material compositions and were then applied during transport calculations: for each shield design, the approach with the fluence conversion coefficients method allowed to obtain a detailed map of the multiples of LL over the CMS cavern and to efficiently evaluate a preliminary radiological zoning.

6.1.5 Main results, conclusions and reliability of the results

Figure 6.6 illustrates the map of the multiples of Swiss clearance limits for stainless steel 304L in the CMS experimental cavern at a cooling time of 4 months in LS 3 after the end of proton-proton operation in the case in which no additional shield is installed. It can clearly be seen that the boundary at which $LL = 1.0$ includes all the areas of the CMS cavern which are not shaded by the barrel. Laterally to the existing shield and in the proximity of the cavern walls where most of the infrastructures are present, the lowest LL value that is reached is approximately above two, while in the vertical direction values between three and four are reached even at the floor level and on the risers of the HF detector.

For the same irradiation conditions and cooling time, figure 6.7 represents instead the expected spatial distribution of the multiples of Swiss clearance limits for stainless steel 304L assuming that the concrete shield in its preliminary design has been installed. By comparing the distributions of figure 6.6 with those in figure 6.7, the differences and the benefit of reinforcing the existing shield are very clear. Thanks to the fluence conversion coefficients method which allows for a direct estimation of the selected hazard factor on a user-defined mesh that is independent of the geometry description, it is immediately possible to verify that at least in the horizontal plane the boundary at which $LL = 1.0$ is now considerably shifted and has moved from being at approximately 14 m from the beamline to being around 8 m from it, thus sparing most of the infrastructures and services on the side walls: with a designed lateral thickness of 1 m for the new reinforcement, the overall reduction of the activation levels at the CMS cavern walls is expected to be up to a factor four. Although still very efficient, the shield appears to be less effective in the vertical direction immediately above and below it: the critical components are here the cavern floor, where destructive works may be performed in the future, and the irreplaceable air pads of the endcap wheels, which owing to several constraints should not be activated above the clearance limits if maintenance has to performed on them. Residual activation in correspondence of the air pads still remains below the clearance limits, while it is possible to observe an overall reduction up to a factor of two at the floor level with respect to the case in which no additional shield is installed.

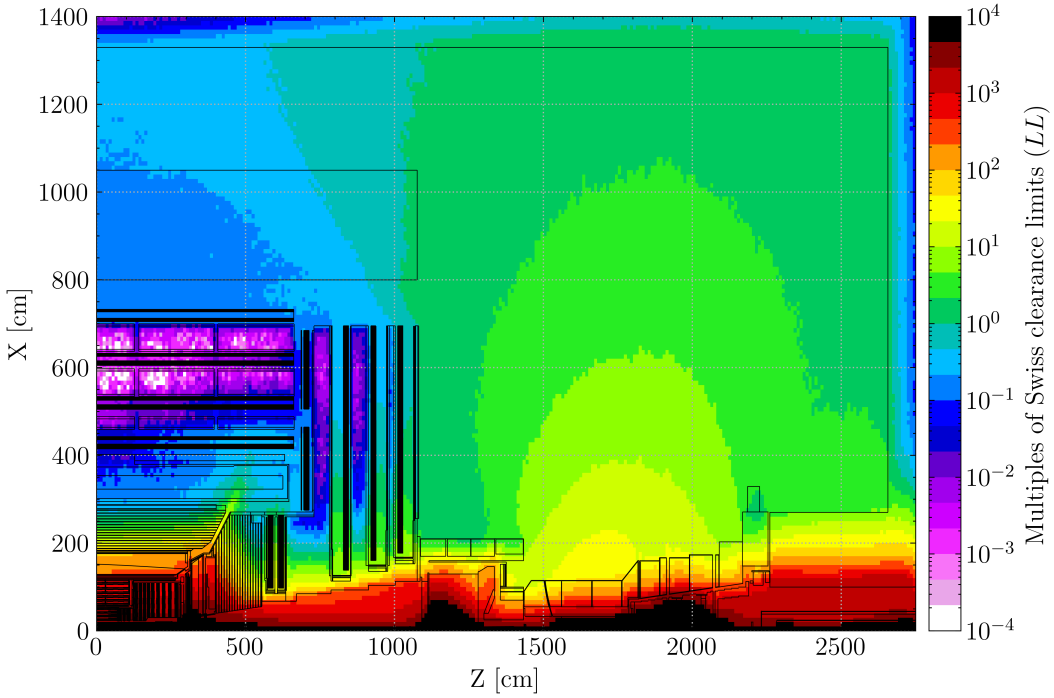

(a) Horizontal projection.

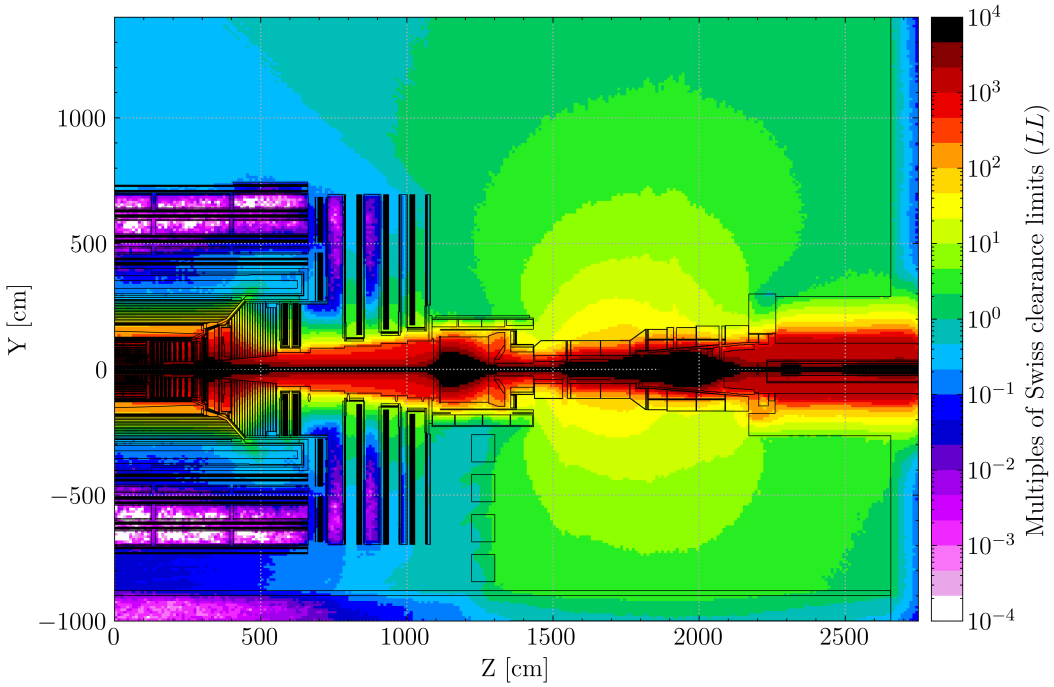

(b) Vertical projection.

Figure 6.6: FLUKA simulation with the fluence conversion coefficients code of the multiples of Swiss clearance limits (LL) for stainless steel 304L in the CMS experimental cavern at a cooling time of 4 months in LS 3 after the end of proton operation. No additional shield is installed.

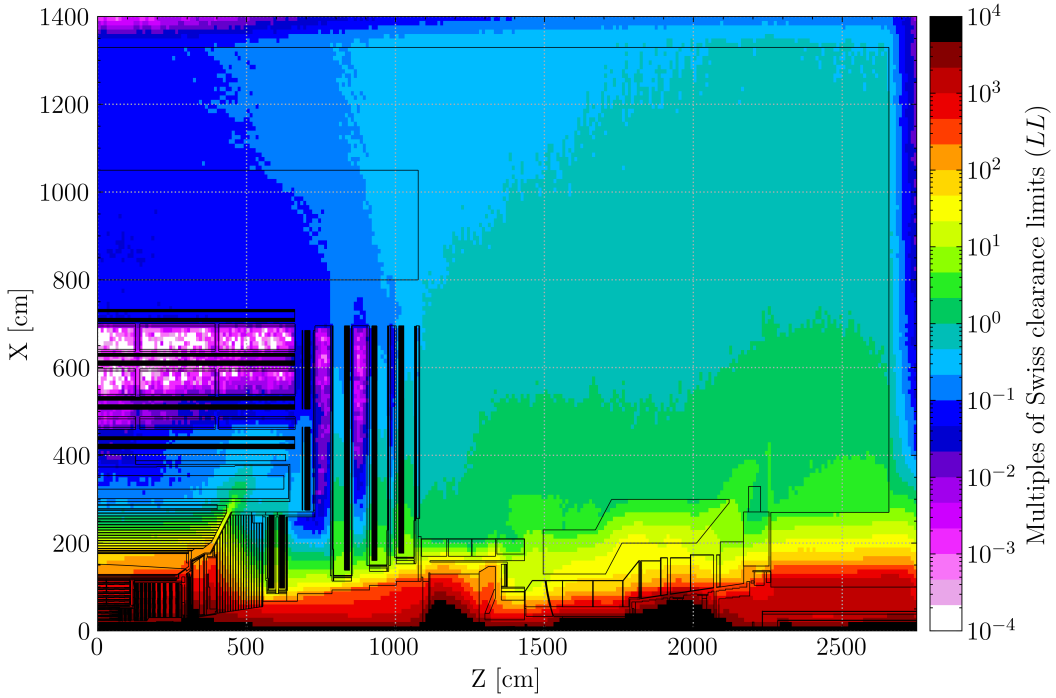

(a) Horizontal projection.

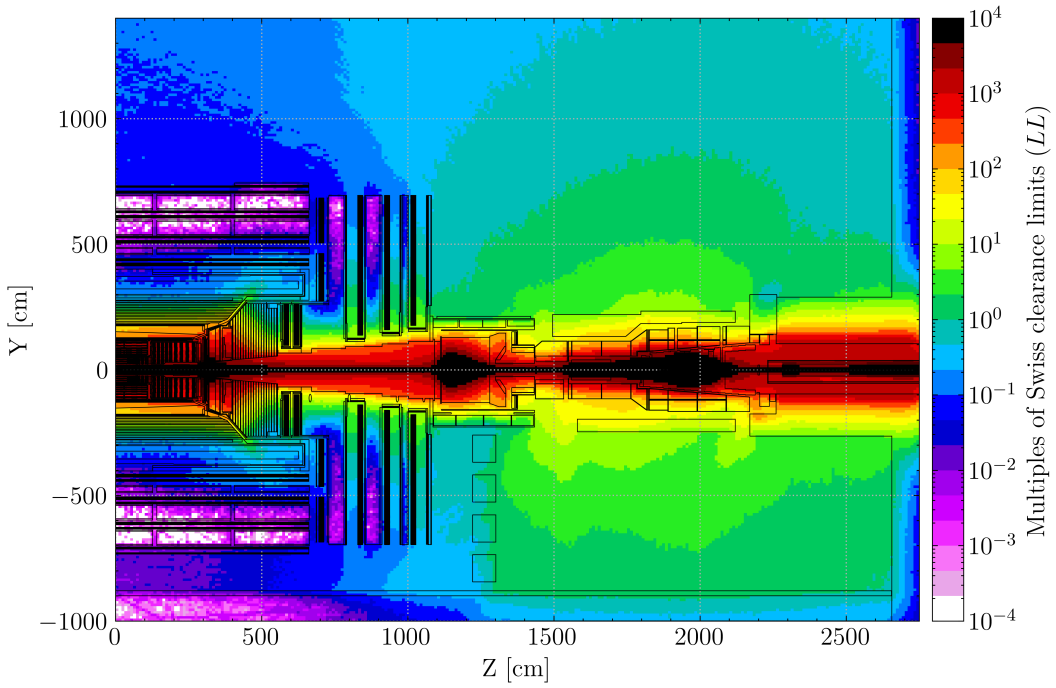

(b) Vertical projection.

Figure 6.7: FLUKA simulation with the fluence conversion coefficients code of the multiples of Swiss clearance limits (LL) for stainless steel 304L in the CMS experimental cavern at a cooling time of 4 months in LS 3 after the end of proton operation. The prototype of the shield reinforcement in its preliminary design (standard concrete as material) is considered for both sides of the cavern.

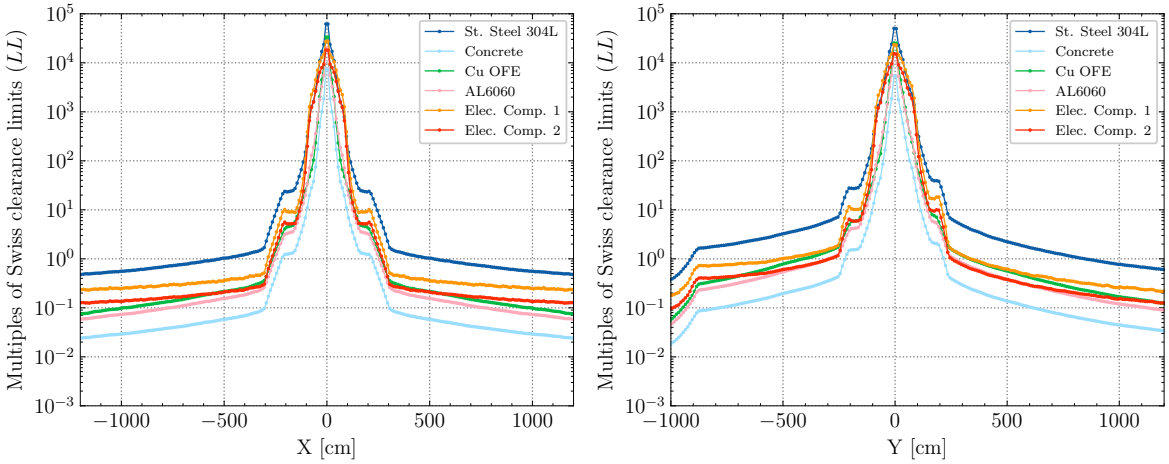

(a) Horizontal projection.

(b) Vertical projection

Figure 6.8: FLUKA simulation with the fluence conversion coefficients code of the multiples of Swiss clearance limits (LL) for various materials in the CMS experimental cavern at a cooling time of 4 months in LS 3 after the end of proton operation. The prototype of the shield reinforcement in its preliminary design (standard concrete as material) is considered and the results are projected considering 1800 cm $< Z <$ 1880 cm.

The maps of the multiples of LL previously shown are for stainless steel 304L which was expected to give conservative estimates based on the preliminary considerations, but several other materials were considered as discussed in the previous paragraphs: the expected spatial distribution of the multiples of LL for all the other materials are summarized in Appendix C.2. In agreement with what was expected, figure 6.8 compares the multiples of LL of various materials in the horizontal and vertical projections in the range 1800 cm $< Z <$ 1880 cm where radiation is expected to be maximum. Stainless steel 304L can indeed be used as reference material for this kind of zoning studies as it provides conservative estimates, followed by the materials representative of electronic components. It can also be observed that the concrete is in this case the less constraining material when activation is considered.

It is important to mention that concrete barite was initially considered as possible shield material in the first round of calculations: a shield in standard concrete, the material considered in the simulation from which the maps in figure 6.7 were obtained, was considered only in a second stage to evaluate the effectiveness of a less expensive and easier to procure material. Thanks to the simulations, it was indeed found out that the performances of concrete barite were better than that of standard concrete by at most of 5 to 10 % depending on the location: not being significantly advantageous, standard concrete was then chosen as a more cost-effective solution. As an example, the multiples of Swiss clearance limits for stainless steel 304L in the horizontal and vertical projection are shown in figure 6.9 where the different design choices are compared.

The first round of calculations provided valuable input to the design engineers and, despite the very tight constraints, allowed to refine and optimize the design of the shield reinforcement, particularly with respect to the choice of the material and the position

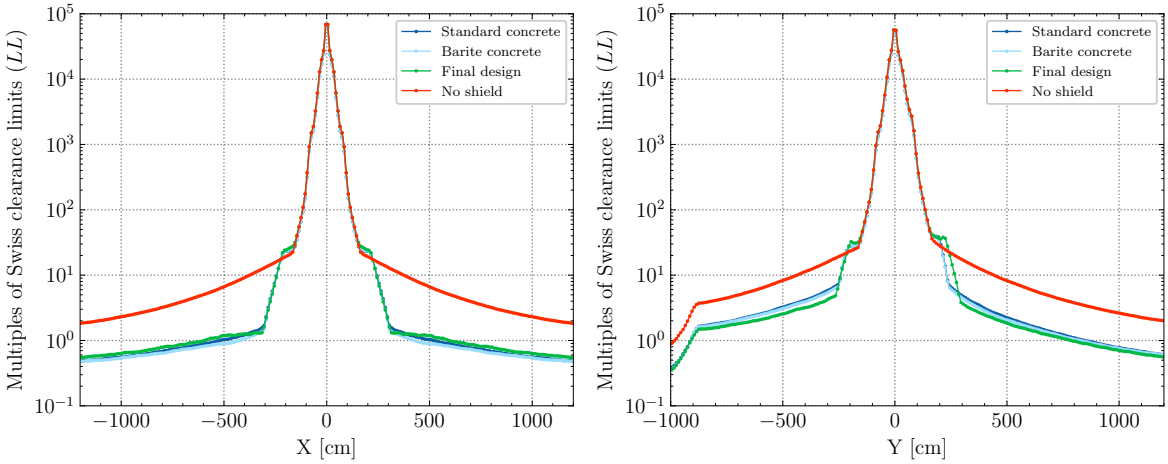

(a) Horizontal projection.

(b) Vertical projection

Figure 6.9: FLUKA simulation with the fluence conversion coefficients code of the multiples of Swiss clearance limits (LL) for stainless steel 304L in the CMS experimental cavern at a cooling time of 4 months in LS 3 after the end of proton operation. Various shield configurations are compared and the results are projected considering $-1880\,\text{cm} < Z < 1800\,\text{cm}$.

of the shield block. As summarized in the comparisons of figure 6.9, the effectiveness of the final prototype is comparable to that of the preliminary design, if not slightly better at least in the vertical direction.

To complement the discussion, figure 6.10 illustrates the expected spatial distribution of the multiples of LL for stainless steel 304L considering the final design of the shield prototype. In this case, the map is shown over the full CMS cavern to illustrate the effect of installing the shield reinforcement on one side only ($Z < 0$). This in practice would imply that, in the horizontal plane, the boundary at which materials are expected to be activated below the clearance limits would lie approximately at 8 m from the beam line only on the left side of the IP, while individual control should be applied on the right side of the IP: it can also be observed that due to the shadowing effect of the barrel, the cross-influence of the radiation field between the two sides of the experimental cavern is minimal.

In conclusion, the fluence conversion coefficients method proved to be a very effective calculation approach for this complex problem in which traditional event-based methods could not be even applied: the fast convergence of the method and the possibility to visualize the results on a user-defined mesh independently from the geometry description allowed to efficiently evaluate different solution for the reinforcement of the CMS forward shield, providing valuable input to the overall design process. The multiples of Swiss clearance limits were evaluated for representative materials: the case of stainless steel 304L, penalized by the ^{54}Mn production, provided in particular the means to establish a preliminary conservative boundary outside which materials would be regarded as activated below the clearance limits. Owing to the relevance of the new forward shield project and the potential benefit to the whole CMS technical operation,

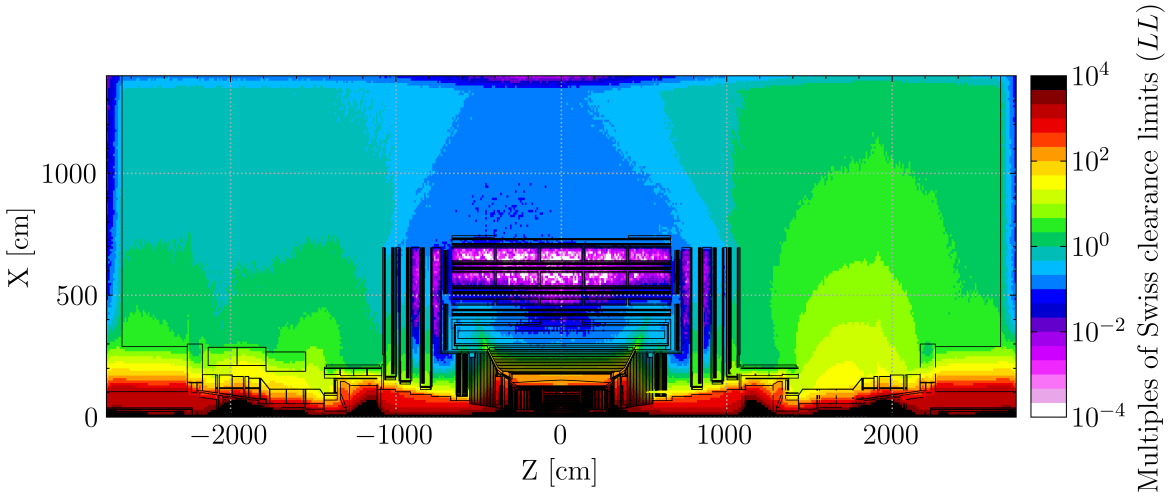

(a) Horizontal projection.

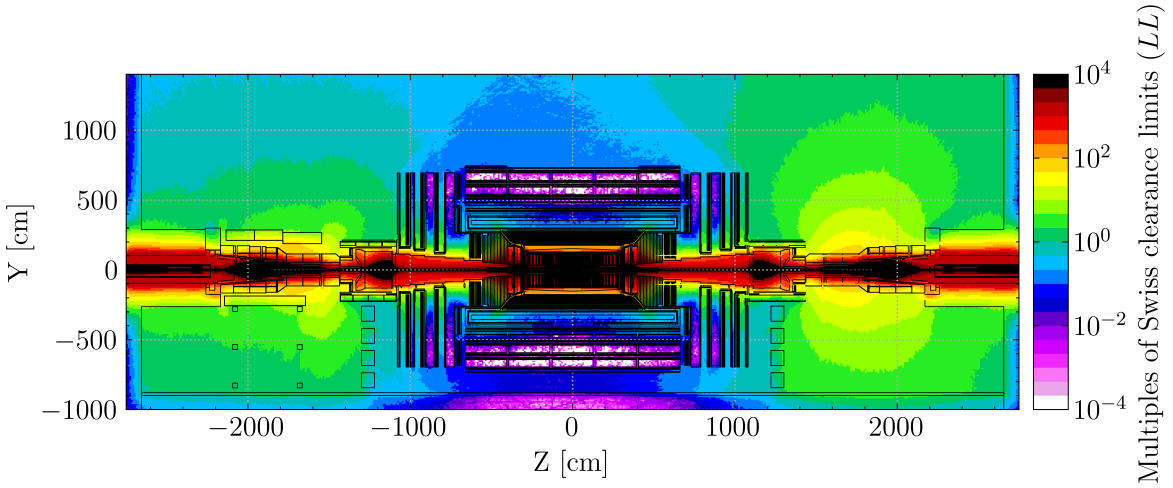

(b) Vertical projection.

Figure 6.10: FLUKA simulation with the fluence conversion coefficients code of the multiples of Swiss clearance limits (LL) for stainless steel 304L in the CMS experimental cavern at a cooling time of 4 months in the LS 3 after the end of proton operation. The prototype of the shield reinforcement in its final design is considered for one side only of the cavern.

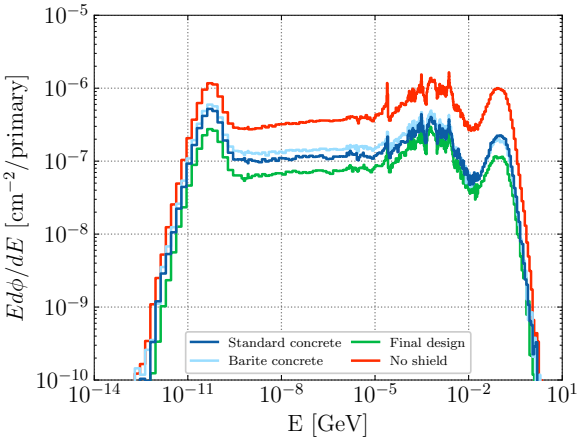

(a)

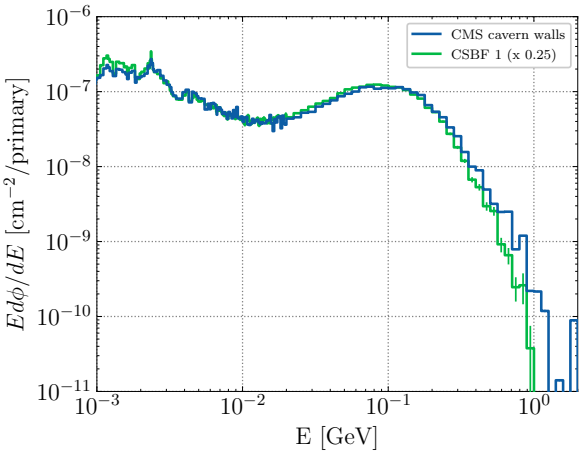

(b)

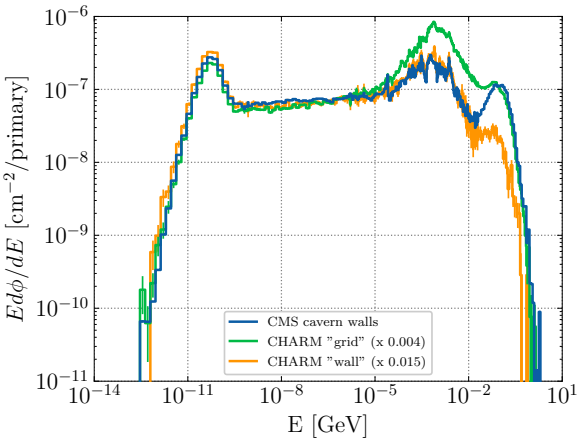

(c)

Figure 6.11: FLUKA simulation of the neutron fluence energy spectra at the CMS cavern walls and their comparison with those at the CERN Shielding Benchmark Facility (CSBF) and in the CERN High energy AcceleRator Mixed field (CHARM) facility: (a) neutron fluence spectra at the CMS cavern walls for various shield designs; (b) neutron fluence spectra above 1 MeV at the CMS cavern walls (final shield installed) compared with those at the first CSBF location; (c) neutron fluence spectra at the CMS cavern walls (final shield installed) compared with those at CHARM.

it is of paramount importance to comment on the reliability of the simulation estimates in light of considerations from the estimation of ^{54}Mn production cross section and the activation benchmarks discussed in Chapter 5.

As it was shown in figure 4.3 and in Appendix A.1, the FLUKA Monte Carlo code well reproduces the production cross section of ^{54}Mn from ^{nat}Fe as far as the available experimental data is concerned. In addition, there are only small differences in the neutron cross sections estimated with the FLUKA and the PHITS Monte Carlo codes for the energy range of interest, as shown for instance in figure 4.4 and in Appendix A.2.

Figure 6.11(a) illustrates the neutron energy spectra at the CMS cavern walls (laterally to the forward shield) estimated for the different shield designs: the four spectra all approximately exhibit the same energy dependency and essentially differ by their intensity. For the energies above 1 MeV, i.e. in the energy range that is relevant for the ^{54}Mn production, figure 6.11(b) compares the neutron fluence energy spectrum at the CMS cavern walls (final prototype installed) with the one that is expected at the first location of the CERN Shielding Benchmark Facility (CSBF) removable holder concrete block, the latter simply scaled by a multiplicative factor. As presented in the benchmark in Section 5.1.3, at that location the estimated ^{54}Mn production was differing only by 20 %, while the agreement for the multiples of LL was better than a factor 1.5. Similarly, figure 6.11(c) is comparing the neutron fluence energy spectrum at the CMS cavern walls with the ones that are expected at the two locations in the CERN High energy AcceleRator Mixed field (CHARM) facility where the activation benchmark was conducted, the latter again simply scaled by a multiplicative factor. At the location closer to the target, the thermal, the slowing-down, and the high-energy component are well matched: the first two are relevant for ^{60}Co production, while the latter for ^{54}Mn production. The overlap is also good for energies below tens of MeV for the location closer to the CHARM walls. The estimation of ^{60}Co in steel for those locations was better than a factor 2.0, while ^{54}Mn and the multiples of LL were predicted within differences of 20 % or less.

Thanks to the benchmarks presented in Chapter 5 and the following considerations summarized above, it is possible to state that, as far as activation studies are concerned, a reasonable safety factor to be taken into account on absolute results is between 1.5 and 2.0: this safety factor is instead much better than 1.5 if the relative, and not the absolute, effectiveness of the shield is considered. Finally, results from the recently installed activation samples following the experience with LHCb will provide further means of assessing the reliability of the simulations and will allow to experimentally assess the effectiveness of the installed shield.

6.2 Radiological pre-characterization of the steel absorber plates of the CMS HGCal

6.2.1 Objectives of the study

Radiation protection physicists at CERN are often required to reliably estimate the residual nuclide inventory for planned exposure situations. The radiological pre-characterization of detector and accelerator components is a very important task: this can already be performed in early design phases with reasonably conservative assumptions. The main objectives of this kind of assessments are, for instance, the establishment of appropriate protection measures during planned interventions and the appropriate disposal pathways (and costs) at the end of the useful lifetime of the component.

The raw material for the absorber plates for the hadronic part of the CMS High Granularity Calorimeter (HGCal) is austenitic stainless steel (AISI 304L) which will have to be purchased in rectangular plates for a total of approximately 589 tons: the rectangular plates will be then cut and machined to produce the polygonal plates of the absorber constituted by a central plate and two side plates. The total final mass of the absorber will approximately be 200 tons per endcap.

Given the fact that the absorber plates will be used in a scientific detector and exposed to an intense radiation environment, special requirements on the impurities in the steel have normally to be met. Despite the usually very low mass content, traces of cobalt may pose a radiological risk even at very long cooling times (i.e. greater than one year) owing to the production of ^{60}Co from the capture of low-energy neutrons on ^{59}Co. Through an evaluation of the radiological risk associated with different steel alloys available on the market, CERN has started to adopt a guideline value of maximum 0.1 % mass fraction for the cobalt content (tolerances included) [115, 116]. This value is not always achievable due to non-negligible practical factors: this was also the case for the HGCal absorber steel owing to the large amount of steel to be purchased, the steel market conditions at the time of the tendering process, and the particular grade of the steel. If guideline values cannot be met, the Radiation Protection group can be asked to perform a dedicated study: this section presents the assessment of the expected induced activation and the related residual radiation of the CMS HGCal absorber steel to justify a possible derogation from the recommended steel composition.

6.2.2 Assessment of the impact of the cobalt content on the steel activation using fluence conversion coefficients

As far as the development of high-energy particle showers is concerned, trace elements are of little if not negligible importance, but critical when assessing residual activation. In order to compare from a radiological point of view two stainless steel compositions having different cobalt content, Monte Carlo calculations were performed

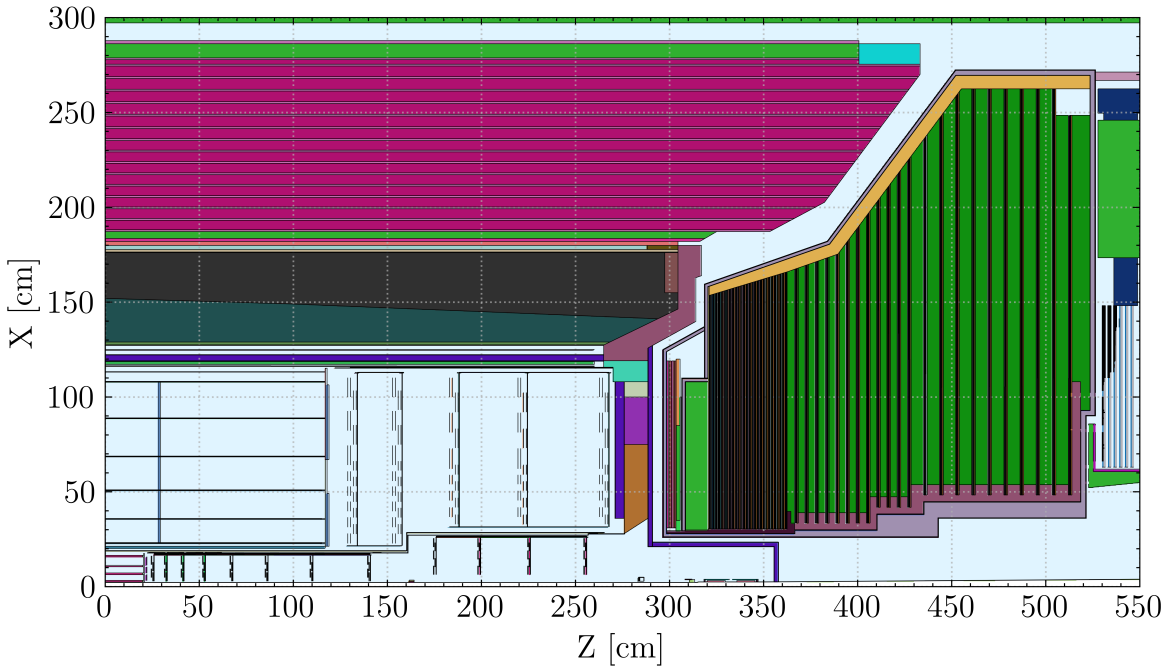

Figure 6.12: Horizontal cross section of the upper half of the CMS Phase II FLUKA simulation geometry used for the calculations: the view shows the Tracker, ECAL, HCAL and HGCal.

with the FLUKA code[4] applying the fluence conversion coefficients method: the advantages of the fluence conversion coefficients method over traditional approaches for this specific case will be discussed in Section 6.2.3 (figures therein) and in more detail in Section 6.2.4. Figure 6.12 illustrates the horizontal cross section of the upper half of the CMS Phase II FLUKA simulation geometry used for the calculations, in particular the detail of HGCal and the other central detectors: a schematic engineering drawing of HGCal is instead offered in figure 1.8. The guideline[5] stainless steel 304L composition with 0.1 % cobalt content was used in one case, while in the other case a stainless steel 304L with 0.3 % cobalt content was considered: for the latter, the additional cobalt content was subtracted from that of iron which is usually given as balance.

Since HGCal is scheduled to be installed in Long Shutdown (LS) 3, only the HL-LHC irradiation conditions were taken into account: the collision profile was computed with the general methodology illustrated in Section 4.8, in particular using the data reported in table 4.4 starting from the year 2029. Although short cooling times of 6 months and 1 year were also considered, for radioactive waste pre-characterization studies it is pertinent to mostly focus on very long cooling times such as 10 or 30 years. The simulation settings were optimized for activation calculations: charged hadrons were transported down to 1 MeV, neutrons were transported down to thermal ener-

[4]The calculations were performed with the code version 4-2.0 as distributed by the FLUKA.CERN Collaboration.

[5]As reported in Appendix C.1 this consists of: 18.5 % Cr, 11.3 % Ni, 2 % Mn, 1 % Si, 0.1 % Co, 0.3 ‰ C, 0.225 ‰ P, 0.015 ‰ S, and Fe as balance.

gies, and photons, electrons and positrons were only accounted for residual radiation calculations with transport thresholds of 10 keV and 100 keV respectively. The calculations were fully analogue and more than 150 000 primary collision events were simulated for each considered case.

With the information on the irradiation history and the material composition, it was possible to compute conversion coefficients from fluence to multiples of Swiss clearance limits (LL) and to the specific activity of selected radionuclides which have either a long half-life or are expected to significantly contribute to the total activity in the component at a given cooling time: this additionally estimated quantities were necessary to better understand if other radionuclides other than ^{60}Co should have been closely monitored.

6.2.3 Main results on the radionuclide specific activities and practical implications

Figure 6.13 shows the longitudinal projection of the contribution of various radionuclides to the total multiples of Swiss clearance limits for stainless steel 304L as estimated with FLUKA using the fluence conversion coefficient method for different cobalt mass fractions and for different cooling times from the end of irradiation in HL-LHC: the considered radionuclides are ^{3}H ($T_{1/2}$ = 12.32 y, LL = 100.0 Bq/g), ^{44}Ti ($T_{1/2}$ = 60.0 y, LL = 0.1 Bq/g), ^{54}Mn ($T_{1/2}$ = 312.2 d, LL = 0.1 Bq/g), ^{55}Fe ($T_{1/2}$ = 2.744 y, LL = 1000.0 Bq/g), ^{60}Co ($T_{1/2}$ = 5.27 y, LL = 0.1 Bq/g), and ^{63}Ni ($T_{1/2}$ = 101.2 y, LL = 100.0 Bq/g). Although of little importance for the present discussion, the results are a projection over the range 110 cm $< R <$ 120 cm.

As illustrated in figures 6.13(a) and (b), the contribution of ^{54}Mn can be higher than that of ^{60}Co at short cooling times when considering the guideline value of cobalt content: for the same cooling time but for a 0.3 % cobalt content, ^{60}Co overtakes ^{54}Mn with the only exception of the front part of the absorber.

For very long cooling times, all the residual ^{54}Mn has essentially decayed and only long-lived radionuclides are left. Despite the fact that the expected specific activity of radionuclides such as ^{63}Ni or ^{3}H would be comparable if not greater than that of ^{60}Co, their radiological relevance in terms of their contribution to the total multiples of LL is much less. At 30 years cooling time, ^{60}Co is then essentially the only effective contributor to the multiples of LL and this is true for both the considered steel compositions as shown in figures 6.13(c) and 6.13(d).

From a global overview of figure 6.13 it is possible to notice that for the same cooling time only the ^{60}Co contribution changes between the different steel compositions, while the contributions to the multiples of LL for other radionuclides are practically unaffected. What follows is that as long as cobalt is a trace element, the increase in the multiples of LL at long cooling times is almost linear with the increase in the cobalt mass fraction: having three times the cobalt guideline value leads to a ^{60}Co specific activity (hence multiples of LL for the above considerations) that is expected to be on average almost three times higher.

For a more precise picture over the full HGCal, figure 6.14 shows the map of the

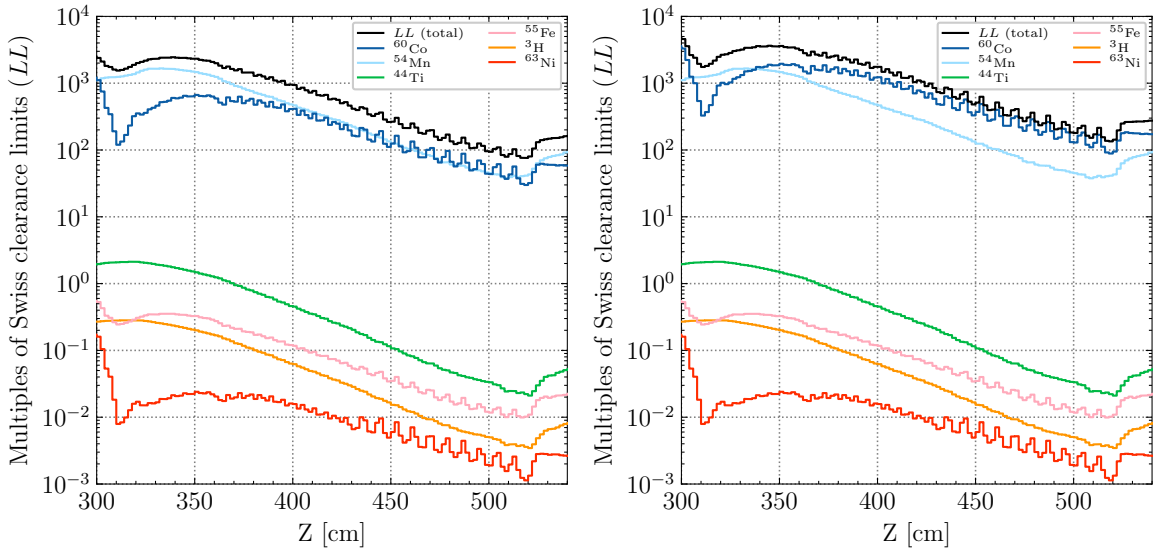

(a) 0.1 % cobalt mass fraction, 6 months cooling time.

(b) 0.3 % cobalt mass fraction, 6 months cooling time.

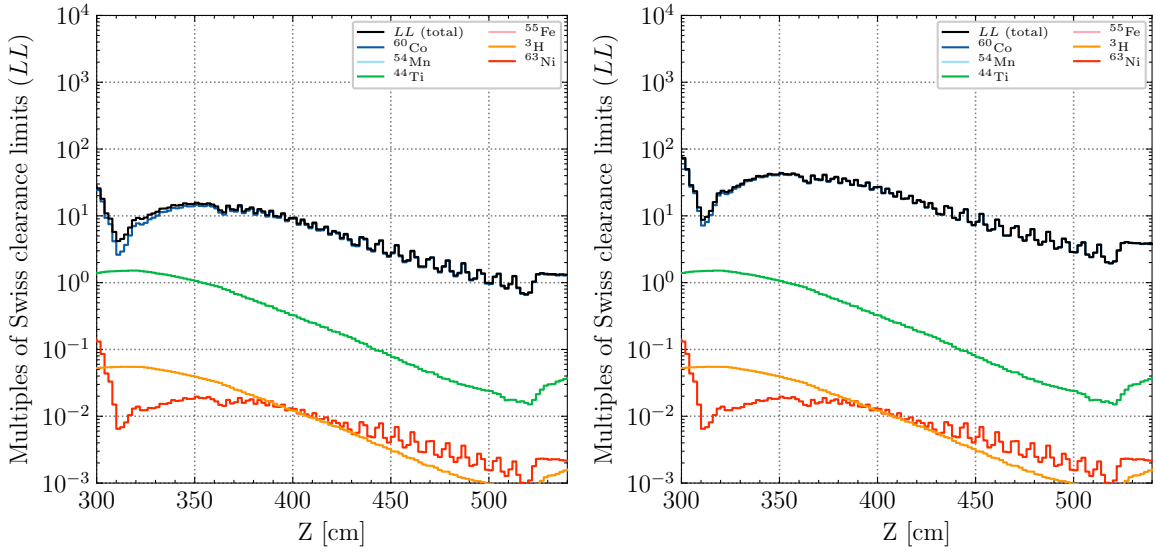

(c) 0.1 % cobalt mass fraction, 30 years cooling time.

(d) 0.3 % cobalt mass fraction, 30 years cooling time.

Figure 6.13: Longitudinal projection of the contribution of various radionuclides to the total multiples of Swiss clearance limits of stainless steel 304L as estimated with FLUKA and the fluence conversion coefficient method for different cobalt mass fractions and for different cooling times from the end of irradiation in HL-LHC. The projection range is 110 cm $< R <$ 120 cm.

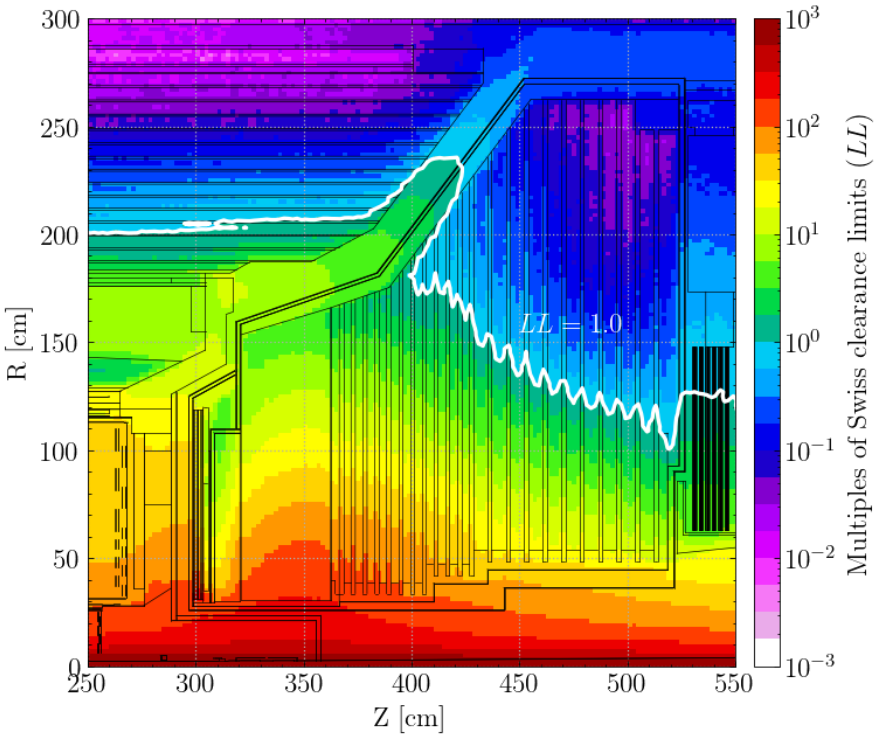

(a) 0.1 % cobalt mass fraction.

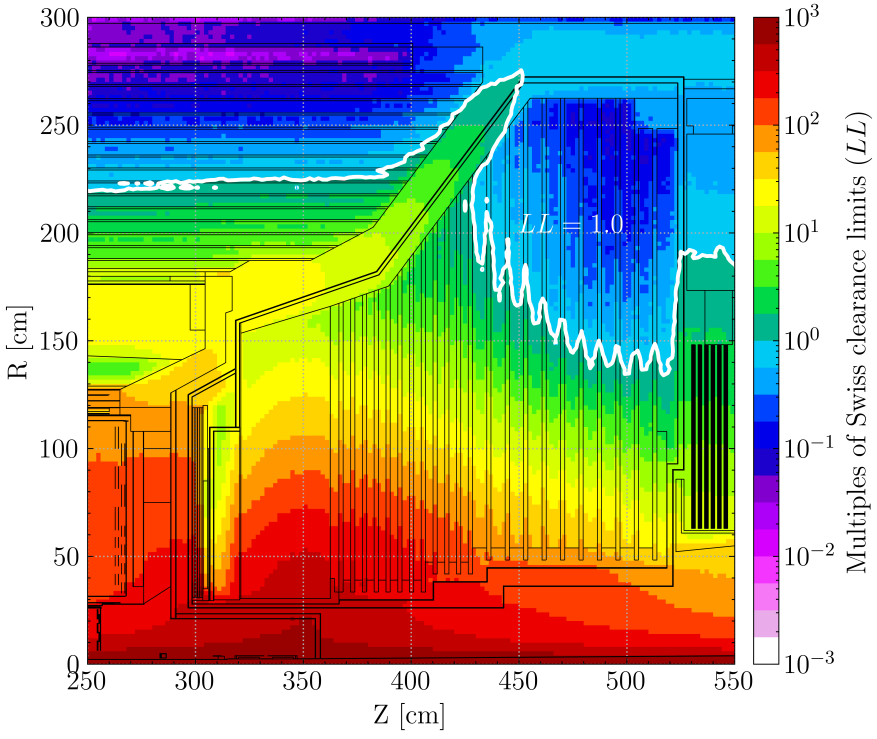

(b) 0.3 % cobalt mass fraction.

Figure 6.14: FLUKA simulation with the fluence conversion coefficient method of the multiples of Swiss clearance limits for stainless steel 304L considering two different cobalt mass fractions for the CMS HGCal steel absorber plates: (a) 0.1% cobalt content; (b) 0.3% cobalt content. The results refer to a cooling time of 30 years from the end of irradiation in HL-LHC and represent an average over the full azimuthal angle.

multiples of Swiss clearance limits for stainless steel 304L after 30 years from the end of irradiation considering cobalt impurities of 0.1% and 0.3%: the geometry overlay of the electromagnetic part of the calorimeter has been omitted to allow a better view of the colour map.

To further stress again the effectiveness of the fluence conversion coefficients method in this kind of radiological assessments, the contour line corresponding to the clearance condition $LL = 1.0$ is drawn in white for the two cases. With this kind of radiological maps it is immediately possible to understand which parts of the steel absorber plates would be a priori clearable. The increase of a factor approximately three in the ^{60}Co specific activity ultimately translates into a shift of this hypothetical boundary between radioactive and clearable material of approximately 15 cm to 20 cm depending on the considered steel plate.

In conclusion, albeit the change shown in figure 6.14 may appear significant, an approximate estimate would yield that by considering a 0.3 % cobalt content the clearable volume would be around 15 % smaller than the volume that would be instead clearable assuming the guideline steel composition. Additionally, the activation benchmarks presented in Chapter 5 have shown that calculations generally tend to overestimate the ^{60}Co production from steel and it is then expected that the results here presented already provide a conservative picture. Finally, it is certainly clear that the calculations would have to be reviewed in the future considering the real collision history for final absolute numbers, but the adopted approach in the computation of the irradiation profile tends to be anyhow conservative. Owing to the very few practical differences and to the conservativeness of the calculations, the results here discussed constituted a valid argument in the derogation from the concerned CERN guidelines. It is important at this stage to remind the fact that a derogation is not against the optimization principle (ALARA) of radiation protection since, as reminded in Section 2.4, economic and social factors should be taken into account when trying to keep doses to levels as low as reasonably achievable.

The present discussion of the results should be complemented by two separate but equally relevant considerations. First, the discussion on the convergence of the fluence conversion coefficients method and its performance with respect to traditional methods is reprised. Then, the argument on the stricter requirement imposed by clearance limits is supported by considerations on residual dose rates [117].

6.2.4 Further considerations on the convergence and advantages of the fluence conversion coefficients method

The numerical consistency of the fluence conversion coefficients method with respect to built-in Monte Carlo estimators was first presented using a simple example in Section 4.6. In the case studies illustrated in Section 6.1 (and Section 6.3 or 6.4), the components for which the radiological assessment is needed cannot be feasibly

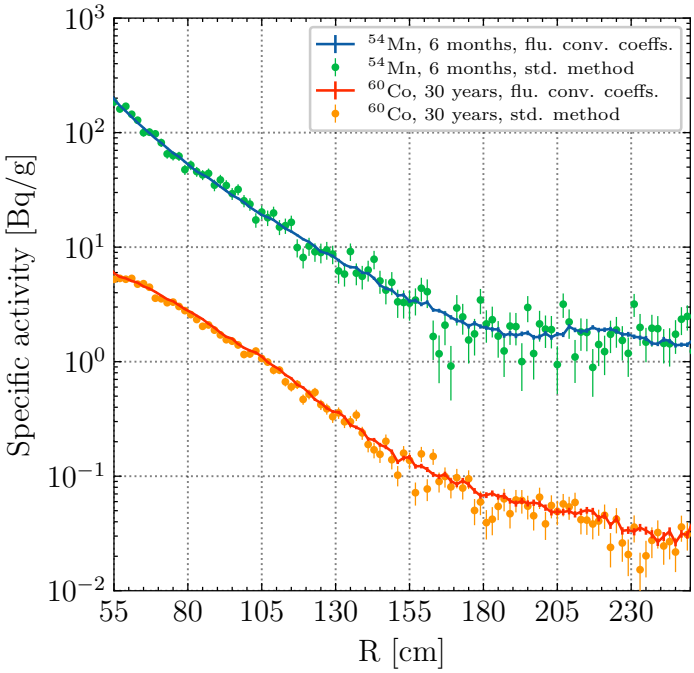

Figure 6.15: FLUKA simulation of radionuclide specific activities (^{54}Mn and ^{60}Co) for selected cooling times from the end of HL-LHC operation in one of HGCal absorber steel plate as estimated using the fluence conversion coefficients method and a standard event-based method for the same number of primary histories.

implemented in the simulation geometry[6]. The present test case, instead, offers the valuable opportunity to compare the same radiological quantities computed in one case employing the fluence conversion coefficients method and in another case relying on event-based estimators whose differences were first discussed in Section 4.3.

As an example, figure 6.15 shows the FLUKA simulation of radionuclide specific activities at selected cooling times in the 15$^{\text{th}}$ HGCal absorber plate as a function of the distance from the beamline: ^{54}Mn and ^{60}Co were chosen as they represent the most important radionuclides governing the radiological characterization procedures for steel at short and long cooling times respectively. The quantities computed with the fluence conversion coefficients method are represented with a continuous line, while the estimates provided by the FLUKA built-in estimator are illustrated using symbols.

What can be immediately understood is that the two methods are numerically consistent, but an additional and important consideration with respect to the performances and advantages of the fluence conversion coefficients method must be made. The convergence of the results obtained with the fluence conversion coefficients method is faster than that of the standard method, which means that for the same number of primary histories simulated (i.e. for the same CPU time) the statistical uncertainty on the estimated quantity is smaller. In other words, one of the great advantages of the fluence conversion coefficients method is that in order to achieve a certain level of sta-

[6]The referred studies aim to compute the residual activity in infrastructures and/or temporary installation for which their implementation in the simulation geometry would not be practical.

tistical uncertainty for a given quantity which one wishes to estimate, less CPU time is required with respect to traditional calculation approaches: the reduction in CPU time that can be achieved with the fluence conversion coefficients method with respect to event-based methods clearly has a strong dependence on the particular problem under examination and on the quantity being estimated. For example, in the specific case of the ^{54}Mn and ^{60}Co specific activities shown in figure 6.15 for $R > 140\,\text{cm}$, the relative statistical uncertainty is of few % for the fluence conversion coefficients method while is between 20 % to 30 % for the event-based method: approximately a factor of 100 more primary histories would need to be simulated in order for the above quantities estimated with the event-based method to reach the same accuracy as presently obtained with the fluence conversion coefficients. Considering that more than 150 000 primary events were initially simulated and that the time required to follow a primary history for CMS FLUKA simulations is in general between one to few minutes, the CPU time saved is considerable.

Recalling the consideration in Chapter 4, the reason why a faster convergence is attained is that fluence is estimated as total track-length per unit volume and the statistical uncertainty in track-length estimation is much lower than the statistical uncertainty in the estimation of rare events such as the radionuclide creation[7]. This effect is clearly more pronounced at higher radii and at larger depths within the absorber: this is also why in order to be able to better appreciate this effect the 15$^{\text{th}}$ plate was considered as an example and not one of the first or last ones.

6.2.5 Expected residual dose rate levels

To conclude this section on the activation of the HGCal steel, it is necessary to make some considerations on the expected ambient dose equivalent levels at the end of operation. In the context of this case study, these estimates are ultimately needed to understand the likelihood that the clearance criterion on the ambient dose equivalent rate is not met (see Section 2.4), but they could also serve as a basis for the preliminary estimation of individual and collective doses that persons are liable to receive during planned exposure situations such as maintenance or dismantling procedures.

During maintenance periods, the LHC experiments do not remain in a fixed configuration: detector components, magnets and even shielding elements are moved or removed from their usual location during beam operation and this further complicates the estimation of residual dose rates. The FLUKA code allows to simulate the generation of residual nuclei and the transport of the decay radiation within the same run while maintaining a certain degree of flexibility: to optimize the calculation to best match typical shutdown conditions, it is possible during the transport of decay radiation to switch off magnetic fields, adjust transport thresholds and set certain ge-

[7] As explained in Chapter 4, event-based methods estimate activities from radionuclide creation events during transport calculations, while for the fluence conversion coefficients method, which is related to a fluence scoring, particle fluence spectra are folded with radionuclide production cross sections.

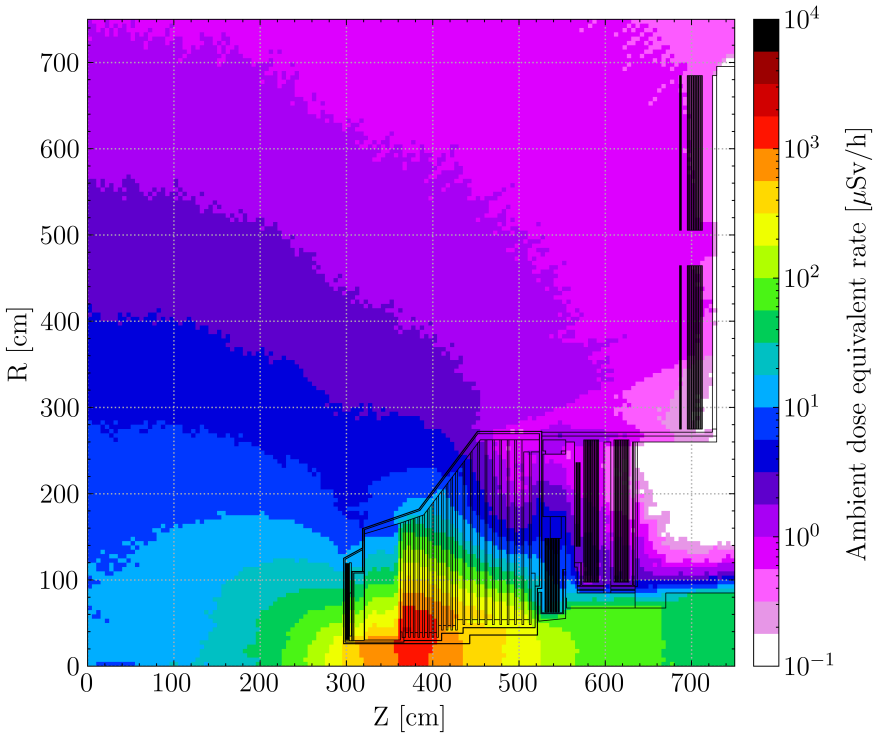

(a) Cooling time of 1 year.

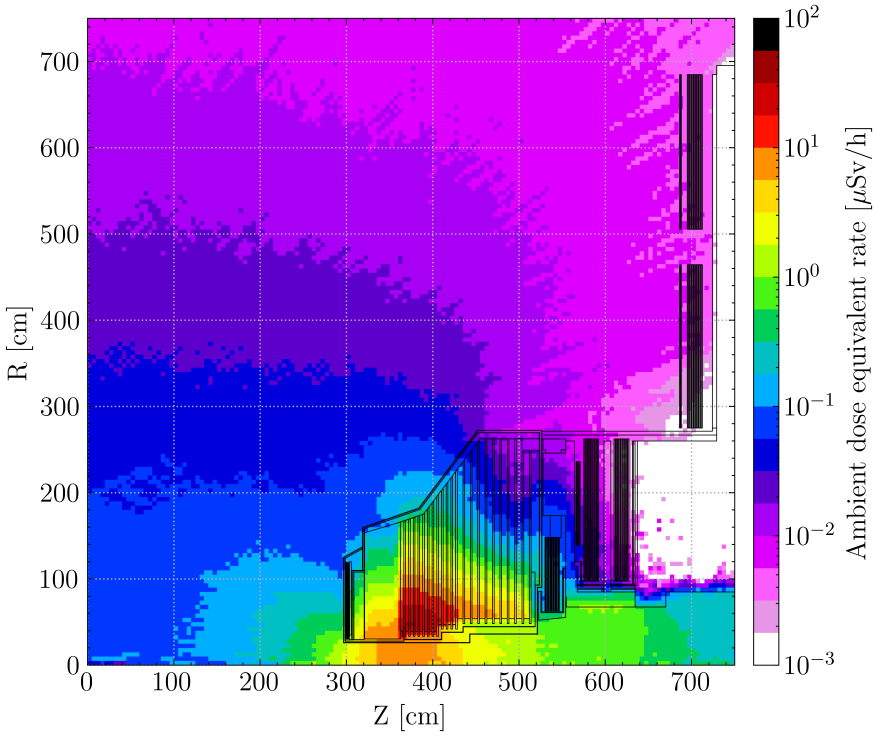

(b) Cooling time of 30 years.

Figure 6.16: FLUKA simulation of residual ambient dose equivalent rates around the CMS endcap nose after 1 year (a) and 30 years (b) from the end of operation of HL-LHC: this map is representative of the configuration in which the CMS detector has been fully opened and the beam pipe has been removed. The results represent an average over the full azimuthal angle.

ometry regions to a different material or to air thus neglecting the radionuclides therein generated.

For the specific case of the activation of HGCal and the assessment of residual dose rates around the CMS endcap nose, one should consider the configuration of the CMS detector during shutdown that allows to perform maintenance or any other activity in close vicinity of HGCal itself. In reality, this situation corresponds to the complete opening of the CMS detector, entailing the opening/removal of the forward shield, the removal of the vacuum chambers, and the translation of the endcaps away from the central barrel elements. In this specific case, residual dose rates levels are completely dominated by the activation of the endcap nose and, given the physical distance from all the other detector elements, contributions from other regions are at most second-order corrections [118]. From the point of view of the simulation of the transport of decay radiation, it is then enough to set to air all the regions except for HGCal. For the residual dose rates calculations, only the worst-case scenario was considered: the steel in HGCal is then assumed to have a 0.3 % cobalt content.

Figure 6.16(a) shows the residual ambient dose equivalent rate levels around the CMS endcap nose after 1 year of cooling time from the end of irradiation of HL-LHC: this situation could be representative of typical maintenance operations. Figure 6.16(b) shows instead the residual ambient dose equivalent rate levels after 30 years of cooling, a case certainly pertinent for radioactive waste considerations. For the latter case, it is clear that the residual dose rate levels at contact are expected to be of the order or well below 0.1 µSv/h for the part of the steel plates that were already good candidates from being cleared from regulatory control. The maximum dose rates for the front plates would be instead of the order of 50 µSv/h. Together with what was discussed for the clearance limits, these results indicate that, even for the penalizing case of a high cobalt content in the steel, the large majority of the non-clearable material would most likely be treated as very low-level radioactive waste and, after proper conditioning, would be disposed of in France as TFA (Très Faiblement Actifs) waste.

A final comment is necessary on the scenario depicted in figure 6.16 and considered in these paragraphs. As far as the present test case is concerned, the analysis of this CMS shutdown configuration could still be performed with FLUKA alone: for studying planned exposure situations with various detector configurations, other additional codes are required. A comprehensive and extensive analysis of several shutdown configurations of CMS for the various Phase II shutdowns is available at Ref. [118].

6.3 Clearance studies for ALICE in Long Shutdown 3 and its decommissioning in Long Shutdown 4

6.3.1 The need for a radiological zoning

During Long Shutdown (LS) 3, the ALICE detector will be upgraded with a new Inner Tracking System (ITS) and a Forward Calorimeter (FoCal) located outside the magnet at approximately 7 m distance from the IP (see Section 1.3.2). The ALICE Collaboration has also expressed an interest in extending the ion programme beyond LS 4 and in replacing the existing detector with a completely new experiment [119]. Independently from the future approval of this proposal, it is not unlikely that the majority of the Run 4 ALICE experiment will have to be decommissioned during LS 4.

For these reasons, two needs emerged: one is to put in place a clearance zoning for interventions during LS 3, and one is to preliminary establish a material-based zoning for decommissioning operations. The latter would allow, for each class of materials used in the experiment, to identify a boundary outside which certain objects/components of that material can be treated as conventional waste after a simplified verification measurement.

6.3.2 Assumptions on the irradiation conditions

For the other LHC experiments, the heavy-ion run has a negligible impact on the activation of materials and on the residual dose rates during shutdown and it can be effectively considered as a cooling period (see Section 4.8): this is certainly not the case for the ALICE experiment. In addition, the study had to take into account differences in the detector configuration between Run 3 and Run 4 so at least two sets of simulations had already been foreseen. For the reasons above, the collision profile had to be carefully computed by compromising between a more realistic description of the irradiation conditions and the overall efficiency and conservativeness of the finally simulated results. It was opted to separately consider the lead-lead run periods from proton-proton and proton-lead periods, the latter being taken into account only in an approximate way as further discussed in the section below: this finally led to four different simulation runs, one for each considered run type and one for each operational period (one till LS 3, and one till LS 4).

The study here presented was performed before the extension of Run 3 by an additional year had been announced and thus the luminosity forecast used for the computation of the collision profile [120] only considered three operational years for both Run 3 and Run 4. The provisional integrated luminosities [120] were $200\,\mathrm{pb}^{-1}$ for proton-proton operation, $200\,\mathrm{nb}^{-1}$ for proton-lead operation, and $13\,\mathrm{nb}^{-1}$ for lead-lead operation: it was also assumed that half of this program would have been achieved by the end of Run 3, thus yielding an equal apportionment of the luminosity between the two Runs. Assuming that the colliding beams would have an energy of 6.8 ZTeV, the cross sections used to compute the collision rates were 80 mb, 2 b and 8 b respectively

for proton-proton, proton-lead and lead-lead operation to remain on the conservative side [120].

Since the ion operation period had to be taken into account, the computation methodology of the irradiation profile was different from that of the studies discussed so far and corresponds to the first approach outlined in Section 4.8. For each year, a total of 160 and 28 days of operation were respectively assumed for the proton and ion run (whether proton-lead or lead-lead) and the ion period was always considered at the end of the operational year: the possible short cooling times between the proton and ion period were neglected for simplicity. With a fixed number of operational days, average instantaneous luminosities were calculated based on the foreseen yearly integrated luminosities, and the average collision rates were then computed for each period by multiplying with the appropriate cross section. For both Run 3 and Run 4, proton-lead collisions were assumed to be performed only at the end of the first year while lead-lead collisions were assumed to take place at the end of the second and third years.

With the integrated luminosity forecasts and a reasonable structure of the operational year, four collision profiles were computed, one for each simulation run. An overview of the full collision profile is shown in figure 6.17: proton-lead and lead-lead collisions are here illustrated as equivalent proton-proton collisions as detailed in Section 6.3.2. As stated in the study objectives, the main goal of these calculations was to provide a preliminary radiological zoning. The LHC long-term schedule will certainly be updated in the coming years and the schedule of the ion program will be certainly refined: for the final absolute results, the real data on the delivered luminosity would have to be taken into account.

Further discussion on the adopted approximations

As anticipated, the proton-lead run was considered by approximating the proton-lead collision rate with an equivalent proton-proton collision rate, thus allowing to consider proton-proton collisions as the source for the Monte Carlo calculations instead. The main reason for this choice was to keep the number of simulation runs to a reasonable amount: considering separately proton-lead collisions would have meant four additional runs, one for each considered operational period and one for each beam configuration (proton-lead or lead-proton), the latter known with much larger uncertainty than the already uncertain operational year organization. This approach was instead not adopted for lead-lead collisions which were simulated separately.

This approximation is based on the idea of computing a conservative scaling factor from the expected maximum charged hadron multiplicities ($dN_{ch}/d\eta$) over the pseudo-rapidity range $|\eta| \leq 3.0$ [121]. For instance, the proton-proton equivalent collision rate for proton-lead collisions would be computed as

$$\left(\frac{dN}{dt}\right)^{pPb}_{pp\ eq.} = \mathcal{L}^{pPb}_{inst}\,\sigma^{pPb}_{inel}\left[\max_{|\eta|\leq 3.0}\left\{\left(\frac{dN_{ch}}{d\eta}\right)^{pPb}\right\}\Big/\max_{|\eta|\leq 3.0}\left\{\left(\frac{dN_{ch}}{d\eta}\right)^{pp}\right\}\right] \tag{6.1}$$

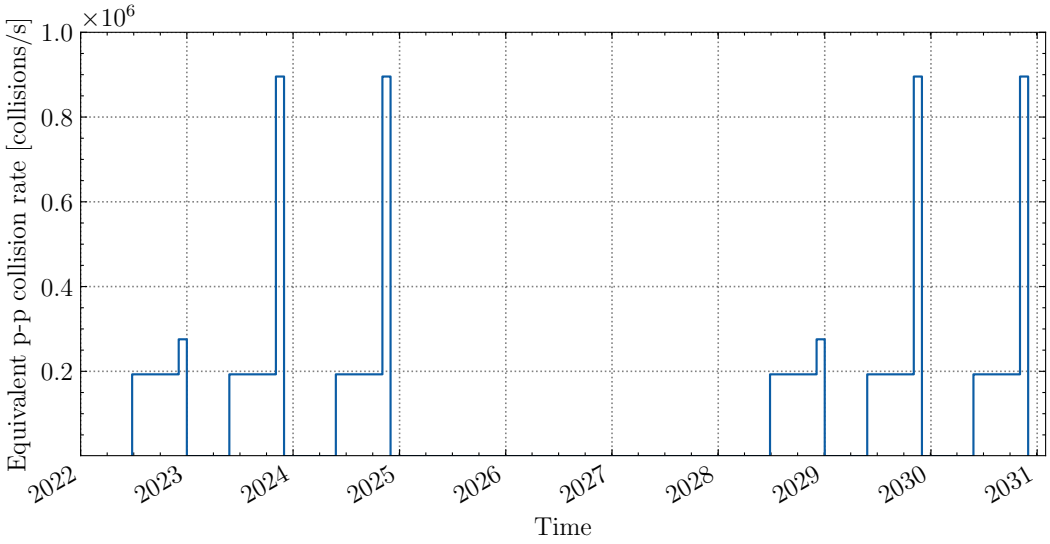

Figure 6.17: Run 3 and Run 4 collision profile for proton and ion physics at ALICE as assumed for the preliminary radiological zoning: proton-lead and lead-lead collisions are illustrated as equivalent proton-proton collisions. The yearly marks on the abscissa refer to January 1st and the LHC long-term schedule corresponds to the one available at the time of the study.

where $\mathcal{L}_{inst}^{pPb}\,\sigma_{inel}^{pPb}$ gives the proton-lead collision rate. The derivation of the conservative scaling factors is discussed in the following paragraph.

Simple considerations from a dedicated FLUKA calculation

Charged hadrons multiplicities from proton-proton, proton-lead and lead-lead collisions were thus estimated with FLUKA and the DPMJET-III event generator [65, 66] in a dedicated study [121]. Collisions were considered in vacuum and customized FORTRAN user routines were used to iterate over the FLUKA particle stack before any transport of the collision secondaries is performed. The estimation of the desired quantities in a user-defined histogram "à la Monte Carlo" is very briefly summarized below.

Let n, $j = 1, \ldots n$, and c_j respectively be the number of pseudorapidity bins for the desired histogramming, the index identifying a given bin, and the value of an auxiliary counter array for the j-th bin for the estimation of the mean and standard deviation (sometimes referred to as first and second moments) for each bin of the histogram. Let e_j and s_j be instead the counters for the estimation of the mean and standard deviation. At the beginning of a new primary history, that is a collision event in this case, the counters c_j are zeroed: if a charged hadron has pseudorapidity within the j-th bin, the c_j counter is then increased by the corresponding statistical weight of the particle. At the end of the iteration over the collision secondaries from a primary event, the counter arrays for the estimation of the first moment are updated ($e_j = e_j + c_j$) and so are the ones for the second moment ($s_j = s_j + c_j^2$): this latter step is crucial to preserve possible correlations within the same primary event [61]. At the end of all the

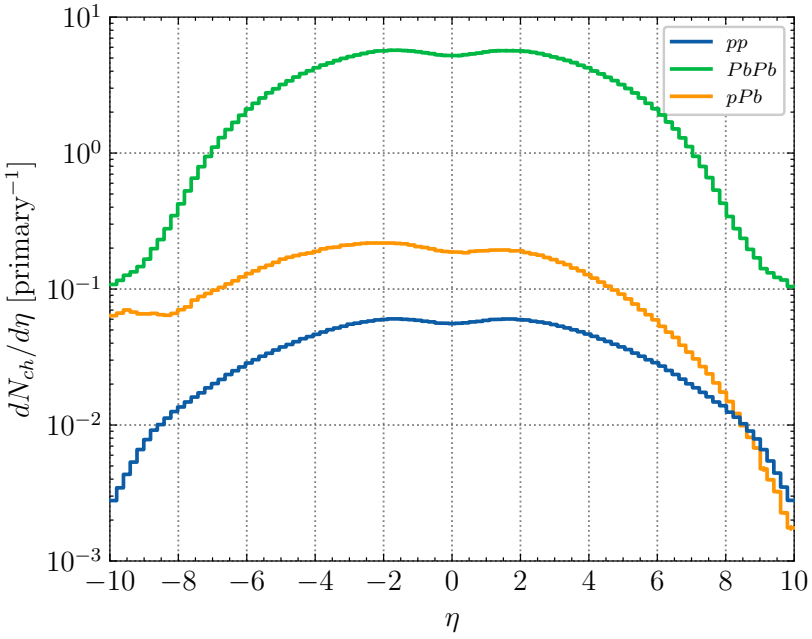

Figure 6.18: FLUKA simulation with the DPMJET-III event generator [65, 66] of the expected charged hadron multiplicities for head-on proton-proton, proton-lead, and lead-lead collisions at 6.8 ZTeV/beam: in the simulation for proton-lead collisions, the proton beam is taken as travelling along the positive direction of the beam axis.

$N_{prim.}$ primary histories, the counts of the j-th bin are normalized by the total primary weight and by the j-th bin width such that the estimated number of particles having pseudorapidity within the j-th bin will be

$$\frac{\Delta N}{\Delta \eta_j} = \frac{e_j}{N_{prim.}\ \Delta \eta_j} \tag{6.2}$$

while, for the central limit theorem [61] (see Section 3.1), the corresponding uncertainty for the j-th bin will be given by

$$\sqrt{\frac{1}{N_{prim.}-1}\left[\frac{s_j}{N_{prim.}\Delta\eta_j^2} - \left(\frac{e_j}{N_{prim.}\ \Delta\eta_j}\right)^2\right]} \tag{6.3}$$

This approach has been illustrated by referring to the estimation of the pseudorapidity distribution of charged hadrons but it may be applied to the estimation of other particle distributions.

Figure 6.18 illustrates the estimated charged hadron multiplicities for proton-proton, proton-lead and lead-lead collisions at 6.8 ZTeV/beam. Based on the maximum value of the distributions within $|\eta| \leq 3.0$, the obtained scaling factors for proton-lead and lead-lead collisions are approximately 20.0/6.0 and 550/6.0 respectively.

These scaling factors have been computed in a very simplified case and do not take into account the interaction of the collision secondaries with the surrounding detector materials. Since the validity of this approximation clearly may depend on the region of interest, its application was first tested in a dedicated full FLUKA simulation study for

ALICE [121]. As far as the central detectors are concerned, the study showed that this simplifying approach gives results in excellent agreement with what would be obtained by simulating directly the protons-lead or lead-lead collisions: the overestimation in the detector acceptance is less than few % while it can be up to a factor 1.25 for $3.0 < |\eta| < 5.0$ and a factor 2.0 for $|\eta| \geq 5.0$.

6.3.3 Calculation approach

Simulations were performed with the FLUKA Monte Carlo code[8] and the fluence conversion coefficients method in order to establish a radiological zoning for LS 3 and decommissioning operations of the Run 4 ALICE detector in LS 4. Four different simulations were run, one for each shutdown and for each type of colliding beams as previously discussed.

As detailed in the previous section, four different irradiation profiles (one for each set of simulations) were computed and cooling times of 1 week, 1 month and 3 months from the end of the full irradiation were considered for each shutdown scenario. This means that, for a given cooling time, the estimated levels of induced activation from proton-proton and lead-lead collisions were then summed to obtain the total amounts at the end of the full irradiation period.

Coefficients from fluence to multiples of Swiss clearance limits (LL) were computed for different representative materials such as stainless steel 304L, concrete (with europium traces), copper oxygen-free electronics, pure copper, aluminium alloy 6060, two electronic compositions, pure silicon, lead-tungstate, and pure lead: the detailed material compositions are listed in Appendix C.1. Considering the combination of irradiation profiles, cooling times and material, a total of 120 sets were calculated.

The transport thresholds were optimized for activation calculations, meaning that charged hadrons were transported down to 1 MeV, neutrons down to thermal energies and electrons, positrons, and photons were not transported. Approximately 100 000 and 800 primary events were simulated for each of the proton-proton and lead-lead simulations respectively.

To fully profit from the most up-to-date simulation geometry of the Run 3 and Run 4 ALICE detector, the simulations were performed in collaboration with the ALICE Software, Physics Data Processing and Computing (SDC) Coordination. The ALICE Collaboration has developed over the years a simulation framework based on the concept of Virtual Monte Carlo (VMC) [122] to allow different Monte Carlo simulation programs to run without changing the geometry definition, the detector response, and input and output formats. This has the great advantage that particle tracking is performed in a geometry which follows the design and upgrade of the detector and that provides, at any given time, the most reliable simulation of the detector [123].

[8]The code version 4-1.1 as hosted by the FLUKA.CERN collaboration was used for this set of simulations.

6.3.4 Main results

Figure 6.19 illustrates the spatial distribution of the multiples of LL for stainless steel 304L in the ALICE experimental cavern at a cooling time of 1 week in LS 4 after the end of irradiation. Since the simulations were performed within the ALICE Virtual Monte Carlo framework, the geometry overlay that is shown in the different maps has to be intended as only qualitative, particularly for what concerns the inner detectors.

From a first overview, the expected residual activation levels are rather contained, even at the end of the full irradiation and for very short cooling times. Thanks to this fact and owing to the equal structure of the irradiation profile for the two Runs, the discussion can be focused on LS 4 only: the results of the simulations for LS 3 [124], not reported for brevity, have indeed shown equal if not slightly lower activation levels, and thus any consideration that will be made for LS 4 can be similarly applied to LS 3. In addition, no significant changes could be observed due to the installation of the new ITS because of its very low material budget.

As is often the case, steel can be taken as the paradigm for the worst-case conditions. The radiological maps for the multiples of LL at 3 months cooling time in LS 4 for concrete, copper oxygen-free electronics, aluminium alloy 6060, the two electronics compositions, pure silicon and lead-tungstate are all reported in Appendix C.3: the results for pure copper are in practice indistinguishable from those of copper oxygen-free electronics and have been omitted. It can also be noticed by comparing figure 6.19 with figure C.4(a) and (b) that the residual activation levels at longer cooling times only slightly differ from those at 1 week cooling time.

The bulk of the activation is concentrated along the beam axis, particularly in correspondence of the points where collision secondaries are intercepted, such as the conical composite absorbers shielding the forward arm and beam pipe flanges: figure 6.19(c) provides a better view in the central detectors. It can clearly be understood that the boundary at which $LL = 1.0$ is practically including the vacuum chamber only, while the multiples of LL remain below 0.6 in all the other regions for $R > 40\,\text{cm}$.

In conclusion, thanks to the fluence conversion coefficients method it was possible to draw a preliminary zoning for clearance and decommissioning operations at ALICE in LS 3 and LS 4. The studies were performed with the luminosity forecast available at the time and would have to be revised once more precise or real estimates are available. For this reason, a safety factor of at least 2.0 was recommended: even in that case, for the majority of the considered classes of materials, the boundary at which they would be still considered as radioactive in the legal sense would remain at a distance of approximately 50 cm from the beam axis.

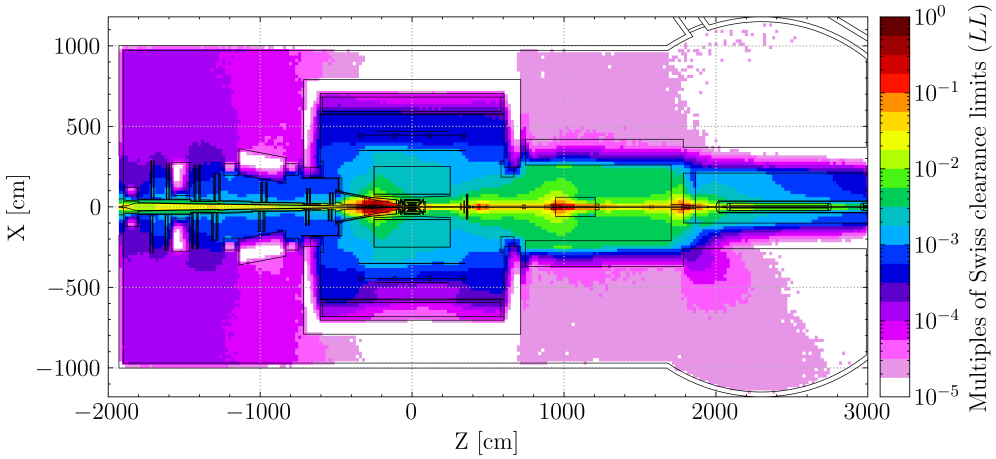

(a) Horizontal projection.

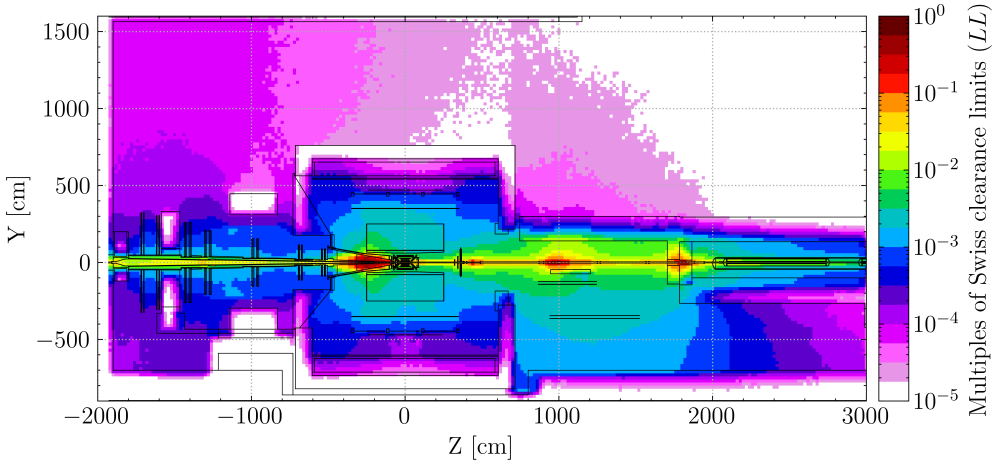

(b) Vertical projection.

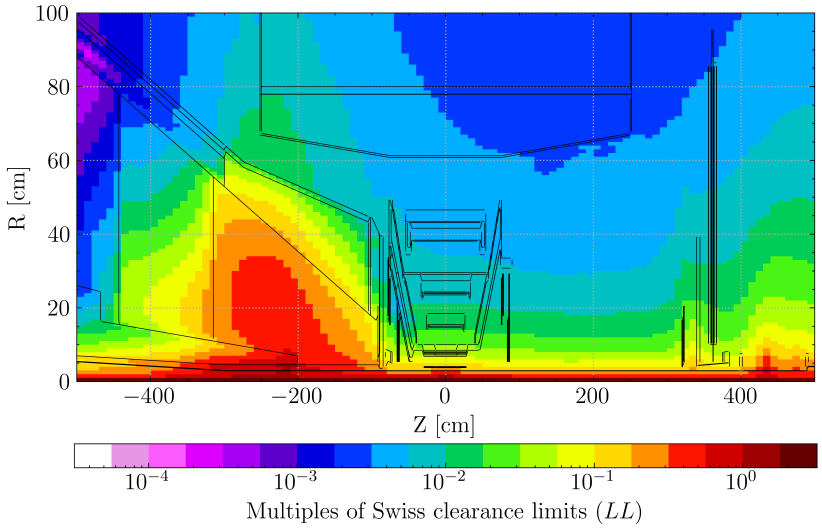

(c) Close-up in the central detector region.

Figure 6.19: FLUKA simulation with the fluence conversion coefficients code of the multiples of Swiss clearance limits (LL) for stainless steel 304L in the ALICE experimental cavern at a cooling time of 1 week in LS 4. The geometry overlay is only qualitative.

6.4 Radiological studies in preparation to the LHC pilot beam

6.4.1 Introduction and motivation

After the major upgrades during the recent Long Shutdown (LS) 2, a pilot beam run was scheduled and completed between October 18 and November 1, 2021, as part of the commissioning in preparation to the restart of the LHC with Run 3 in early 2022.

Owing to the fact that the pilot beam was scheduled still within a shutdown period, maintenance and other activities in the major experimental installations were ongoing in the days prior to and following the test. From a practical point of view, this meant that the four large LHC experiments were in a configuration differing from their nominal one: ATLAS and CMS in particular required a dedicated radiation protection assessment in view of their unique arrangements.

The CMS detector was almost in the nominal shielding configuration: the full detector was closed, the shielding plug of the PX56 access shaft was sealed, and the forward shield had been closed, but the HF detector was still in its parking position and thus not yet in place. The ATLAS detector, instead, was in a much less shielded condition: while on the so-called side A[9] of the experimental cavern (from the Interaction Point 1, or IP 1, towards IP 8) the forward shield was removed and the muon wheel was moved, on the so-called side C (from IP 1 towards IP 2) the endcap detector was moved in its standard opening position, the forward shield was removed, the endcap toroid magnet had been moved, a temporary steel beam pipe together with its support was installed, and light infrastructures were still present along the beam line. Photos representative of the two configurations are shown in figure 6.20.

The radiological assessment had a twofold objective. Given the fact that the temporary infrastructures installed had never been exposed to the beam and at the end of the pilot run would have been removed from the experimental areas, it was first necessary to estimate the levels of induced activation for radiological characterization purposes. Then, an evaluation of the levels of prompt radiation was also required due to the less shielded conditions. Before presenting the main results, the assumptions of the study and the adopted methodology are here described.

6.4.2 Application of the fluence conversion coefficients method for the evaluation of radiological zoning

The beam parameters for the pilot beam run were proposed by the Beam Operation group at CERN and were evaluated by the Radiation Protection group in close collaboration with the Technical Coordination of all the LHC experiments.

[9]With the conventional coordinate systems adopted by the LHC experiments (see Section 1.3), the side A of the experimental cavern corresponds to $Z > 0$, while the side C corresponds to $Z < 0$.

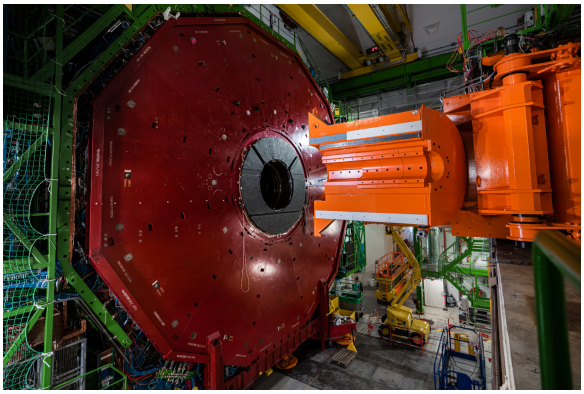

(a) CMS forward shielding during closing procedure. The HF detector is not in place.

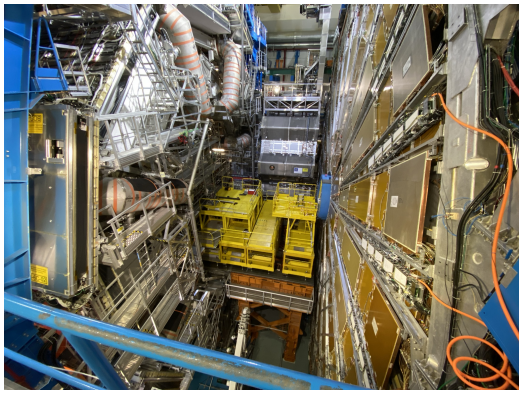

(b) Side C of the ATLAS experimental cavern with the open detector and the displaced toroid. Temporary infrastructures are visible.

Figure 6.20: Photos illustrating the configuration of the CMS and ATLAS experiments during the LHC pilot beam run between October 18 and November 1, 2021.

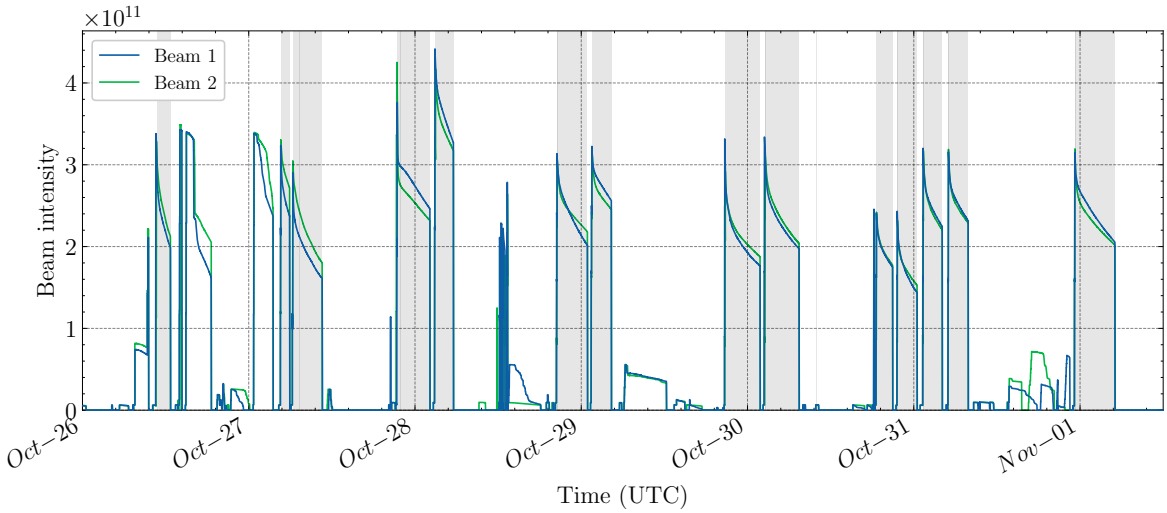

Figure 6.21: Number of protons (intensity) of the two beams circulating in the LHC machine during the second half of the pilot beam period as retrieved from the CERN Accelerator Logging Service: the shaded areas indicate collisions during stable beam operation.

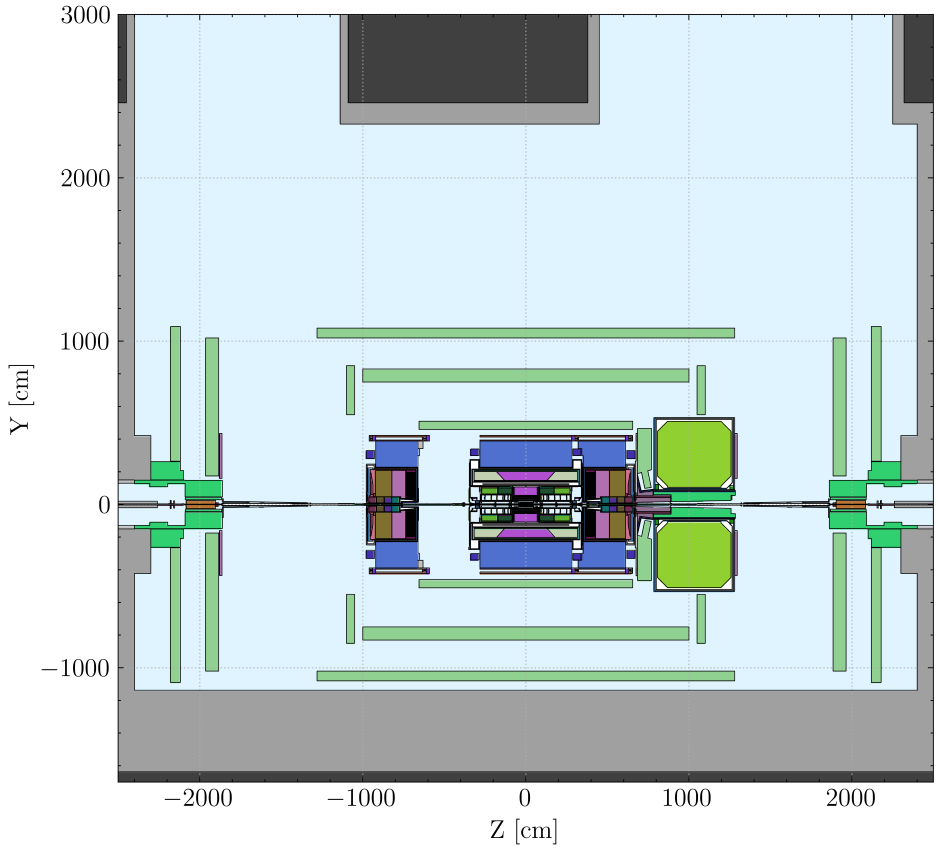

(a)

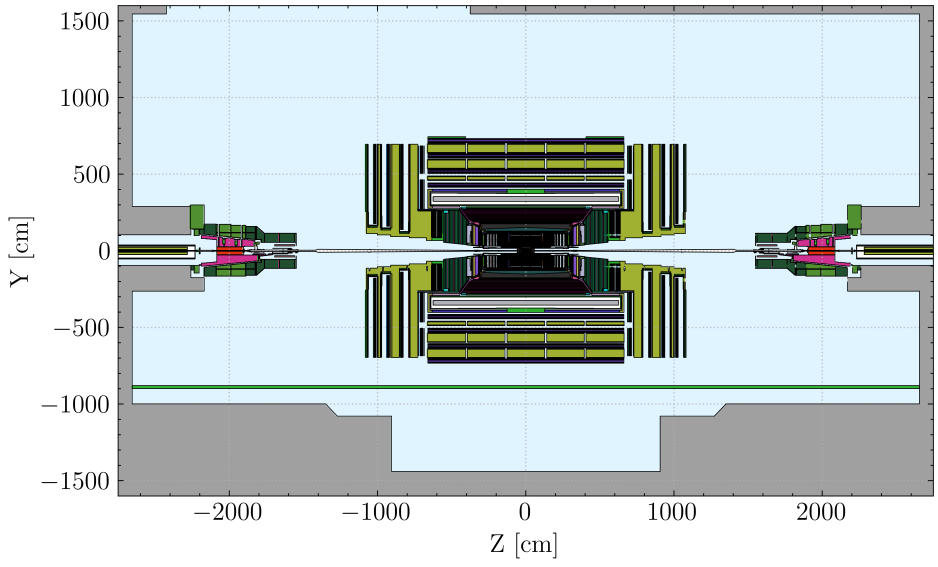

(b)

Figure 6.22: Vertical cut of the FLUKA simulation geometries of the (a) ATLAS and (b) CMS detectors as in their configuration during the pilot beam period.

As far as the beams are concerned, it was foreseen that they would have circulated at the injection energy of 450 GeV and that collisions would only have been head-on. The maximum allowed number of protons in each beam was assumed to be 3×10^{11}, corresponding to three nominal bunches of 1×10^{11} protons each. The exact machine performances could not be known a priori: a continuous irradiation period of one day, corresponding to four consecutive shifts with a beam lifetime of 6 hours, at the maximum foreseen collision rate of 2.5 kHz was conservatively assumed for the preparatory studies. Further considerations on the limitation on the beam intensity are discussed in Section 6.4.3.

Collisions were successfully attained from October 26, 2021, and figure 6.21 shows the total number of protons of the two beams during the second half of the pilot beam period: the shaded areas indicate the periods of stable beam operation with collisions in the LHC experiments. The average beam lifetime was approximately 3 hours (maximum 5 hours) while the average and peak collision rates during the various fills with stable beams were 1.25 kHz and 2.5 kHz respectively.

The radiation protection assessment was performed with the FLUKA Monte Carlo code [10] and applying the fluence conversion coefficients method to assess the levels of induced activation in ATLAS and CMS. Figure 6.22 illustrates the FLUKA simulation geometries of ATLAS and CMS with the detectors in the configuration of the pilot beam run: extensive modifications were performed to the nominal simulation input files to best match the removal and/or displacement of the major components. Due to the innate complexity of the problem, the detailed description of temporary installations in the experimental cavern in the simulation geometry is not feasible nor practical. With similar consideration as those made for the studies on the CMS forward shield reinforcement in Section 6.1.4 and in light of the extensive discussion in Chapter 4, the application of the fluence conversion coefficients method has in this case two unmatched advantages. First, the usage of an event-based method would not be possible at all since, relying on the events of creation of radionuclides, it would require that the concerned objects (i.e. the infrastructures in this case) are well represented in the simulation geometry: fluence-based methods remain the only viable solution. Second, the quantities of interest need to be estimated over extended regions of space and thus good visualization capabilities are fundamental (see Section 6.4.3 and figures therein).

Since the goal of the assessment was to ultimately verify that the temporarily installed materials complied with clearance requirements, multiples of Swiss clearance limits (LL) were estimated for the specific irradiation conditions for representative materials, namely the aluminium alloy 6060 (AL6060), the copper oxygen-free electronics (Cu OFE) and the stainless steel alloy 304L (St. Steel 304L): their composition is summarized in Appendix C.1. The cooling times considered from the end of the irradiation ranged from one day to several weeks. In order to assess the prompt radiation field owing to the colliding beams, the ambient dose equivalent rate ($\dot{H}^*(10)$, see Section 2.4) was also estimated.

[10] The code version 4-2.2 as distributed by the FLUKA.CERN Collaboration was used for the simulations.

6.4.3 Main results

Considerations on induced activation

As an example, figure 6.23 shows the spatial distribution of the multiples of LL for the aluminium alloy 6060 at one day of cooling from the end of the assumed irradiation in the ATLAS experimental cavern as obtained from a FLUKA simulation with the fluence conversion coefficient method: the results are averaged over the full azimuthal angle.

In the case of ATLAS it is clear that, despite the open configuration, the bulk of the activation is still concentrated along the beamline and is very limited: the line at which $LL = 0.001$, thus well below the clearance limits, essentially lies within the vacuum pipe with the exception of few locations. Figure 6.24 shows the multiples of Swiss clearance limits for the aluminium alloy 6060, stainless steel 304L and copper oxygen-free electronics as a function of the distance from the IP: the values refer to a projection at 40 cm distance from the beam axis and at a cool-down of one day from the end of the assumed irradiation. The induced activation in a material at a given location clearly depends on the particle species and their energy spectrum that are present: although in this case the practical differences between the various materials are minimal, the calculation approach allowed to understand which is the most penalizing material at any given distance from the interaction point, as clearly depicted in figure 6.24.

Similar considerations can be drawn for the CMS experiment. Figure 6.25 shows the map of the multiples of LL for copper oxygen-free electronics at a cooling time of one day from the end of assumed irradiation. Luckily for the CMS experiment, no temporary infrastructures were installed along the beamline so it was more relevant to consider the induced activation on the components that are located in the proximity of the side walls. In this regard, figure 6.26 illustrates the multiples of LL for various materials and for different cooling times as a function of the radial distance from the beam line: the radial projection is considered at a 1500 cm distance from the interaction point. Also in this case, the absolute values of the additional induced activity are lower enough compared to the clearance limits to have practically little or no consequences. It is also very relevant to point out, particularly commenting on figure 6.26, that the fluence conversion coefficients method can efficiently identify the most penalizing case not only at a given location, but also for each cooling time: for instance, copper oxygen-free electronics provides conservative estimates at the cavern walls for cooling times shorter than one day, while already at one week the worst case is represented by stainless steel 304L.

Considerations on prompt radiation

As anticipated, another important objective of the simulations was to assess the level of prompt stray radiation from the collision events. Figure 6.27 gives an overview of the prompt ambient dose equivalent rate in the ATLAS and CMS experimental caverns for a peak collision rate of 2.5 kHz. Albeit the open and less shielded arrangement of the two experiments, at injection energy and with beam intensities that are lower

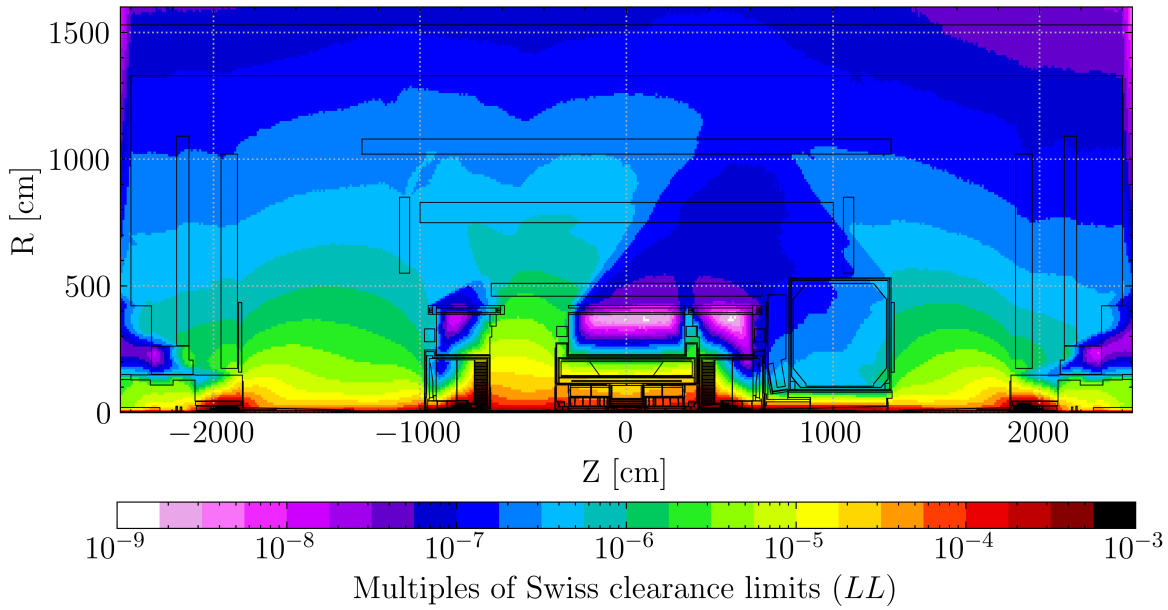

Figure 6.23: FLUKA simulation with the fluence conversion coefficients method of the multiples of Swiss clearance limits (LL) for the aluminium alloy 6060 in the ATLAS experimental cavern in its configuration during the pilot beam run: a one-day cool-down is considered from the end of irradiation. The results represent an average over the full azimuthal angle.

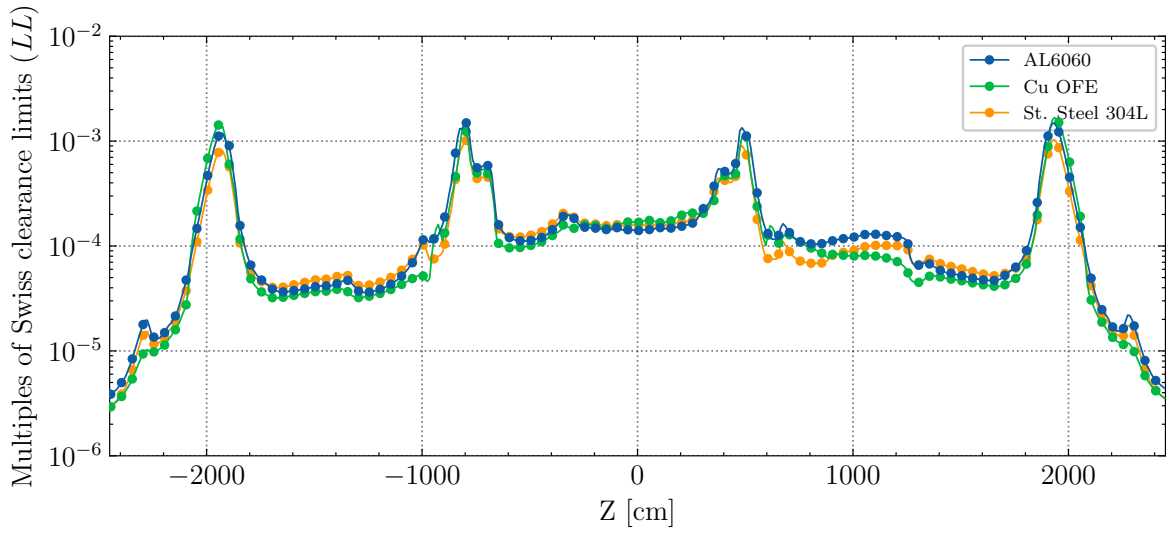

Figure 6.24: FLUKA simulation with the fluence conversion coefficients method of the multiples of Swiss clearance limits (LL) for various materials in the ATLAS experimental cavern in its configuration during the pilot beam run: the longitudinal projection is considered at a 40 cm distance from the beamline and a one-day cool-down is considered from the end of irradiation. The relative statistical uncertainty is below 0.1% and not shown for better clarity.

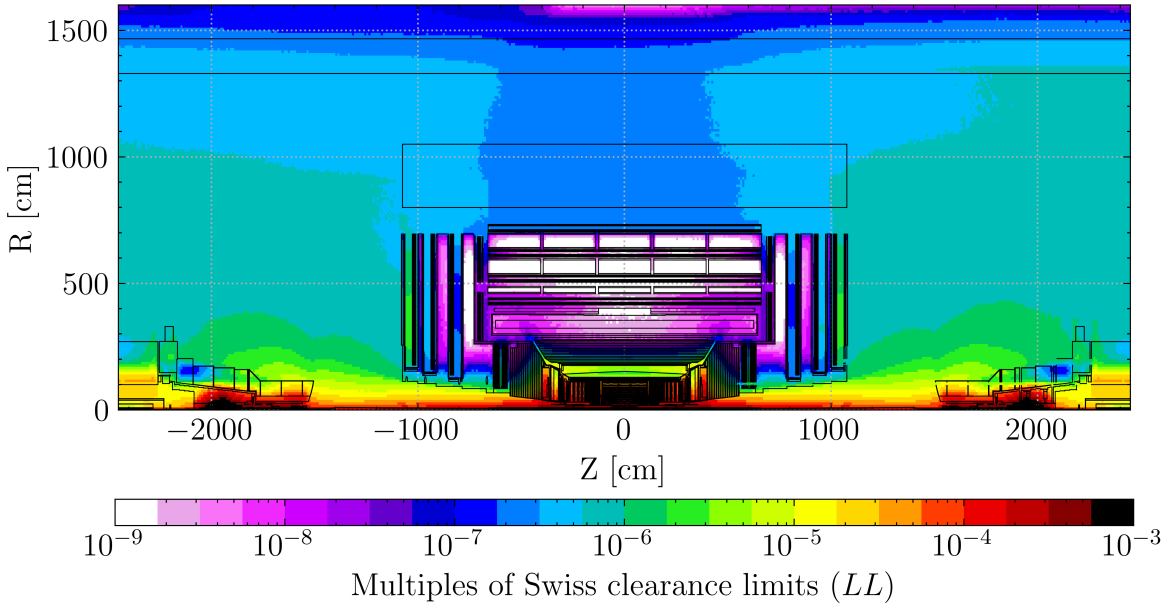

Figure 6.25: FLUKA simulation with the fluence conversion coefficients method of the multiples of Swiss clearance limits (LL) for oxygen-free electronics copper in the CMS experimental cavern in its configuration during the pilot beam run: a one-day cool-down is considered from the end of irradiation. The results represent an average over the full azimuthal angle.

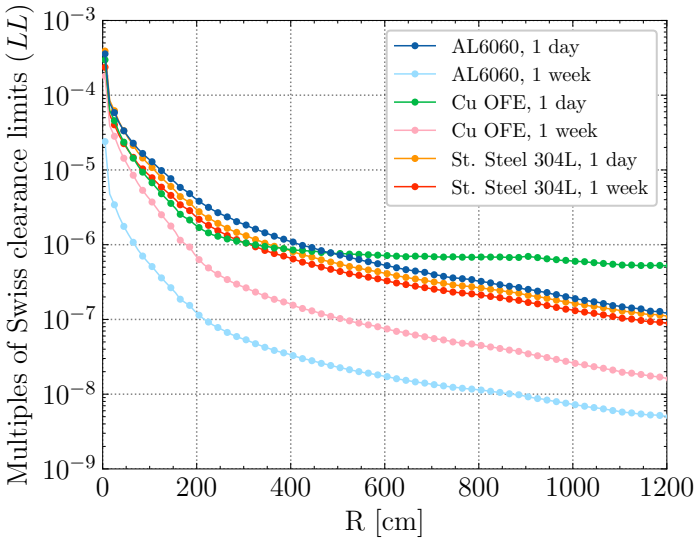

Figure 6.26: FLUKA simulation with the fluence conversion coefficients method of the multiples of Swiss clearance limits (LL) for various materials in the CMS experimental cavern in its configuration during the pilot beam run: the radial projection is considered at a 1500 cm distance from the interaction point and at one day and one week cooling times from the end of irradiation. The relative statistical uncertainty is below 0.1% and not shown for better clarity.

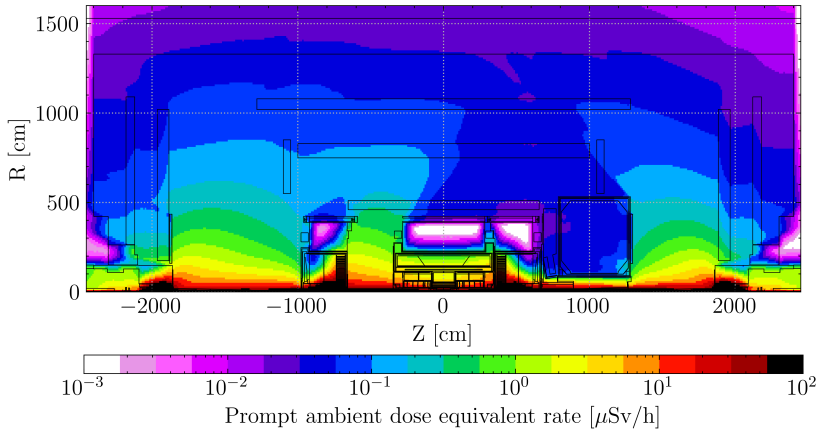

(a)

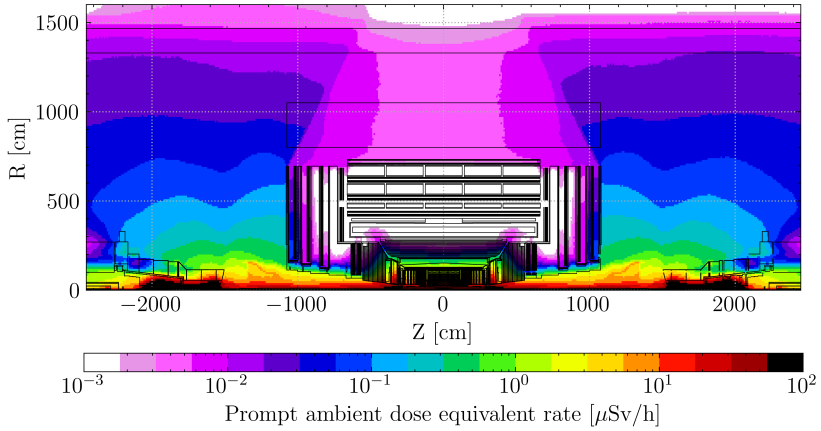

(b)

Figure 6.27: FLUKA simulation of the prompt ambient dose equivalent rate, $\dot{H}^*(10)$, in the (a) ATLAS and (b) CMS experimental caverns for the irradiation conditions of the pilot beam. The results represent an average over the full azimuthal angle.

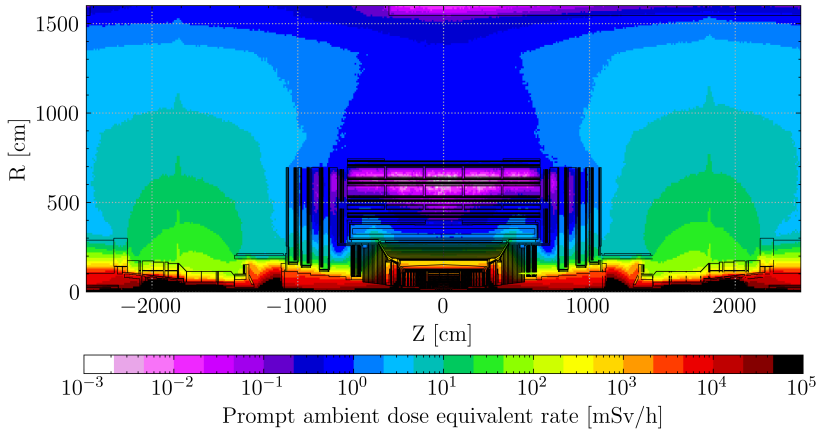

Figure 6.28: FLUKA simulation of the prompt ambient dose equivalent rate in the CMS experimental cavern in nominal run conditions. Although inappropriate, values above the threshold for deterministic effects are still represented as ambient dose equivalent and not absorbed dose to maintain a reference with the low dose values. The results represent an average over the full azimuthal angle.

than what is attained in nominal conditions, the prompt radiation due to collisions does not impose additional protection measures. In support to the previous argument, figure 6.28 illustrates the ambient dose equivalent rate in the CMS experimental cavern during nominal run conditions[11] and allows to appreciate the difference by several orders of magnitude.

It was then immediately clear that the prompt radiation due to collisions did not demand additional measures with respect to nominal operation. As a general fact, prompt radiation due to unexpected beam losses or accidental scenarios is instead far more constraining than prompt radiation due to collisions, even in the case in which the beams are circulating at injection energy. As a generic, yet valuable, example, figure 6.29 shows the FLUKA simulation of effective dose (assuming an anterior-posterior irradiation) from the full loss of proton beams at LHC injection (450 GeV) and design (7 TeV) energies for probe (1×10^{10} protons) and nominal (1×10^{11} protons) bunch populations on a generic copper target: as long as it is representative of a bulky and heavy object against which the beam could be mis-steered (for instance the TAS, or a quadruple) the choice of material is of secondary importance for this kind of considerations. As illustrated in figure 6.29, for the case of one nominal 7 TeV bunch, one would hypothetically reach values close to or above the dose limit for 12 consecutive months for non-occupationally exposed persons (1 mSv), even at the distance of several tenths of meters from the impact point: the real situation is much more complicated and depends on several other factors, but this simple reasoning not only highlights that beam losses are far more constraining, but also gives an explanation on the limit on the maximum number of protons foreseen for the 2021 LHC pilot beam given the LHC experiments configurations.

Operational radiation protection implications

As discussed in the previous paragraphs, the good visualization capabilities and flexibility of the fluence conversion coefficients method allowed the comparisons of induced activity levels in various materials and at different cooling times: it is important to add that the simulation results also provided valuable feedback to operational radiation protection. The first practical implication of these studies was the optimized installation of dedicated sets of activation samples to confirm the radiological zoning preliminary established on the basis of the Monte Carlo calculations. Aluminium, copper and steel samples were installed either along the beamline, or directly on the components that would then have been removed from the experimental areas. The samples were retrieved immediately after the pilot beam and analysed with a High-Purity Germanium (HPGe) detector but no specific activity was measured by gamma spectrometry above the minimum detectable activity (MDA) which were significantly lower than the respective clearance limits [125, 126].

[11] Nominal run conditions means in this case a fully closed detector, 6.8 TeV beams, and an instantaneous luminosity of $2.0 \times 10^{34}\,\mathrm{cm}^{-2}\,\mathrm{s}{-}1$ (corresponding to a collision rate of approximately 1.6 GHz).

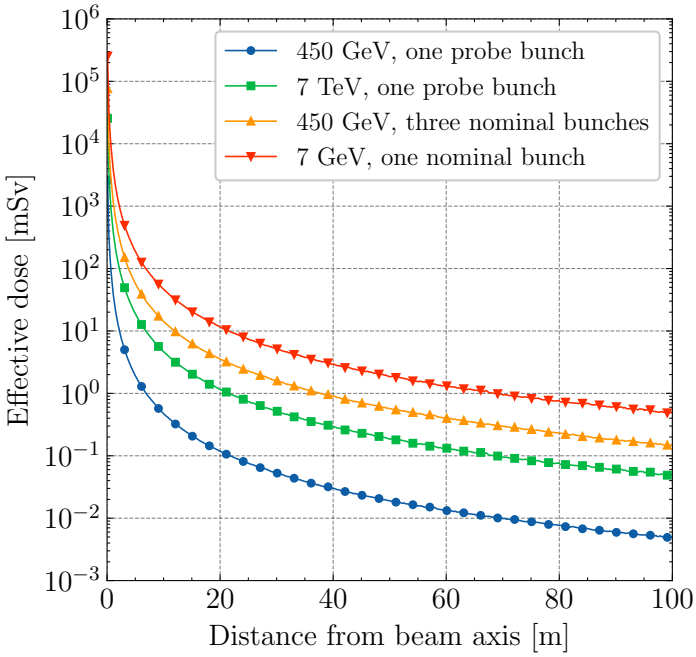

Figure 6.29: FLUKA estimate of the effective dose (anterior-posterior irradiation, ICRP116 [55]) from the full loss of proton beams on a generic copper target at injection and design energies for probe and nominal bunch populations. Although inappropriate, values above the threshold for deterministic effects are still represented as effective dose and not absorbed dose to maintain a reference with the low dose values.

6.4.4 Further consideration on the simulation assumptions

At the end of this section, it is pertinent to spend a few words on the conservativeness of the study assumptions. Among the parameters that were initially considered for the study, the beam energy and intensity had been fixed with the Beam Operation group, but the exact machine performance could not be known a priori. The conservativeness of the irradiation history adopted in the preliminary study had to be assessed a posteriori, in the immediate aftermath of the pilot beam: to facilitate the evaluation, the time evolution of the activity of an extensive set of radionuclides was computed analytically by considering a time-dependent production term derived from a more realistic irradiation history in one case and as assumed for the Monte Carlo simulations in the second case. Considering the time scales of the beam lifetime during the pilot beam, this set of radionuclides comprised short and medium-lived ones that are radiologically relevant for waste considerations and that can be produced in typical materials ranging from plastics, aluminium, copper, and steel.

The realistic radionuclide production rate can be expressed as the radionuclide yield per collision multiplied by the collision rate dN_{coll}/dt which, with the information on the beam intensities and beam parameters, can be at first order calculated by estimating the instantaneous luminosity with equation 1.3 and multiplying it by the appropriate cross section. Owing to the collisions being head-on, the geometric reduction factor can be reasonably and conservatively considered equal to 1.0 [1]. The relativistic gamma

factor is trivially computed once the beam energy is known, the revolution frequency in the machine is a known constant, while the number of colliding bunch pairs (two for the majority of the pilot beam run) is determined by the specific filling scheme. The value of β^* was equal to 11 m in both IP 1 (ATLAS) and IP 5 (CMS), while the transverse emittance ε_n was in the order of 1.5 µm. The values of the measured bunch populations and beam parameters were retrieved using the graphical interface of the CERN Accelerator Logging Service TIMBER [86]: figure 6.21 already showed the two beam intensities as the sum over all bunch populations of each beam.

Figure 6.30 shows for instance the activity evolution computed with the realistic and simplified production terms for ^{11}C ($T_{1/2}$ = 20.37 min), ^{24}Na ($T_{1/2}$ = 14.96 h), ^{52}Mn ($T_{1/2}$ = 5.595 d), ^{57}Ni ($T_{1/2}$ = 35.60 h), and ^{64}Cu ($T_{1/2}$ = 12.70 h): this comparison has to be intended as relative, meaning that the activities have been normalized to a production yield of one radionuclide per collision and thus shown in arbitrary units. The simplified irradiation history assumed for the simulations clearly led to the estimation of the activity of short-lived radionuclides within large safety margins, while being reasonably conservative for the medium to long-lived ones [125, 126].

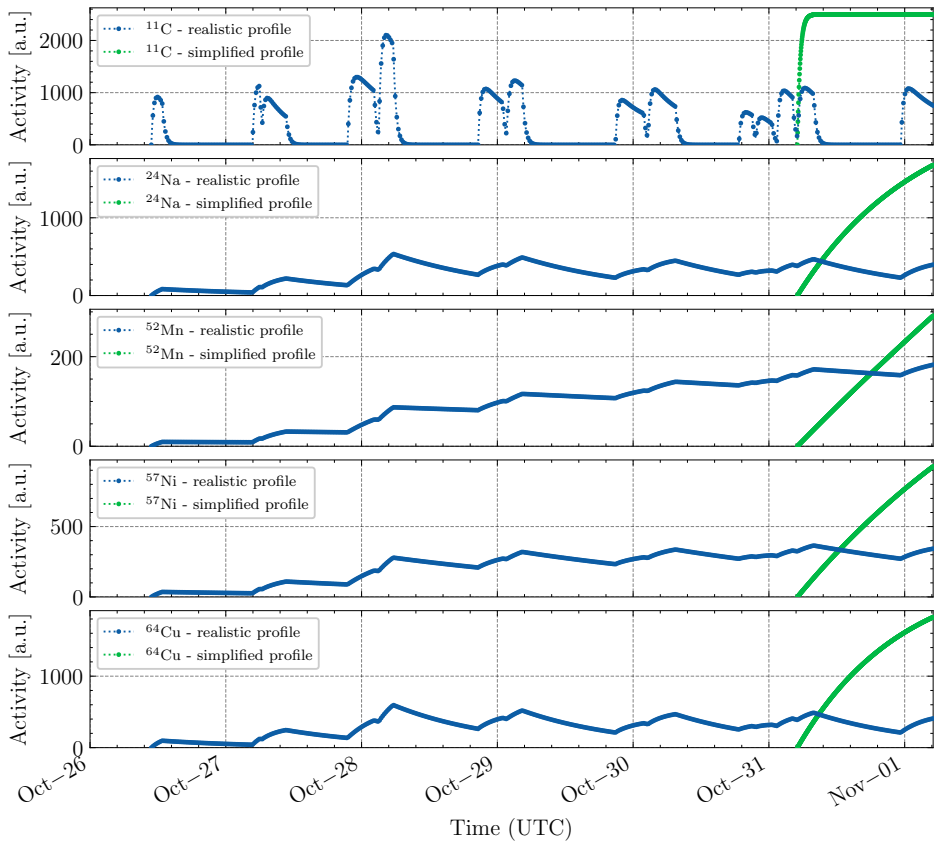

Figure 6.30: Example of the activities of ^{11}C, ^{24}Na, ^{52}Mn, ^{57}Ni, and ^{64}Cu activities computed with the realistic and simplified production terms. The activities of each radionuclide have been normalized to a production yield of one radionuclide per collision and thus shown in arbitrary units.

Chapter 7

Conclusions

7.1 Summary

The CERN Large Hadron Collider (LHC) located between the Franco-Swiss border is currently the largest existing particle accelerator and collider: proton and ion beams can be accelerated in opposite directions to the record energy of 6.8 ZTeV and made collide at dedicated interaction points where the large high-energy physics detectors, ATLAS, ALICE, CMS, and LHCb, have been built to perform precision measurements of the Standard Model and searches for new physics.

The discussion of this work started with an overview of the LHC and LHC experiments in Chapter 1. Their radiation environment (and in general that of high-energy particle accelerators) is characterized by various particle species whose energies can span several orders of magnitude, from fractions of meV to thousands of GeV: owing to these features, this radiation environment is responsible for inducing residual activation in detector and infrastructure components. Since it impacts the technical operation of the accelerators and experiments, the calculation of induced radioactivity is an essential part of various steps of the life cycle of any component to be installed, from the selection of appropriate materials in the design phase, to the establishment of appropriate protection measures during maintenance and handling of radioactive objects, and to the assessment of their appropriate disposal pathways and related costs. Furthermore, the start of the High Luminosity LHC (HL-LHC) is planned for 2029 and it is expected that instantaneous luminosities from 5.0×10^{34} to $7.5 \times 10^{34}\,\mathrm{cm}^{-2}\,\mathrm{s}^{-1}$ would be reached, allowing to almost tenfold the integrated luminosity by the early 2040s. Owing to much harsher conditions, the computation of induced radioactivity will even become a more relevant and pressing need to fully ensure a smooth and safe operation of the LHC and its large experiments over a very extended period of time.

The first main objective of this work conducted within the Radiation Protection group at CERN was the further development of an efficient computation method for induced activity and radiological quantities derived from it. To better frame the underlying motivations, it was extensively discussed in Chapter 2 that the amount of radioactivity that can be generated strongly depends on the material being irradiated, on the duration of the irradiation (or more generally on the irradiation history), and

clearly on the radiation field, that is the ensemble of particles (possibly of different species) and their energies. It was also argued that the study of the generation and time evolution of the induced radioactivity becomes challenging as soon as one deviates from idealized situations and, for complex tasks such as those faced by radiation protection physicists at CERN, Monte Carlo radiation transport codes have to be necessarily employed. Starting from an overview of the methods traditionally used in radiological studies, it emerged that a complementary approach offering automatic normalization, fast convergence and good visualization capabilities is in most cases needed.

Chapter 4 explained in detail the foundation principles and range of applicability of the novel fluence conversion coefficients method applied to radiological studies. Radiation protection assessments typically consist in estimating hazard factors which are quantities defined within European or national regulations in matter of radiation protection: in almost the entirety of the situations, a hazard factor is a quantity derived from radionuclide activities and can often be expressed as a weighted sum of the mass-specific activities of the radionuclides that are present in a given mixture, with weights that depend on the particular radionuclide. The fluence conversion coefficients method is based on the idea of computing radionuclide activities and the quantities that may be derived from them by folding particle fluences directly during transport calculations using pre-computed energy- and particle-dependent coefficients: these coefficients can be calculated for a given irradiation condition, material to be characterized and desired quantity to be estimated.

After a detailed discussion on this method, the Python-based code for the computation of the coefficients was also presented: thanks to its user-friendly scripting interface, users can compute the energy- and particle-dependent coefficients for the desired application with a minimum number of input parameters and with little or no additional computing skills required. Then, the integration of the fluence conversion coefficients code with the FLUKA and PHITS Monte Carlo codes was also extensively outlined. Finally, since the computation of the conversion coefficients relies on the knowledge and availability of energy- and particle-dependent radionuclide production data, the large efforts undertaken in the compilation of the radionuclide production cross section database were also summarized.

Another important objective of the thesis at hand and that was tackled in Chapter 5 was the testing of the method and the related radionuclide production databases in controlled experiments. Different experimental campaigns were conducted at CHARM (CERN High energy AcceleRator Mixed field facility, a facility at the CERN East Experimental Area in which the 24 GeV/c proton beam from the Proton Synchrotron is sent on a target to generate a secondary radiation field) and at CSBF (CERN Shielding Benchmark Facility), an experimental installation located in the roof shielding above the CHARM target.

A first extensive test of the fluence conversion coefficients method was conducted employing measured data of radionuclide production yields from activation samples of C, Al, In, and Bi for various CSBF shielding materials (concrete and steel) and configurations (studies with the so-called removable sample holder concrete block and

with a collimated neutron beam at the so-called material test location): considering the combinations between the nine reaction channels monitored and the different configurations, more than 120 activation measurements were compared with simulation results. These results showed that the differences between the calculated quantities with FLUKA and the values experimentally measured were on average within 20 % for the different configurations of the facility and also provided further proof that, thanks to their simplicity and relatively low cost, this set of activation samples can be a very efficient solution for monitoring the high energy component of neutron fields.

The other benchmarks were instead tailored to clearance studies, another very relevant practical application of the fluence conversion coefficients method for which a significant part of this work was developed. It had been discussed in the introductory chapters that with the term clearance it is meant the removal of radioactive materials or radioactive objects within notified or authorized facilities and activities from any further regulatory control: if applicable, clearance conditions are defined in national regulations and, as far as CERN is concerned, the reference legislation in this matter is the Swiss one. It was also extensively presented that, for a mixture of artificial radionuclides, as is the case for activated components, the most constraining condition is on the so-called multiples of Swiss clearance limits (LL), defined as the sum of the radionuclide mass-specific activities weighted by the clearance limits for the specific radionuclide: a comparison of this quantity with a threshold value of 1.0 allows to distinguish between conventional and radioactive waste.

Owing to its wide use and distribution throughout the LHC accelerators and LHC experiments, most of the radioactive waste at CERN is constituted by metallic waste, out of which steel alloys and copper represent a significant fraction. It was of paramount importance to then understand the overall predictions of FLUKA and of the fluence conversion coefficients code as far as the activation of these classes of materials is concerned. The second benchmark performed at CSBF saw the use of activation samples in copper and two steel alloys to focus on the production of radionuclides which typically dominate the activation levels in these materials and often determine their disposal pathway: the samples had been irradiated for over one month while being inserted into the concrete holder block to mimic the irradiation conditions which can be found in shielded areas laterally to beam loss points or devices intercepting the collision debris. It was found that for several isotopes, including ^{57}Co, ^{58}Co, and ^{54}Mn, the agreement was satisfactory, in general within a factor of 1.5, while the predictions for the multiples of LL remained between a factor 1.5 to 2.0. Experiments with similar activation samples were also conducted inside CHARM where more intense and harder particle fluence spectra can be obtained. For most of the measured radionuclide activities, the agreement was found to be between 0.6 and 1.2, while the predictions for the multiples of LL were very close to the measured results. In virtue of the very similar radiation field where some of the samples were located with respect to the one which is expected in the CMS experimental cavern, the results on ^{54}Mn and the multiples of LL for steel gave the valuable opportunity to critically evaluate the studies on the reinforcement of the existing CMS forward shield presented in Section 6.1.

To complement the experiments at CHARM, the fluence conversion coefficients code setup was also benchmarked directly for an LHC experiment by exploiting more than 130 activation samples installed in LHCb which were retrieved during the past Long Shutdown 2 and for which gamma spectroscopy was performed to determine the residual nuclide inventory. Despite the complexities linked to the geometry of the problem and the irradiation history further complicated by the polarity switches of the LHCb main dipole, the average agreement satisfactory settled between 0.7 to 2.2 with very few exceptions among the different installation locations in the experimental cavern: furthermore, for the relevant radionuclides for steel and copper, the same trends observed at the CHARM experiments were found. All this additional data proved to be a very valuable input for a critical evaluation of the results discussed in Chapter 6.

With the aim of fully illustrating the capabilities, versatility and advantages of the fluence conversion coefficients method, several practical examples for the LHC experiments were presented in Chapter 6. These were tailored to either the radiological pre-characterization of materials or to clearance studies: in virtue of the definition of the multiples of LL and of the formulation of the fluence conversion coefficients method, clearance and decommissioning studies are indeed the best candidates for applications of the novel approach.

The first major test case focused on the design studies of the reinforcement of the present CMS forward shield which were driven, among others, by the need of reducing activation levels in the CMS cavern infrastructures for maintenance and interventions in the upcoming shutdown periods. The origin of the problem was analysed in extensive detail by considering the expected activation levels of several classes of common materials: it was explained that the most penalizing cases are those of steel and iron (unfortunately ubiquitous) and that activation levels at the periphery of CMS are essentially dominated by ^{54}Mn ($T_{1/2} = 312.5\,\mathrm{d}$) produced by high-energy neutrons on $^{\mathrm{nat}}$Fe.

To best assess the effectiveness of the shield from a radiation protection point of view, it was necessary to consider the activation of the infrastructure materials in the periphery of the CMS cavern. With considerations on the complexity of the problem and the simulation geometry, it was argued that traditional computation approaches would not have been at all applicable and that the presented assessment would have been possible only with the fluence conversion coefficients method. In addition, the advantage of the good visualization capabilities of the method was explained by illustrating how the quantities of interest can be estimated over extended regions of space.

Using as reference the penalizing case of stainless steel 304L it was possible to show that a reduction in activation levels of more than a factor two can be achieved and it was also possible to establish a preliminary conservative boundary outside which materials may be regarded as activated below the clearance limits. Owing to the relevance of the new forward shield project and the potential benefit to the whole CMS technical operation, the reliability of the simulation estimates was also discussed in light of the results from the estimation of ^{54}Mn and the multiples of LL for steel discussed in

Chapter 5.

The second application of the fluence conversion coefficients method also had very relevant consequences for CMS and it was dedicated to the assessment of the activation of the absorber steel plates of its future HGCal. In virtue of its applications, special requirements on the impurities in the steel have normally to be met, particularly on traces of cobalt which may pose a radiological risk even at very long cooling times owing to the production of ^{60}Co. The CERN guideline value of 0.1 % mass fraction for the cobalt content is not always achievable for practical reasons such as a large amount of steel to be purchased, its grade, and even the steel market conditions at the time of the tendering process. The dedicated study was performed to understand the consequences of a higher content of cobalt and to eventually justify a derogation from the guidelines.

The simulation highlighted how at long cooling times ^{60}Co is essentially the only effective contributor to the multiples LL in the steel of the HGCal absorber plates and, for small variations of the cobalt content, the ^{60}Co specific activity and, by consequence the multiples of LL, would almost scale linearly. The spatial distribution of the multiples of LL for stainless steel 304L with a 0.3% cobalt content was compared to that obtained with the reference composition: the fluence conversion coefficients method allowed to visualize the shift of the boundary at which the multiples of LL would be equal to 1.0 and to immediately understand which parts of the steel absorber plates would be a priori non-radioactive. A simple estimate based on the simulation results yielded that by considering a 0.3 % cobalt content the clearable volume would be around only 15 % smaller than the volume that would be instead clearable assuming the guideline steel composition. This argument, together with consideration on the still-low residual dose rates and the overall conservativeness of the results in light of the benchmarks of Chapter 5 allowed for the derogation from the concerned CERN guidelines and the procurement of approximately 600 tons of steel. In addition, it was explained that in this case it was possible to directly compare the performances of the fluence conversion coefficients method with respect to traditional computation approaches: in relation to the examples provided, it was argued that a CPU time-saving factor up to approximately 100 could be achieved.

The third example was fully dedicated to the ALICE experiment and to the establishment of a material-based zoning for clearance operations for the Long Shutdown 3 and the decommissioning of the Run 4 detector in the Long Shutdown 4. After extensive considerations on the need to refine the irradiation history to include the heavy-ion periods and to properly simulate them, the results for the preliminary zoning were discussed. For each considered class of materials (ranging from steel and aluminium alloys to electronic composition and calorimetric material) the fluence conversion coefficients code allowed to estimate the spatial distribution of the multiples of LL and to efficiently identify a boundary outside which certain objects/components of that material may be regarded as a priori non-radioactive and considered as conventional waste.

Finally, the last discussed study focused on the radiation protection assessment for ATLAS and CMS in preparation to the LHC pilot beam run conducted from October 18

to November 1, 2021, as part of the commissioning in preparation to the restart of the LHC with Run 3 in early 2022. Owing to the fact that the pilot beam was scheduled still within a shutdown period, maintenance and other activities in the major experimental installations were ongoing in the days prior to and following the test. From a practical point of view, this meant that the four large LHC experiments were in a configuration differing from their nominal one.

The study had the twofold objective of estimating the levels of induced activation of temporary infrastructures that would have been removed from the experimental caverns and assessing the levels of prompt radiation. Due to the complexity of the problem and the need of having a fast but effective calculation, it was explained that the fluence conversion coefficients method was the only valid solution and that the usage of traditional methods would not have been at all applicable. The good visualization capabilities and flexibility of the method allowed the comparisons of induced activity levels in various materials and at different cooling times, providing extremely valuable input to operational radiation protection (such as the installation of dedicated samples and radiation monitors) and to the definition of the beam parameters for the test run.

7.2 Outlook

By putting all the results discussed in this thesis work into perspective, it is possible to conclude that the fluence conversion coefficients method is in its present status a mature and reliable calculation approach to address the complex problem of the assessment of induced activation in the radiation environment of high-energy accelerators and collider experiments.

Its applicability has been discussed in relation to the FLUKA and PHITS Monte Carlo codes, but in virtue of the user-friendly scripting interface developed, it lends itself to be easily extended to other Monte Carlo codes as well.

The benchmarks that were presented constitute a valuable set of data which may be used as a reference for similar future studies. Furthermore, thanks to the significant know-how and code infrastructure which were developed for the activation benchmarks, particularly the one at LHCb, large-scale activation campaigns have been prepared for ATLAS, ALICE, and CMS for the upcoming Long Shutdowns at CERN: these would not only allow to simplify the establishment of a material-based radiological zoning but they would also give the unique opportunity for comparing the radiation environment with predictions from Monte Carlo calculations. In the particular case of CMS, these activation detectors would be extremely valuable to directly assess the effectiveness of the forward shield reinforcement prototype once its installation will be completed and to evaluate the possible need of a complete redesign of the forward shield in view of the HL-LHC operation.

The flexibility, fast convergence and good visualization capabilities of the method were shown through a series of studies for the radiological characterization of LHC experiment or their components. Applications other than clearance operations and radioactive waste pre-characterization are possible. The quantification of radionuclide

inventories can be time-consuming and often requires a lot of experience: the fluence conversion coefficients code may be for instance employed for the optimization of large-scale activation campaigns. Other possible applications may be envisaged for cases in which activation calculation by means of traditional approaches would be severely limited by convergence.

At present, the code is already a standard tool regularly used within the Radiation Protection group at CERN: apart from the LHC experiments, examples of its application include earth activation studies for ISOLDE, clearance studies for the East Experimental Area (EA), the Experimental Hall North 1 (EHN1), and n_TOF facility, and radiological zoning studies for the LHC machine.

In conclusion, in virtue of its generality, relative simplicity and reliability, it is foreseen that the fluence conversion coefficients method will continue to be an important radiological assessment method employed at CERN and it may be soon applied to other facilities and other accelerators impacting positively on their technical operation.

Appendix A

Additional plots for Section 4.7

A.1 Experimental data

As illustrated in Section 4.7, the amount of cross section data computed for applications with the fluence conversion coefficients code is quite extensive. Albeit a systematic cross-check with experimental data is beyond the scope of this thesis work, a qualitative comparison was at least performed for a reduced set of reactions on natural Al, Si, Mn, Fe and Cu. Owing to the larger availability of monoenergetic proton beams with respect to other particle species such as charged pions or neutrons, the comparison is limited to proton-induced reactions only: reference data were extracted from the EXFOR [84, 85] database and only data sets with a large number of experimental points have been considered.

Figure A.1: Qualitative comparison of computed radionuclide production data with available experimental measurements. The experimental points are referenced via the corresponding EXFOR [84, 85] entries.

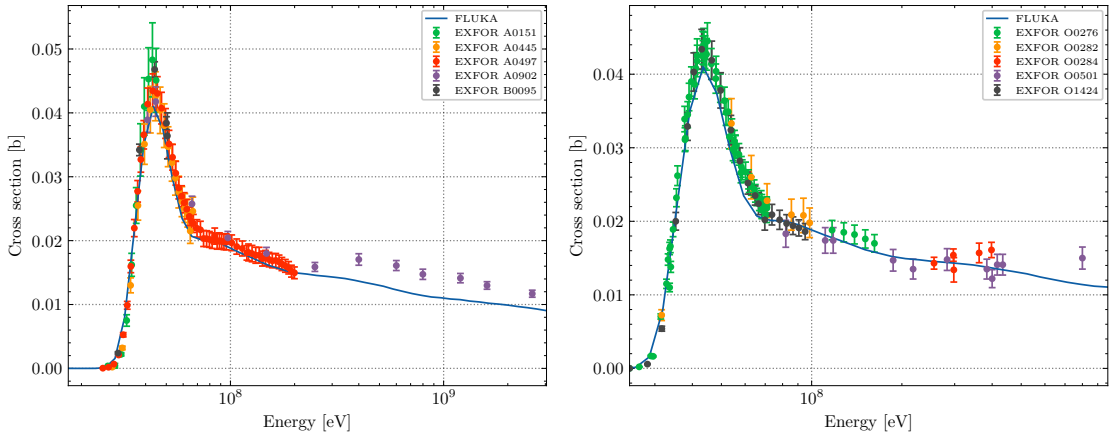

(a) $^{27}\mathrm{Al}(p,x)^{22}\mathrm{Na}$ (b) $^{27}\mathrm{Al}(p,x)^{22}\mathrm{Na}$ (cont.)

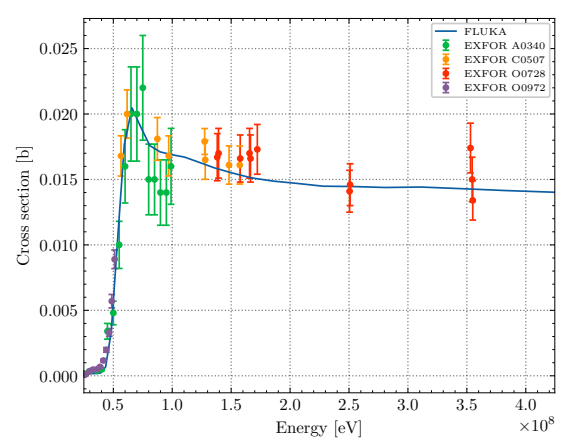

(c) $^{\text{nat}}\text{Si}(p,x)^{22}\text{Na}$

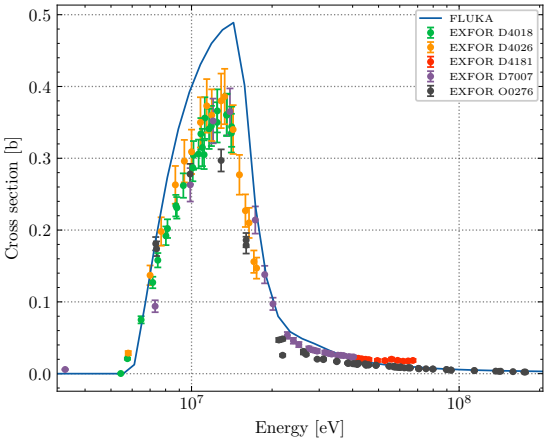

(d) $^{\text{nat}}\text{Fe}(p,x)^{56}\text{Co}$

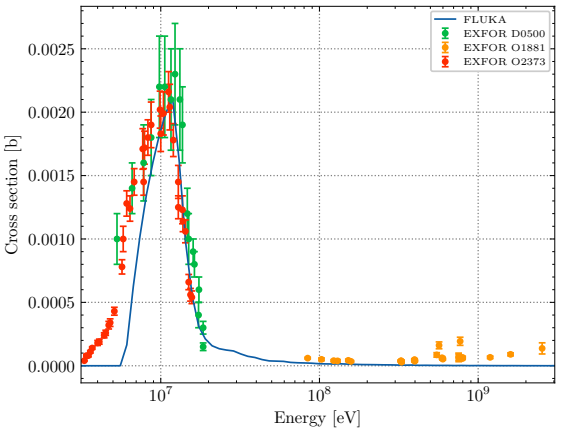

(e) $^{\text{nat}}\text{Fe}(p,x)^{58}\text{Co}$

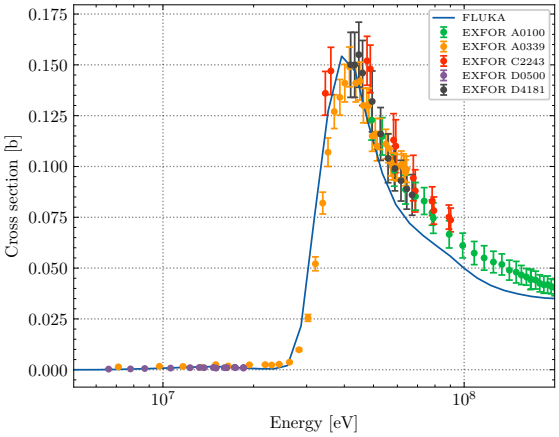

(f) $^{\text{nat}}\text{Fe}(p,x)^{54}\text{Mn}$

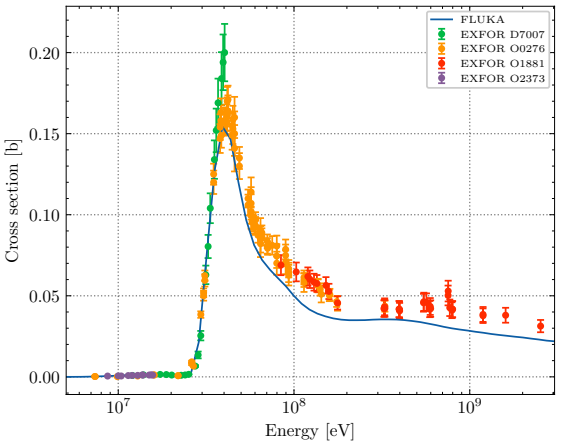

(g) $^{\text{nat}}\text{Fe}(p,x)^{54}\text{Mn}$ (cont.)

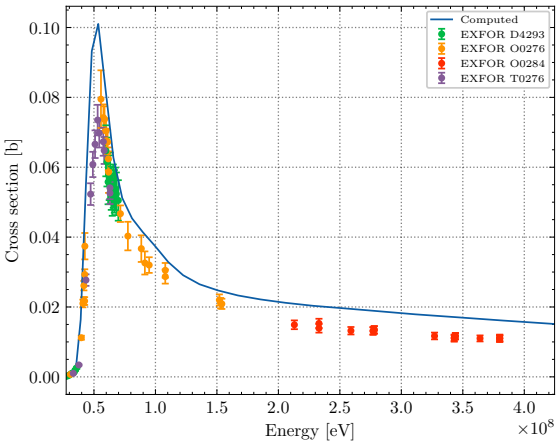

(h) $^{59}\text{Co}(p,x)^{56}\text{Co}$

Figure A.1: Qualitative comparison of computed radionuclide production data with available experimental measurements. The experimental points are referenced via the corresponding EXFOR [84, 85] entries (cont.).

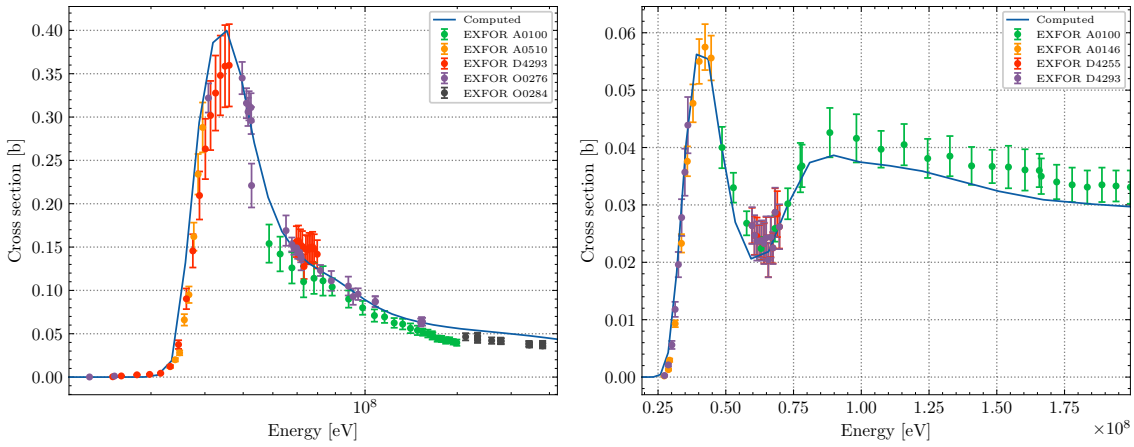

(i) $^{59}\mathrm{Co}(p,x)^{57}\mathrm{Co}$

(j) $^{59}\mathrm{Co}(p,x)^{54}\mathrm{Mn}$

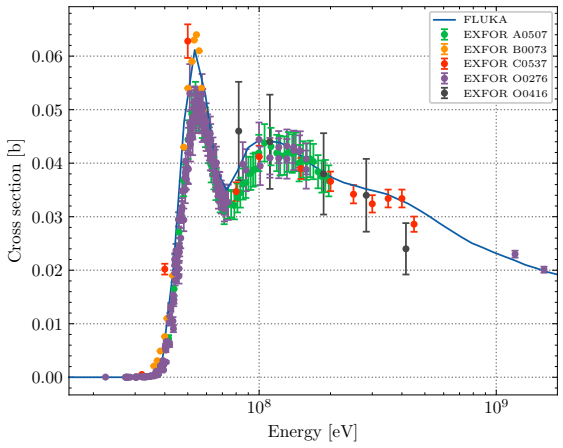

(k) $^{\mathrm{nat}}\mathrm{Cu}(p,x)^{57}\mathrm{Co}$

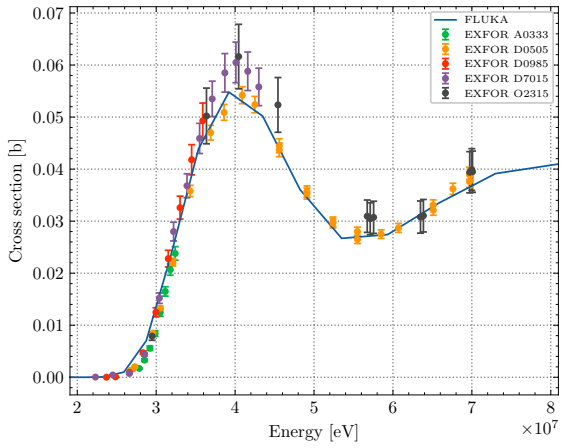

(l) $^{\mathrm{nat}}\mathrm{Cu}(p,x)^{58}\mathrm{Co}$

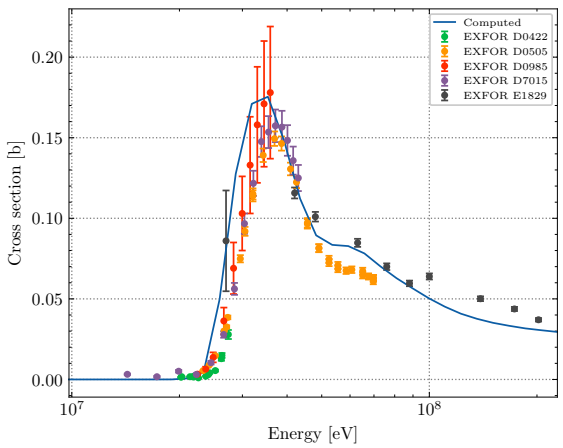

(m) $^{\mathrm{nat}}\mathrm{Cu}(p,x)^{61}\mathrm{Cu}$

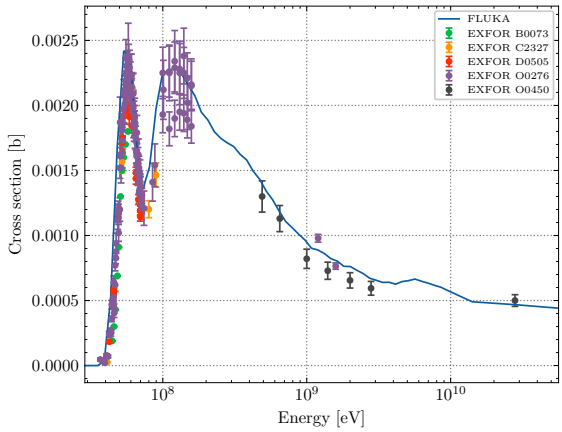

(n) $^{\mathrm{nat}}\mathrm{Cu}(p,x)^{57}\mathrm{Ni}$

Figure A.1: Qualitative comparison of computed radionuclide production data with available experimental measurements. The experimental points are referenced via the corresponding EXFOR [84, 85] entries (cont.).

A.2 Monte Carlo calculations

For the same very reason on the extent of the database, systematic inter-comparison between the data computed with FLUKA and PHITS is not at all a trivial task. Comparisons were at least made for a selection of reactions on natural Al, Si, Mn, Fe and Cu: despite the fact that, thanks to the choice of a common energy grid, ratios can be computed without adding additional systematic uncertainties owing to any attempted fitting procedure, the outcome of these comparisons cannot be definitive. Indeed, the ratios shown in the following are computed giving the same importance to each value of the cross sections. For any final conclusion, for instance on the sensitivity of the computed activity with respect to the variation in the cross sections used, it would be necessary to fully take into account the energy-dependent spectra of the particles inducing activation in the specific object irradiated to properly weight these ratios.

Figure A.2: Comparison of radionuclide production data computed with FLUKA and PHITS for selected elements and relevant radionuclides.

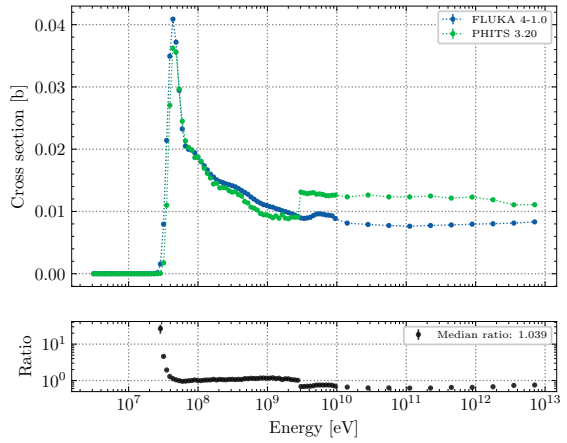

(a) $^{27}\mathrm{Al}(p,x)^{22}\mathrm{Na}$

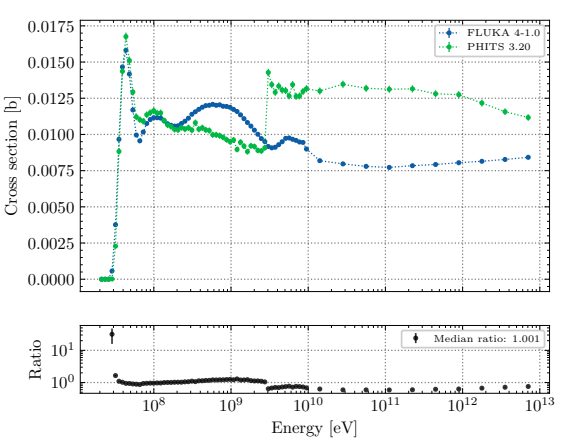

(b) $^{27}\mathrm{Al}(n,x)^{22}\mathrm{Na}$

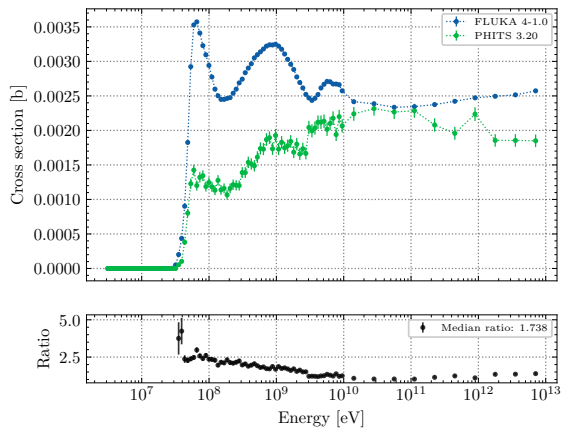

(c) $^{27}\mathrm{Al}(p,x)^{24}\mathrm{Na}$

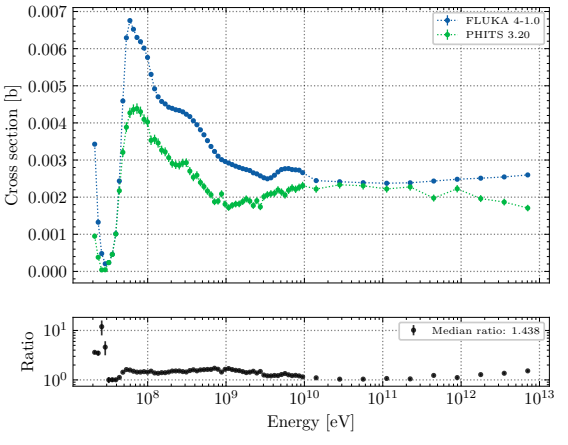

(d) $^{27}\mathrm{Al}(n,x)^{24}\mathrm{Na}$

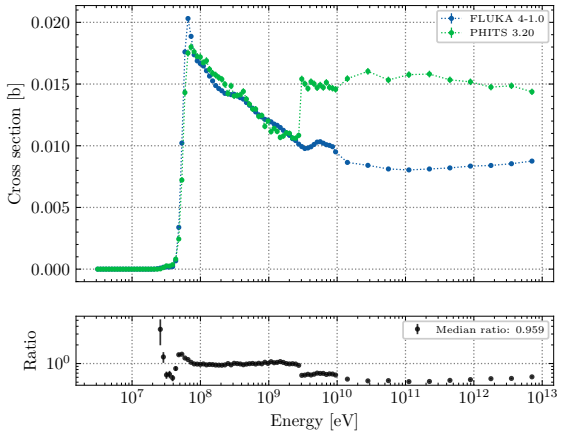

(e) $^{\text{nat}}\text{Si}(p,x)^{22}\text{Na}$

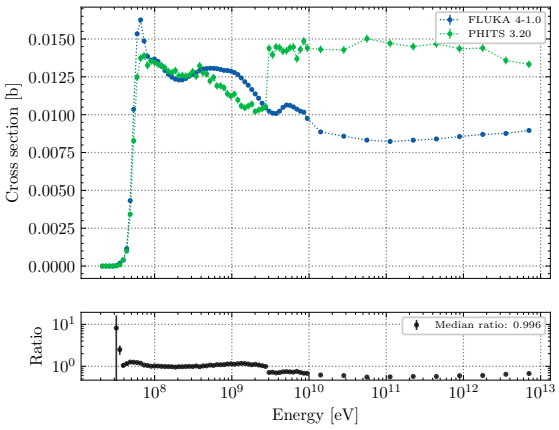

(f) $^{\text{nat}}\text{Si}(n,x)^{22}\text{Na}$

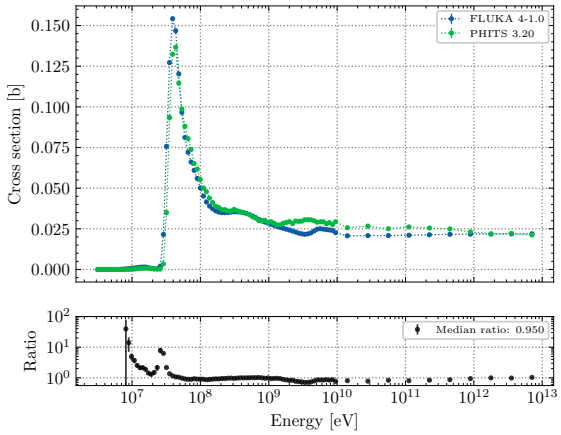

(g) $^{\text{nat}}\text{Fe}(p,x)^{54}\text{Mn}$

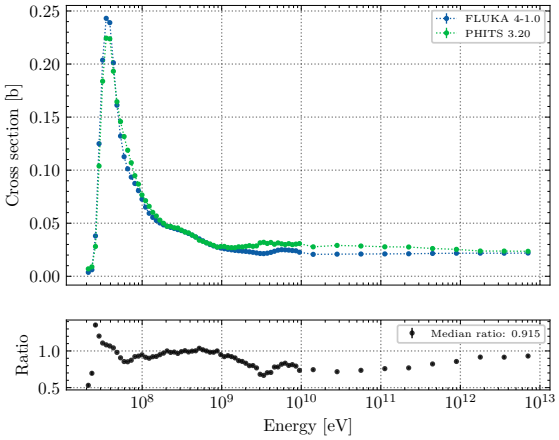

(h) $^{\text{nat}}\text{Fe}(n,x)^{54}\text{Mn}$

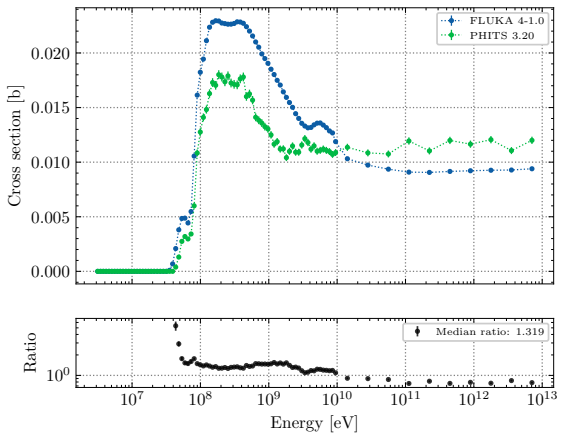

(i) $^{\text{nat}}\text{Fe}(p,x)^{48}\text{V}$

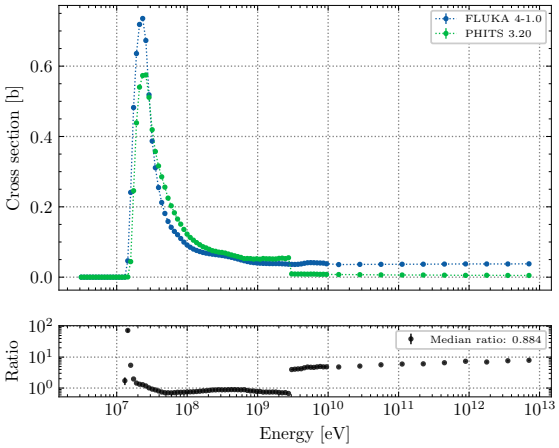

(j) $^{\text{nat}}\text{Fe}(p,x)^{55}\text{Fe}$

Figure A.2: Comparison of radionuclide production data computed with FLUKA and PHITS for selected elements and relevant radionuclides (cont.).

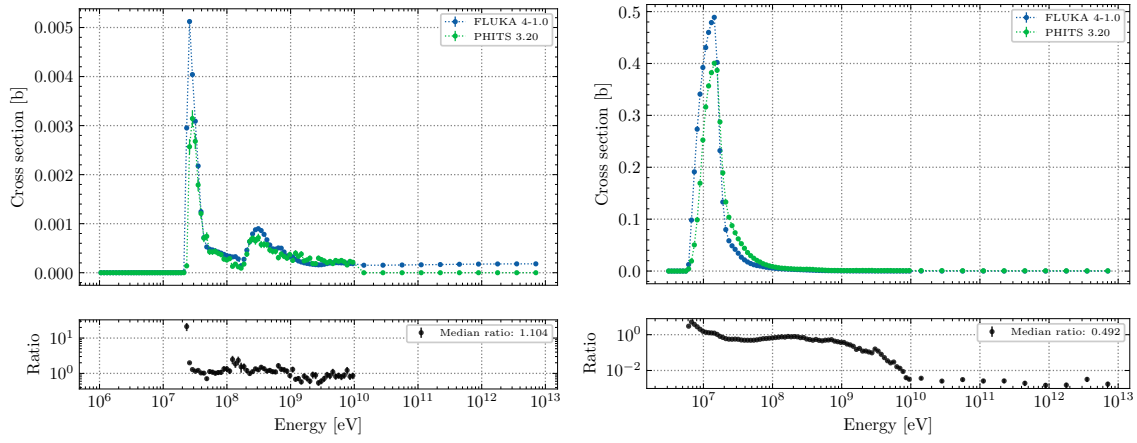

(k) $^{\text{nat}}\text{Fe}(\gamma, x)^{54}\text{Mn}$

(l) $^{\text{nat}}\text{Fe}(p, x)^{56}\text{Co}$

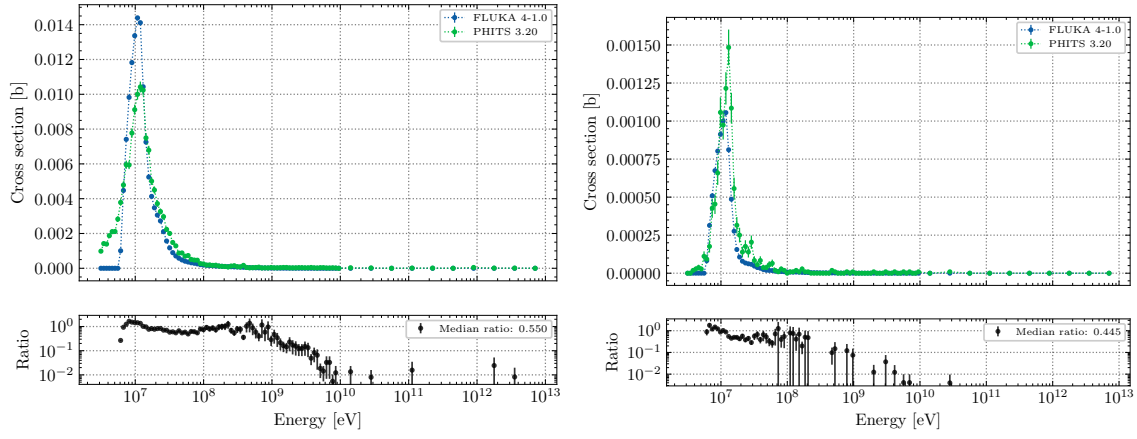

(m) $^{\text{nat}}\text{Fe}(p, x)^{57}\text{Co}$

(n) $^{\text{nat}}\text{Fe}(p, x)^{58}\text{Co}$

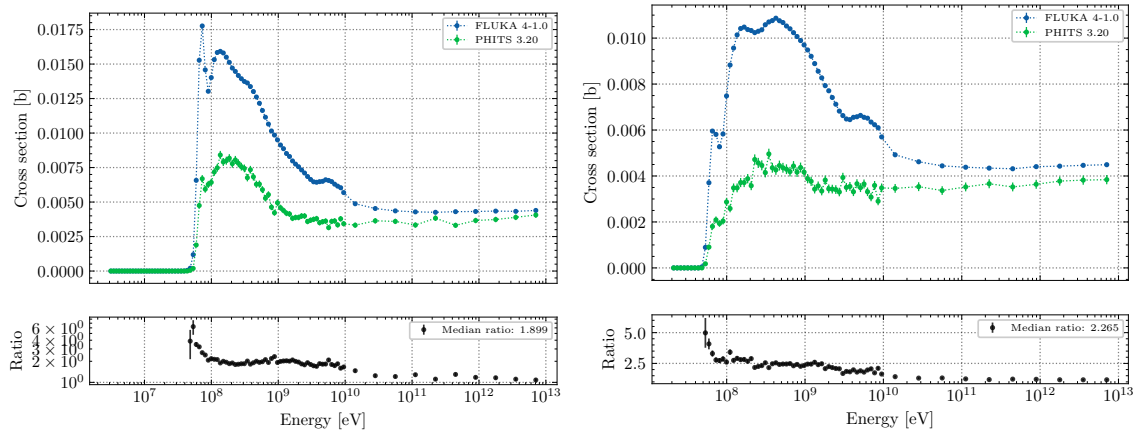

(o) $^{\text{nat}}\text{Cu}(p, x)^{56}\text{Co}$

(p) $^{\text{nat}}\text{Cu}(n, x)^{56}\text{Co}$

Figure A.2: Comparison of radionuclide production data computed with FLUKA and PHITS for selected elements and relevant radionuclides (cont.).

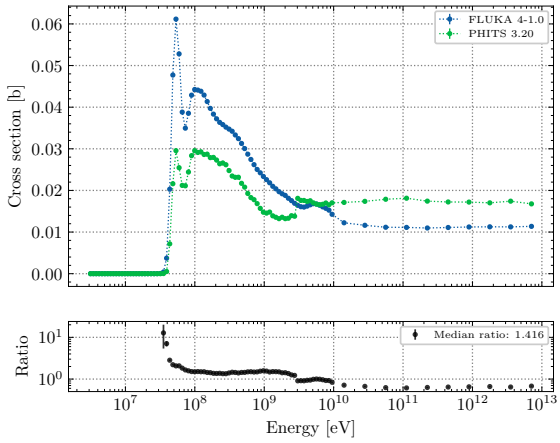

(q) $^{\text{nat}}\text{Cu}(p,x)^{57}\text{Co}$

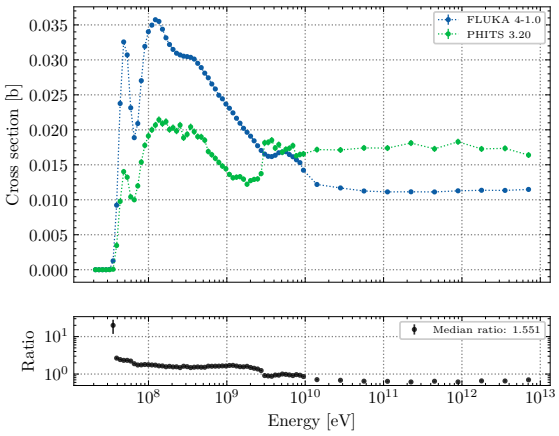

(r) $^{\text{nat}}\text{Cu}(n,x)^{57}\text{Co}$

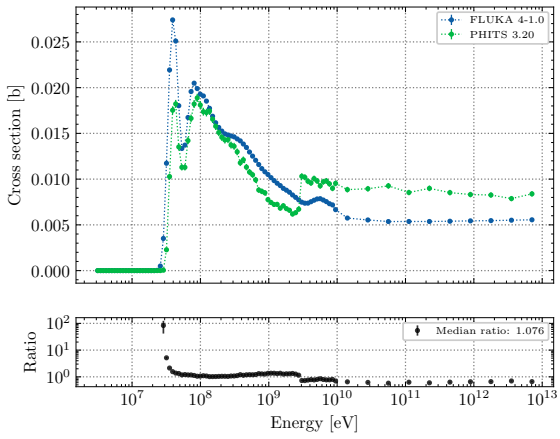

(s) $^{\text{nat}}\text{Cu}(p,x)^{58}\text{Co}$

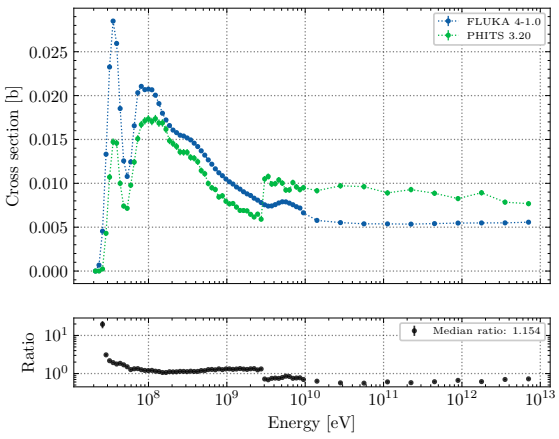

(t) $^{\text{nat}}\text{Cu}(n,x)^{58}\text{Co}$

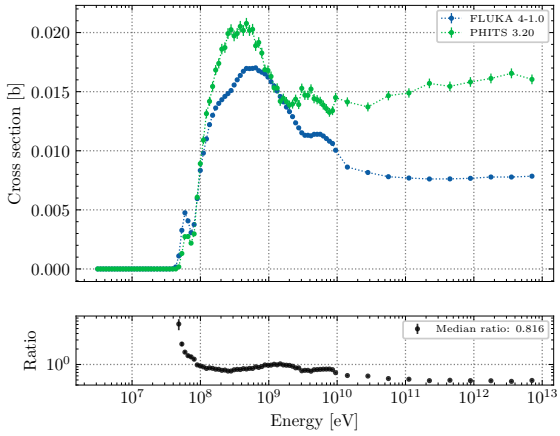

(u) $^{\text{nat}}\text{Cu}(p,x)^{54}\text{Mn}$

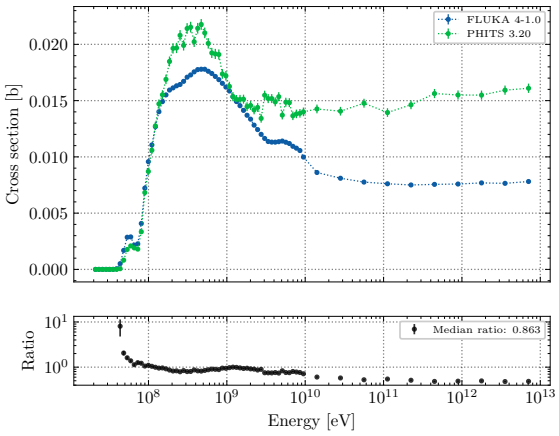

(v) $^{\text{nat}}\text{Cu}(n,x)^{54}\text{Mn}$

Figure A.2: Comparison of radionuclide production data computed with FLUKA and PHITS for selected elements and relevant radionuclides (cont.).

Appendix B

Additional tables for Chapter 5

B.1 Overview of the samples installed in the LHCb experimental cavern

The table below provides a summary of the samples installed in LHCb in terms of material, mass of the samples, installation date and corresponding date of analysis. A brief description is given for each installation location: the numbering corresponds to that of figure 5.17.

Table B.1: Description of the set of activation samples installed in the LHCb experimental cavern.

	Location	Material	Mass [g]	Installation date	Analysis date
1	Bunker extension	Copper	15.931	2009	27/11/2018 10:14:12
		Steel	14.413	2009	27/11/2018 11:21:49
		Aluminium	4.761	2009	27/11/2018 14:37:38
2	Middle of bunker below RICH2 rack	Copper	16.254	2009	12/11/2018 18:16:45
		Steel	15.606	2009	13/11/2018 10:33:33
		Aluminium	5.297	2009	13/11/2018 12:02:36
3	Balcony racks	Copper	16.977	2009	14/11/2018 18:45:55
		Steel	15.004	2009	15/11/2018 10:06:58
		Aluminium	4.45	2009	15/11/2018 11:10:15
4	VELO boards (C side)	Copper	16.621	2009	24/05/2019 13:40:23
		Steel	13.999	2009	24/05/2019 11:30:14
		Aluminium	5.881	2009	24/05/2019 12:35:19
5	Bottom of RICH1 (A side)	Copper	16.833	2009	24/05/2019 20:43:07
		Steel	15.439	2009	24/05/2019 17:59:46
		Aluminium	4.563	2009	24/05/2019 19:04:51
6	Bottom of RICH2 (A side)	Copper	16.675	2009	19/11/2018 13:31:43
		Steel	14.372	2009	19/11/2018 14:39:24
		Aluminium	4.69	2009	19/11/2018 15:47:16
7	Outer Tracker frame	Copper	15.975	2009	25/05/2019 02:07:16
		Steel	14.741	2009	25/05/2019 01:02:43
8	Inner Tracker service boxes	Copper	16.376	2009	25/05/2019 09:10:34
		Steel	14.475	2009	25/05/2019 07:00:23
		Aluminium	4.769	2009	25/05/2019 08:05:28

Table B.1 (continued)

	Location	Material	Mass [g]	Installation date	Analysis date
9	TT service boxes (A-side)	Copper	16.998	2009	04/01/2019 13:19:50
		Steel	15.05	2009	04/01/2019 15:29:42
		Aluminium	5.145	2009	04/01/2019 14:24:46
10	HCAL and ECAL racks	Copper	17.06	2009	14/11/2018 08:55:45
		Steel	14.544	2009	14/11/2018 10:17:59
		Aluminium	5.415	2009	14/11/2018 11:39:04
11	Side of M2 intermediate board	Copper	16.844	2009	15/11/2018 17:15:56
		Steel	14.007	2009	15/11/2018 19:38:29
		Aluminium	5.677	2009	16/11/2018 08:35:24
12	M1 service board	Copper	16.787	2009	28/11/2018 14:51:59
		Steel	14.937	2009	29/11/2018 10:55:43
		Aluminium	4.727	2009	29/11/2018 14:25:34
13	ECAL power supplies	Copper	16.713	2009	20/11/2018 13:39:11
		Steel	15.045	2009	20/11/2018 15:11:09
		Aluminium	4.942	2009	21/11/2018 11:33:33
14	Upstream the VELO, close to the beam pipe	Copper	16.239	2009	29/05/2019 15:25:08
		Steel	14.973	2009	29/05/2019 13:14:55
		Aluminium	4.847	2009	29/05/2019 14:20:04
15	TT outer frame	Copper	15.685	2009	29/05/2019 22:27:56
		Steel	15.41	2009	29/05/2019 19:44:31
		Aluminium	4.776	2009	29/05/2019 20:49:41
16	Electronics below TT	Copper	15.85	2009	30/05/2019 04:57:31
		Steel	14.941	2009	30/05/2019 02:47:53
		Aluminium	5.315	2009	30/05/2019 03:52:57
17	SPD electronic cards	Copper	16.489	2009	22/11/2018 11:23:28
		Steel	15.084	2009	22/11/2018 12:39:39
		Aluminium	5.222	2009	22/11/2018 14:07:14
18	Close to PMIL8512 detector	Copper	16.731	2009	23/11/2018 14:47:02
		Steel	14.733	2009	23/11/2018 16:04:00
		Aluminium	4.42	2009	26/11/2018 10:41:50
19	ECAL stairways	Copper	16.633	2009	04/01/2019 19:49:39
		Steel	14.707	2009	04/01/2019 21:59:29
		Aluminium	3.535	2009	04/01/2019 20:54:34
20	Close to fog horn	Copper	16.486	2009	03/12/2018 15:43:37
		Steel	14.681	2009	03/12/2018 16:51:08
		Aluminium	4.915	2009	04/12/2018 11:57:44
21	Visitors Passerelle	Copper	126.67	18/09/2017	04/12/2018 17:33:23
		Steel	112.446	18/09/2017	29/12/2018 20:18:42
		Aluminium	117.218	18/09/2017	05/12/2018 09:18:40
		Kovar	10.365	18/09/2017	29/12/2018 23:58:12
22	HERSCHEL detector (outside UX85B)	Copper	126.647	18/09/2017	02/01/2019 13:34:00
		Steel	112.497	18/09/2017	02/01/2019 16:35:59
		Aluminium	117.426	18/09/2017	02/01/2019 14:38:55
		Kovar	10.364	18/09/2017	02/01/2019 17:40:53
23	Between muon tower and platform (close)	Copper	126.882	18/09/2017	02/01/2019 18:45:48
		Steel	112.112	18/09/2017	02/01/2019 20:55:37
		Aluminium	117.078	18/09/2017	02/01/2019 19:50:43
		Kovar	10.4	18/09/2017	02/01/2019 22:00:32
24	Between muon tower and platform (far)	Copper	126.573	18/09/2017	02/01/2019 23:05:31
		Steel	112.269	18/09/2017	03/01/2019 01:15:24
		Aluminium	117.302	18/09/2017	03/01/2019 00:10:30
		Kovar	10.367	18/09/2017	03/01/2019 02:20:21
25	Ceiling at bunker entrance	Copper	126.457	18/09/2017	30/12/2018 01:03:06

Table B.1 (continued)

	Location	Material	Mass [g]	Installation date	Analysis date
		Steel	112.439	18/09/2017	30/12/2018 03:12:56
		Aluminium	117.556	18/09/2017	30/12/2018 02:08:01
		Kovar	10.335	18/09/2017	30/12/2018 04:17:55
26	Muon tower upstream support (C side)	Copper	126.584	18/09/2017	30/12/2018 05:22:55
		Steel	112.506	18/09/2017	30/12/2018 07:32:45
		Aluminium	116.938	18/09/2017	30/12/2018 06:27:48
		Kovar	10.399	18/09/2017	30/12/2018 09:18:28
27	M5 cable trays at beam height (A side)	Copper	126.678	18/09/2017	30/12/2018 10:52:37
		Steel	111.408	18/09/2017	30/12/2018 13:29:01
		Aluminium	117.411	18/09/2017	30/12/2018 12:20:59
		Kovar	10.353	18/09/2017	30/12/2018 14:33:57
28	Balcony racks	Copper	126.788	18/09/2017	30/12/2018 15:38:52
		Steel	112.515	18/09/2017	30/12/2018 17:48:40
		Aluminium	117.171	18/09/2017	30/12/2018 16:43:45
		Kovar	10.388	18/09/2017	30/12/2018 18:53:40
29	Balcony end of racks	Copper	126.771	18/09/2017	03/01/2019 03:25:15
		Steel	114.405	18/09/2017	03/01/2019 05:35:08
		Aluminium	116.816	18/09/2017	03/01/2019 04:30:09
		Kovar	10.414	18/09/2017	03/01/2019 06:40:08
30	Middle of the bucnker (C side)	Copper	126.954	18/09/2017	03/01/2019 07:45:07
		Steel	112.402	18/09/2017	03/01/2019 09:54:56
		Aluminium	117.373	18/09/2017	03/01/2019 08:50:01
		Kovar	10.365	18/09/2017	03/01/2019 10:59:50
31	Top of the M5 shielding	Copper	126.644	18/09/2017	03/01/2019 12:04:48
		Steel	112.451	18/09/2017	03/01/2019 14:14:40
		Aluminium	117.217	18/09/2017	03/01/2019 13:09:46
		Kovar	10.334	18/09/2017	03/01/2019 15:19:33
32	Top of calorimeters	Copper	126.571	18/09/2017	30/12/2018 19:58:39
		Steel	112.375	18/09/2017	30/12/2018 22:08:30
		Aluminium	116.834	18/09/2017	30/12/2018 21:03:35
		Kovar	10.345	18/09/2017	30/12/2018 23:13:24
33	Wall opposite to TT service box (A side)	Copper	126.938	10/08/2017	12/11/2018 11:31:11
		Steel	112.688	10/08/2017	09/11/2018 15:39:10
		Aluminium	117.311	10/08/2017	12/11/2018 16:39:45
		Kovar	10.231	10/08/2017	09/11/2018 17:56:35
34	Gallery above balcony	Copper	126.9	10/08/2017	03/01/2019 16:24:27
		Steel	112.33	10/08/2017	03/01/2019 18:34:16
		Aluminium	117.309	10/08/2017	03/01/2019 17:29:21
		Kovar	10.397	10/08/2017	03/01/2019 19:39:14
35	Cable tray below balcony	Copper	126.794	10/08/2017	31/12/2018 00:18:19
		Steel	112	10/08/2017	31/12/2018 02:28:21
		Aluminium	117.214	10/08/2017	31/12/2018 01:23:21
		Kovar	10.401	10/08/2017	31/12/2018 03:33:15
36	Pipes on wall below balcony	Copper	126.709	10/08/2017	03/01/2019 20:44:14
		Steel	112.313	10/08/2017	03/01/2019 22:54:04
		Aluminium	116.937	10/08/2017	03/01/2019 21:49:09
		Kovar	10.3	10/08/2017	03/01/2019 23:58:58
37	Support next to TT3 (A side)	Copper	126.877	10/08/2017	05/01/2019 02:19:16
		Steel	112.273	10/08/2017	05/01/2019 04:29:07
		Aluminium	116.871	10/08/2017	05/01/2019 03:24:11
		Kovar	10.33	10/08/2017	05/01/2019 05:34:03
38	Support above RICH2 Tower	Copper	126.703	10/08/2017	05/01/2019 06:38:58
		Steel	112.665	10/08/2017	05/01/2019 08:48:57
		Aluminium	117.286	10/08/2017	05/01/2019 07:43:57
		Kovar	10.405	10/08/2017	06/01/2019 15:20:54

Appendix C

Additional tables and plots for Chapter 6

C.1 Summary of the composition of the materials for zoning and clearance studies

Table C.1 summarizes the compositions of compounds that are representative of classes of materials that can be commonly found in the LHC experiments and machine and that are often used for radiological zoning and clearance studies. These compositions are extracted from the CERN material catalogue providing guidance for the selection of materials to be employed in the accelerator environment [127].

Table C.1: Composition of the materials considered for radiological zoning and clearance studies.

Element	Mass fraction [%]	Element	Mass fraction [%]	Element	Mass fraction [%]
Stainless Steel 304L					
Fe	6.71×10^{-1}	Mn	2.00×10^{-2}	C	3.00×10^{-4}
Cr	1.85×10^{-1}	Si	1.00×10^{-2}	P	2.25×10^{-4}
Ni	1.13×10^{-1}	Co	1.00×10^{-3}	S	1.50×10^{-4}
Concrete (with Eu traces)					
O	4.82×10^{-1}	Mg	1.51×10^{-2}	S	4.14×10^{-3}
Ca	2.39×10^{-1}	Fe	1.26×10^{-2}	Ti	1.73×10^{-3}
Si	1.62×10^{-1}	K	8.33×10^{-3}	Eu	3.00×10^{-6}
C	4.38×10^{-2}	H	5.61×10^{-3}		
Al	2.11×10^{-2}	Na	4.46×10^{-3}		
Copper Oxygen-Free Electronics					
Cu	balance	Pb	1.00×10^{-5}	Cd	1.00×10^{-6}
S	1.80×10^{-5}	Bi	1.00×10^{-5}	Hg	1.00×10^{-6}
Se	1.00×10^{-5}	O	5.00×10^{-6}		
Te	1.00×10^{-5}	Zn	1.00×10^{-6}		

Table C.1 (continued)

Element	Mass fraction [%]	Element	Mass fraction [%]	Element	Mass fraction [%]
Aluminium alloy 6060					
Al	9.84×10^{-1}	Fe	2.00×10^{-3}	Mn	1.00×10^{-3}
Mg	4.75×10^{-3}	Zn	1.50×10^{-3}	Cu	1.00×10^{-3}
Si	4.50×10^{-3}	Ti	1.00×10^{-3}	Cr	5.00×10^{-4}
Electronic composition 1					
C	4.13×10^{-1}	Br	5.40×10^{-3}	Cr	5.00×10^{-4}
Cu	2.68×10^{-1}	Mn	4.70×10^{-3}	Ga	3.50×10^{-4}
O	7.05×10^{-2}	Ni	4.70×10^{-3}	Zr	3.00×10^{-4}
Fe	5.30×10^{-2}	Ag	3.30×10^{-3}	Cd	1.50×10^{-4}
Al	4.70×10^{-2}	I	2.00×10^{-3}	As	1.00×10^{-4}
Ti	3.40×10^{-2}	Ba	2.00×10^{-3}	Kr	1.00×10^{-4}
H	2.81×10^{-2}	Bi	1.70×10^{-3}	Mo	3.00×10^{-5}
Cl	1.74×10^{-2}	S	1.00×10^{-3}	Be	1.10×10^{-5}
Zn	1.50×10^{-2}	F	9.40×10^{-4}	Hg	1.00×10^{-5}
Pb	1.50×10^{-2}	Au	8.00×10^{-4}		
Sn	1.00×10^{-2}	Sb	6.00×10^{-4}		
Electronic composition 2					
C	5.10×10^{-1}	H	4.52×10^{-2}	Ag	1.00×10^{-3}
Cu	1.60×10^{-1}	Sn	3.00×10^{-2}	Au	2.50×10^{-4}
O	1.13×10^{-1}	Pb	2.00×10^{-2}	Pd	9.88×10^{-5}
Al	5.00×10^{-2}	Ni	1.00×10^{-2}		
Fe	5.00×10^{-2}	Zn	1.00×10^{-2}		

C.2 Additional plots for the CMS New Forward Shield studies in Section 6.1

The fluence conversion coefficients method was efficiently applied to evaluate the effectiveness of various designs of the reinforcement of the existing CMS forward shielding. The main discussion was based on the estimation of multiples of Swiss clearance limits (LL) for stainless steel 304L since this material was known to provide the most penalizing case. To maintain a global overview, multiples of LL for other materials were also considered as discussed in Section 6.1.

This section collects the additional plots illustrating the expected spatial distribution of the multiples of LL for all the considered material at a cooling time of 4 months in LS 3 after the end of proton operation: figure C.1 shows the case without additional shielding (baseline), figure C.2 the case with additional shielding in standard concrete installed in both sides of the CMS experimental cavern, and figure C.3 the final design of the shield as installed on one side only.

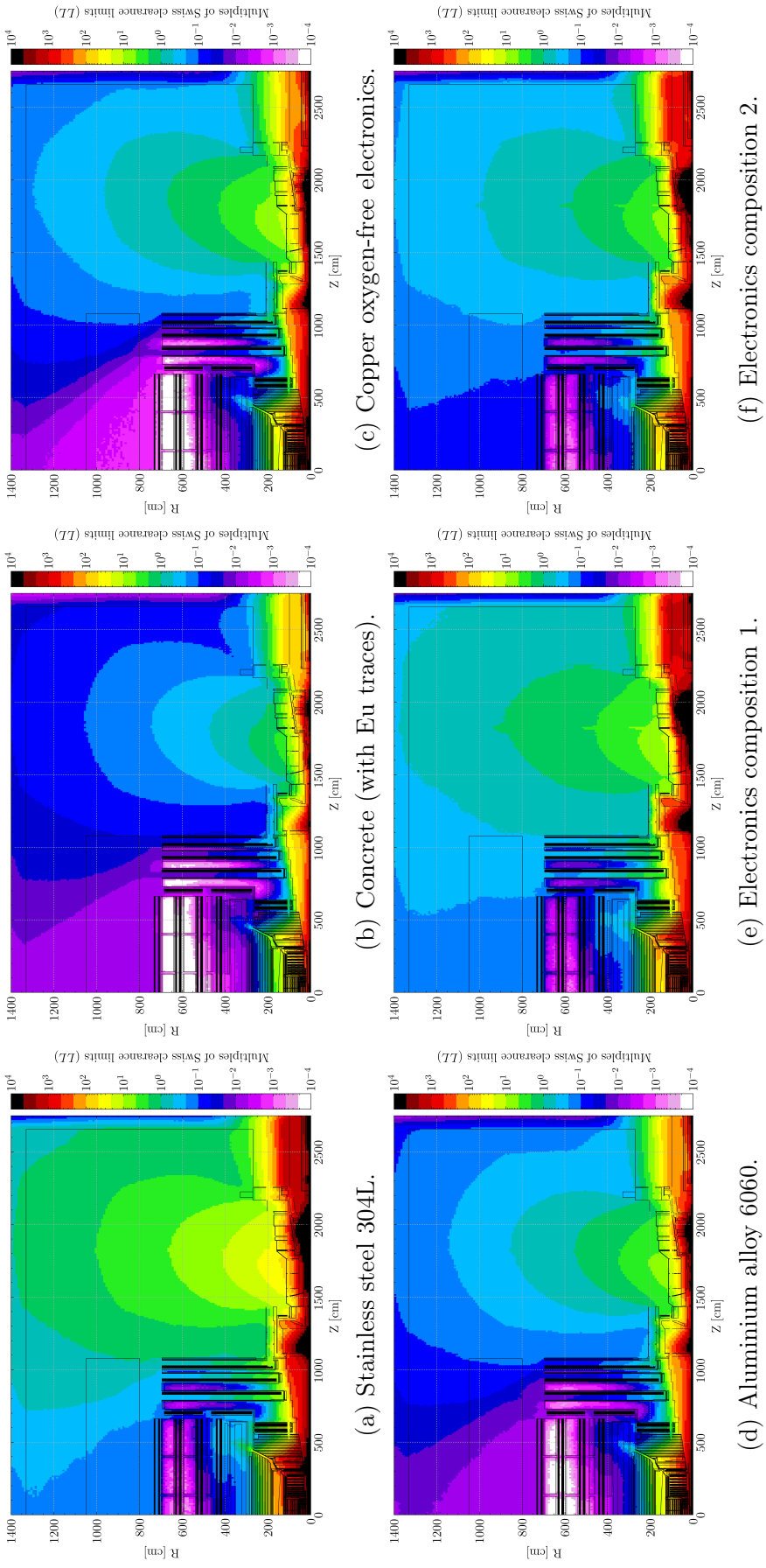

(a) Stainless steel 304L. (b) Concrete (with Eu traces). (c) Copper oxygen-free electronics.

(d) Aluminium alloy 6060. (e) Electronics composition 1. (f) Electronics composition 2.

Figure C.1: FLUKA simulation with the fluence conversion coefficients code of the multiples of Swiss clearance limits (LL) for various materials in the CMS experimental cavern at a cooling time of 4 months in LS 3 after the end of proton operation. No shielding reinforcement is considered. The results are representative of an average over the azimuthal angle.

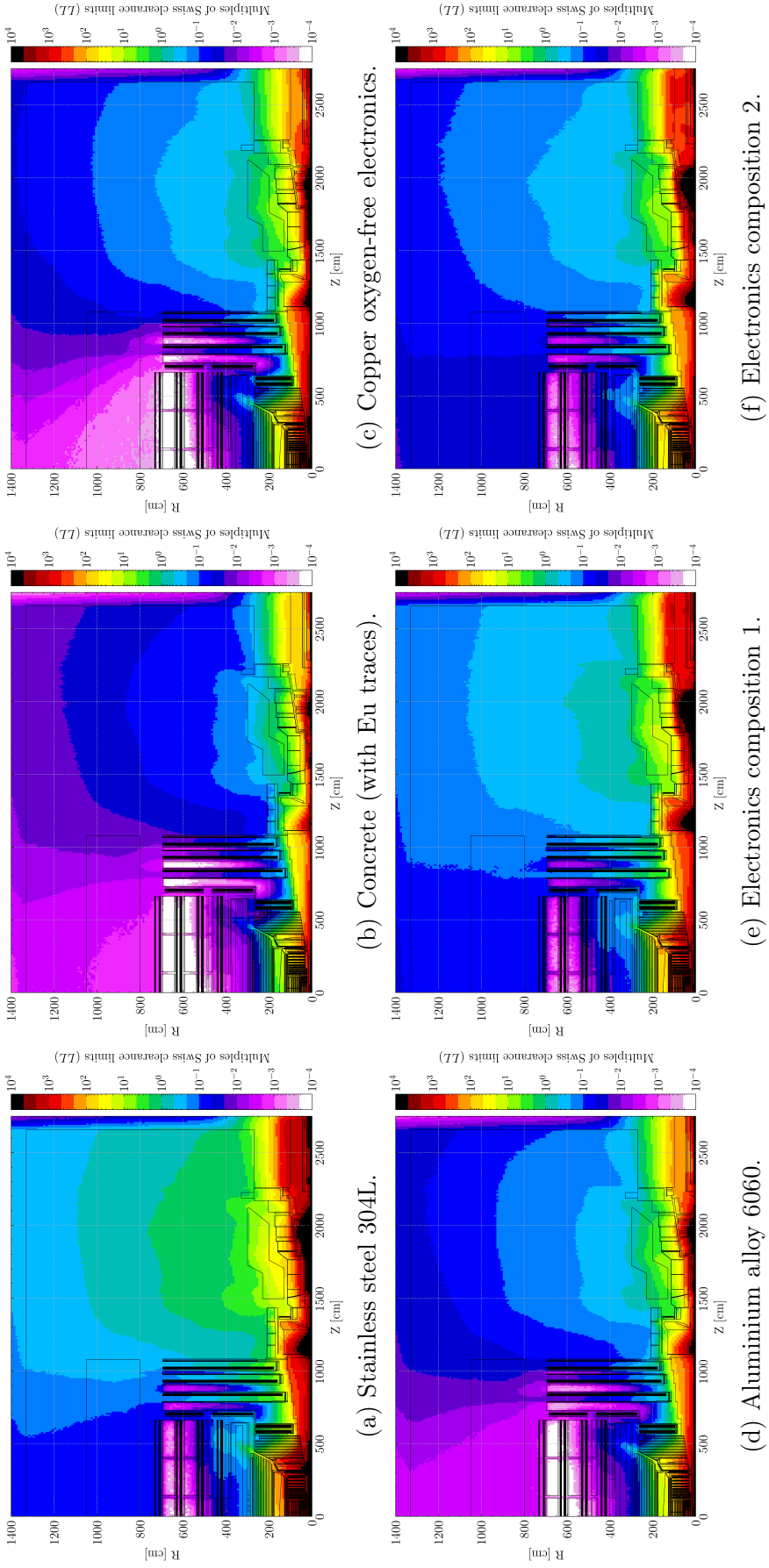

(a) Stainless steel 304L. (b) Concrete (with Eu traces). (c) Copper oxygen-free electronics.

(d) Aluminium alloy 6060. (e) Electronics composition 1. (f) Electronics composition 2.

Figure C.2: FLUKA simulation with the fluence conversion coefficients code of the multiples of Swiss clearance limits (LL) for various materials in the CMS experimental cavern at a cooling time of 4 months in LS 3 after the end of proton operation. The prototype of the shield reinforcement in its preliminary design (standard concrete as material) is considered. The results are representative of an average over the azimuthal angle.

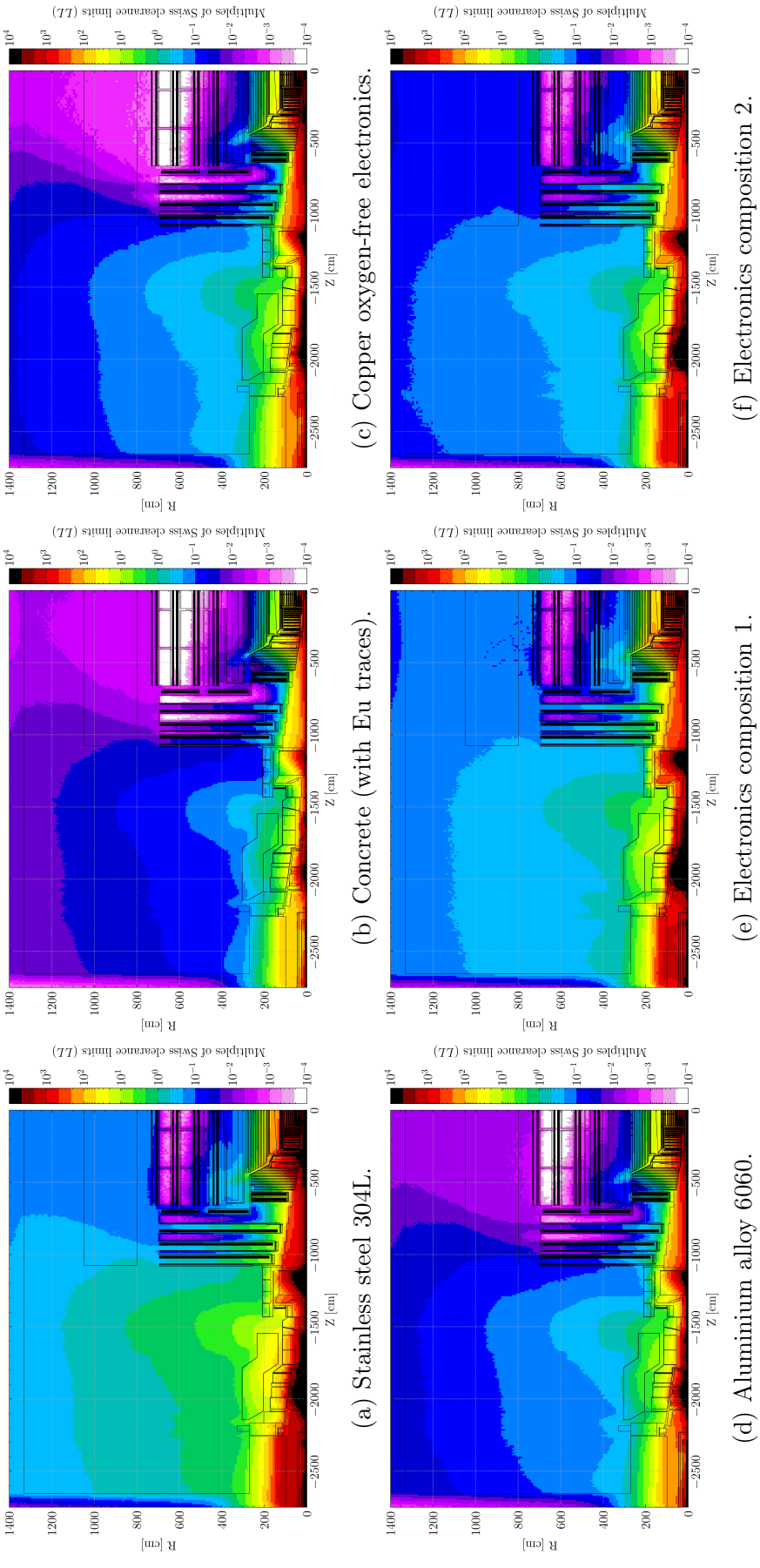

(a) Stainless steel 304L. (b) Concrete (with Eu traces). (c) Copper oxygen-free electronics.

(d) Aluminium alloy 6060. (e) Electronics composition 1. (f) Electronics composition 2.

Figure C.3: FLUKA simulation with the fluence conversion coefficients code of the multiples of Swiss clearance limits (LL) for various materials in the CMS experimental cavern at a cooling time of 4 months in LS 3 after the end of proton operation. The prototype of the shield reinforcement in its final design is considered for one side only of the cavern. The results are representative of an average over the azimuthal angle.

C.3 Additional plots for the ALICE clearance studies in Section 6.3

As presented in Section 6.1, a radiological zoning will be needed at ALICE for clearance operations in Long Shutdown (LS) 3 and for the decommissioning of the Run 4 detector in LS 4. To complement and support the discussion, the radiological maps for the multiples of Swiss clearance limits (LL) at 3 months cooling time in LS 4 for concrete, copper oxygen-free electronics, aluminium alloy 6060, two electronics compositions, pure silicon and lead-tungstate are here reported.

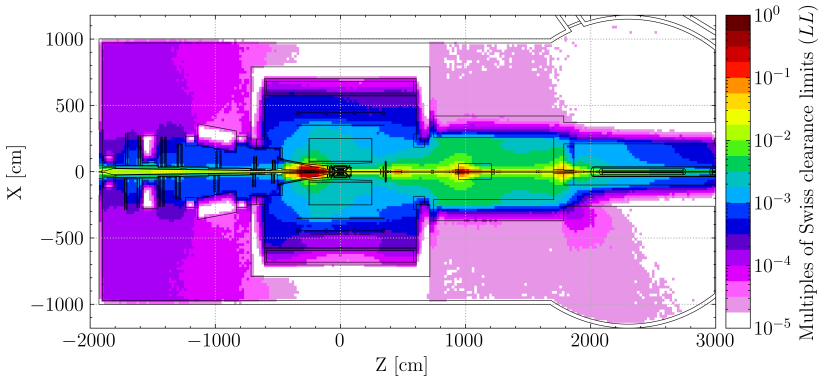

(a) Stainless steel 304L, horizontal.

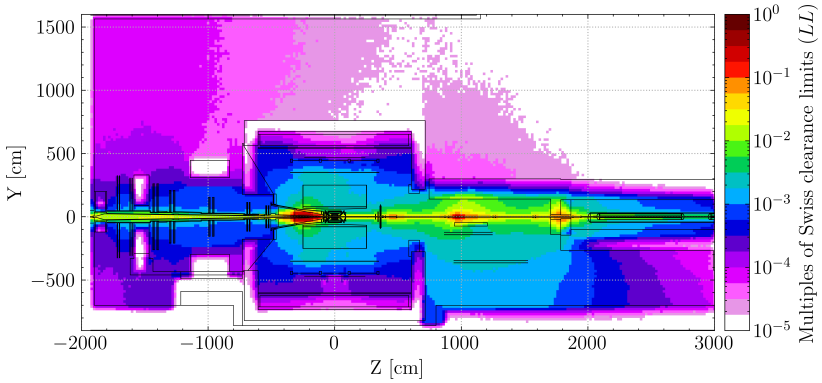

(b) Stainless steel 304L, vertical.

Figure C.4: FLUKA simulation with the fluence conversion coefficients code of the multiples of Swiss clearance limits (LL) for various materials in the ALICE experimental cavern at a cooling time of 3 months in the LS 4.

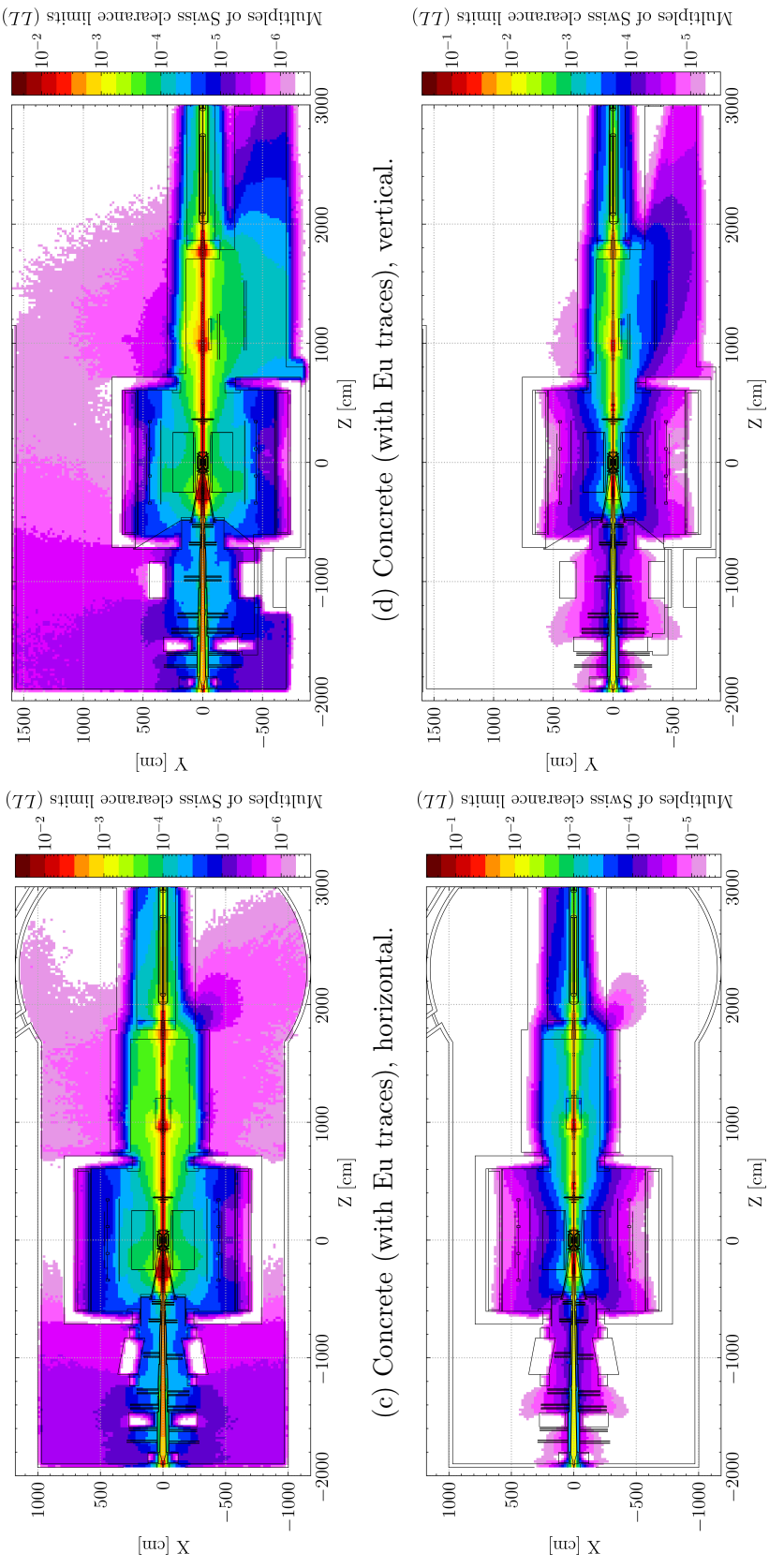

(c) Concrete (with Eu traces), horizontal.

(d) Concrete (with Eu traces), vertical.

(e) Copper oxygen-free electronics, horizontal.

(f) Copper oxygen-free electronics, vertical.

Figure C.4: FLUKA simulation with the fluence conversion coefficients code of the multiples of Swiss clearance limits (LL) for various materials in the ALICE experimental cavern at a cooling time of 3 months in the LS 4 (cont.).

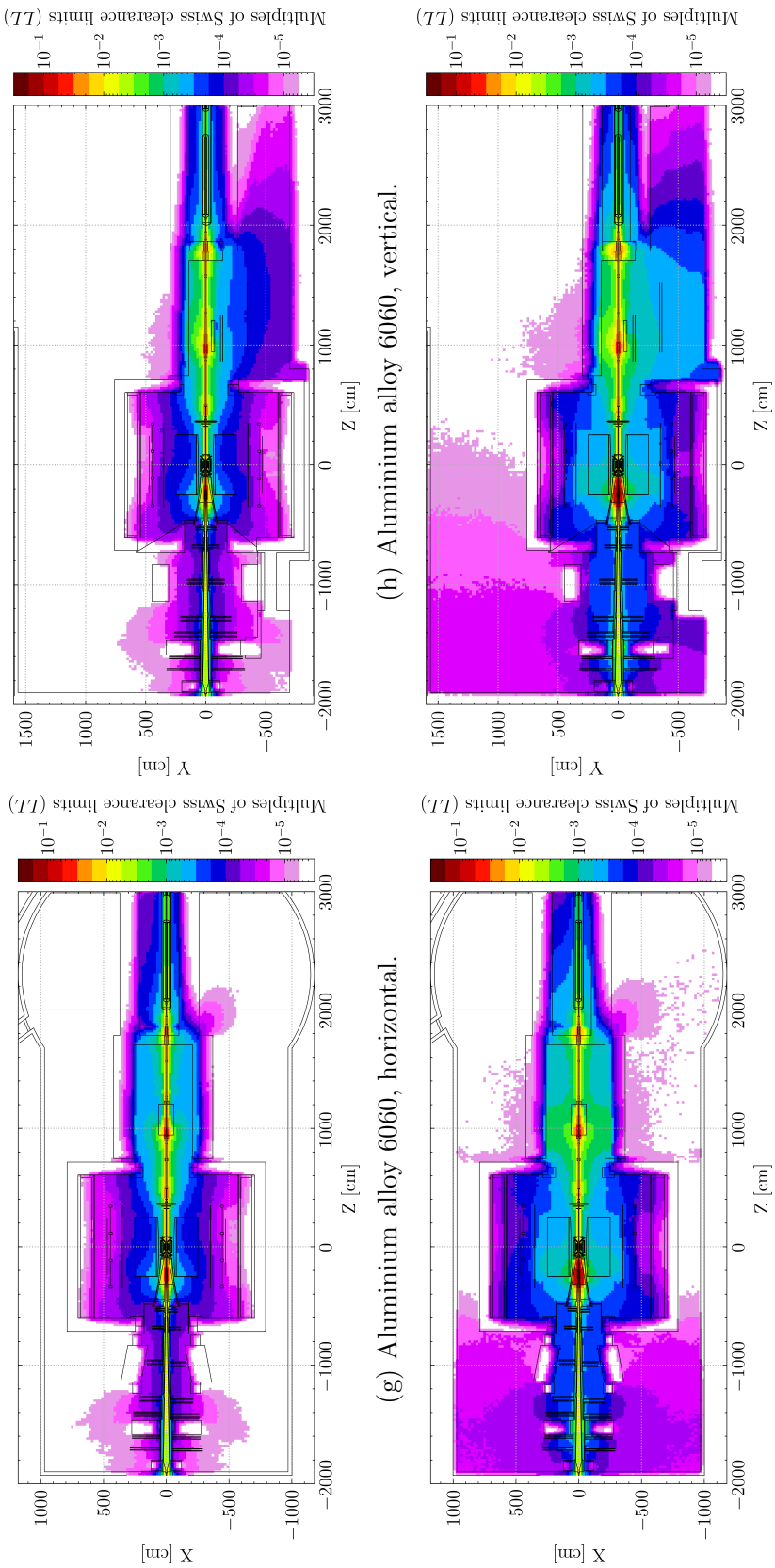

(g) Aluminium alloy 6060, horizontal.

(h) Aluminium alloy 6060, vertical.

(i) Electronics composition 1, horizontal.

(j) Electronics composition 1, vertical.

Figure C.4: FLUKA simulation with the fluence conversion coefficients code of the multiples of Swiss clearance limits (LL) for various materials in the ALICE experimental cavern at a cooling time of 3 months in the LS 4 (cont.).

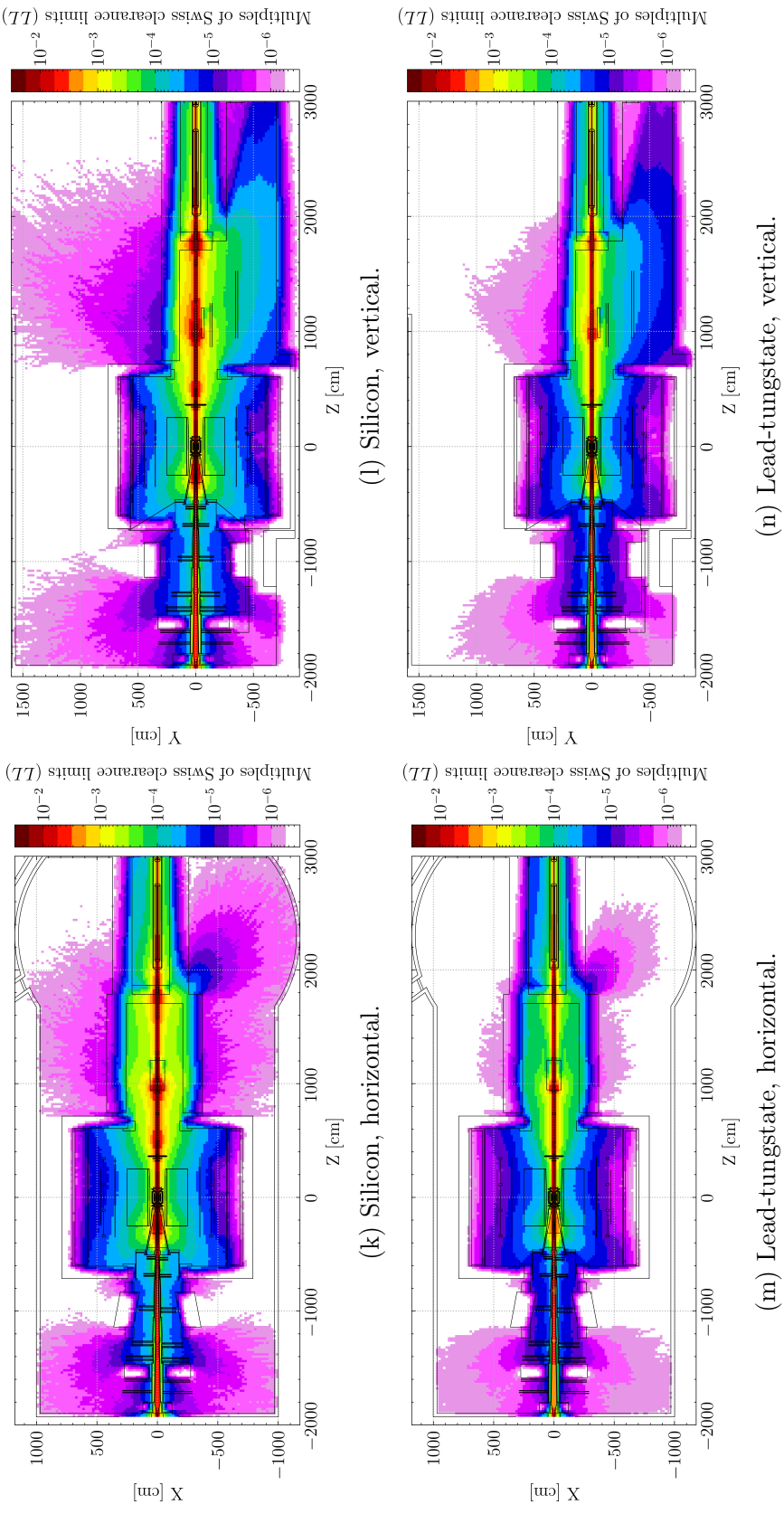

(k) Silicon, horizontal.

(l) Silicon, vertical.

(m) Lead-tungstate, horizontal.

(n) Lead-tungstate, vertical.

Figure C.4: FLUKA simulation with the fluence conversion coefficients code of the multiples of Swiss clearance limits (LL) for various materials in the ALICE experimental cavern at a cooling time of 3 months in the LS 4 (cont.).

List of Figures

The complete and ordered list of figures included in this thesis and the corresponding number of the page at which they appear are here reported for convenience.

List of Tables

The complete and ordered list of tables included in this thesis and the corresponding number of the page at which they appear are here reported for convenience.

Bibliography

[1] E. Lyndon and P. Bryant. *LHC Machine*. In: *JINST* **3** (2008), S08001. DOI: 10.1088/1748-0221/3/08/S08001.

[2] E. Lopienska. *The CERN accelerator complex, layout in 2022. Complexe des accélérateurs du CERN en janvier 2022*. CERN CDS record 2800984 (2022).

[3] The ATLAS Collaboration. *Observation of a new particle in the search for the Standard Model Higgs boson with the ATLAS detector at the LHC*. In: *Physics Letters B* **716**.1 (2012), pp. 1–29. DOI: https://doi.org/10.1016/j.physletb.2012.08.020.

[4] The CMS Collaboration. *Observation of a new boson at a mass of 125 GeV with the CMS experiment at the LHC*. In: *Physics Letters B* **716**.1 (2012), pp. 30–61. DOI: https://doi.org/10.1016/j.physletb.2012.08.021.

[5] The High Luminosity LHC Project website.
URL: https://hilumilhc.web.cern.ch/ (last accessed July 2022).

[6] O. Aberle, I. Béjar Alonso, O. Brüning, P. Fessia, L. Rossi, L. Tavian, and M. Zerlauth. *High-Luminosity Large Hadron Collider (HL-LHC): Technical design report*. In: *CERN Yellow Reports: Monographs* **10** (2020). DOI: 10.23731/CYRM-2020-0010.

[7] European Strategy Group. *2020 Update of the European Strategy for Particle Physics*. Tech. rep. CERN-ESU-013 (2020). DOI: 10.17181/ESU2020.

[8] The TOTEM Collaboration. *First measurement of elastic, inelastic and total cross-section at $\sqrt{s} = 13\,\text{TeV}$ by TOTEM and overview of cross-section data at LHC energies*. In: *Eur. Phys. J. C* **79**.103 (2019). DOI: 10.1140/epjc/s10052-019-6567-0.

[9] F. Hartmann and A. Sharma. *Multipurpose detectors for high energy physics, an introduction*. In: *Nucl. Instrum. Methods Phys. Res. A: Accel. Spectrom. Detect. Assoc. Equip.* **666** (2012), pp. 1–9. DOI: https://doi.org/10.1016/j.nima.2011.11.023.

[10] The ATLAS Collaboration website.
URL: https://atlas.cern/ (last accessed July 2022).

[11] The ATLAS Collaboration. *The ATLAS Experiment at the CERN Large Hadron Collider*. In: *JINST* **3** (2008), S08003. DOI: 10.1088/1748-0221/3/08/S08003.

[12] The ATLAS Collaboration. *New Small Wheel Technical Design Report*. Tech. rep. CERN-LHCC-2013-006, ATLAS-TDR-020. CERN CDS record 1552862 (2013).

[13] The ATLAS Collaboration. *Technical Design Report for the ATLAS Inner Tracker Strip Detector*. Tech. rep. CERN-LHCC-2017-005, ATLAS-TDR-025. CERN CDS record 2257755 (2017).

[14] The ATLAS Collaboration. *Technical Design Report for the ATLAS Inner Tracker Pixel Detector*. Tech. rep. CERN-LHCC-2017-021, ATLAS-TDR-030. CERN CDS record 2285585 (2017).

[15] The ATLAS Collaboration. *Technical Design Report: A High-Granularity Timing Detector for the ATLAS Phase-II Upgrade*. Tech. rep. CERN-LHCC-2020-007, ATLAS-TDR-031. CERN CDS record 2719855 (2020).

[16] The ALICE Collaboration. *The ALICE Experiment at the CERN Large Hadron Collider*. In: *JINST* **3** (2008), S08002. DOI: 10.1088/1748-0221/3/08/S08002.

[17] The ALICE Collaboration website.
URL: https://alice.cern/ (last accessed July 2022).

[18] The ALICE Collaboration. *Schematics of ALICE as during Run 3*. CERN CDS Record 2263642 (2017).

[19] The ALICE Collaboration. *Letter of Intent for an ALICE ITS Upgrade in LS3*. Tech. rep. CERN-LHCC-2019-018, LHCC-I-034. CERN CDS Record 2703140 (2019).

[20] The ALICE Collaboration. *Letter of Intent: A Forward Calorimeter (FoCal) in the ALICE experiment*. Tech. rep. CERN-LHCC-2020-009, LHCC-I-036. CERN CDS record 2719928 (2020).

[21] The CMS Collaboration. *Cutaway diagrams of CMS detector*. CERN CDS Record 2665537 (2019).

[22] The CMS Collaboration. *CMS Detector Slice*. CERN CDS Record 2120661 (2016).

[23] The CMS Collaboration. *The CMS Experiment at the CERN LHC*. In: *JINST* **3** (2008), S08004. DOI: 10.1088/1748-0221/3/08/S08004.

[24] The CMS Collaboration website.
URL: https://cms.cern/ (last accessed July 2022).

[25] The CMS Collaboration. *The CMS trigger system*. In: *JINST* **12** (2017), P01020. DOI: 10.1088/1748-0221/12/01/P01020.

[26] The CMS Collaboration. *The Phase-2 Upgrade of the CMS Tracker*. Tech. rep. CERN-LHCC-2017-009, CMS-TDR-014. CERN CDS record 2272264 (2017).

[27] The CMS Collaboration. *The Phase-2 Upgrade of the CMS Endcap Calorimeter*. Tech. rep. CERN-LHCC-2017-023, CMS-TDR-019. CERN CDS record 2293646 (2017).

[28] The CMS Collaboration. *A MIP Timing Detector for the CMS Phase-2 Upgrade.* Tech. rep. CERN-LHCC-2019-003, CMS-TDR-020. CERN CDS record 2667167 (2019).

[29] The LHCb Collaboration. *LHCb Tracker Upgrade Technical Design Report.* Tech. rep. CERN-LHCC-2014-001, LHCB-TDR-015. CERN CDS record 1647400 (2014).

[30] The LHCb Collaboration. *The LHCb Detector at the LHC.* In: *JINST* **3** (2008), S08005. DOI: 10.1088/1748-0221/3/08/S08005.

[31] The LHCb Collaboration website.
URL: https://lhcb-outreach.web.cern.ch/ (last accessed July 2022).

[32] The LHCb Collaboration. *Framework TDR for the LHCb Upgrade II - Opportunities in flavour physics, and beyond, in the HL-LHC era.* Tech. rep. CERN-LHCC-2021-012, LHCB-TDR-023. CERN CDS record 2776420 (2021).

[33] The Particle Data Group Collaboration. *Review of Particle Physics.* In: *PTEP* **2022** (2022), p. 083C01. DOI: 10.1093/ptep/ptac097.

[34] H. Bethe. *Zur Theorie des Durchgangs schneller Korpuskularstrahlen durch Materie.* In: *Annalen der Physik* **397**.3 (1930), pp. 325–400. DOI: 10.1002/andp.19303970303.

[35] C. Leroy and P. Rancoita. *Principles of radiation interaction in matter and detection.* World Scientific, 2011.

[36] M. S. Livingston and H. Bethe. *Nuclear Physics C. Nuclear Dynamics, Experimental.* In: *Rev. Mod. Phys.* **9** (1937). DOI: 10.1103/RevModPhys.9.245.

[37] W. H. Barkas, W. Birnbaum, and F. M. Smith. *Mass-Ratio Method Applied to the Measurement of L-Meson Masses and the Energy Balance in Pion Decay.* In: *Phys. Rev.* **101** (1956). DOI: 10.1103/PhysRev.101.778.

[38] J. Lindhard and A. H. Sörensen. *Relativistic theory of stopping for heavy ions.* In: *Phys. Rev. A* **53** (1996). DOI: 10.1103/PhysRevA.53.2443.

[39] M. J. Berger and S. M. Seltzer. *Tables of Energy Losses and Ranges of Electrons and Positrons.* Tech. rep. NASA-SP-3012. NASA NTRS Document 19650002905 (1964).

[40] A. Lechner. *Particle interactions with matter.* In: *CERN Yellow Rep. School Proc.* **5** (2018), p. 47. DOI: 10.23730/CYRSP-2018-005.47.

[41] Y.-S. Tsai. *Pair production and Bremsstrahlung of charged leptons.* In: *Rev. Mod. Phys.* **46** (1974). DOI: 10.1103/RevModPhys.46.815.

[42] N. V. Mokhov and F. Cerutti. *Beam–Material Interactions.* In: *CERN Yellow Reports* (). Proceedings of the 2014 Joint International Accelerator School: Beam Loss and Accelerator Protection. Newport Beach, USA, November 5-14 2014 (2016). DOI: 10.5170/CERN-2016-002.83.

[43] W. Heitler. *The Quantum Theory of Radiation.* Clarendon Press, 1954.

[44] A. Ferrari and P. R. Sala. *The Physics of High Energy Reactions*. Tech. rep. ATL-PHYS-97-113, ATL-GE-PN-113. Proceedings of the Workshop on Nuclear Reaction Data and Nuclear Reactors, Physics, Design and Safety, Trieste, Italy, 15 April-17 May 1996. CERN CDS record 682497 (1997).

[45] A. H. Sullivan. *Guide to radiation and radioactivity levels near high energy particle accelerators*. Ashford: Nucl. Techn. Publ., 1992.

[46] A. J. M. Plompen, O. Cabellos, C. De Saint Jean, M. Fleming, A. Algora, M. Angelone, P. Archier, E. Bauge, O. Bersillon, A. Blokhin, et al. *The joint evaluated fission and fusion nuclear data library, JEFF-3.3*. In: *Eur. Phys. J. A* **56**.181 (2020). DOI: 10.1140/epja/s10050-020-00141-9.

[47] K. S. Krane. *Introductory nuclear physics*. Wiley, 1988.

[48] F. Hartmann. *Evolution of Silicon Sensor Technology in Particle Physics*. Springer, 2017.

[49] M. Moll. *Radiation damage in silicon particle detectors: Microscopic defects and macroscopic properties*. PhD thesis. University of Hamburg, 1999.

[50] H. Bateman. *The solution of a system of differential equations occurring in the theory of radio-active transformations*. In: *Proc. Cambridge Philos. Soc.* **15** (1910).

[51] J. Cetnar. *General solution of the Bateman equations for nuclear transmutations*. In: *Annals of Nuclear Energy* **33** (2006). DOI: doi:101016/janucene200602004.

[52] Raymond Dreher. *Modified Bateman solution for identical eigenvalues*. In: *Annals of Nuclear Energy* **53** (2013), pp. 427–438. DOI: https://doi.org/10.1016/j.anucene.2012.06.019.

[53] International Commission on Radiological Protection. *1990 Recommendations of the International Commission on Radiological Protection. ICRP Publication 60*. In: *Ann. ICRP* **21** (1991).

[54] International Commission on Radiological Protection. *The 2007 Recommendations of the International Commission on Radiological Protection. ICRP Publication 103*. In: *Ann. ICRP* **37** (2007).

[55] International Commission on Radiological Protection. *Conversion Coefficients for Radiological Protection Quantities for External Radiation Exposures. ICRP Publication 116*. In: *Ann. ICRP* **40** (2010).

[56] *IAEA Safety Glossary: 2018 Edition*. Vienna: IAEA, 2019. URL: https://www.iaea.org/publications/11098/iaea-safety-glossary-2018-edition.

[57] *Accord entre l'Organisation Europeenne pour la Recherche Nucleaire, le Conseil Federal Suisse, et le Gouvernement de la Republique Française relatif à la Protection contre les rayonnements ionisants et à la Sûreté des Installations de l'Organisation Europeenne pour la Recherche Nucleaire.*
URL: https://hse.cern/content/rprs-tripartite-agreement (last accessed September 2022).

[58] D. Forkel-Wirth, S. Roesler, M. Silari, M. Streit-Bianchi, C. Theis, H. Vincke, and H. Vincke. *Radiation protection at CERN*. In: *Proc. of the CAS: Course on High Power Hadron Machines, 24 May - 2 Jun 2011, Bilbao, Spain* (2013). DOI: 10.5170/CERN-2013-001.415.

[59] Swiss Federal Council. *Ordonnance sur la radioprotection (ORaP) du 26 avril 2017. Recueil officiel des lois fédérales, Ordonnance n. 814.501* (2018).

[60] A. Fassò, A. Ferrari, and P. R. Sala. *Radiation transport calculations and simulations*. In: *Radiation Protection Dosimetry* **137** (2009), pp. 118–133. DOI: 10.1093/rpd/ncp190.

[61] S. A. Dupree and S. K. Fraley. *A Monte Carlo Primer*. Springer, 2002.

[62] J.D. Cossairt and M. Quinn. *Accelerator Radiation Physics for Personnel and Environmental Protection*. CRC Press, 2019.

[63] C. Ahdida, D. Bozzato, D. Calzolari, F. Cerutti, N. Charitonidis, A. Cimmino, A. Coronetti, G. L. D'Alessandro, A. Donadon Servelle, L. S. Esposito, R. Froeschl et al. *New Capabilities of the FLUKA Multi-Purpose Code*. In: *Frontiers in Physics* **9** (2022), p. 788253. DOI: 10.3389/fphy.2021.788253.

[64] G. Battistoni, T. Boehlen, F. Cerutti, P. W. Chin, L. S. Esposito, A. Fassò, A. Ferrari, A. Lechner, A. Empl, A. Mairani et al. *Overview of the FLUKA code*. In: *Annals of Nuclear Energy* **82** (2015), pp. 10–18. DOI: 10.1016/j.anucene.2014.11.007.

[65] S. Roesler, R. Engel, and J. Ranft. *The Monte Carlo Event Generator DPMJET-III*. In: *Proceedings of the Monte Carlo 2000 Conference, Lisbon, October 23-26 2000* (2001), pp. 1033–1038.

[66] A. Fedynitch. *Cascade equations and hadronic interactions at very high energies*. PhD thesis. Karlsruhe Institute of Technology, 2015.

[67] M. Cavinato, E. Fabrici, E. Gadioli, E. Gadioli Erba, and E. Galbiati. *Monte Carlo calculations using the Boltzmann Master Equation theory of nuclear reactions*. In: *Physics Letters B* **382**.1 (1996), pp. 1–5. DOI: 10.1016/0370-2693(96)00652-1.

[68] M. Cavinato, E. Fabrici, E. Gadioli, E. Gadioli Erba, and G. Riva. *Monte Carlo calculations of heavy ion cross-sections based on the Boltzmann Master equation theory*. In: *Nuclear Physics A* **679**.3 (2001), pp. 753–764. DOI: 10.1016/S0375-9474(00)00357-2.

[69] F. Cerutti, G. Battistoni, G. Capezzali, P. Colleoni, A. Ferrari, E. Gadioli, A. Mairani, and A. Pepe. *Low energy nucleus-nucleus reactions: the BME approach and its interface with FLUKA*. In: *Proc. 11th International Conference on Nuclear Reaction Mechanisms, Varenna (Italy) June 12-16* (2006).

[70] H. Sorge, H. Stöcker, and W. Greiner. *Poincaré invariant Hamiltonian dynamics: Modelling multi-hadronic interactions in a phase space approach*. In: *Annals of Physics* **192**.2 (1989), pp. 266–306.

[71] H. Sorge, H. Stöcker, and W. Greiner. *Relativistic quantum molecular dynamics approach to nuclear collisions at ultrarelativistic energies*. In: *Nuclear Physics A* **498** (1989), pp. 567–576.

[72] A. Lechner, B. Auchmann, T. Baer, C. Bahamonde Castro, R. Bruce, F. Cerutti, L. S. Esposito, A. Ferrari, J. M. Jowett, A. Mereghetti et al. *Validation of energy deposition simulations for proton and heavy ion losses in the CERN Large Hadron Collider*. In: *Phys. Rev. Accel. Beams* **22** (2019), p. 071003. DOI: 10.1103/PhysRevAccelBeams.22.071003.

[73] V. Vlachoudis. *FLAIR: A Powerful But User Friendly Graphical Interface For FLUKA*. In: *Proc. Int. Conf. on Mathematics, Computational Methods & Reactor Physics (M&C 2009), Saratoga Springs, New York, 2009.* (2009), pp. 790–800.

[74] International Commission on Radiological Protection. *Conversion Coefficients for use in Radiological Protection against External Radiation. ICRP Publication 74*. In: *Ann. ICRP* **26** (1996).

[75] International Commission on Radiation Units and Measurements. *Operational Quantities for External Radiation Exposure*. In: *ICRU Report 95* **20** (2020).

[76] T. Sato, Y. Iwamoto, S. Hashimoto, T. Ogawa, T. Furuta, S. Abe, T. Kai, P.-E. Tsai, N. Matsuda, H. Iwase et al. *Features of Particle and Heavy Ion Transport code System (PHITS) version 3.02*. In: *Journal of Nuclear Science and Technology* **55**.6 (2018), pp. 684–690. DOI: 10.1080/00223131.2017.1419890.

[77] Y. Iwamoto, T. Sato, S. Hashimoto, T. Ogawa, T. Furuta, S. Abe, T. Kai, P.-E. Tsai, N. Matsuda, R. Hosoyamada, and K. Niita. *Benchmark study of the recent version of the PHITS code*. In: *Journal of Nuclear Science and Technology* **54**.5 (2017), pp. 617–635. DOI: 10.1080/00223131.2017.1297742.

[78] R. Froeschl, M. Magistris, F. Leite Pereirea, and C. Theis. *Computation of radioactivity in particle accelerators and propagation of uncertainties with the JEREMY code*. Tech. rep. CERN–RP–2014–065–REPORTS–TN (2014).

[79] H. Vincke and C. Theis. *ActiWiz – optimizing your nuclide inventory at proton accelerators with a computer code*. In: *Prog. Nucl. Sci. Tech.* **4** (2014), pp. 228–232. DOI: 10.15669/pnst.4.228.

[80] R. Froeschl. *A method for radiological characterization based on fluence conversion coefficients*. In: *J. Phys.: Conf. Ser.* **1046**.1 (2018), p. 012006. DOI: 10.1088/1742-6596/1046/1/012006.

[81] D. Bozzato and R. Froeschl. *The Fluence Conversion Coefficients method: applications to radiological characterization with the FLUKA and PHITS codes.* Tech. rep. CERN CDS Record 2730147 (2020).

[82] D. Bozzato and R. Froeschl. The Fluence Conversion Coefficients code GitLab repository.

[83] A. Santamarina, D. Bernard, P. Blaise, M. Coste, A. Courcelle, T.D. Huynh, C. Jouanne, P. Leconte, O. Litaize, S. Mengelle, et al. *The JEFF-3.1.1 Nuclear Data Library*. JEFF Report 22. Nuclear Energy Agency, Paris (2009).

[84] N. Otuka, E. Dupont, V. Semkova, B. Pritychenko, A. I. Blokhin, M. Aikawa, S. Babykina, M. Bossant, G. Chen, S. Dunaeva et al. *Towards a More Complete and Accurate Experimental Nuclear Reaction Data Library (EXFOR): International Collaboration Between Nuclear Reaction Data Centres (NRDC)*. In: *Nuclear Data Sheets* **120** (2014), pp. 272–276. DOI: https://doi.org/10.1016/j.nds.2014.07.065.

[85] V. V. Zerkin and B. Pritychenko. *The experimental nuclear reaction data (EXFOR): Extended computer database and Web retrieval system*. In: *Nucl. Instrum. Methods Phys. Res. A: Accel. Spectrom. Detect. Assoc. Equip.* **888** (2018), pp. 31–43. DOI: https://doi.org/10.1016/j.nima.2018.01.045.

[86] CERN. *TIMBER web interface*. URL: https://timber.cern.ch (last accessed November 2022).

[87] D. Bozzato, L. Elie, R. Froeschl, A. Infantino, V. Kouskoura, and T. Lorenzon. *LHC and HL-LHC luminosity and irradiation profiles for Radiation Protection studies*. Tech. rep. CERN CDS Record 2641646 (2022).

[88] G. Arduini, O. Brüning, R. De Maria, R. Garoby, B. Gilardoni, B. Goddard, B. Gorini, M. Meddahi, G. Rumolo, and R. Tomás. *Beam parameters at LHC injection*. CERN CDS Record 1644771 (2014).

[89] J. Mekki, M Brugger, R. G. Alia, A. Thornton, N. C. Dos Santos Mota, and S. Danzeca. *CHARM: A Mixed Field Facility at CERN for Radiation Tests in Ground, Atmospheric, Space and Accelerator Representative Environments*. In: *IEEE Trans. Nucl. Sci.* **63**.4 (2016), pp. 2106–2114. DOI: 10.1109/TNS.2016.2528289.

[90] A. Thornton. *CHARM Facility Test Area Radiation Field Description*. Tech. rep. CERN CDS Record 2149417 (2016).

[91] L. Gatignon. *Beam properties for the East Area irradiation facility in the T8 beam line*. Tech. rep. CERN EDMS record 1270807.

[92] F. Ravotti, R. B. Ruffieux, A. G. Ollacarizqueta. *Calibration of the T08.XSEC devices by means of Al-foil activation and BCTF measurements*. Tech. rep. CERN EDMS record 2783968.

[93] F. Ravotti. *New beam instrumentation for the EA-IRRAD facility on the T08 beam line*. Tech. rep. CERN EDMS record 2379119.

[94] R. Froeschl. *Radiation Protection Assessment of the Proton Irradiation facility and the CHARM facility in the East Area*. Tech. rep. CERN EDMS record 1355933.

[95] E. Iliopoulou. *Commissioning Characterization and Exploitation of the CERN Shielding Benchmark Facility (CSBF)*. PhD thesis. Aristotle University, Thessaloniki, 2018.

[96] R. Froeschl, M. Brugger, and S. Roesler. *The CERN High Energy Accelerator Mixed Field (CHARM) Facility in the CERN PS East Experimental Area*. In: *Proceedings of the 12^{12} meeting of the task-force on Shielding Aspects of Accelerators, Targets and Irradiation Facilities (SATIF12), NEA/NSC/R(2015)3, Batavia, Illinois, United States* (2015), pp. 14–25.

[97] E. Iliopoulou, P. Bamidis, M. Brugger, R. Froeschl, A. Infantino, T. Kajimoto, N. Nakao, S. Roesler, T. Sanami, and A. Siountas. *Measurements and FLUKA simulations of bismuth and aluminium activation at the CERN Shielding Benchmark Facility (CSBF)*. In: *Nucl. Instrum. Methods Phys. Res. A: Accel. Spectrom. Detect. Assoc. Equip.* **885** (2018), pp. 79–85. DOI: https://doi.org/10.1016/j.nima.2017.12.058.

[98] N. Nakao, T.Sanami, T. Kajimoto, H. Yashima, R. Froeschl, D. Bozzato, E. Iliopoulou, A. Infantino, E. Lee, T. Oyama, M. Hagiwara, S. Nagaguro, T. Matsumoto, A. Masuda, Y. Uwamimno, S. Roesler, and M. Brugger. *Measurement and simulations of high-energy neutrons through a various thickness of concrete and steel shield using activation detectors at CHARM*. In: *Journal of Nuclear Science and Technology* (2023). [To be submitted for publication].

[99] N. Nakao, T.Sanami, T. Kajimoto, R. Froeschl, D. Bozzato, E. Iliopoulou, A. Infantino, H. Yashima, E. Lee, T. Oyama, M. Hagiwara, S. Nagaguro, T. Matsumoto, A. Masuda, Y. Uwamimno, S. Roesler, and M. Brugger. *Benchmark experiments for bulk and maze shielding using activation detectors with* 24 GeV/c *protons at CERN/CHARM*. In: *Nuclear Science and Engineering* (2023). [Submitted for publication].

[100] J. Allison et al. *Recent developments in Geant4*. In: *Nucl. Instrum. Methods Phys. Res. A: Accel. Spectrom. Detect. Assoc. Equip.* **835** (2016), pp. 186–225. DOI: https://doi.org/10.1016/j.nima.2016.06.125.

[101] J. Allison et al. *Geant4 developments and applications*. In: *IEEE Trans. Nucl. Sci.* **53** (2006), pp. 270–278. DOI: 10.1109/TNS.2006.869826.

[102] F. Maekawa, U. von Mollendorff, P. P. H. Wilson, M. Wada, and Y. Ikeda. *Production of a dosimetry cross section set up to* 50 MeV. In: *Proc. 10^{th} International Symposium on Reactor Dosimetry, Sep 12-17, 1999, Osaka, Japan* (2001).

[103] T. Oyama, T. Sanami, H. Yashima, M. Hagiwara, N. Nakao, A. Infantino, E. Iliopoulou, R. Froeschl, S. Roesler, T. Kajimoto, E. Lee, S. Nagaguro, T. Matsumoto, A. Masuda, and Y. Uwamino. *Measurements of secondary-particle emissions from copper target bombarded with 24-GeV/c protons*. In: *Nucl. Instrum. Methods Phys. Res. A: Accel. Spectrom. Detect. Assoc. Equip.* **990** (2021). DOI: https://doi.org/10.1016/j.nima.2020.164977.

[104] CERN Geographic Information System.
URL: `https://gis.cern.ch/gisportal/` (last accessed November 2022).

[105] S. Roesler. *Radiological Control of Material from CERN's Radiation Areas.* Tech. rep. CERN EDMS record 942171.

[106] M. Karacson, G. Corti, H. Vincke, D. Wiedner. *Samples for Material Classification in the LHCb Experiment.* Restricted Document.

[107] J. Wenninger. *Operation and Configuration of the LHC in Run 2.* Tech. rep. CERN-ACC-NOTE-2019-0007. CERN CDS record 2668326 (2019).

[108] Online LHCb Run Database.
URL: `https://https://lbrundb.cern.ch/` (last accessed October 2022).

[109] D. Forkel-Wirth. *Zonage radiologique au CERN.* Tech. rep. CERN EDMS record 810149.

[110] S. Roesler. *Radiological control of materials from CERN's radiation area.* Tech. rep. CERN EDMS record 942171.

[111] F. Aberle, G. Dumont, R. Froeschl. *Mesures radiologiques du matériel et des déchets au CERN.* Tech. rep. CERN EDMS record 1968658.

[112] A. Cimmino and R. Froeschl. *Radiological characterization of material in the CMS cavern for LS2.* Tech. rep. CERN EDMS record 2116795.

[113] S. J. Hertzog. *CMS rotating shielding around beam pipe.* CERN CDS record 2749500 (2021).

[114] M. Huhtinen. *Optimization of the CMS forward shielding.* Tech. rep. CMS-NOTE-2000-068. CERN CDS record 687289 (2000).

[115] S. Sgobba and F. Leaux. *CERN technical specification N° 1004 - Ed. 6 – 11.12.2013, 1.4306 (X2CrNi19-11, AISI 304L) stainless steel sheets/plates for vacuum applications not requiring vacuum firing at* 950 ℃. CERN EDMS record 790767 (2013).

[116] A. Infantino, D. Björkman, E. Elie, M. Maietta, C. Tromel, and H. Vincke. *Radiation Protection at the Large Hadron Collider: Problematics, Challenges and Advanced Monte Carlo Simulation Techniques.* In: *Environments* **9**.5 (2022). DOI: `10.3390/environments9050054`.

[117] D. Bozzato, R. Froeschl, and V. Kouskoura. *Operational radiation protection challenges for the LHC experiments.* In: *Radiation Protection Dosimetry* (2023). DOI: `10.1093/rpd/ncad126`.

[118] D. Bozzato and R. Froeschl. *Preliminary estimates of residual dose rates for CMS Phase II open scenarios.* Tech. rep. CERN EDMS record 2787631 (2022).

[119] D. Adamová et al. *A next-generation LHC heavy-ion experiment.* Input to the 2020 Update of the European Particle Physics Strategy. CERN CDS record 2666847 (2019).

[120] W. Riegler, A. Morsch, and A. Tauro. Private communication. CERN, Geneva, 2021.

[121] D. Bozzato and R. Froeschl. *Considerations on heavy ion collisions for radiation protection studies with the FLUKA Monte Carlo code*. Tech. rep. CERN EDMS record 2669373 (2022).

[122] I. Hrivnacova, D. Adamova, V. Berejnoi, R. Brun, F. Carminati, A. Fassó, E. Futo, A. Gheata, I. Gonzalez Caballero, A. Morsch. *The Virtual Monte Carlo*. In: *Proceedings of the 2003 Conference on Computing in High Energy and Nuclear Physics (CHEP03), La Jolla, Ca, USA, March 2003* (2003).

[123] R. Brun, P. Buncic, F. Carminati, A. Morsch, F. Rademakers, and K. Safarik. *Computing in ALICE*. In: *Nucl. Instrum. Methods Phys. Res. A: Accel. Spectrom. Detect. Assoc. Equip.* **502**.2 (2003), pp. 339–346. DOI: https://doi.org/10.1016/S0168-9002(03)00440-6.

[124] D. Bozzato, R. Froeschl and A. Morsch. *Radiological zoning for the ALICE experiment in Long Shutdown 3 and 4*. Tech. rep. CERN EDMS record 2629466 (2021).

[125] D. Bozzato and R. Froeschl. *LHC 2021 Pilot Beam Preparation: FLUKA Monte Carlo Simulations and Operational Radiation Protection Aspects*. In: *Proceedings of the 14th International Conference on Radiation Shielding and 21st Topical Meeting of the Radiation Protection and Shielding Division (ICRS 14/RSPD 2022), Seattle, WA, USA, September 25-29, 2022* (2022).

[126] D. Bozzato and R. Froeschl. *Radiological characterization with a fluence conversion coefficients based method: a practical example of the preparatory studies to the pilot beam at the CERN Large Hadron Collider*. In: *Nuclear Science and Engineering* (2023). [Submitted for publication].

[127] R. Froeschl, F. P. La Torre, and N. Walter. *The ActiWiz material composition catalogue*. Tech. rep. CERN-RP-2012-002-REPORTS-TN. CERN EDMS record 1277395.

Acknowledgments

First and foremost, I wish to warmly and profoundly thank my CERN supervisor Dr. Robert Froeschl for giving me this opportunity in the first place, for his continuous guidance, and for his exceptional personal and professional support throughout my work period at CERN.

I am also deeply grateful to my KIT supervisor PD Dr. Frank Hartmann for his extremely valuable advice and help, and to Prof. Dr. Thomas Müller for kindly agreeing to be my second reviewer.

For many aspects of my work, I am much obliged to several colleagues without whose input it would have been much harder to achieve many results. Therefore, I wish to thank Dr. Francesco Cerutti and Dr. Francesc Salvat Pujol for the useful discussions on FLUKA and cross sections; Sophie Mallows and the CMS BRIL Radiation Simulation Group for providing baseline simulation files and for always being available to review my results; the ATLAS Radiation Simulation Group for providing the ATLAS FLUKA simulation geometry; Dr. Matthias Karacson for sharing the LHCb FLUKA simulation geometry and for the useful discussions on the activation samples; Dr. Andreas Morsch for the fruitful collaboration on the ALICE simulations; Dr. Noriaki Nakao and Dr. Toshiya Sanami for the collaboration with the measurements at CHARM and CSBF.

I would also like to express my gratitude to my colleagues Isabel Brunner and Christelle Saury for their help with operational radiation protection activities, and to Dr. Nabil Menaa and the colleagues from the Radiation Protection Analytical Laboratory for the gamma spectrometry of the activation samples.

Special thanks go to my colleague and friend Tommaso Lorenzon for the many personal and professional conversations we had and for the fun and relaxed times we shared. I am also very happy that in these three years I met marvellous people who, on many occasions, made my days better despite the stressful times. Therefore, I wish to personally thank Claudia Ahdida, Arnaud Devienne, Patrycja Dyrcz, Lucie Elie, Alice Formento, Andrea Gomes, Angelo Infantino, Vasiliki Kouskoura, Giacomo Lavezzari, Giuseppe Mazzola, Elzbieta Nowak, Fabio Pozzi, Francisco Ogallar Ruiz, Xavier Ouvrard, Marco Tisi, and Markus Widorski.

I am grateful to my CERN friends that have encouraged me (and most importantly have put up with me) over these years. Thanks to Adam, Alice, Ana, Daniele, Dimitra, Foteini, Giulia, Joao, Nadir, Pinelopi, Miltos, and Sharon.

I feel very lucky to have lifelong friends that, despite the distance, have always

been there for me, especially when I needed them most. I am profoundly grateful to Lorenzo, Lucilla, Matteo, Mattia, and Samantha.

Finally, I would like to wholeheartedly thank my grandparents Gianfranco and Margherita and my whole family for their support, and again my parents Enrica and Roberto and my sister Sara for always believing in me and for their many sacrifices over the years that allowed me to complete this achievement.

Infine, vorrei ringraziare di cuore i miei nonni Gianfranco e Margherita e tutta la mia famiglia per il loro supporto, e di nuovo i miei genitori Enrica e Roberto e mia sorella Sara per aver sempre creduto in me e per i loro numerosi sacrifci che mi hanno permesso di completare questo traguardo.

Geneva, January 2023
Davide Bozzato